DISSERTATION

SMOKY SKIES AND POLAR AIR: AEROSOL MICROPHYSICS ACROSS SCALES

Submitted by

Nicole Ann June

Department of Atmospheric Science

In partial fulfillment of the requirements

For the Degree of Doctor of Philosophy

Colorado State University

Fort Collins, Colorado

Summer 2025

Doctoral Committee:

Advisor: Jeffrey R. Pierce

Jeffrey L. Collett Jr.
Sonia M. Kreidenweis
Shantanu H. Jathar
Megan D. Willis

ABSTRACT

SMOKY SKIES AND POLAR AIR: AEROSOL MICROPHYSICS ACROSS SCALES

Atmospheric aerosol particles are important to understand as they have implications on climate and human health. These particles may be emitted directly or form in the atmosphere through secondary processes. In this dissertation, we focus on two systems of aerosol sources, microphysics, and chemistry: 1) wildfires and 2) the springtime marine Arctic.

Biomass Burning Plume Injection Height: The magnitude of biomass burning impacts on air quality and climate are altered by the biomass burning plume injection height (BB-PIH). However, these alterations are not well-understood on a global scale. We present the novel implementation of BB-PIH in global simulations with an atmospheric chemistry model (GEOS-Chem) coupled with detailed TwO-Moment Aerosol Sectional (TOMAS) microphysics (GC-TOMAS). We conduct BB-PIH simulations under three scenarios: 1) all smoke is well-mixed into the boundary layer, and 2) and 3) smoke injection height is based on Global Fire Assimilation System (GFAS) plume heights. Elevating BB-PIH increases the simulated global-mean aerosol optical depth (10%) despite a global-mean decrease (1%) in near-surface $PM_{2.5}$. Increasing the tropospheric column mass yields enhanced cooling by the global-mean clear-sky biomass burning direct radiative effect. However, increasing BB-PIH places more smoke above clouds in some regions; thus, the all-sky biomass burning direct radiative effect has weaker cooling in these regions as a result of increasing the BB-PIH. Elevating the BB-PIH increases the simulated global-mean cloud condensation nuclei concentrations at low-cloud altitudes, strengthening the global-mean cooling of the biomass burning aerosol indirect effect with a more

than doubling over marine areas. Elevating BB-PIH also generally improves model agreement with the satellite-retrieved total and smoke extinction coefficient profiles. Our two-year global simulations with new BB-PIH capability enable understanding of the global-scale impacts of BB-PIH modeling on simulated air-quality and radiative effects, going beyond the current understanding limited to specific biomass burning regions and seasons.

Aerosol Aging in Wildfire Smoke: The evolution of organic aerosol (OA) composition and aerosol size distributions within smoke plumes are uncertain due to variability in the rates of OA evaporation/condensation and coagulation within a plume. It remains unclear how the evolution varies across different parts of individual plumes. We use a large eddy simulation model coupled with aerosol-microphysics and radiation models to simulate the Williams Flats fire sampled during the FIREX-AQ field campaign. At aircraft altitude, the model captures observed aerosol changes through 4 hr of aging. The model evolution of primary OA (POA), oxidized POA (OPOA), and secondary OA (SOA) shows that >90% of the SOA formation occurs before the first transect (~40 min of aging). Lidar observations and the model show a significant amount of smoke in the planetary boundary layer (PBL) and free troposphere (FT), with the model having equal amounts of smoke in the PBL and FT. Due to faster initial dilution, PBL concentrations are more than a factor of two lower than the FT concentrations, resulting in slower coagulational growth in the PBL. A 20 K temperature decrease with height in the PBL influences faster POA evaporation near the surface, while net OA evaporation in the FT is driven by continued dilution after the first aircraft transect. Net OA condensation in the PBL after the first transect is the result of areas with higher OH concentration leading to OPOA formation. Our results motivate the need for systematic observations of the vertical gradients of aerosol size and composition within smoke plumes.

Springtime Marine Arctic Sulfur Chemistry: Dimethyl sulfide (DMS) and methanethiol (MeSH) are important natural sources of sulfur to the atmosphere and influence the aerosol populations in the marine atmosphere. We use GC-TOMAS and data from the ARTofMELT field campaign to analyze sulfur chemistry in the Fram Strait during May and June 2023. We find that updating the model to include the emission of DMS from regions of partial ice cover improves model-observation agreement of DMS and MeSH by over half-an-order-of-magnitude. Model-observation agreement of MeSH is less than that of DMS suggesting model biases in MeSH emissions and/or lifetime. The model-observation agreement of DMS and MeSH varies depending on the oceanic DMS concentration dataset. The monthly oceanic DMS climatology has the lowest magnitude bias of atmospheric DMS during periods of ocean influence, while the daily oceanic DMS prediction by an artificial neural network has the most consistent bias for atmospheric DMS across the differing source regions. The primary DMS oxidation pathway in the model is OH-addition with 64% of the DMS oxidation occurring through that pathway in the campaign average; however, the model likely underestimates the importance of the BrO oxidation pathway due to biases in halogen sources and chemistry. During fog, the aqueous oxidation of DMS with O_3 becomes important. The DMS oxidation product of DMSO is underestimated in the model due to the biases in DMS, wet deposition of DMSO, and biases in oxidants. Our results motivate the need for continued improvement of the representation of the sulfur budget in the marine Arctic.

Aerosol Size and Composition in the Springtime Marine Arctic: Aerosol size and composition are key to understanding aerosol radiative effects as they impact aerosol lifetime, scattering and absorption properties, and ability to be cloud condensation nuclei. In this study, we aim to understand GC-TOMAS biases of aerosol size and composition during ARTofMELT.

We conduct several sensitivity model simulations to determine the impact of blowing snow emissions, more vigorous wet-removal, a marine source of SOA precursor, and nucleation from organics with sulfuric acid on model-observation agreement. We find that there is likely an Arctic marine source of SOA precursor contributing to the OA mass and accumulation mode number concentrations during the campaign. However, the model has a high bias in OA mass and in the accumulation mode throughout the campaign, indicating the assumed model emission flux of the marine SOA precursor is high. There is limited ammonia in the region of the ship, limiting the new particle formation (NPF) through ternary nucleation. As a result, the simulations suggest the importance of the organics with sulfuric acid nucleation mechanism to explaining the observed NPF events. Lastly, we find that the removal of accumulation mode particles through drizzle in marine Arctic low-level clouds helps to reduce the overestimate of the accumulation mode, but increases the underestimate of the nucleation mode. Overall, despite continued efforts to understand the aerosol population in the Arctic, there remain deficits in the ability of a regional model to accurately represent the size and composition of aerosols.

ACKNOWLEDGEMENTS

First, I would like to thank my advisor, Jeff Pierce, for all the thoughtful research discussions, guidance, and patience. Moving across the country to Colorado in July 2020 in the middle of the pandemic proved to be more difficult than I thought it would be, and Jeff was always patient and willing to work with me to ensure my happiness both at work and in life. Next, I would like to thank my committee members for their thoughtful feedback and willingness to serve on my committee. To the Pierce Group: thanks for the group lunches with sometimes random topics of conversation that rarely had to do with research; they always provided a nice break in the day.

Three years ago, I started volunteering to walk dogs at Animal Friends Alliance. The other volunteers at the shelter and the dogs have given me an outside of work activity to look forward to every week. I love seeing the dogs find their forever homes. My time at Animal Friends Alliance will be one of my favorite memories of my time in Fort Collins.

My interest in atmospheric science has evolved a lot from when I decided I wanted to be a meteorologist when I was 8 years old. The interest and love of weather at that young age was instilled in me by my Grandma Cora and my dad. My dad calls me his personal meteorologist. Although forecasting isn't my favorite, I will always forecast for him. I also want to thank my mom for always taking my post-test panic phone calls and calming me down.

Lastly, Allen, thanks for believing in me and always reminding me that graduate school is temporary. I also want to thank him for all the times he provided feedback on my figures, even though I nearly always sent them as blurry pictures of a computer screen.

TABLE OF CONTENTS

Chapter 1: Introduction

1.1 Background and Motivation

Aerosols are found throughout the atmosphere and have both direct and indirect effects on climate (Bellouin et al., 2020; Boucher et al., 2013; Haywood and Boucher, 2000). The aerosol direct radiative effect (DRE) is caused by particles scattering/absorbing incoming solar radiation (Boucher et al., 2013; Charlson et al., 1991). The aerosol indirect effect (AIE) results from aerosols altering the cloud drop number concentration (CDNC) which leads to changes in cloud albedo, lifetime, and precipitation efficiency (Albrecht, 1989; Clement et al., 2009; Gryspeerdt et al., 2014; Lee et al., 2013; Pierce and Adams, 2007; Twomey, 1974). Overall, the combined climate effects of aerosols through the DRE and AIE remain one of the most uncertain pieces in understanding past and future climate in part due to the uncertainty in the pre-industrial state of aerosols and in part due to uncertainty in the emission and representation of aerosol microphysics in models (Boucher et al., 2013).

Particle size and composition influence the magnitude of the DRE and AIE (Lee et al., 2013; Seinfeld and Pandis, 2016; Spracklen et al., 2011; Twomey, 1974), as well as the possible health implications of aerosols (Kodros et al., 2018a). Particles are deposited into different locations in the respiratory tract based on particle size, with smaller particles being more harmful because they can make it deeper into the lungs (Hinds, 1999; Kodros et al., 2018a). Additionally, particle toxicity has been connected to particle size (Jalava et al., 2006; Johnston et al., 2019; Leonard et al., 2007). The scattering and absorption efficiencies of aerosols influence the magnitude and sign of the DRE and are determined by the composition and size of aerosols with the efficiencies generally peaking between 100 nm and 1 μm in diameter dependent on composition (Seinfeld and Pandis, 2016). Only particles that can act as cloud condensation

nuclei (CCN) can influence CDNC to impact the AIE. Generally CCN have a size larger than 40-100 nm; however, the supersaturation required for a CCN to activate into a cloud drop is altered by its hygroscopicity parameter (κ) (Petters and Kreidenweis, 2007). Particles with a higher κ require a lower critical supersaturation to activate, allowing for activation into cloud drops at smaller diameters (Petters et al., 2009; Petters and Kreidenweis, 2007). Primary sources of aerosol particles include emission from land, marine and ice surfaces (e.g. dust, sea spray, snow; (Gong et al., 2023; Huang et al., 2020; Jaeglé et al., 2011; Zender et al., 2003)), and combustion sources (e.g. biomass burning, vehicles, power plants; (Akagi et al., 2011; Jathar et al., 2014; Jen et al., 2019)). Particulate matter with a diameter smaller than 1 μm (PM1) can be comprised of organic aerosol (OA), black carbon (BC), and inorganics (e.g. sulfate, chlorine, ammonium, nitrate, and many trace metals) (Jimenez et al., 2009; Shrivastava et al., 2017; Sillanpää et al., 2006). The exact composition and size of particulate matter (PM) varies depending on the source. For example, in biomass burning smoke PM smaller than 1 μm in diameter tends to be greater than 90% OA by mass (Bond et al., 2013; Hodshire et al., 2019a; June et al., 2022; Reid et al., 2005b). In Arctic marine environments there can be more variable in composition with the Aitken and accumulation modes being made up mostly of sulfate and organics, while particulate larger than 1 μm in diameter is mostly sea salt (Barrett et al., 2015; Croft et al., 2016; Frossard et al., 2011; Willis et al., 2018).

New particle formation and growth (NPF&G) is an important global source of aerosols (Fanourgakis et al., 2019; Gordon et al., 2017; Kulmala and Kerminen, 2008; Zhao et al., 2024). To survive and reach sizes that influence the DRE and AIE, particlees must avoid being scavenged through coagulation by larger pre-existing particles and grow primarily through condensation of low-volatility gases to larger sizes (Pierce and Adams, 2007; Wang et al., 2020;

Westervelt et al., 2014). There is spatial and temporal variability in NPF events, making them difficult to accurately represent in large scale models that need to represent a diverse range of environmental conditions (Lee et al., 2019). In models, NPF is often represented using theoretical and empirical relationships often depending on sulfuric acid and some combination of ammonia, iodine, amines, water vapor, and organic species (Allan et al., 2015; Baccarini et al., 2020; Dunne et al., 2016; Lee et al., 2019; O'Donnell et al., 2023; Riccobono et al., 2014; Zhao et al., 2024).

Organic aerosol (OA) is a large fraction of submicron particulate matter mass with much of OA coming from secondary organic aerosol (SOA) formation (Akherati et al., 2020; Jimenez et al., 2009; Pierce et al., 2011; Shrivastava et al., 2017). The atmosphere contains many volatile organic compounds (VOCs), semi-volatile organic compounds (SVOCs), and low volatility organic compounds (LVOCs), which can then react with compounds such as OH, O_3, and NO_3 to functionalize to form compounds with lower volatility and higher solubility (Jathar et al., 2014; Jimenez et al., 2009; Robinson et al., 2007; Shrivastava et al., 2017). As a result of the reduced volatility these particles have increased favorability of partitioning to the aerosol phase to form SOA and helping to grow pre-existing particles through condensation (Jimenez et al., 2009; Shrivastava et al., 2017). Additionally, OA may evaporate through gas-phase dilution or through an increase in temperature, reducing the size of OA (Donahue et al., 2006; Hodshire et al., 2019a, b; June et al., 2022; Pagonis et al., 2023).

In this dissertation, we first focus on biomass burning (landscape fires, including wildfires) as it is a significant source of aerosols to the atmosphere, but the impacts and evolution of smoke remain uncertain due to the complexities and variability between different plumes and within the same plume (Akagi et al., 2011; Hodshire et al., 2019a; June et al., 2022).

The aerosols from biomass burning have climate (Hobbs et al., 1997; Hodshire et al., 2019a; Lee et al., 2013; Ramnarine et al., 2019; Spracklen et al., 2011) and health (Chen et al., 2017; McClure et al., 2020; O'Dell et al., 2019, 2021; Schill et al., 2020; Yue et al., 2013) impacts with particle size, composition and abundance determining the magnitude of the effects (Kodros et al., 2018b; Lee et al., 2013; Seinfeld and Pandis, 2016; Spracklen et al., 2011).

One uncertainty of biomass burning that we aim to address is the biomass burning plume injection height (BB-PIH). While BB emissions are often emitted into the planetary boundary layer (PBL), observations have shown emissions can be injected above the PBL (Heinold et al., 2022; Jian and Fu, 2014; Ma et al., 2024; Val Martin et al., 2010, 2018; Wilkins et al., 2020; Ye et al., 2022). BB-PIH has important impacts on smoke dispersion and long-range transport due to faster winds in the free troposphere than in the boundary layer, more efficient removal processes in the boundary layer, vertical sensitivities to chemical evolution, and vertical sensitivities to smoke-cloud interactions (Boy et al., 2008; Damoah et al., 2004; Feng et al., 2024; Forster et al., 2001; Li et al., 2023; Walter et al., 2016; Zhu et al., 2018). Therefore, it is important to accurately represent the BB-PIH in models and understand the impact of BB-PIH on air quality and radiative effects. However, prior studies have generally focused on specific regions during their BB season, significant wildfire events, or specific field campaigns, rather than on the global scale interannual impacts of BB-PIH.

Another uncertainty in wildfire smoke examined in this dissertation is the variability in the horizontal and vertical evolution within a wildfire smoke plume. The processes driving aging (coagulation, dilution, OA evaporation/condensation, photochemistry) can vary due to mixing and gradients in concentration (Decker et al., 2021; Hodshire et al., 2021; June et al., 2022; Pagonis et al., 2023; Peng et al., 2020; Wang et al., 2021; Xu et al., 2021). June et al. (2022)

found faster coagulation and faster evaporation in the concentrated centers of plumes sampled during FIREX-AQ. Prior observational studies have typically focused on plume average evolution and variability in evolution at a single height. While Wang et al. (2021) examined the vertical gradient of ozone chemistry in a plume sampled during FIREX-AQ, they did not include analysis of OA or aerosol size distributions.

The marine Arctic atmosphere is rapidly changing due to climate change, but large uncertainties remain in the emission, and evolution of gas and aerosol phase species in the Arctic (Holland and Bitz, 2003; Schmale et al., 2021; Willis et al., 2018, 2023). Dimethyl sulfide (DMS) and methanethiol (MeSH) are emitted from the ocean to the atmosphere; however, there remain uncertainties in the oceanic concentrations and air-sea flux calculations of DMS and MeSH used in models, particularly in the Arctic. In the Arctic NPF&G is an important source of CCN (Croft et al., 2016; Gordon et al., 2017); however, the representation of NPF mechanisms and precursors in atmospheric chemistry models remains uncertain.

1.2 Scope of Dissertation

The focus of this dissertation is on the modeling of atmospheric aerosols at different spatial and temporal scales in two different environments. The first half of research presented focuses on wildfire smoke, while the second half looks at the springtime marine Arctic atmosphere. The following paragraphs provide a brief overview of the chapters of this dissertation. A more detailed introduction containing background and motivation for each chapter can be found at the start of each respective chapter.

Chapter 2 presents a global study on the implications of adding biomass burning plume injection height to a global atmospheric chemistry model coupled with a sectional aerosol

microphysics model. We first present the implications of including biomass burning plume injection height as opposed to emitting all smoke at the surface on model observation agreement. We then present the impacts on surface $PM_{2.5}$, column integrated aerosol mass, and the biomass burning direct radiative effect. Last, we present results of biomass burning plume injection height on CCN and the biomass burning aerosol indirect effect.

Chapter 3 is a case study of a single wildfire smoke plume sampled during the FIREX-AQ field campaign to examine horizontal and vertical gradients in in-plume aerosol aging using a high-resolution cloud resolving model. We first present model-observation comparisons for the August 3, 2019, DC-8 aircraft sampling of the Williams Flats Fire. We then discuss the impacts of horizontal and vertical in-plume concentration gradients on smoke plume evolution. Finally, in the conclusions for the chapter, we suggest ideas for future field campaigns to further the understanding of horizontal and vertical plume gradients observationally.

Chapter 4 examines the emission and oxidation of DMS and MeSH in the Arctic atmosphere in May and June 2023 using regional simulations and ship-based field campaign observations from ARTofMELT. We first discuss the implications of using different oceanic DMS estimates and assumptions for the sea-air flux of oceanic DMS/MeSH on the atmospheric concentrations along the ship track. We then discuss the model-observation comparisons for DMSO and the oxidation pathways of DMS. Lastly, we show a case study that occurred during fog at the onset of melt on June 10 to 12, 2023.

Chapter 5 focuses on understanding the aerosol size distribution and composition in the springtime Arctic through combining regional simulations and field campaign observations. We first show model-observation comparisons along the ship-track for aerosol mass under different sensitivity simulations to understand the impacts of various model developments. We then focus

on the aerosol size distribution both along the ship-track and at the long-term Arctic monitoring site, Villum Research Station. We then present analysis of two case studies that had 48 h back trajectories from the ship pass near Villum, providing the opportunity to understand the evolution of aerosols in the Arctic.

Finally, in Chapter 6, we provide a synthesis and implications of the previous chapters. We also make suggestions for future work.

Chapter 2: Inclusion of Biomass Burning Plume Injection Height in GEOS-Chem-TOMAS: Global-Scale Implications for Atmospheric Aerosols and Radiative Forcing[1]

2.1 Introduction

Biomass burning (BB), which includes wildfires, prescribed burns, and agricultural fires, is a significant source of aerosols, primarily organic aerosols, as well as black carbon, inorganic matter, and volatile organic compounds to the global atmosphere (Andreae, 2019; Hecobian et al., 2011; Jen et al., 2019; Reid et al., 2005b; Wiedinmyer et al., 2011). Aerosols from BB impact the health and wellbeing of communities exposed to smoke due to associated impacts on respiratory and cardiovascular health (Cascio, 2018; Chen et al., 2017; Ford et al., 2018; Gan et al., 2017; Keywood et al., 2015; Kodros et al., 2018a; Liu et al., 2015; O'Dell et al., 2019, 2021; Reid et al., 2016). Smoke can also cause reductions in visibility and impact the Earth's radiative budget and climate (Carrico et al., 2008; Chen et al., 2017; Ford et al., 2018; Keywood et al., 2015; Petters et al., 2009; Ramnarine et al., 2019; Shrivastava et al., 2017; Wu et al., 2017). The biomass burning direct radiative effect (BB-DRE) results from BB aerosols scattering and absorbing shortwave radiation altering the planetary albedo (Alonso-Blanco et al., 2014; Charlson et al., 1991; Haywood and Boucher, 2000; Jacobson, 2001; Ramnarine et al., 2019). BB has been found to have a net cooling DRE globally (Alonso-Blanco et al., 2014; Ramnarine et al., 2019). The BB cloud albedo aerosol indirect effect (BB-AIE) results from BB aerosols acting as cloud condensation nuclei (CCN), which alters the albedo and lifetime of clouds (Albrecht, 1989; Lee et al., 2013; Pierce and Adams, 2007; Ramnarine et al., 2019; Spracklen et al., 2011;

[1] June, N. A., B. Ford, B. Croft, R. Y.-W. Chang, & J. R. Pierce (in press, 2025), Inclusion of Biomass Burning Plume Injection Height in GEOS-Chem-TOMAS: Global Scale Implications for Atmospheric Aerosols and Radiative Forcing. *JAMES.*

Twomey, 1974). Globally, the BB-AIE is a cooling effect due to BB increasing CCN concentrations, (Lee et al., 2013; Li et al., 2022; Ramnarine et al., 2019; Spracklen et al., 2011).

Understanding the global-mean health and radiative effects of BB is important as wildfires are changing and are predicted to increase in the future (Dennison et al., 2014; Ford et al., 2018). In the United States, annual average surface $PM_{2.5}$ concentrations have decreased in recent years, but the contribution of BB to surface $PM_{2.5}$ has increased (Burke et al., 2023; Childs et al., 2022; O'Dell et al., 2019). These trends are expected to continue in the future due to the potential for ongoing reduction of anthropogenic $PM_{2.5}$ emissions coupled with increasing BB $PM_{2.5}$ emissions (Ford et al., 2018). Global BB emissions are also projected to increase in the future, which may lead to a net negative radiative forcing of BB on future climate (Daniau et al., 2012; Di Virgilio et al., 2019; Dowdy et al., 2019; Ford et al., 2018; Jolly et al., 2015; Keywood et al., 2013; Marlon et al., 2008; Moritz et al., 2012; Yu et al., 2022).

BB emissions are often emitted into the planetary boundary layer (PBL), close to the surface; however, observations have shown emissions can be injected above the PBL (Heinold et al., 2022; Jian and Fu, 2014; Ma et al., 2024; Val Martin et al., 2010, 2018; Wilkins et al., 2020; Ye et al., 2022). BB emissions can make it into the free troposphere depending on the dynamical heat flux of the fire, ambient atmospheric stability profile, and the entrainment of ambient air into the plume (Kahn et al., 2007; Paugam et al., 2016). Using satellite plume heights, it has been shown that the frequency at which smoke is injected into the free troposphere varies by region and season (Val Martin et al., 2010, 2018). For example, in Indonesia and the Amazon, satellites show most BB emissions are in the planetary boundary layer (Tosca et al., 2011; Val Martin et al., 2018), while about 25 to 50% of boreal forest fires in the Northern Hemisphere have significant injection into the free troposphere during summer, although with significant

interannual variability (Val Martin et al., 2010, 2018). Previous studies have shown that fires in Australia can produce enough buoyancy to inject smoke into the upper troposphere and lower stratosphere (Heinold et al., 2022; Mims et al., 2010). Stratospheric injections of smoke have been observed elsewhere as a result of pyro-convection (Peterson et al., 2018; Trentmann et al., 2006; Wilkins et al., 2020). However, the impacts of these regional differences in BB emissions height on global air quality and climate are not well-quantified. Our study aims to address this knowledge gap.

Biomass burning plume injection height (BB-PIH) has important impacts on smoke dispersion and long-range transport due to faster winds in the free troposphere than in the boundary layer, more efficient removal processes in the boundary layer, vertical sensitivities to chemical evolution, and vertical sensitivities to smoke-cloud interactions (Boy et al., 2008; Damoah et al., 2004; Forster et al., 2001; Freitas et al., 2006, 2007, 2010; Samset and Myhre, 2011). Therefore, it is important to accurately represent BB-PIH in global models. Some models parameterize plume rise; others, such as GEOS-Chem, prescribe BB-PIH either through an emissions inventory, assuming a single BB-PIH, or assuming a BB-PIH climatology based on satellite observations to determine average of BB-PIHs for different land cover types (Heinold et al., 2022; Jian and Fu, 2014; Leung et al., 2007; Li et al., 2023; Lu et al., 2024; Walter et al., 2016; Ye et al., 2022; Zhu et al., 2018). Here we implement a state-of-the-science model of plume rise in an aerosol-size resolved microphysics scheme coupled with GEOS-Chem to examine the impact on global air quality and climate.

Previous studies with model-observation comparisons have shown that injecting smoke above the PBL can offer constraints on the impacts of transported smoke on air quality; however, these studies typically focused on regional or single fire plume impacts (Feng et al., 2024; Jian

and Fu, 2014; Li et al., 2023; Walter et al., 2016; Zhu et al., 2018), rather than on the inter-annual and global scale impacts we consider in this study. For example, a case study of the 2019-2020 Australian fires redistributed smoke in and above the PBL and found better model-observation agreement on days with observed pyro-convection (Heinold et al., 2022). Including these stratospheric injections of smoke increased the modeled aerosol optical thickness in the Southern Hemisphere and altered the shortwave radiative forcings (Heinold et al., 2022). Furthermore, Zhu et al. (2018) implemented a plume height climatology in GEOS-Chem and showed improved agreement with observations. However, a climatology-based approach using average satellite observed plume heights for each land-cover type cannot capture variability between fires at the same location or potential interannual variability. Our study presents novel model developments that enable representation of such variability in global simulations of size-resolved aerosol microphysics.

Despite the known importance of BB-PIH on constraining simulations of the air quality and climate impacts of BB, previous studies have been limited to specific regions during their BB season, significant wildfire events, or specific field campaigns. In our study, we instead quantify the global-scale impacts of BB-PIH with simulations of size-resolved aerosol microphysics fusing plume heights from the GFAS emissions inventory for a two-year study period (2019-2020), to allow for physically based interannual and fire-based variability in the plume heights. The GFAS inventory is of particular use to the smoke-modeling community as it uses a plume-rise model to calculate BB-PIH based on fire behavior, hence providing variable plume heights for use in global models lacking the capability for an online plume rise calculation. In this paper, we present the development of the new capability to include a physically based BB-PIH in the GEOS-Chem-TOMAS atmospheric composition model with

online size-resolved aerosol microphysics. We examine the global and regional impacts of BB-PIH under this novel implementation of physically based plume rise in global simulations of aerosol microphysics. We consider 3 scenarios 1) injection of all BB emissions into the planetary boundary layer, and plume injection height based on 2) standard and 3) increased GFAS plume rise. We first examine the impact of BB-PIH on comparisons to retrievals of AOD, extinction coefficient vertical profiles, and $PM_{2.5}$ in Chapter 2.3.1. We then look at the simulated impacts of BB-PIH on global-mean air quality and climate variables in Chapter 2.3.2, including impacts on surface $PM_{2.5}$ (Chapter 3.2.1), aerosol mass and BB-DRE (Chapter 2.3.2.2), and CCN and BB-AIE (Chapter 2.3.2.3). To our knowledge, we present the first global-scale evaluation of GFAS plume heights in a global model with size-resolved aerosol microphysics, as well as the first analysis of the resultant global-mean air quality and radiative impacts of these heights.

2.2 Methods

2.2.1 Model Overview of GEOS-Chem-TOMAS

We conduct global simulations with the atmospheric composition model GEOS-Chem version 13.3.3 in its classic configuration coupled with the TwO-Moment Aerosol Sectional (TOMAS) microphysics model. In this study, we present novel updates to the TOMAS emissions module within GEOS-Chem to allow GEOS-Chem-TOMAS to enable use of 3D BB emissions modeling. All global simulations used in our study have a horizontal resolution of 4° x 5° with 47 vertical levels and use offline meteorology from the MERRA-2 reanalysis fields for 2019 and 2020. The coarse spatial resolution of GEOS-Chem-TOMAS limits the ability to examine specific high concentration events; however, it is able to help us understand global and large-scale features in the context of use of a detailed aerosol microphysics scheme (TOMAS). This resolution has been used previously to study air quality and climate variables on the timescales

we analyze in this study (e.g, AboEl-Fetouh et al., 2022; Kodros et al., 2016; Ramnarine et al. 2019). Our updates to the GEOS-Chem-TOMAS model can be used with the nested grid horizontal resolutions (e.g., 0.5°x0.625°). Due to computational burden, it was not feasible for us to run that resolution globally for two years. However, we do conduct a nested grid simulation at 0.5°x0.625° over the United States for August and September 2020 to test the implementation of the BB-PIH schemes in a high-resolution version of GEOS-Chem-TOMAS during an active period of wildfires. We briefly compare the results of these fine- and coarse-resolution simulations in this study.

We use the version of TOMAS with 15 aerosol size sections from about 3 nm to 10 μm and simulate size-resolved sulfate, sea salt, organic aerosol (OA), black carbon (BC), and dust, and diagnose size-resolved aerosol ammonium, nitrate, and water. OA mass is assumed to be 1.8 times that of OC (Philip et al., 2014). TOMAS simulates aerosol number and mass in each size section and includes the processes of aerosol nucleation, condensation, coagulation, dry and wet deposition, and aqueous sulfur chemistry (Adams and Seinfeld, 2002; Kodros and Pierce, 2017). Anthropogenic, dust, and sea salt emissions are consistent across all simulations in this study. Anthropogenic emissions are from the Community Emissions Data System (CEDS). Dust emissions follow the dust entrainment and deposition (DEAD) scheme (Zender et al., 2003) and sea salt emissions follow the Jaegle scheme (Jaeglé et al., 2011). BB emissions come from the Global Fire Assimilation System (GFAS), which assimilates fire radiative power measurements from the Moderate Resolution Imaging Spectroradiometer (MODIS) to make daily estimates of BB emissions for 41 species, burnt dry matter, and fire radiative power (FRP) at 0.5° x 0.5° horizontal resolution globally (Kaiser et al., 2012). We assume the biomass burning emissions to

be lognormally distributed with a number median diameter of 100 nm and modal width of 2.0 to distribute the emissions across the TOMAS size sections.

2.2.2 GEOS-Chem-TOMAS Radiative Transfer Calculations

We use an offline version of the Rapid Radiative Transfer Model for Global Climate Models (RRTMG) to estimate the radiative impacts of the BB-PIH (Bilsback et al., 2020b; Kodros et al., 2015, 2016). We use daily average aerosol concentrations from our simulations and meteorological inputs in our calculations of aerosol radiative effects. For estimating AOD and DRE, we assume a fully internal mixing state within each aerosol size section with a core-shell morphology, where internally mixed BC is a spherical core, and other species (e.g., sulfate and organics) are a homogeneously mixed shell around that core (Jacobson, 2001). The refractive index is calculated for the shell using a volume weighted average, while the core has a refractive index of pure BC. The Bohren and Huffman Mie code for concentric spheres is used to calculate the scattering and absorption efficiencies and the asymmetry parameter. As a sensitivity test for the DRE, we estimate the impact of absorbtive OA (brown carbon, BrC) on the imaginary component of the OA refractive index using the modeled OA to BC ratio and the Saleh (2014) parameterization (Kodros et al., 2016; Saleh et al., 2014).

For estimating the AIE, we assume all species, except fresh BC, are internally mixed within each aerosol size section to calculate the hygroscopicity parameter (κ) as a volume-weighted average of the individual species (Petters and Kreidenweis, 2007). Fresh BC is externally mixed with a κ of 0. The fresh BC becomes internally mixed on a fixed e-folding timescale of 1.5 days gradually becoming fully mixed with the other species in each size bin (Pierce et al., 2007). The daily average mass and number concentrations from our GEOS-Chem-TOMAS simulations and the activation parameterization of Abdul-Razzak & Ghan (2002) are

used to calculate cloud drop number concentrations. Full details of the AOD, DRE, and AIE calculations can be found in Kodros et al. (2015).

2.2.3 Addition of BB-PIH to GEOS-Chem-TOMAS

The GFAS plume-rise model calculates daily averaged plume heights governed by the equations defined in Freitas et al. (2007, 2010) and updated in Paugam et al. (2015). The GFAS plume-rise model includes: a 1-D cloud-resolving model forced by satellite-derived FRP, convective heat flux and active fire area, and a bulk microphysical scheme. The plume-rise model also uses ambient atmospheric profiles of temperature, wind and specific humidity from European Centre for Medium-Range Forecasts (ECMWF) (Paugam et al., 2015; Rémy et al., 2017). The altitudes of plume top (TOP) and plume bottom (BOT) are derived quantities in the GFAS plume-rise model based on the entrainment and detrainment vertical profiles. Rémy et al. (2017) showed GFAS plume heights agree well with the MISR plume height climatology except for in cases with poor input data for the boundary layer height or for large fires with underestimates in FRP. Walter et al. (2016) showed GFAS plume heights to have a low-bias due to the use of a single daily value and use of FRP inputs from MODIS overpass times (10:30 and 13:30 LT), which do not always coincide with the peak in fire activity. Despite these limitations, the GFAS plume heights are of value as the only global emissions inventory to include plume heights, which can be used in global simulations of size-resolved aerosol microphysics (such as with the model GEOS-Chem-TOMAS) that are unable to calculate online plume heights based on fire behavior.

Since both our global and regional GEOS-Chem-TOMAS simulations are at a coarser resolution than the GFAS inventory, we use an emissions weighted averaging to determine the BOT, and TOP altitude in each grid box at each time step. In the GFAS inventory, emission rates

of combustion species are calculated based on assimilated FRP; so, within the emitted species in the inventory, all are positively related to FRP, which has been shown to be positively correlated with plume height. Due to this relationship with FRP, any variable in the GFAS inventory could be used to weight averages of the plume-heights; differences in averages only result when there is more than one ecoregion within a gridbox. Any uncertainties resulting from this potential variability are encapsulated in the three different BB-PIH scenarios we test. We use the organic carbon emissions from the GFAS inventory to weight the averages. Equation 2.1 shows an example of the equation to re-grid,

$$Height_{Coarse} = \frac{\sum_{i=1}^{n} Height_{GFAS,i} * OC_i}{\sum_{i=1}^{n} OC_i} \quad (2.1)$$

Where OC_i is the organic carbon emissions in one GFAS grid box, n is the number of GFAS grid boxes in the GEOS-Chem-TOMAS grid box. In this method, the BB-PIHs are weighted more towards fires with more emissions, which are more likely to have higher BB-PIHs. We acknowledge that this could potentially result in a lower fraction of emissions in the PBL in cases with multiple fires of varying size in the gridbox. After emission weighting the heights to 4°x5° resolution, BOT is above the PBL for 5.3% of the annual emissions, and TOP is above the PBL for 12.1% of annual emissions (Figure A.1).

We conduct four global GEOS-Chem-TOMAS simulations: No Biomass Burning (NBB) and three BB-PIH scenarios (Table A.1, Figure 2.1). Simulations are for two years (2019 and 2020) with an additional six months of spin-up. We list the simulations in Table A.1 and provide a visual representation of these scenarios in Figure 2.1. Figure A.3 shows the vertical distribution of emissions in each of Earth's biomass burning source regions (source regions defined in Figure A.2). The 'PBL' simulation follows the default behavior of GEOS-Chem with TOMAS, where all

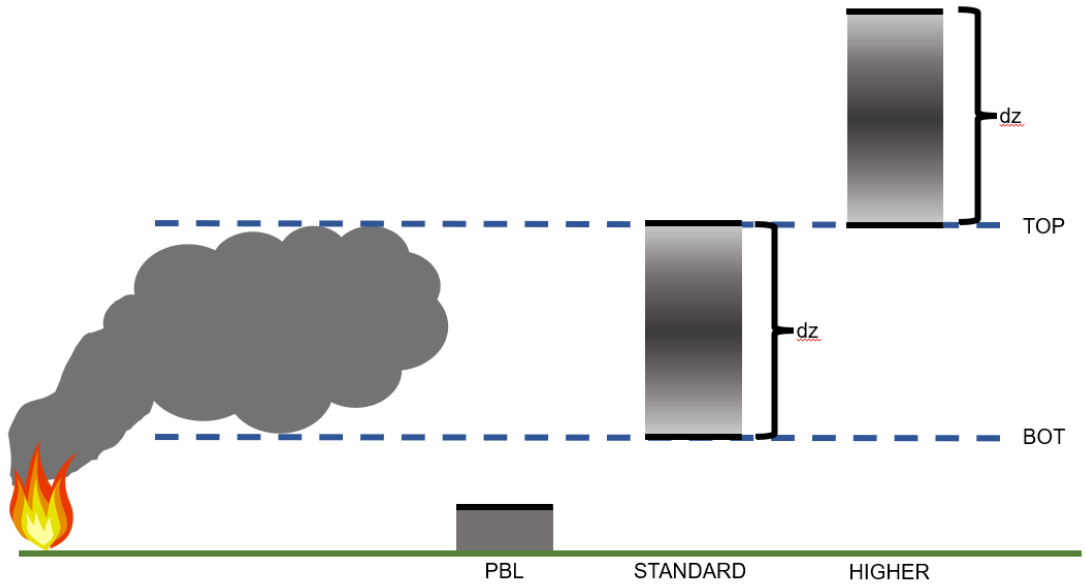

Figure 2.1: Visual representation of the three BB simulations used in our study as defined by Table A.1. The horizontal dashed blue lines represent the altitude of plume bottom (BOT), and altitude of plume top (TOP). Note that this schematic is not to scale vertically, and at times all scenarios could overlap with the PBL scenario. For all simulations, emissions in the PBL are well-mixed between the surface and top of the PBL.

BB emissions are injected into the surface layer and then well-mixed through the planetary boundary layer. For the 'STANDARD' and 'HIGHER' simulations, we have developed the TOMAS module in GEOS-Chem to allow for a 3D field of emissions, as opposed to emitting all biomass burning emissions into a single layer at the surface, as the current version of the standard model does. The STANDARD simulation is the standard height simulation in which BB emissions are normally distributed from BOT to TOP, with the BOT and TOP placed at ± 2 standard deviations from the mean altitude, with no smoke extending beyond these limits. To examine the possibility that the GFAS-estimated injection heights are biased low (Rémy et al., 2017; Walter et al., 2016), we perform a simulation where we have shifted the GFAS heights up. In the HIGHER simulation, the BB-PIH is shifted up such that BB emissions are normally distributed from TOP to TOP plus the plume depth (same depth as the STANDARD simulation).

This specific configuration for higher heights (TOP to TOP+ΔZ) was selected because the fraction of emissions placed above the PBL top in this scenario more closely matches those from the Multi-angle Imaging SpectroRadiometer (MISR) plume height project as described in Val Martin et al. (2018). The vertical BB emission distribution is normalized, so that total BB emissions are conserved between all simulations with BB emissions. For the STANDARD and HIGHER simulations, emissions within the PBL are well-mixed between the surface and PBL top. The changes to the BB-PIH in HIGHER do not necessarily improve the BB-PIH representation on a fire-by-fire basis; however, we evaluate each of the BB-PIH sensitivity cases with Cloud-Aerosol Lidar and Infrared Pathfinder Satellite Observations (CALIPSO) extinction coefficient profiles to see if some model configurations perform better, in the global average, than others. Additionally, the highest BB-PIH scenario (HIGHER) allows us to examine the global-mean air quality and climate implications of higher BB-PIH, which may become more frequent in the future due to changes in fire intensity (Spracklen et al., 2009; Wilmot et al., 2022).

2.2.4 Nested Simulation Implications

These plume height configurations and weighted-averaging scheme are used for the nested simulations at 0.5°×0.625° resolution over the United States (US) for August and September 2020. These nested simulations show the functionality of using the GFAS plume heights in GEOS-Chem-TOMAS at fine resolution. As shown in Figure A.4, the aerosol mass is generally within 50% of that of the 4°x5° simulation within the nested domain. With changing BB-PIH, the relative shifts in the amount of biomass burning aerosol in the planetary boundary layer and free troposphere are similar between the nested and 4°x5° simulations particularly in the eastern US. During the time frame simulated, the BB mass in the eastern US is mostly due to

long-range-transport from the western US. The similar relative shifts in BB mass between the two resolutions suggest that the 4°x5° simulation is well suited for understanding relative impacts of BB-PIH on a global-scale. Additionally, the differences between changing resolution are minimized in the HIGHER simulation, suggesting that the need for PIH is particularly important at coarser resolutions, which do not allow for as much vertical transport (Yu et al., 2018). We do not extensively discuss the nested simulation in the main results as our focus is to examine the global-scale impacts of raising the BB-PIH and across several global regions dominated by transported smoke.

2.2.5 Evaluation Data

We use the CALIPSO Lidar Tropospheric Profiles, Cloud-Free, Night, Version 4 at 532 nm (Kim et al., 2018) and make comparisons with simulated extinction coefficient profiles at a wavelength of 532 nm. For quality screening of CALIPSO data, the following criteria are used (Ford and Heald, 2012; Tackett et al., 2018). Profiles with a cloud-aerosol discrimination (CAD) score outside of the range of -100 to -20 are excluded due to lack of confidence in discriminating aerosol from cloud. Low-confidence extinction retrievals are removed by only including aerosol layers with extinction QC flags equal to 0, 1, 16, or 18. Tackett et al. (2018) shows the frequency of rejection based on quality control criterion and further describes the detection limit and quality control parameters. Extinction coefficients below the detection limit are assumed to be 0 km^{-1}. We make comparisons using monthly averaged CALIPSO extinction coefficient profiles re-gridded to the GEOS-Chem 4°×5° with 47 vertical layers grid. Monthly average GEOS-Chem extinction coefficients at 532 nm are calculated by averaging GEOS-Chem grid boxes with a valid CALIPSO profile within 6-hours of the model time (model output is every 6-hours), using the night-time overpass time of ~0130 local solar time. For consistency with the CALIPSO data,

GEOS-Chem extinction coefficient values below CALIPSO's detection limit are also assigned a value of 0 km^{-1}. Setting values below the detection limit to either the detection limit or half of the detection limit makes little difference in the results for the impact of BB-PIH on observation agreement.

The Aerosol Robotic Network (AERONET) provides direct-Sun measurements of spectral AOD from surface-based columnar measurements around the globe. We use Version 3, Level 1.5 cloud-screened and quality-controlled direct-Sun products. We make comparisons between AEONET and simulated AOD at 440 nm for 2019 and 2020. The AERONET AOD is compared to the GEOS-Chem AOD in the 4°×5° grid-box corresponding to the site location and at the closest available time of observation. Model output is every 6-hours, so model and observation comparisons are within 6-hours of each other.

We use the van Donkelaar et al. (2021) dataset of surface $PM_{2.5}$ over land to make comparisons to the GEOS-Chem modeled $PM_{2.5}$. This dataset combines retrievals from satellites, ground measurements, and chemical-transport models to estimate monthly averaged surface $PM_{2.5}$ at 0.1°×0.1° resolution over land areas in 2019 and 2020 (van Donkelaar et al., 2021). We re-grid these data to the same 4°×5° grid that is used for our simulations.

Additionally, over the contiguous US (CONUS), comparisons are made between the $PM_{2.5}$ product developed in O'Dell et al. (2019) and our simulated total surface $PM_{2.5}$, smoke-attributed surface $PM_{2.5}$, and non-smoke-attributed surface $PM_{2.5}$.The O'Dell et al. (2019) product combines interpolated surface observations and smoke extent from the Hazard Mapping System to provide daily surface total $PM_{2.5}$ and smoke-attributed $PM_{2.5}$ estimates on a 15-km grid over the CONUS. We make comparisons for monthly averages re-gridded to the 4°×5° grid

used by our simulations. These additional comparisons allow us to examine the biases due to non-smoke and smoke sources.

For model evaluation, comparisons are made for all available observations and additionally at times designated as smoke-impacted. A model-column is designated as smoke-impacted if there is a 50% increase of AOD in the PBL simulation compared to the NBB simulation. This criterion is met about 5% of the time over the two years of our simulations, globally, with higher frequencies in biomass burning source regions (Figure A.5). We use the same set of profiles for smoke-impacted comparisons for all simulations. Globally there is an increase in the frequency of samples designated as smoke-impacted as the BB-PIH increases. However, we determined that our conclusions are not sensitive to which BB-simulation is used to determine the set of smoke-impacted columns.

2.3 Results

2.3.1 Impact of BB-PIH on Model-Observation Agreement

To our knowledge there have been no previous evaluations of the impact of physically based BB-PIH on global simulations with detailed size-resolved aerosol microphysics. To address this knowledge gap, here we present such comparisons by using CALIPSO extinction coefficient profiles, CALIPSO smoke-specific extinction coefficient profiles. Further evaluation of the model against AERONET AOD and the global total surface $PM_{2.5}$ dataset from van Donkelaar et al. (2021) are given in Appendix A Text 1 and Figures A.6 to A.9. The comparisons to surface $PM_{2.5}$ and AOD are less directly connected to the vertical structure of smoke in the atmosphere and BB-PIH has a smaller influence globally on reducing the bias of these variables.

As GEOS-Chem-TOMAS uses fixed meteorology (MERRA-2), all changes in model biases are due to the isolated impact of the different BB-PIH scenarios on the simulated aerosols,

and not due to any meteorological feedbacks. Despite the small model-measurement improvements due to elevated BB-PIH shown in this section; these comparisons are an important support of our novel quantification of the strong climate impacts of physically based BB-PIH elevation in global simulations, which will be discussed in Chapter 2.3.2.

2.3.1.1 Comparison with CALIPSO Extinction Coefficient Profiles

We evaluate extinction coefficient profiles from our global size-resolved aerosol microphysics simulations against CALIPSO during periods impacted by BB for six BB source regions and globally (regions defined in Figure A.2). Overall, the global normalized mean bias (NMB) in the vertical profile of the extinction coefficient (Figure 2.2) is improved by 1.9% and 9% for the STANDARD and HIGHER simulation respectively relative to the PBL simulation. In general, the improvement in NMB is larger in the free troposphere than near the surface due to there often being times where the TOP or/and BOT of the plume are located in the boundary layer. Improving the representation of the vertical profile of smoke is important as it can influence the atmospheric lifetime of smoke and its vertical location relative to clouds, which can have implications for climate effects (Chapter 2.3.2.2 & 2.3.2.3). In CONUS, BB-PIH elevation yields closer model-CALIPSO agreement within parts of the boundary layer and free troposphere (Figure 2.2b.). In boreal North America, there are larger improvements in bias in the free troposphere than near the surface (Figure 2.2c.). In boreal Asia, there is improved agreement below about 4 km, but an increased high bias above 4 km. However, the NBB simulation also overpredicts at these altitudes suggesting a high bias due to non-BB sources influencing this region at higher altitudes (Figure 2.2d.). Over our entire two-year simulation, the biases in the CALIPSO extinction coefficient profile are consistent with prior studies without physically based BB-PIH and detailed size-resolved aerosol microphysics (Ford and Heald, 2012, 2013;

Generoso et al., 2008; Li et al., 2019; Ma and Yu, 2015). Here, we also expand on prior evaluations of GEOS-Chem by focusing on times impacted by BB. During these specific periods of BB, raising the BB-PIH improves agreement with CALIPSO extinction coefficient profiles (Figure 2.2).

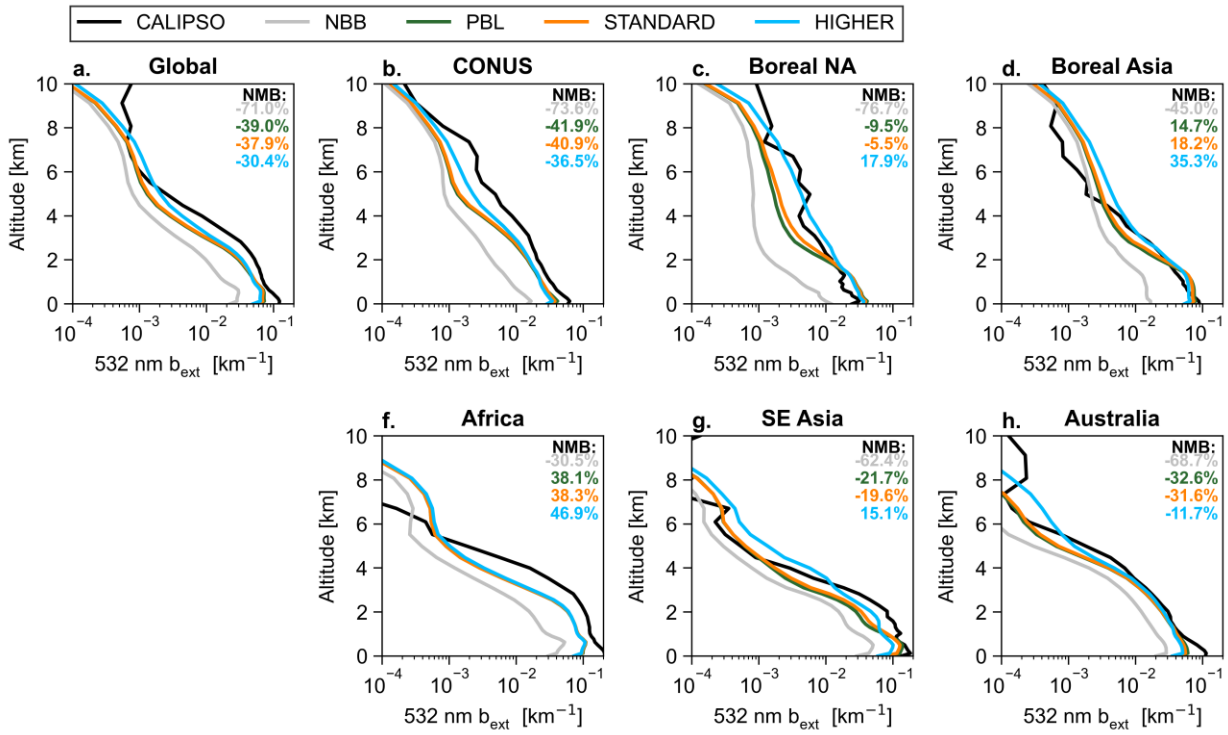

Figure 2.2: Extinction coefficient (b_{ext}) at 532 nm vertical profiles for CALIPSO (black) and each plume injection height (PIH) scenario (described in Table A.1 and Figure 2.1): PBL (green), STANDARD (orange), HIGHER (blue) in each of the different regions shown in Figure A.2. The simulation with no biomass burning emissions (NBB) is shown in gray. Each panel shows the average of profiles from 2019 and 2020 that are designated as smoke-impacted (50 % increase in AOD due to BB in the PBL simulation). The NMB over the column is shown for each simulation and each region.

Further evidence that our elevated BB-PIH global simulations are putting smoke closer to the correct altitude in the global average is provided by comparisons between simulated and observed smoke-specific extinction coefficients (also a CALIPSO product, Figure 2.3). For our global simulations, the smoke-specific extinction coefficient is determined by subtracting the extinction coefficient for the NBB simulation from each of the three simulations that included

smoke emissions. It should be noted that comparisons between GEOS-Chem smoke extinction coefficients and the CALIPSO smoke-extinction coefficients are complicated by smoke layers needing to be elevated (extend beyond 2.5 km agl) in CALIPSO to not be classified as polluted continental or polluted dust (Ford and Heald, 2012; Omar et al., 2009). The HIGHER simulation has the lowest bias of the three BB simulations in all regions for times designated as smoke-impacted and above 2.5 km (Figure 2.3a.). Our 4° x 5° resolution simulation may have weaker vertical transport than finer resolution simulations (Yu et al., 2018). The improvements in observation agreement of extinction coefficient due to increasing BB-PIH may also compensate for some of this vertical transport bias; but less so in our nested case study (Figure A.4). The general improvement in the CALIPSO profile comparisons in the HIGHER simulation compared to the STANDARD simulation agrees with previous studies suggesting that there may be low biases in the GFAS plume heights. These biases may be due to the lack of a diurnal cycle (Walter et al., 2016), and/or underestimated fire radiative power by satellites for the largest fires (Freitas et al., 2007). The vertical profile comparisons shown in Figures 2.2 and 2.3 also indicate that the performance of the BB-PIH scheme based on GFAS heights varies by region, suggesting that our crude approach to increasing GFAS injection heights likely needs future physically based refinement.

2.3.2 Global Effects of BB-PIH

Figure 2.4 provides global- and 2-year average and individual-year averages of the impacts of BB-PIH on aerosol and their radiative forcing (separated by land and ocean regions) that will be discussed in this section. We also explore associated geographic distributions. We consider both of the elevated BB-PIH simulations as there are times when either outperforms the other compared to observations; additionally, the HIGHER simulation allows us to consider the

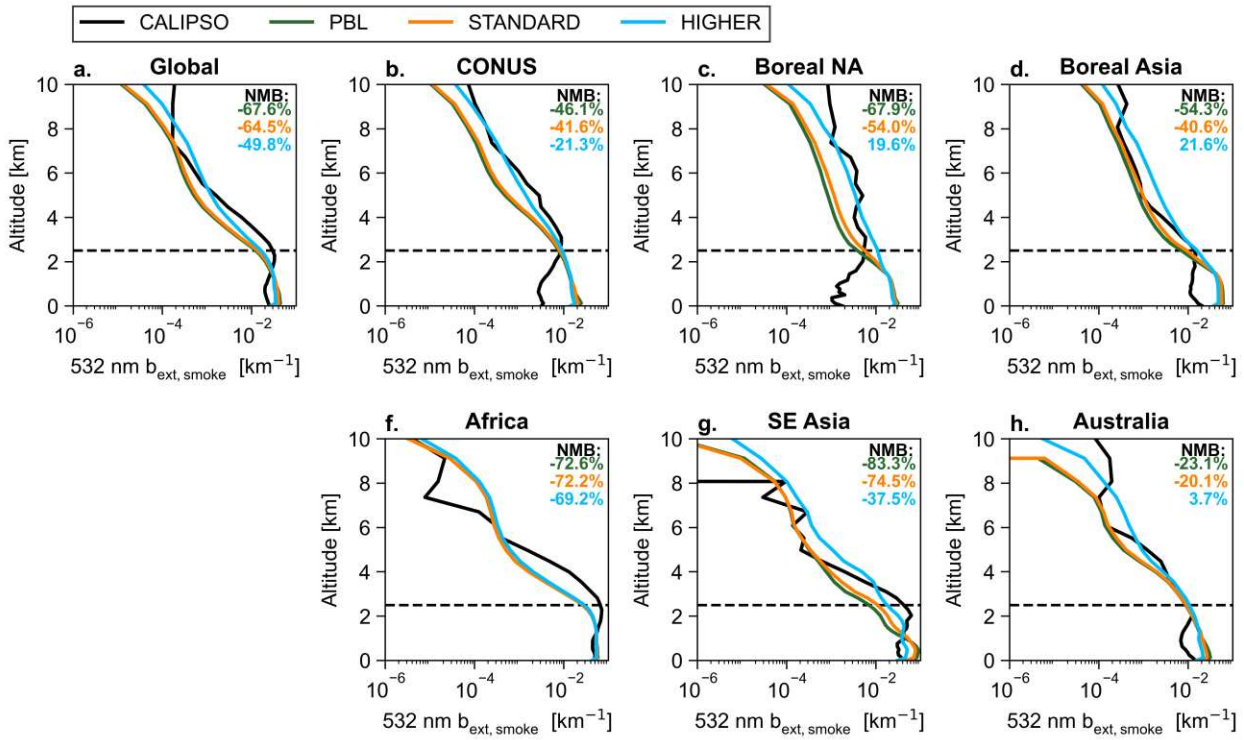

Figure 2.3: Average smoke extinction coefficient ($b_{ext,smoke}$) at 532 nm as a function of altitude in 2019 and 2020 by region during times designated as influenced by smoke. The CALIPSO observations of the elevated smoke type (top of layer > 2.5 km) are in black. Model simulations are co-located to time and location of CALIPSO observations and are in different colors for each BB PIH scenario: PBL (green), STANDARD (orange), HIGHER (blue). For the model simulations, the $b_{ext,smoke}$ is determined by subtracting the NBB b_{ext} at 532 nm from the b_{ext} from the four BB simulations. The NMB over the column above 2.5 km is shown for each simulation and each region.

potential impacts of future fires, which are expected to have elevated BB-PIH as a result of increased intensity from climate change. Raising the BB-PIH has varying impacts on BB $PM_{2.5}$, BB AOD, and BB N80 (CCN sized particles from BB); and therefore, on BB-DRE and BB-AIE over land and ocean areas. The figure also shows that despite differences in BB emissions between the two-years, the impacts of BB-PIH are consistent between 2019 and 2020, suggesting that our results are robust for our model's response to the changes in BB-PIH.

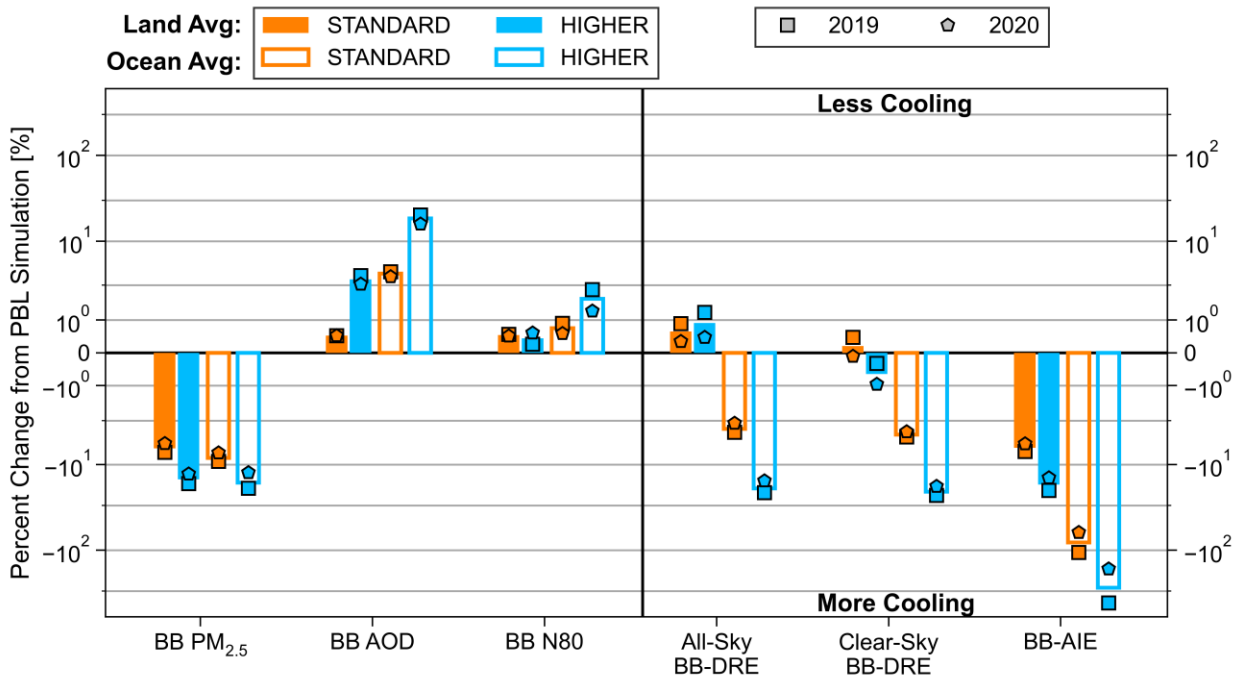

Figure 2.4: Two-year averages (bars) of the percent differences for the two BB-PIH simulations relative to the PBL simulation for surface $PM_{2.5}$ from biomass burning (BB $PM_{2.5}$), the biomass burning AOD at 440 nm (BB AOD), the biomass burning concentration of N>80 nm (BB N80), the all-sky and clear-sky biomass burning direct radiative effect (BB-DRE), and the biomass burning aerosol indirect effect (BB-AIE) in the BB-PIH scenarios relative to the PBL simulation. The points indicate the 2019 (square) and 2020 (pentagon) averages as an indicator of the variability in the quantities on a global scale. The percent changes for the radiative effects are reversed in sign from the mathematical definition such that a negative (positive) percent change indicates a more cooling (warming) effect.

2.3.2.1 Predicted Impact of BB-PIH on Surface $PM_{2.5}$

In the two-year average, raising the BB-PIH reduced simulated BB $PM_{2.5}$ in BB source regions and increases in BB $PM_{2.5}$ away from source regions, primarily in marine areas, Greenland, and Antarctica (Figure 2.5a-2.5c). The global average percent decreases in BB $PM_{2.5}$ relative to the PBL simulation are 7.2% and 15.4% in the STANDARD and HIGHER BB-PIH simulations, respectively (Figure 2.4). The decreases in BB $PM_{2.5}$ in source regions are due to aerosol mass being moved vertically away from the surface, an unsurprising result that has also been shown in previous studies (Jian and Fu, 2014; Leung et al., 2007; Menut et al., 2018; Zhu et al., 2018). As BB-PIH increases, there are decreases in BB $PM_{2.5}$ in the Southern Pacific Ocean

downwind of Australia. These decreases in surface concentrations are due to the increase in smoke in the free troposphere and westerlies moving the BB aerosols out of the region (Heinold et al., 2022). The regions with increases in BB $PM_{2.5}$ are primarily in regions away from source fires and with sinking motion resulting in smoke aloft descending towards the surface (see Figure A.10 for context of vertical and horizontal winds from the MERRA-2 Reanalysis used in all simulations). The largest percent increases in BB $PM_{2.5}$ are in areas of the Pacific Ocean where concentrations of surface BB $PM_{2.5}$ are the lowest in the PBL simulation. The largest absolute increases in BB $PM_{2.5}$ are in the eastern Indian Ocean (Figure A.11).

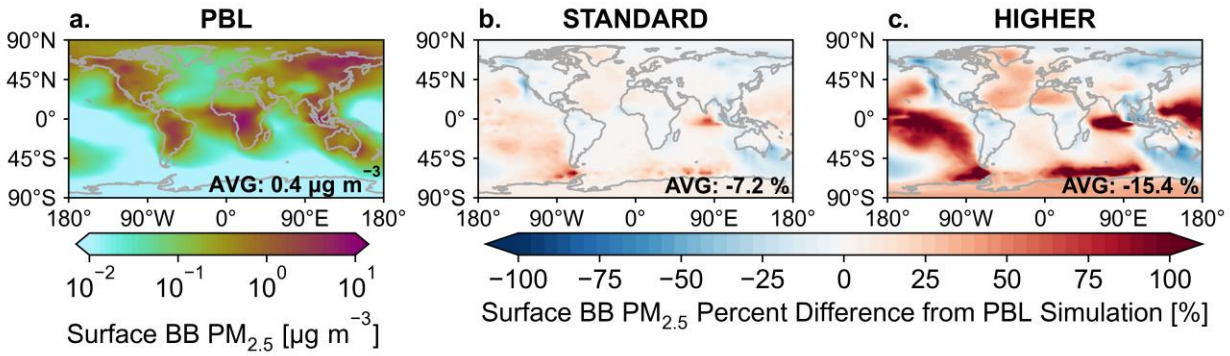

Figure 2.5: (a.) Average Surface $PM_{2.5}$ from biomass burning (BB $PM_{2.5}$) for 2019 and 2020 in the PBL simulation. Percent difference in surface average BB $PM_{2.5}$ from 2019 and 2020 relative to the PBL simulation for (b.) STANDARD, (c.) HIGHER. Figure A.11 shows the absolute changes in BB $PM_{2.5}$. The complimentary figure showing percent differences for total surface $PM_{2.5}$ is shown in Figure A.12.

2.3.2.2 Predicted Impact of BB-PIH on Aerosol Mass and Direct Radiative Effect

As BB-PIH increases, the global-mean lifetime of BB BC and BB OA increases (Table 1) due to increases in BB mass in the free troposphere (Figure 2.6, Figure A.13), where dry and wet deposition tend to be less efficient. Due to these increases in lifetime, the global 2-year average BB OA column mass increases by 2.6% and 15.2% for the STANDARD and HIGHER BB-PIH simulations relative to the PBL simulation (Figure A.12a-A.12c), while the percent changes in BB BC column mass are 1.7% and 10.5% in the STANDARD and HIGHER BB-PIH simulations

relative to the PBL simulation (Figure A.12d-A.12f). The larger increases in the BB OA lifetime compared to the BB BC lifetime are likely due to OA being more susceptible to wet deposition, such that the OA lifetime increases more when BB aerosol is moved at or above cloud levels and away from precipitation. The differences in the impact of BB-PIH on BB OA and BB BC column mass are consistent with an increase seen in the BB OA to BB BC ratio (Figure A.12g-A.12i).

Table 2.1: The global two-year average atmospheric lifetime of biomass burning OA and biomass burning BC in each BB-PIH scenario.

Simulation	BB OA Lifetime [days]	BB BC Lifetime [days]
PBL	5.23	5.84
STANDARD	5.37	5.94
HIGHER	6.03	6.45

As a result of the increased lifetime of BB aerosol, BB-specific AOD at 440 nm (BB AOD) has global percent increases of 2.0% and 9.9% in the STANDARD and HIGHER BB-PIH simulations relative to the PBL simulation with variability between BB source and remote regions (Figure 2.7b-2.7c). BB source regions have slight decreases in BB AOD, and transport regions have increases in BB AOD. The magnitude of increase in BB AOD at 440 nm is somewhat lower than that for both BB OA and BB BC column mass (Figure A.14). A contributing factor is that the increases in BB mass in the BB-PIH scenarios tend to be in vertical layers of the atmosphere with lower relative humidity (e.g., free troposphere rather than boundary layer, Figure A.16), which decreases the water content of the aerosols and hence AOD. The decreases in BB AOD near the southeast coast of Australia with corresponding increases in BB AOD in the Pacific Ocean towards Chile, which are enhanced as the BB-PIH increases, are likely due to the stronger free tropospheric winds than in the planetary boundary layer leading to greater transport of smoke (Figure A.10) (Chang et al., 2021; Heinold et al., 2022; Sellitto et al., 2022). The large BB AOD increases in the Indian Ocean are associated with increases in the BB-

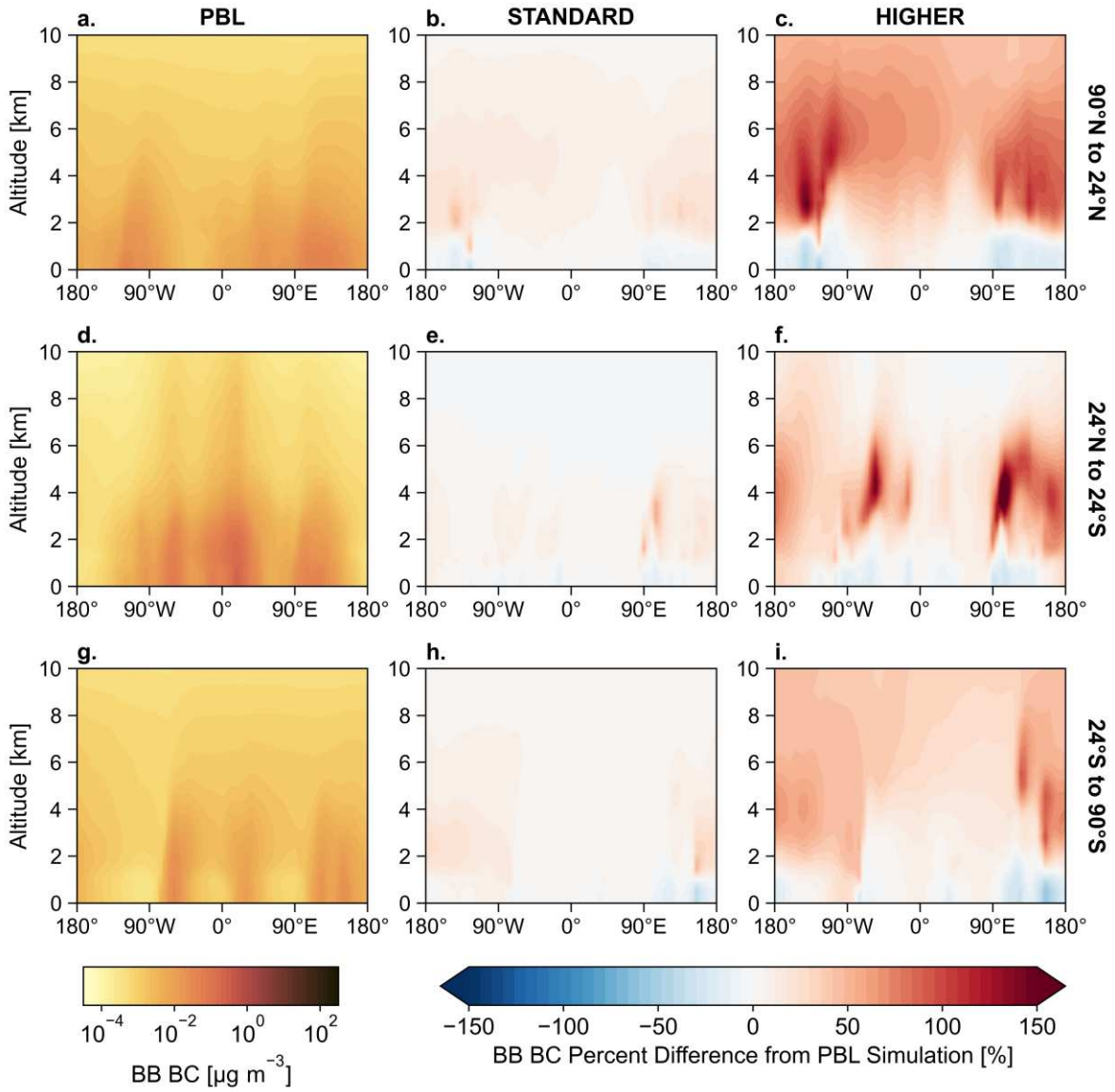

Figure 2.6: Average BC from BB concentration in 2019 and 2020 as a function of longitude and altitude in the PBL simulation in the (a.) Northern Hemisphere Extratropics (24°N to 90°N), (d.) Tropics (24°S to 24°N), and (g.) Southern Hemisphere Extratropics (90°S to 24°S). Percent difference in BC from BB relative to the PBL simulation in the Northern Hemisphere Extratropics for the BB-PIH scenarios (b.) STANDARD and (c.) HIGHER. Percent difference in BC from BB relative to the PBL simulation in the Tropics for the BB-PIH scenarios (e.) STANDARD and (f.) HIGHER. Percent difference in BC from BB relative to the PBL simulation in the Southern Hemisphere Extratropics for the BB-PIH scenarios (h.) STANDARD and (i.) HIGHER. The same figure as this, but for BB OA is shown in Figure A.13.

PIH in SE Asia and, potentially, atmospheric circulation patterns keeping the smoke in that area rather than transporting smoke away. The increases in AOD in the Indian Ocean and in the

Pacific Ocean in the SE Asia region as BB-PIH increases are consistent with efforts of prior studies to improve the forecasts of smoke transport in this region through raising the BB-PIH (Ooi et al., 2021). Over the northwestern Pacific Ocean, southeast of China, the patterns of BB AOD and magnitude of column mass increase with BB-PIH are consistent with a previous modeling study in the area for fires in March 2001 (Jian and Fu, 2014) in which they attributed the changes in total column and vertical distribution of BC mass as BB-PIH increased to March/April transport of pollutants through the Pacific subtropical high pressure system and subsiding flow. The March/April circulation pattern in this part of the Pacific (Figure A.10) in our simulations follows the same pattern in March/April of 2019 and 2020, with the smoke coming from Indonesian biomass burning in both years leading to increased BB AOD as BB-PIH increased (Figure A.17). The monthly BB AOD time series (Figure A.17) further complements the 2-year averages by showing the seasonal and interannual variability between regions.

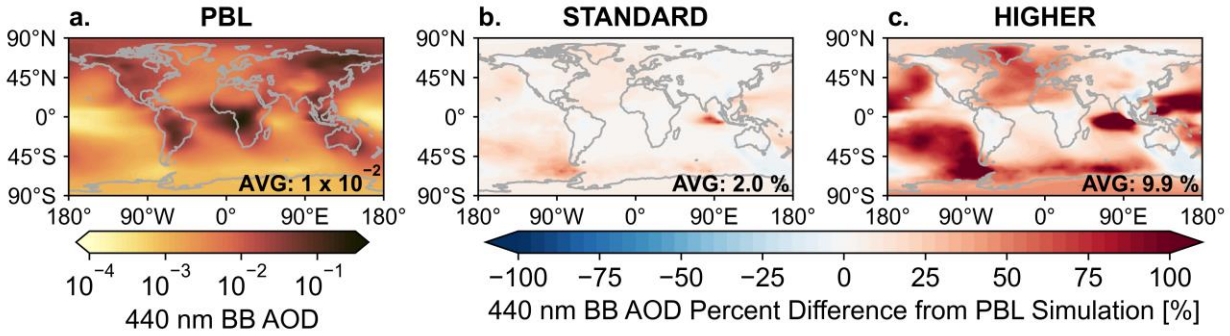

Figure 2.7: (a.) Average AOD from biomass burning (BB AOD) for 2019 and 2020 in the PBL simulation. Percent difference in surface average BB AOD from 2019 and 2020 relative to the PBL simulation for (b.) STANDARD and (c.) HIGHER. The complimentary figure for AOD is shown in Figure A.15.

The BB-DRE cooling is stronger as the BB-PIH increases due to the increase in aerosol mass loading from BB (Figure 2.8a-2.8h). The global average clear-sky BB-DRE is -164.3 mW m^{-2} in the PBL simulation and -183.0 mW m^{-2} in the HIGHER simulation, an increase in cooling of over 10% (Figure 2.4). In general, the clear-sky BB-DRE increases in magnitude as BB-PIH

increases (Figure 2.8d-2.8f), with more warming over high-albedo surfaces such as Greenland and Antarctica and more cooling over low-albedo surfaces such as oceans and darker land areas (e.g., forests). The stronger clear-sky BB-DRE as BB-PIH increases is consistent with the geographic distribution of changes in BB AOD (Figure 2.7b-2.7c). Regions with an increase in column mass have an increase in clear-sky BB-DRE magnitude (sign determined by surface albedo), and regions with a decrease in column mass have a decrease in clear-sky BB-DRE magnitude.

In the all-sky BB-DRE (Figure 2.8a-2.8c), the global average BB-DRE is -123.1 mW m^{-2} for the PBL simulation and decreases in the HIGHER simulation to -133.8 mW m^{-2}, a slightly smaller percent change than in the clear-sky BB-DRE (Figure 2.4). The smaller relative increase is due to more aerosol mass from biomass burning above clouds in all regions in the three BB-PIH simulations (Figure 2.9, Figure A.19) whereas in the PBL simulation, most BB mass is below clouds.

If we consider the potential role of brown carbon (BrC) in our calculation of the BB-DRE, the all-sky BB-DRE cooling increases less than if we ignore the impact of BrC, due to an increase in the effect of the now-more-absorbtive smoke going above clouds as BB-PIH increases (Figure 2.8g-2.8l). Including this BrC absorption results in a clear-sky BB-DRE of -126.7 mW m^{-2} in the PBL simulation and -85.9 mW m^{-2} all-sky BB-DRE. Both BB OA and BB BC have an absorbing component in the BrC BB-DRE calculations. Since the smoke is darker with the BrC BB-DRE calculation than in the non-BrC calculation, the warming impact of the aerosol being a lower albedo than the clouds is larger (Figure 2.9). As a result, with increasing BB-PIH the global all-sky BB-DRE cooling increases by 1.2 mW m^{-2} and 4.6 mW m^{-2} in the

STANDARD and HIGHER simulations compared to the PBL simulation when including the impact of BrC.

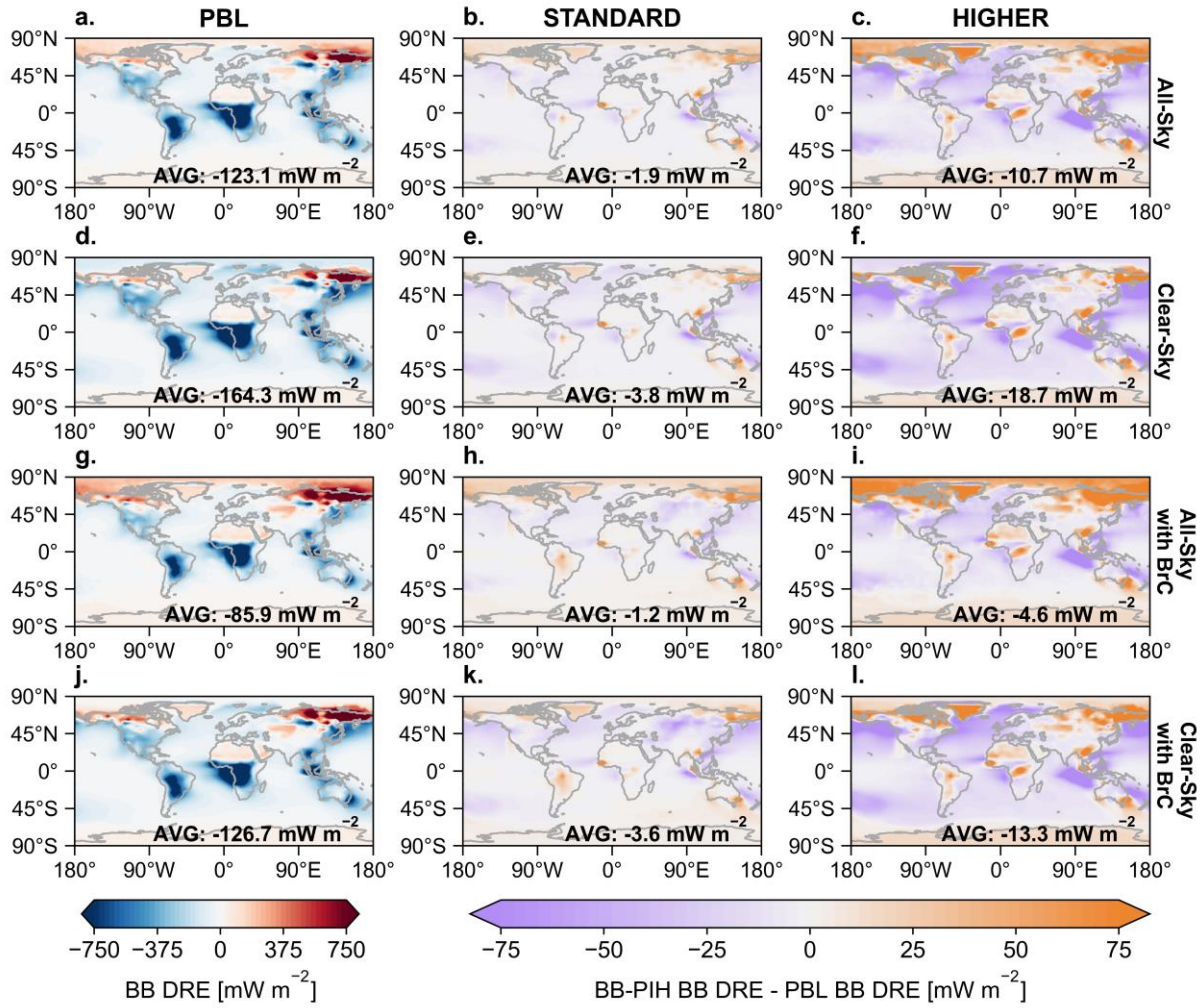

Figure 2.8: (a.) Average all-sky BB-DRE in the PBL simulation for 2019 and 2020. Average difference in all-sky BB-DRE in 2019 and 2020 relative to the PBL simulation for (b.) STANDARD and (c.) HIGHER. (d.) Average clear-sky BB-DRE in the PBL simulation for 2019 and 2020. Average difference in clear-sky BB-DRE in 2019 and 2020 relative to the PBL simulation for (e.) STANDARD and (f.) HIGHER. (g.) Two-year (2019-2020) mean all-sky BB-DRE including the impact of BrC in the PBL simulation. Average difference in two-year mean all-sky BB-DRE with BrC relative to the PBL simulation for (h.) STANDARD and (i.) HIGHER. (j.) Two-year (2019-2020) mean clear-sky BB-DRE including the impact of BrC in the PBL simulation. The average difference in two-year mean clear-sky BB-DRE with BrC relative to the PBL simulation for (k.) STANDARD, (l.) HIGHER. For the panels showing the difference relative to the PBL simulation, the BB-DRE is obtained by adding these values to the PBL values. The BB-DRE for all four BB simulations is shown in Figure A.18.

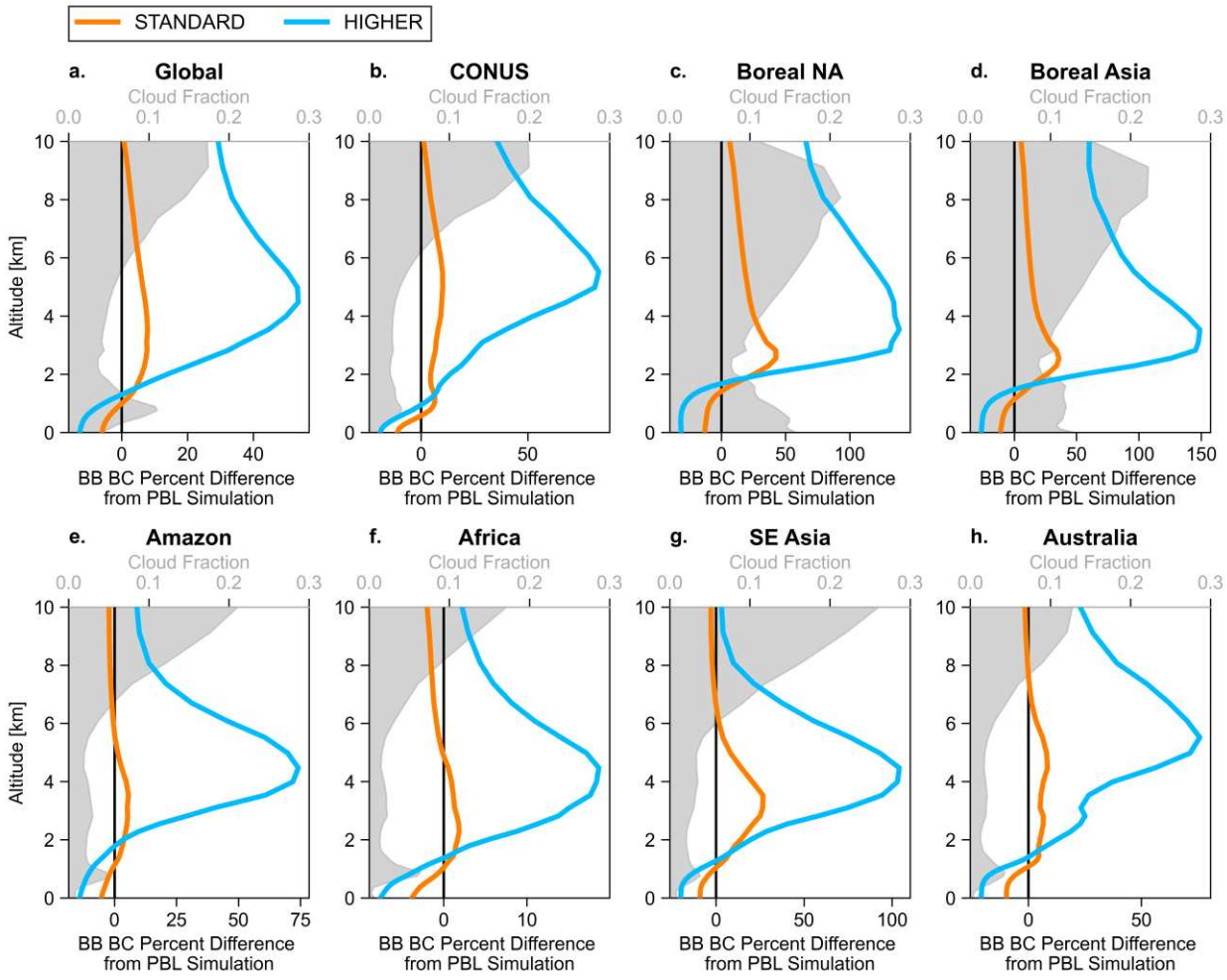

Figure 2.9: Percent difference in black carbon from biomass burning (BB BC) on the bottom horizontal axis from the PBL simulation as a function of altitude for STANDARD (orange) and HIGHER (blue). On the top horizontal axis, MERRA-2 (reanalysis used in all simulations) cloud fraction as a function of altitude in gray. Each panel is a different source region (Figure A.2) indicated by the text in black bold font above each panel. The same figure for BB OA is shown in Figure A.19.

2.3.2.2 Predicted Impacts of BB-PIH on CCN and the Aerosol Indirect Effect

At typical low-cloud levels ($\eta = 0.9$ to $\eta = 0.7$), in the PBL simulation BB increases the number concentration of particles larger than 80 nm (N80) (Figure 2.10a.) compared to the NBB simulation. The terrain-following η coordinate is used in modeling. For a grid box with a surface at sea-level, this low-cloud altitude range corresponds to pressure levels from 900 hPa to 700 hPa. These levels are relevant for understanding the impact of BB as cloud condensation nuclei,

which we represent as N80. In the PBL simulation at low cloud levels, BB increases N80 in source regions and downwind of source regions; some marine areas and Antarctica have decreases in N80 in the simulations with BB compared to the NBB simulation as a result of the enhanced condensation sink and suppressed new particle formation. In parts of the upper troposphere in all regions and near the surface in marine areas, BB decreases N80 in the PBL simulation compared to the NBB simulation due to these feedbacks on nucleation (Figure A.20).

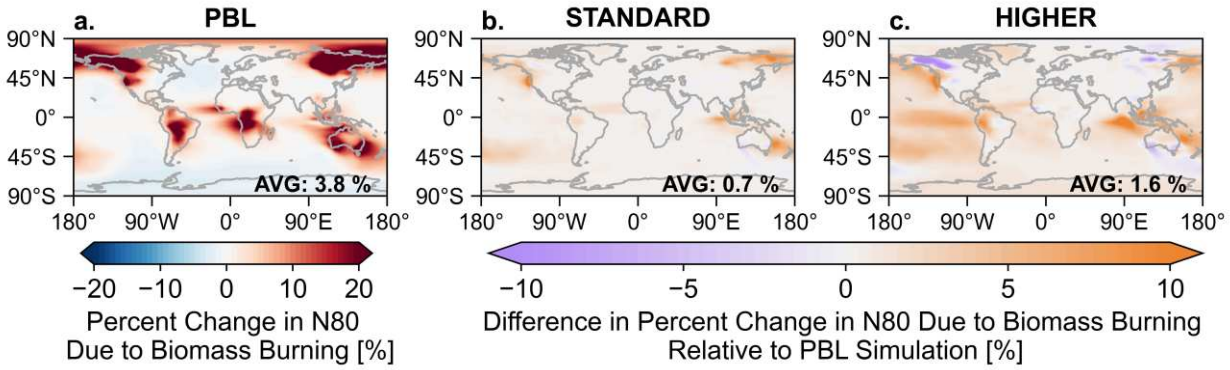

Figure 2.10: (a.) Average percent change in the number of particles larger than 80 nm (N80) at the low cloud levels ($\eta = 0.9$ to $\eta = 0.7$) due to biomass burning in the PBL simulation in 2019 and 2020. Difference in the percent change in the number of particles larger than 80 nm (N80) at the low cloud levels due to biomass burning in 2019 and 2020 relative to the PBL simulation for (b.) STANDARD and (c.) HIGHER.

As the BB-PIH increases, low-cloud levels have an increase in N80 from BB, except for some BB source regions with decreases (Figure 2.10b-2.10c). The increase in N80 is 1.6% globally in the HIGHER simulation compared to the PBL simulation, with greater increases over marine areas (2.7%) than land areas (0.5%) (Figure 2.4). As BB-PIH increases, there is a decrease in N80 from BB near the Earth surface, with the strongest increases being at low cloud levels (Figure A.20). Most of the Southern Hemisphere Pacific Ocean has a positive percent increase in N80 from BB in the HIGHER simulation. These changes indicate that as BB-PIH increases, the effect of increased BB aerosol loading aloft/longer lifetimes can dominate over the effects of new particle formation suppression by this loading i.e., while BB emissions can cause

a percent decrease in N80 in the PBL simulation relative to the NBB simulation, N80 can increase due to BB for higher BB-PIH simulations.

Raising the BB-PIH increases the cooling due to the BB-AIE (Figure 2.11). In the PBL simulation, the global two-year-average BB-AIE in the PBL simulation is -15.6 mW m^{-2}. The BB-AIE cooling increases by 5.3 mW m^{-2} and 17.4 mW m^{-2} in the STANDARD and HIGHER simulation, respectively relative to the PBL simulation. There are, however, regions with weakening of BB-AIE cooling, such as over and downwind of Australia, parts of boreal North America, and boreal Asia. This weakening is spatially consistent with decreases in N80. Over the Pacific Ocean, there are regions that had a warming BB-AIE in the PBL simulation that have a cooling BB-AIE in the STANDARD and HIGHER simulations. The spatial extent of the sign change increases as BB-PIH increases, which contributes to the BB-AIE more than doubling in the HIGHER simulation (Figure 2.11). These regions of sign change in the BB-AIE also have sign changes in the percent change of N80 from BB at low-cloud levels (Figure 2.10).

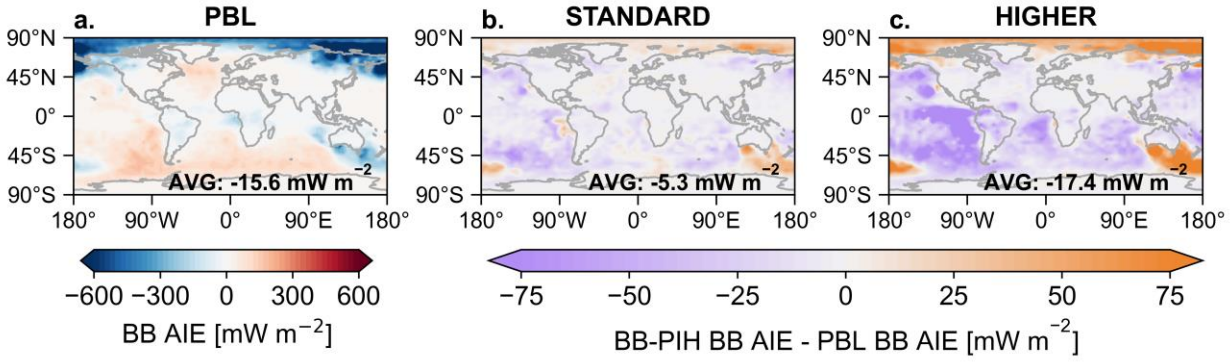

Figure 2.11: (a.) Average BB-AIE in the PBL simulation for 2019 and 2020. Average difference in BB-AIE in 2019 and 2020 relative to the PBL simulation for (b.) STANDARD and (c.) HIGHER. In panels (b.) and (c.), the BB-AIE is obtained by adding these values to the PBL values. The BB-AIE for all three BB simulations are shown in Figure A.21.

2.4 Conclusions

In this study, we presented the novel implementation of 3-dimensional biomass burning emissions in global simulations with detailed size-resolved aerosol microphysics. We developed this capability in the GEOS-Chem-TOMAS model. We conducted a two-year simulation (2019 and 2020) with GFAS-model plume heights, which enabled us to present the first global-scale analysis of effects of using GFAS-model plume heights in size-resolved aerosol microphysics simulations. We explored the impacts of elevated plume heights on model-observation agreement, air quality, the biomass burning direct radiative effect (BB-DRE), and the biomass burning aerosol indirect effect (BB-AIE). The following conclusions were the main results of this analysis:

1. Relative to injecting all BB emissions into the planetary boundary layer near to the Earth surface, raising the BB-PIH decreased the global-and two-year-mean surface BB $PM_{2.5}$ by 7% to 15% (for the two BB-PIH scenarios tested, standard and further elevated GFAS-model plume heights, respectively) with large decreases in BB source regions and slight increases in some remote land regions and marine regions.

2. The atmospheric global mean lifetime of BB aerosol increased by over 0.5 d in our highest BB-PIH scenario relative to injecting all the BB emissions into the planetary boundary layer near the Earth's surface. Global- and annual-mean BB-specific AOD increased by 10% globally in this scenario.

3. Elevating the BB-PIH increased the global- and annual- mean cooling of the clear-sky BB-DRE. These BB-DREs were -164.3 mW m^{-2} all BB emissions at the

surface), -168.1 mW m^{-2}, (using GFAS BB-PIH) and -183.0 mW m^{-2} (further upward shift of GFAS BB-PIH). Due to the effect of injecting BB emissions above high albedo surfaces (eg., ice, clouds), there were regions with a decrease in the cooling all-sky BB-DRE in the elevated BB-PIH scenarios.

4. The global-average BB-AIE were -15.6 mW m^{-2} (all BB emissions at the surface), -20.9 mW m^{-2} (using GFAS BB-PIH), and -32.9 mW m^{-2} (further upward shift of GFAS BB-PIH). The large increase in cooling as BB-PIH increases resulted from increased CCN at low-cloud levels as BB-PIH increased.

5. The BB-AIE over the ocean is the most sensitive to BB-PIH, while BB $PM_{2.5}$, BB-DRE, and BB-AIE over land have relative changes of similar magnitude.

6. Our results show robust and consistent global averages and spatial patterns of the impacts of BB-PIH in each of the two-years analyzed. Additionally, the shown impacts of BB-PIH on air quality and radiative effects are supported by improvements in model-satellite agreement of aerosol extinction coefficient profiles when using GFAS plume heights to inject BB emissions relative to emitting all BB at the surface.

Our results suggest that future global-model studies of aerosols and their impacts on climate and air quality, should give consideration to the careful inclusion of the biomass burning plume injection height. This is particularly relevant in the understanding of long-range transport of size-resolved aerosols. We acknowledge that there are limitations to this study including coarse model resolution and potential biases in the biomass burning emissions and plume heights. Our BB-PIH sensitivity simulation with injections above the standard GFAS values uses

crude adjustments to GFAS plume heights and is not meant to improve agreement with model-observation agreement for any specific BB plume but to reduce the systematic bias of heights being underestimated. Continued work on improving BB-PIH in emission inventories and simulations is needed, and exciting new opportunities are arising through various satellite applications (Cheeseman et al., 2020; Chen et al., 2021b; Lyapustin et al., 2020). The process of systematically elevating the BB-PIH with some constraints based on GFAS and its association with observed plume heights allows us to understand the impacts of higher plume heights on global air quality and climate. Our findings are of relevance for consideration of future fire impacts since fires may become more intense in the future with climate change, which would favor increases in BB-PIH. Our results also are relevant for the communities looking at historical and current fire impacts on aerosols and climate on a global scale. We have shown a strong sensitivity of global-mean aerosol-climate effects to biomass burning plume injection height.

2.5 Data Availability

This research has been supported by the National Science Foundation (grant no. AGS-1950327) and National Aeronautics and Space Administration (NASA) Health and Air Quality Applied Sciences Team Grant Number 80NSSC21K0429.

GEOS-Chem-TOMAS source code [FORTRAN] used in this study are available (https://doi.org/10.5281/zenodo.5748260). GEOS-Chem-TOMAS analysis code [Python and Fortran] are available (https://doi.org/10.5281/zenodo.14164744). Emissions and meteorology data are publicly available through the Washington University in St. Louis data server (http://geoschemdata.wustl.edu/). AERONET is available for download at https://aeronet.gsfc.nasa.gov/new_web/download_all_v3_inversions.html. CALIPSO data is available for download at

https://doi.org/10.5067/CALIOP/CALIPSO/CAL_LID_L3_Tropospheric_APro_CloudFree-Standard-V4-20. The van Donkelaar et al. 2021 $PM_{2.5}$ data is available through the Washington University in St. Louis (https://sites.wustl.edu/acag/datasets/surface-pm2-5/). The O'Dell et al. 2021 $PM_{2.5}$ data is publicly available (http://doi.org/10.25675/10217/233962).

Chapter 3: Look Within: Intraplume Differences on Smoke Aerosol Aging Driven by Concentration Gradients[2]

3.1 Introduction

Wildfires, which span orders of magnitude in size, are an important source of aerosol and gas-phase aerosol precursors to the atmosphere (Akagi et al., 2011; Andreae, 2019; Andreae and Merlet, 2001; Capes et al., 2008; Garofalo et al., 2019; Reid et al., 2005a; Wiedinmyer et al., 2011). Biomass burning aerosol is predominantly in the accumulation mode (100-1000 nm mode diameters) with a variable but often less abundant coarse mode (Adachi et al., 2022; Hodshire et al., 2019b; Janhäll et al., 2010; Reid et al., 2005a). The submicron mass in wildfire smoke is predominantly (>90%) organic aerosol (OA), with additional minor contributions from black carbon and inorganic species (Bond et al., 2013; Capes et al., 2008; Carrico et al., 2008; Cubison et al., 2011; Garofalo et al., 2019; Hecobian et al., 2011; Mardi et al., 2018; Reid et al., 2005a). This OA has been shown to impact the Earth's radiative budget (Hobbs et al., 1997; Ramnarine et al., 2019), air quality (McClure et al., 2020; O'Dell et al., 2019; Schill et al., 2020; Yue et al., 2013), and human health (Chen et al., 2017; Ford et al., 2018; O'Dell et al., 2021) with aerosol size, composition, and abundance determining the magnitude of the effects (Kodros et al., 2018a; Lee et al., 2013; Seinfeld and Pandis, 2016; Spracklen et al., 2011). However, uncertainties still remain surrounding OA emissions, evolution, and composition from wildfire smoke, particularly in how these processes vary as a result of vertical and horizontal concentration gradients within smoke plumes.

---

[2] June, N. A., Wiggins, E. B., Winstead, E. L., Robinson, C. E., Thornhill, K. L., Sanchez, K. J., et al. (2025). Look within: Intraplume differences on smoke aerosol aging driven by concentration gradients. *Journal of Geophysical Research: Atmospheres*, 130, e2024JD042359. https://doi.org/10.1029/2024JD042359

Wildfires directly emit primary organic aerosol (POA), much of which is semi-volatile and evaporates as smoke dilutes (Hatch et al., 2018; Huffman et al., 2009; May et al., 2013). The POA emissions from individual fires span orders of magnitude as a result of varying fire sizes, fuel types, and combustion properties (Bian et al., 2017; Gkatzelis et al., 2024; Hodshire et al., 2019b, a). Dilution rates of fires also tend to span orders of magnitude (Bian et al., 2017; Hodshire et al., 2019b). The dilution and emission variabilities, as well as measurement uncertainties lead to high uncertainty in OA emission ratios used in models. Aircraft field campaigns tend to sample larger wildfires and often miss the first half-hour of aging, due to flying risks, meaning there is still an observational gap in understanding evolution (Hodshire et al., 2019a).

POA and the vapors in equilibrium with the POA (semivolatile organic compounds, SVOC) react to produce oxidized primary organic aerosol (OPOA), although some refer to this material as SOA and reserve the term OPOA for that formed by particle-phase oxidation of POA (Dzepina et al., 2009; Hatch et al., 2018; Hennigan et al., 2010; Jen et al., 2019). Additionally, wildfires emit important OA precursor vapors with higher volatility, including oxygenated and non-oxygenated aromatics, heterocyclic organic compounds, and biogenic VOCs which can oxidize in the atmosphere to form secondary organic aerosol (SOA) (Gkatzelis et al., 2024; Hatch et al., 2015, 2017; Jathar et al., 2014; Koss et al., 2018; Palm et al., 2020; Sekimoto et al., 2018; Smith et al., 2014; Stockwell et al., 2015). Despite fires being a large source of VOCs to the atmosphere, the contribution of biomass burning to SOA/OPOA is uncertain (Granier et al., 2011; Lamarque et al., 2010; Reid et al., 2005a; Shrivastava et al., 2017). Since the processes accounting for SOA and OPOA in models are typically parameterized due to uncertainties and computational limitations of simulating a large number of VOC species individually (Bilsback et

al., 2023; Charan et al., 2019), the evolution of OPOA and SOA in wildfire smoke needs to be well understood to improve estimates of biomass burning on climate and health impacts.

Further complicating the understanding of OA, the evolution of the OA enhancement ratio (OAER; ΔOA/ΔCO) as smoke ages has been observed to either increase, decrease, or remain constant (Akagi et al., 2012; Cubison et al., 2011; Hecobian et al., 2011; Hobbs et al., 2003; Jolleys et al., 2015; May et al., 2015; Pagonis et al., 2023; Sakamoto et al., 2015; Vakkari et al., 2014; Yokelson et al., 2009; Zhou et al., 2017). The ΔOA/ΔCO corrects for dilution, showing the net change in OA as smoke ages due to the effects of POA evaporation and OPOA/SOA formation (Akagi et al., 2012). Field studies have suggested that OPOA/SOA condensation and POA evaporation balance each other in the wildfire plume leading to little net change in OA during the first few hours of aging (Akherati et al., 2022; Hodshire et al., 2019a, 2021; May et al., 2015; Palm et al., 2020). This hypothesis was supported by simulations of wildfire plumes measured during the WE-CAN field campaign that showed dilution-driven evaporation of POA and simultaneous production of SOA explain the lack of change in OA enhancement ratios observed during the first 2 to 8 hr of physical aging (Akherati et al., 2022). At approximately 4 hours of aging, the OA in these plumes was 65% POA, 25% OPOA, and 10% SOA according to the simulations (Akherati et al., 2022). The variability in ΔOA/ΔCO evolution may also be influenced by the concentration of the plume (Bian et al., 2017; Hodshire et al., 2021; June et al., 2022). For example, plumes sampled during the Fire Influence on Regional to Global Environments and Air Quality (FIREX-AQ) campaign tended to have an observed ΔOA/ΔCO decrease in more concentrated plumes and an ΔOA/ΔCO increase in less concentrated plumes after the first transect (June et al., 2022; Pagonis et al., 2023). Prior to the first transect, there is observational evidence for rapid evaporation in less concentrated plumes

evidenced by the ΔOA/ΔCO at the first transect tending to be lowest in the most dilute plumes sampled during FIREX-AQ (June et al., 2022).

Aerosol size distributions generally shift toward larger sizes as smoke ages, which is predominantly due to coagulation with slight impacts due to net condensation or evaporation of OA (Hodshire et al., 2019a; June et al., 2022; Sakamoto et al., 2016). Coagulation reduces the particle number concentration, shifts the distribution to larger sizes, and narrows the modal width of the size distribution as a result of collisions resulting in faster loss of smaller particles, while the larger particles grow in size slightly (Hodshire et al., 2019a; Janhäll et al., 2010; June et al., 2022; Sakamoto et al., 2016). Number median diameters have been observed to increase from 40 to 150 nm in fresh smoke (<1 hr aging) to 175 nm to 290 nm in smoke that has aged for 3 to 6 hours (Hodshire et al., 2021; Janhäll et al., 2010; June et al., 2022; Reid and Hobbs, 1998). The coagulation rate is proportional to the square of the number concentration (when the sizes are fixed), meaning that more concentrated plumes have more rapid coagulation (Seinfeld and Pandis, 2016). The dilution rate of the plume also has an impact, since a plume mixing into the clean background air at a slower rate will have a slower decrease in number concentration allowing for sustained coagulation (June et al., 2022; Sakamoto et al., 2016).

Within a single smoke plume, the processes driving aging can vary due to mixing and gradients in concentration (differences in concentrations in different regions of the plume) (Decker et al., 2021; Hodshire et al., 2021; June et al., 2022; Pagonis et al., 2023; Peng et al., 2020; Wang et al., 2021; Xu et al., 2021). Studies using observational data from the Biomass Burning Observation Project (BBOP) and FIREX-AQ have shown there to be differences in coagulation and net OA evaporation/condensation between the edge and core of a plume (Hodshire et al., 2021; June et al., 2022). June et al. 2022 found faster coagulation and faster

evaporation in the concentrated centers of plumes sampled during FIREX-AQ; however, there was also evidence of rapid changes in ΔOA/ΔCO before the first transect. Studies examining the composition of ΔOA/ΔCO evolution, specifically looking at POA, OPOA, and SOA in smoke plumes have often focused on either the plume average at the altitude of an aircraft or horizontal, cross-wind variability at that altitude (Akherati et al., 2022; Hodshire et al., 2021; June et al., 2022; Palm et al., 2020, 2021). There is less understanding of how smoke ages at varying heights in a smoke plume, and improving this understanding would be beneficial to understanding impacts on air quality at the surface and aloft (Pagonis et al., 2023). Pagonis et al. (2023) compared ΔOA/ΔCO measurements from recent field campaigns sampled at aircraft altitude and in smoke plumes sampled at the ground, finding that the ground measurements had an ΔOA/ΔCO a third of that at the aircraft measurements. These findings are explained by temperature differences: at aircraft altitude (270 K) the semi-volatile organic compounds (SVOC) favor the particle phase, while the surface (310 K) SVOC partitioning favors the gas phase (Pagonis et al., 2023). For example, the Sheridan Fire sampled under a range of temperatures during FIREX-AQ showed a decrease in ΔOA/ΔCO with increasing temperature consistent with the plume-by-plume analysis (Pagonis et al., 2023). The vertical variances in plume evolution are likely influenced by the initial smoke injection height and environmental conditions that a plume is emitted into, such as a deep planetary boundary layer (PBL) versus a shallow one, or into the free troposphere (FT). Despite recent field campaigns improving the sampling of smoke plumes and the gradients within them, studies have typically focused on plume average evolution and variability in evolution at a single height. Additionally, understanding the evolution of smoke prior to the first transect remains an ongoing field of research.

Simulations of heterogeneity within smoke plumes have been done before with models such as SAM-ASP (Lonsdale et al., 2020), WRF-LES-Chemistry (Wang et al., 2021), SAM-TOMAS (Sakamoto et al., 2016), CRM6 (Alvarado et al., 2009). Lonsdale et al. (2020) used the SAM-ASP 2D Lagrangian model to simulate gas and aerosol chemistry in a wildfire smoke plume. Although the model showed strong intraplume gradients in CO, gradients were less pronounced in OA and O_3 due to the impact of the plume not being included in the photolysis rates. Additionally, this study did not include evaluation of simulated aerosol size distributions due to a lack of measurements (Lonsdale et al., 2020). Wang et al. (2021) examined ozone and NO_x chemistry using a large eddy simulation (LES) of a plume sampled during FIREX-AQ in the WRF-LES-Chemistry model. They found chemistry to be suppressed at the center of the plume as well as below the concentrated free tropospheric plume (Wang et al., 2021). This study did not include analysis of OA or aerosol size distributions.

In this study, we use a 2D Lagrangian model (SAM-ASP) coupled with the tropospheric ultraviolet and visible model to further the understanding of vertical variability of OA and aerosol size distributions in near-term (first 4 hours) aging of a wildfire plume sampled during FIREX-AQ that had emissions into both the FT and PBL. In Chapter 3.2, we describe the observational data and model setup. In Chapter 3.3, we first analyze the model performance against observations at the aircraft altitude. We then analyze the impacts of in-plume concentration gradients on differences in aging between the boundary layer and free troposphere.

3.2 Materials and Methods

3.2.1 FIREX-AQ Field Campaign Data

The FIREX-AQ campaign sampled wildfire smoke in the western United States in July-August 2019 (Warneke et al., 2023). In our study, we use data from the first sampling of the

Williams Flats Fire around 22 UTC on August 3, 2019. It should be noted that the aircraft moved downwind 4 times faster than the smoke, meaning that the smoke sampled farther from the fire generally had been emitted by the fire earlier in the day than the smoke sampled close to the fire. For this reason, transects used for model-observation comparison are limited to those identified as the most Lagrangian: transects in the vertically densest section of the plume as identified by lidar measurements with fairly consistent modified combustion efficiency (0.89 to 0.92) suggesting relatively constant burning conditions (June et al., 2022; Wang et al., 2021). Additionally, we also limit our analysis to the first 4 hours of physical aging due to the limits of the pseudo-Lagrangian sampling pattern (aircraft moving downwind faster than the plume). The FIREX-AQ campaign also included a mobile laboratory truck; however, for this day and fire, the analysis measurements of aerosol size smaller than 500 nm and aerosol mass spectrometer measurements are not available.

The TSI laser aerosol spectrometer (LAS) measured the aerosol size distribution between 0.1 and 5 μm at 1 Hz resolution (Moore et al., 2021). The LAS uses a helium-neon laser to detect particles across this size range with 20% uncertainty across all sizes. The LAS was calibrated using size-classified ammonium sulfate aerosols. More detailed information on the LAS calibration and performance during FIREX-AQ can be found in the work of Moore et al. (2021). As described by June et al. (2022), we apply corrections to the LAS measurements for evaporation due to heating in the sampling lines and optical saturation of the LAS sensor.

The Aerodyne high-resolution time-of-flight aerosol mass spectrometer (AMS) measured OA at 1 or 5 Hz resolution (Pagonis et al., 2021; Warneke et al., 2023). The uncertainty for OA measured by the AMS has been estimated to be 38% (2 sigma), mostly due to uncertainties in collection efficiency and the relative ionization energy of OA (Bahreini et al., 2005, 2009; Guo et

al., 2021). An evaporation correction is applied to the AMS measurements to account for evaporation due to heating in the sampling lines (Pagonis et al., 2023).

The NASA Langley Research Center's airborne Differential Absorption Lidar and High Spectral Resolution Lidar (DIAL-HSRL) provides measurements of 180-degree aerosol backscatter at 532 nm. It is used here to provide qualitative comparisons to the model of the vertical distribution of aerosol particles throughout the smoke plume.

Gas phase measurements include CO, O_3, NO_x, as well as photolysis rates. CO was measured by the NOAA LGR at 5 Hz resolution and averaged to 1 Hz. The instrument operated with 2% uncertainty during FIREX-AQ (Bourgeois et al., 2022). The O_3 and NO_x measurements were made by the NOAA NOyO3 4-channel chemiluminescence instrument (Ryerson et al., 2000). The photolysis frequencies were measured by the NCAR CCD Actinic Flux Spectroradiometers (CAFS) instrument (Shetter and Müller, 1999).

3.2.2 SAM-ASP-TUV Model

We use a version of the System for Atmospheric Modeling coupled to the Aerosol Simulation Program (SAM-ASP) model now coupled with the Tropospheric Ultraviolet and Visible (TUV) model. Lonsdale et al. (2020) introduces the coupling of SAM v6.10 to ASP v2.1; we briefly describe the details here. In SAM-ASP, SAM is the Large-Eddy Simulation (LES) component that is configured as a moving, 2D Lagrangian wall, oriented perpendicular to the mean wind in the layer of smoke injection (1320 m to 2200 m). Due to the use of the mean wind, one limitation of the model is the inability to capture differences in physical age that occur between the edge and core of the plume, as well as between the FT and PBL. The grid boxes in the 2D moving wall have a 500 m × 500 m horizontal resolution with the total domain width being 120 km in the perpendicular to the wind direction (and 500 m in the with-wind direction).

The vertical resolution is 40 m with a total vertical extent of 3.2 km. One limitation of the model is that it does not include the topography. We acknowledge that this means the model may have biases in turbulence due to the roll of terrain on boundary layer dynamics; however, prior studies have shown that these simulations with no terrain can be valuable in understanding the evolution seen in smoke plumes (Lonsdale et al., 2020; Wang et al., 2021). The meteorological conditions used in the model use the 3 hr, 32 km resolution North American Regional Reanalysis from the time of the flight (August 3, 2019, 21:00 UTC to August 4, 2019, 00:00 UTC). SAM allows various configurations for the advection scheme, turbulence parameterization, radiation and cloud microphysics. The configuration used here is as described by Lonsdale et al. (2020), including the use of a positive definite monotonic advection scheme with a non-oscillatory option, the 1.5-order turbulent kinetic energy closure for subgrid-scale turbulence, and the cloud microphysics scheme of Morrison et al. (2005) (although clouds are not predicted nor were observed in the domain on our investigated day). Initial turbulence in the model is spun up for 3 hours using a warm bubble to allow for repeatable turbulence between sensitivity simulations. The turbulence is nudged to the reanalysis fields on a timescale of three hours. SAM transports all of the gas-phase and aerosol species calculated by ASP (Lonsdale et al., 2020). ASP is used to simulate the chemical and physical aging of biomass-burning plumes (Alvarado et al., 2015; Alvarado and Prinn, 2009). A sectional aerosol size distribution with 10 bins (0.025 μm to >1 μm) is used to represent the aerosol size distribution in ASP, which also includes inorganic and organic aerosol thermodynamics, condensation and evaporation, coagulation of aerosol particles, and aerosol optical properties (Alvarado et al., 2016).

In this version of SAM-ASP-TUV, we couple SAM-ASP v1.0 to the TUV model (Bais et al., 2003; Lonsdale et al., 2020). The coupling of SAM-ASP to TUV allows for online

calculations of photolysis rates including the impact of aerosols. Aerosol optical depth, single scattering, and asymmetry parameter are sent from SAM-ASP to TUV. TUV predicts the photolysis rates across each column for 48 reactions (Table B.1), which are sent back to ASP for chemistry.

We made updates to the SAM-ASP-TUV representation of OA chemistry to better represent SOA precursors and processes from recent field campaigns and modeling studies of wildfire plumes. The previous version of SAM-ASP used nine volatility bins spanning from saturation concentrations (C*) of 10^{-2} to 10^{6} μg m^{-3} at 298 K (each bin covering 1 order of magnitude) tracking POA, OPOA, and SOA together. To track POA/OPOA and SOA separately in our simulations, without adding additional species, we use four volatility bins (each covering 2 orders of magnitude) from 10^{-2} to 10^{6} μg m^{-3} for POA/OPOA and a second set of four volatility bins from 10^{-2} to 10^{6} μg m^{-3} for SOA. POA emissions are split into the 4 POA/OPOA volatility bins as shown in Figure B.1 (Akherati et al., 2020, 2022; Bilsback et al., 2023; May et al., 2013). This range of C* bins spans from low-volatile organic compounds (LVOC) to intermediate-volatile organic compounds (IVOC). For POA/OPOA, these C* have previously been shown to be the range observed in fresh wildfire smoke (Bian et al., 2017; Hatch et al., 2017; May et al., 2013). Using the configuration described here allows the POA/OPOA bins to have the same spacing and C* as the SOA bins for which we have updated information for the SOA processes in smoke. Kinetic partitioning is used to determine the amount of organics in the particle/gas phase in each of these bins. Based on Shrivastava et al. (2024), we use a reduced scheme for SOA precursors using two lumped precursor classes, OXARO and OTHER. OXARO represents all oxygenated aromatic precursors and OTHER represents all remaining SOA precursors including heterocyclics, aromatic hydrocarbons, biogenics, and acyclic VOCs (Shrivastava et al.,

2024). The use of these two SOA precursor classes was based on previous biomass-burning work (Akherati et al., 2020, 2022; Bilsback et al., 2023), which showed that these precursor classes can capture the majority of the SOA potential in wildfire plumes. The sum of OXARO and OTHER represents the total amount of SOA precursors in our simulations (SOA_{Pre}). OXARO and OTHER each react with OH into the SOA volatility bins with yields and reaction rates shown in Figure B.1 (Shrivastava et al., 2024). Once SOA products are in the volatility bins, they do not react with OH to change volatility after formation; the parameterized volatilities already include multi-general aging representative of the first several hours in the plume.

Since OPOA is not tracked explicitly, we run five simulations with different POA/OPOA aging schemes (Table B.2). A no-aging case, where the POA/OPOA volatility bins do not react with OH is used to estimate the OPOA fraction in the other four simulations, by using the difference between POA between a simulation with an aging scheme and the no-aging case. For the simulations with POA aging, the POA/OPOA volatility bins react with OH to form lower-volatile VOC and higher-volatile VOC. The total yield of these reactions is 1.075 based on Robinson et al. (2007) and Ahmadov et al. (2012). Each sensitivity simulation tests a different fraction of fragmentation from 0% to 50% (Table B.2). All of the POA aging scheme simulations are run twice, once with a base case SOA precursor emission rate and once with a doubling of the SOA precursor emission rate. We primarily discuss results for the configuration with the base case SOA_{Pre} emissions, with the POA following the 0.825 functionalization mass yield and 0.25 fragmentation mass yield. However, we also discuss the sensitivity of model-observation agreement due to the assumptions made for OA aging.

Emissions to SAM-ASP-TUV occur after turbulence spin-up over a time period of 1 hour while the 2D wall passes over the fire area. During this hour chemistry does not happen in the

plume, but mixing occurs. Emissions ratios, initial CO, and aerosol size distribution initial conditions are determined following the methodology of Lonsdale et al. (2020). Some emissions ratios were updated using the Gkatzelis et al. (2024) study which gives emission ratios and emission factors for US wildfires based on FIREX-AQ measurements. Emissions ratios for the SOA precursor classes, OXARO and OTHER, are from Shrivastava et al. (2024). A scaling factor is used to adjust total emissions in order to yield agreement in CO, OA, and total aerosol number concentration at the time of the first transect. Although the emissions ratios used are consistent with estimates for Western US wildfires; the process of adjusting to match the model and observations at the first transect likely impacts our conclusions on processes prior to the first transect where there is no observational constraint. The emitted aerosol median diameter and modal width, 110 nm and 1.5, respectively, was selected to yield agreement in modeled and observed diameter at the first transect assuming a lognormal mode. This selection was done through an iterative process of adjusting emitted aerosol median diameter and modal width within the range of prior studies (eg. Grieshop et al. 2009) until there was a match in the median diameter at the first transect. Other than the SOA precursor emission rate, which is adjusted for some sensitivity simulations, all emissions are fixed between the sensitivity simulations.

3.2.3 Derived Quantities

In the observations, flags provided in the FIREX-AQ dataset are used to determine measurements in background air and in-plume. The enhancement of species X due to the presence of smoke (ΔX) is determined by subtracting the average background concentration ($X_{background}$) from the in-plume concentration ($X_{inplume}$). The minimum observed ΔCO was 135 ppbv. For the model, we use ΔCO greater than 135 ppbv as the threshold for determining if a model grid box is considered in-plume. Enhancement ratios ($\Delta X/\Delta CO$) are used to evaluate the

dilution-corrected evolution of a species. Lastly, averages within the plume are concentration weighted such that the more concentrated parts of the plume contribute more to the averaged quantity.

For the observations, the number median diameter (D_{pm}) and number concentration (N) are calculated using the same methodology as June et al. (2022) by fitting a lognormal distribution from 50 nm to 2 μm to the binned $dN/dlogD_p$ measurements from the LAS. A single mode is enough to describe the size distributions sampled in this plume (June et al., 2022; Moore et al., 2021). For the model, the N and D_{pm} are calculated using the same methodology as for the model output, also limiting the model to the size ranges from 50 nm to 2 μm. In the 4 hours of aging used in our study, few particles in the model and observations grow outside of this size range.

For model evaluation against the DIAL-HSRL observations, we calculate an estimate of the backscatter at 532 nm. We use Mie Code to calculate the backscatter at 532 nm (Bohren and Huffman, 2008). We use an assumed ambient particle refractive index (1.47 + 0.007i) in our backscatter calculations based on Moore et al. (2021), which calculated refractive indices for different FIREX-AQ plumes. Although this assumption for a refractive index introduces some uncertainties, it allows for a qualitative comparison of the vertical distribution of the modeled and observed plume.

We additionally define a quantity of $\Delta CO_{loading}$ to understand the total amount of smoke in the PBL and FT for any vertical/cross-wind cross-section of the plume (Eq. 3.1).

$$\Delta CO_{Loading} = \sum_{z}\sum_{x} \Delta CO_{\frac{\mu g}{m^3},box} \Delta z_{grid} \Delta x_{grid} U_{wall} \quad (3.1)$$

Where Δz_{grid} is equal to 40 m, Δx_{grid} is equal to 500 m, and U_{wall} is equal to the speed that the 2D Lagrangian wall is advected downwind. We sum over the entire plume, the plume in the PBL, and the plume in the FT to determine the fraction of $\Delta CO_{loading}$ in the FT and the PBL. We use a PBL height of 1880 m above ground level (AGL), based on the reanalysis meteorology vertical profiles of temperature used in the model and the height to which ΔCO is well mixed in the model after 1 hr of aging. The plume above this height is considered to be FT. In reality the PBL height likely evolves slightly during our 4 hr simulation, but given that the aircraft samples the plane in about 2 hr, these effects would be difficult to disentangle from other observational uncertainties. This quantity is not directly input into the model and does not influence the model output; it is used to aid in interpretation of the model results. The model is rather spinning up turbulence and creating a PBL like environment, and being nudged to the re-analysis on 3 hr timescales.

3.3 Results

3.3.1 Model-Observation Comparisons

Both the DIAL-HSRL observations (Figure 3.1a-c) and the model (Figure 3.1 d-f) backscatter at 532 nm show a plume located in the free troposphere and in the PBL. We have not removed the background backscatter from either the observations or the model. Therefore, there are horizontal discrepancies outside of the plume due to the model having an assumed constant background everywhere. On the observation panels (3.1a-c), there is a level of white where data are not reported for approximately 500 m around the aircraft level. Additionally, data are not reported when attenuation in the plume is too large, or near the surface due to the impacts of the ground. Data not being reported due to plume attenuation is the primary cause of missing data in 3.1a and 3.1b, while 3.1c is more affected by the terrain. Our model does not include topography,

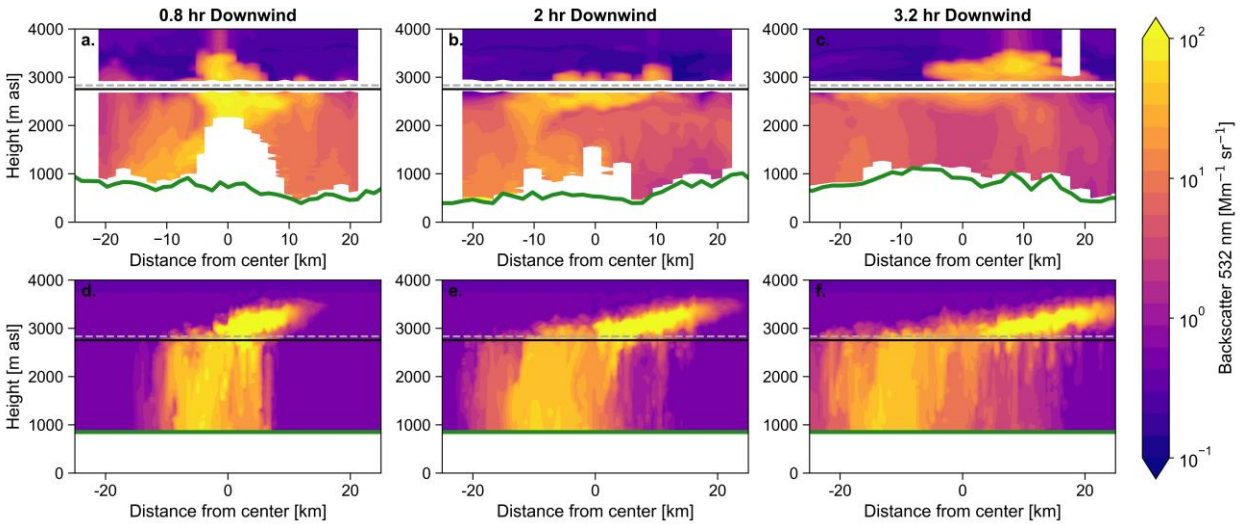

Figure 3.1: (a.)-(c.) Observed DIAL-HSRL backscatter at 532 nm for three transects observed during the August 3, 2019, sampling of the Williams Flats Fire. (d.)-(f.) The corresponding backscatter at 532 nm for the SAM-ASP-TUV model. Note that the alignment horizontally between the top and bottom rows may differ as the center in (a.)-(c.) is based on the time it took the aircraft to complete the transect, while the center in (d.)-(f.) is the center of the model. In the observed panels, there are areas of white where data are not reported at the altitude of the aircraft, as well as topography effects near the surface or from in-plume attenuation. Topography is not included in the model. The vertical axes limits are set such that the vertical extent is approximately equal between the model and observation in units of m above sea level (m asl). The solid black horizontal line is the height of the PBL determined from the reanalysis used in the model. The dashed gray line is the height of the aircraft that sampled the plume. The ground altitude is plotted in green.

and therefore, cannot represent these topographical features. The mixing to the surface pattern is similar to that shown for the same sampling of the Williams Flats Fire simulated with WRF-LES by Wang et al. (2021). At the time of the first transect (Figure 3.1a. and 3.1d.), the plume has yet to disperse much horizontally, but has mixed to the surface in both the model and observation. After 2 hr of aging (Figure 3.1b. and 3.1e.), the free tropospheric plume has dispersed horizontally, with one side of the plume showing stronger mixing to the surface due to the Ekman spiral (Wallace and Hobbs, 2006). At 2 hr, the model has the most concentrated part of the plume just above the aircraft, while the observations suggest that the aircraft sampled directly at the most concentrated part of the plume. At 3.2 hr of aging (Figure 3.1c. and 3.1f.), both the

model and observations continue to show a free tropospheric plume and stronger mixing on one side of the plume to the surface. At this time both the model and observations have a concentrated smoke layer above the aircraft. Although there is generally qualitative agreement between the DIAL-HSRL and the simulated backscatter, there are some discrepancies, potentially due to both the pseudo-Lagrangian sampling and topographical effects on dispersion and PBL dynamics. Differences between the model and observations in terms of the amount of entrainment that occurs between the FT and the PBL could exist as a result of the observational limitation of pseudo-Lagrangian sampling and the model limitation of not including topography. However, without truly lagrangian observations, we cannot quantify how much of the model biases are due to lacking terrain, or potential biases in turbulence. Although not a direct comparison, these backscatter comparisons suggest that the SAM-ASP-TUV qualitatively represents both the horizontal and vertical dispersion of the plume in the near-term aging.

The aircraft only sampled the free tropospheric portion of the plume, so our quantitative model evaluation (Figure 3.2) is for this portion of the plume only. The model captures the observed CO concentration dilution rate at the altitude of the aircraft and ΔCO concentrations throughout the first 4 hours of aging. Although there are higher ΔCO values just above the aircraft (blue lines) and lower ΔCO values just below (green lines) (Figure 3.2a). The model representation of dilution at the aircraft altitude gives further confidence (beyond the DIAL-HSRL comparisons) that the model represents the dispersion of the plume.

The model generally captures the evolution of the plume average ΔN/ΔCO (Figure 3.2b.) and D_{pm} (Figure 3.2c.) measured by the aircraft within the variability of the transect. There are sensitivities to the altitude of comparison with faster coagulation above the aircraft and slower coagulation below. Prior to the first transect, the changes in ΔN/ΔCO and D_{pm} are due to rapid

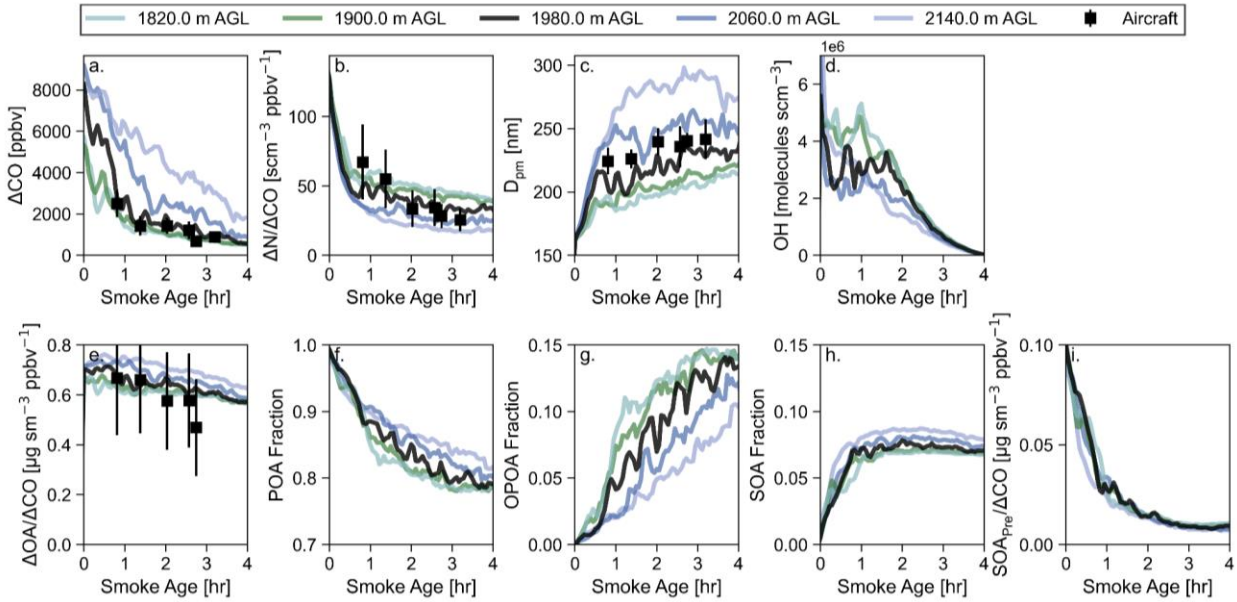

Figure 3.2: The transect average evolution of (a.) ΔCO, (b.) ΔN/ΔCO, (c.) D_{pm}, (d.) OH, (e.) ΔOA/ΔCO, (f.) POA fraction, (g.) OPOA fraction, (h.) SOA fraction, and (i.) SOA_{Pre}/ΔCO. The solid-colored lines are the model plume average at five heights with the 1980.0 m AGL line being the altitude closest to the height of the aircraft. The transect-average aircraft observations for the August 3, 2019 sampling of the Williams Flats Fire are shown as black squares for panels (a.)-(d.) with the error bars showing the standard deviation of the measurements.

coagulation resulting in a factor-of-3 drop in number and a 30-50% increase in D_{pm}. After 1 hr of aging, the coagulation rate slows as seen by the slower rate of decrease in ΔN/ΔCO. The slower increase in D_{pm} after 1 hr of aging is due to the slower coagulation rate; however, there are minor effects of evaporation due to the net decrease in ΔOA/ΔCO. The net decrease in ΔOA/ΔCO results in approximately 5% smaller particles at 4 hours of aging compared to if there was no net change in ΔOA/ΔCO (Figure B.2).

The model and observations suggest net OA evaporation with a decrease in ΔOA/ΔCO from 0.7 to 0.58 μg sm^{-3} ppb^{-1} at approximately 3 hours of aging (Figure 3.2e.). The final observation transect has a lower ΔOA/ΔCO than the model; however, this point does not follow the trend of the prior observation transects. In the model levels surrounding the aircraft, there are

only slight impacts of the altitude on the ΔOA/ΔCO comparison. However, the comparisons reveal that the more concentrated levels above (2060 m to 2140 m) had faster evaporation than the layers below (1820 m to 1900 m), likely due to effects of there being more semi-volatile OA to evaporate at higher concentrations. The OA evaporation primarily occurs in the C*(298 K) 10^4 μg m^{-3} bin, with some evaporation in the C*(298 K) 10^2 μg m^{-3} bin (Figure B.3). The evaporation in the volatility bin space is consistent with the approximately 280 K temperature at the aircraft altitude and the modeled ΔOA concentrations decreasing from 5870 μg sm^{-3} to 607 μg sm^{-3} at 3.2 hours. The reduction in ΔOA/ΔCO is the result of POA evaporation being greater than the increases in OPOA and SOA (Figure 3.2e-h). We acknowledge that there is likely some uncertainty induced by the selection of volatility bins used in the model. However, given the consistency with observations at the aircraft altitude and the volatility bin setup being consistent with recent studies (e.g., Bian et al., 2017; Bilsback et al., 2017), we believe the setup used here to be reasonable within the uncertainties of current knowledge. After 4 hours of aging, the combined fraction of OPOA and SOA is about 21%, which is similar to the fractions of OPOA and SOA seen in simulations of wildfire plumes sampled during the WE-CAN field campaign (Akherati et al., 2022). The increases in SOA and OPOA are largest prior to the first transect (0.8 hr); after that point in time the SOA fraction remains approximately constant, while the OPOA continues to increase. The SOA fraction stops increasing due to the lack of SOA precursors remaining in the plume after 1 hour of aging (Figure 3.2i). The rapid changes in ΔOA/ΔCO before first measurement are consistent with prior studies which have suggested the need to understand processes controlling the evolution in the first half hour of wildfire aging (Akherati et al., 2022; Bian et al., 2017; Cubison et al., 2011; Hodshire et al., 2019a).

The OA aging sensitivity simulations (Table B.2) all show net OA evaporation in agreement with the observations (Figure B.4); however, there are minor impacts on ΔOA/ΔCO and D_{pm} observation agreement as well as the amounts of OPOA and SOA (Figure B.4). For the scenarios with 2× SOA_{Pre} emissions, the main difference is ΔOA/ΔCO is higher at all times relative to the 1× SOA_{Pre} emissions due to the increase in SOA_{Pre} increasing the amount of SOA formed in the first hour of aging. However, nearly all of the differences in ΔSOA/ΔCO come prior to the first transect, meaning it is difficult to tell which SOA_{Pre} scenario agrees best with observations. The SOA fraction at 4 hours is around 15% in the higher emissions scenario and around 8% in the lower (Figure B.5). The rapid formation of SOA in fresh smoke (<1 h) has been noted in prior studies (eg. Akherati et al., 2022; Bian et al., 2017), and the lack of observations in this range has been noted as a potential explanation for discrepancies in OA evolution between lab and field studies. Our study supports these prior claims. The OPOA Off simulation has the lowest amount of Δ(POA+OPOA)/ΔCO as it only represents evaporated POA. As the fragmentation fraction (F) decreases, the Δ(POA+OPOA)/ΔCO is higher throughout the simulation due to the oxidation reaction of the POA volatility bins yielding a higher fraction in lower volatility bins, which favors the aerosol phase leading to less of a net decrease in ΔOA/ΔCO. The impact of the fragmentation fraction on observation agreement is minor through the first four transects, where all simulations have ΔOA/ΔCO within the error bars of the observations (Figure B.4e). At the last transect, the simulations with less fragmentation (more functionalization) have ΔOA/ΔCO slightly above the uncertainty of the observations; however, the observed ΔOA/ΔCO at the final transect does not seem consistent with the trend of the prior transects. The OPOA fraction increases ranging from around 5% up to 15%. The fraction of POA remaining at 4 hours in the highest fragmentation cases is high compared to that suggested by

recent studies, while the fraction of POA remaining in simulations with fragmentation less than or equal to 0.25 is comparable to recent studies (Akherati et al., 2020, 2022). There are some impacts on the D_{pm} as the scenarios with more evaporation tend to have smaller particles. However, the impact of the OA aging sensitivity simulations on D_{pm} (Figure B.4) is smaller than the near aircraft altitude impact on D_{pm} (Figure 3.2).

We are focused on the evolution of aerosols in the smoke plume; however, the model does capture some of the observed evolution of O_3, NO_X, and j_{HONO}, prior to 2 hours of aging (Figure B.6). Additionally, the OH concentrations in the model are consistent with Wang et al. (2021) and Liao et al. (2021). After 2 hours of aging, there are discrepancies in the trend in j_{HONO} as a result of the sun setting in the model, but due to the non-Lagrangian sampling, the sun has not set at that smoke age in the observations. This effect of the solar zenith angle is also seen in the decrease in OH (Figure 3.2d.). Gas-phase evolution in this wildfire plume was the focus of the Wang et al. (2021) study; at the aircraft altitude the results of our study are similar in the near- term aging, suggesting that the new coupling of TUV in our simulations is working as expected.

3.3.2 Simulated Vertical and Horizontal Variability in In-Plume Evolution

As discussed for the DIAL-HSRL comparisons, both the simulated plume and the observed plume have a concentrated portion in the FT with a less concentrated portion that mixes down to the surface (Figure 3.1). There are no measurements at altitudes other than the aircraft altitude, besides the DIAL-HSRL, available for this smoke plume. The ability of the model to represent the DIAL-HSRL measurements and the aerosol evolution at aircraft level (as was discussed in Chapter 3.3.1) leads us to believe there is credibility to the model in both the FT (where the aircraft sampled) and in the PBL. In Chapter 3.4, we discuss suggestions for future

field campaigns to improve the vertical sampling of smoke plumes. According to the model, at 0 hr of aging, the total ΔCO burden in the FT and the PBL are roughly equal at 0 hr of aging with a slight increase in the PBL fraction as the plume ages due to dilution differences and entrainment between the FT and PBL (Figure 3.3). Due to the equal amounts of smoke present in the FT and PBL, we make comparisons between the evolution of the PBL and FT portions of the plume and discuss implications of the horizontal and vertical structure on the modeled evolution.

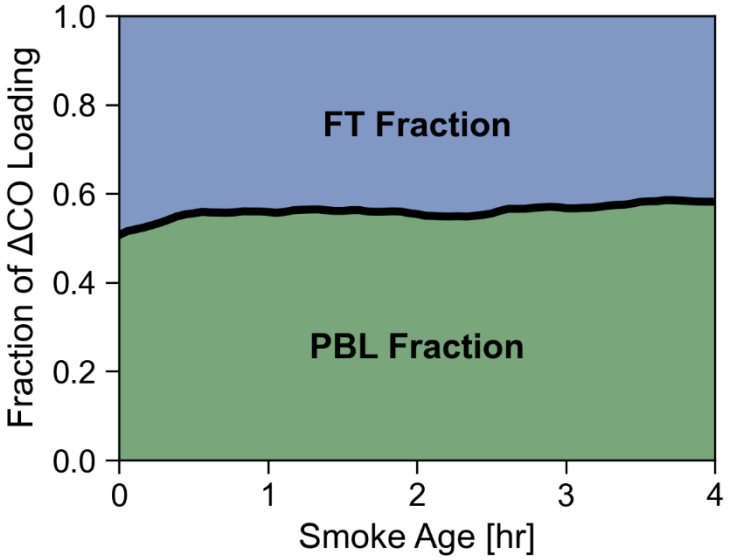

Figure 3.3: The fraction of total ΔCO loading in the free troposphere (blue) and in the PBL (green) as a function of smoke age. The ΔCO loading is defined in equation 3.1.

The ΔCO structure in the plume (Figure 3.4a) illustrates the concentration gradients between the FT and PBL portions of the plume. At 0 hr of aging, the plume is not yet well mixed in the PBL, with concentrations generally being lowest (ΔCO < 1000 ppbv) near the surface and increasing with height until peaking around 2100 m AGL at a ΔCO of around 8000 ppbv (Figure B.7a). By 0.8 hr, the ΔCO in the PBL is well-mixed vertically, with horizontally average concentrations around 1100 ppbv throughout, while horizontally average concentrations in the FT are above 6000 ppbv. From 0.8 hr aging (first observation transect) to 3.2 hr aging (last observation transect), the in-plume ΔCO mean in the PBL decreases from 1000 ppbv to 720 ppbv

while the FT in-plume mean decreases from 8000 ppbv to 3000 ppbv in the FT. Additionally, near the top of the PBL ΔCO tends to be greater than near the surface of the PBL, due to entrainment from the more concentrated PBL into the FT. There is also movement from the PBL into the FT, as shown by the top left side of the plume increasing in altitude from 0.8 hr to 2.0 hr. In terms of horizontal variability, the FT plume generally has larger variations in ΔCO than the PBL plume. Overall, after the initial fast dilution vertically in the PBL (creating the lower overall mixing ratios), the subsequent dilution tends to be slower in the PBL than in the FT.

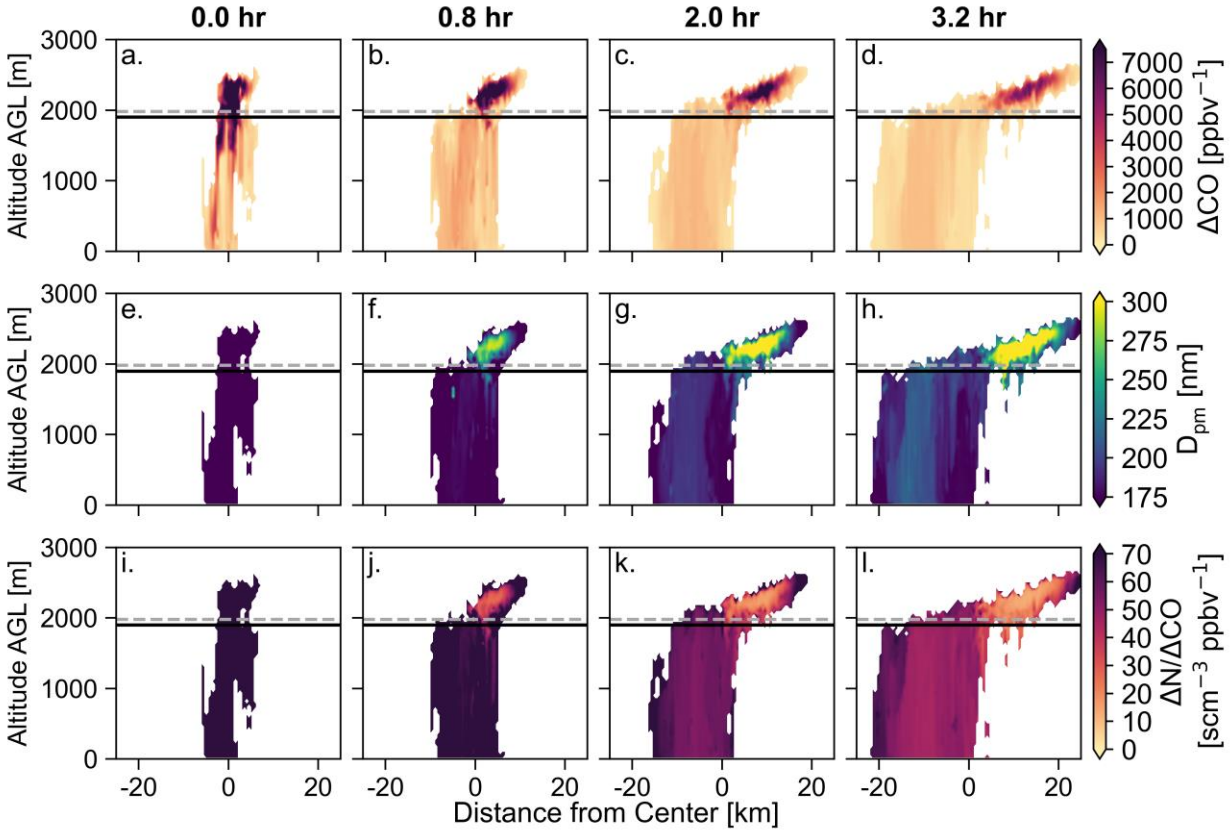

Figure 3.4: (a.)-(d.) ΔCO, (e.)-(h.) modeled D_{pm}, (i.)-(l.) modeled ΔN/ΔCO as a function of distance from center and altitude above ground level (AGL) at four smoke ages downwind. The solid black horizontal line is the height of the PBL. The dashed gray line is the height of the aircraft that sampled the plume. Plume-average vertical profiles of these quantities are located in Figure B.7.

Coagulation is faster in the FT than in the less concentrated PBL portion (Figure 3.4e-3.4l). At the time of the last transect (3.2 hr aging), this vertical gradient in coagulation results in

a D_{pm} of 300 nm in the most concentrated portion of the FT and 200 nm at the surface, meaning aerosol diameter increased more in the FT than the PBL relative to the initial diameter of 110 nm. $\Delta N/\Delta CO$ is initially around 125 scm^{-3} $ppbv^{-1}$ throughout all altitudes of the plume. At 3.2 hr of aging, the faster coagulation in the FT has decreased the $\Delta N/\Delta CO$ to 15 scm^{-3} $ppbv^{-1}$, while the $\Delta N/\Delta CO$ in the PBL is approximately 50 scm^{-3} $ppbv^{-1}$. An important limitation of our study is the lack of ground observations with size distribution measurements in this size range; we believe that future field campaigns should plan to take measurements at multiple altitudes at similar times to better understand the vertical gradients in plumes. At the aircraft altitude, we can understand some of the horizontal gradients in the diameter. At 0.8 hr, there is a 10 nm difference between D_{pm} at the edge of the plume (215 nm) and the core of the plume (225 nm) for the model and the observations. At 3.2 hr of aging, the observed difference in D_{pm} between the edge (245 nm) and core (280 nm) of the plume was about 35 nm (June et al., 2022), whereas the model has 40 nm difference between the edge (240 nm) and core (280 nm) of the plume at the same time. These results confirm that the mixing throughout the plume influences particle size on the dilute edges of the plume, as the SAM-ASP-TUV simulation more closely represents the gradients in D_{pm} growth than a box model simulation which assumes no mixing (June et al., 2022). Although coagulation dominates the changes in D_{pm}, there are also effects on the D_{pm} due to gradients in $\Delta OA/\Delta CO$, which will be discussed below.

Figure 3.5 shows the cross sections through the plume at four smoke ages of OA-relevant properties. $\Delta OA/\Delta CO$ (Figure 3.5a-3.5d) shows slight net OA condensation in the PBL and net OA evaporation in the FT with horizontal gradients at each altitude. At 0.8 hr of aging, the more concentrated parts of the plume at each altitude horizontally tend to have higher $\Delta OA/\Delta CO$. Prior studies have also tended to see that at the time of the first transect, the most concentrated

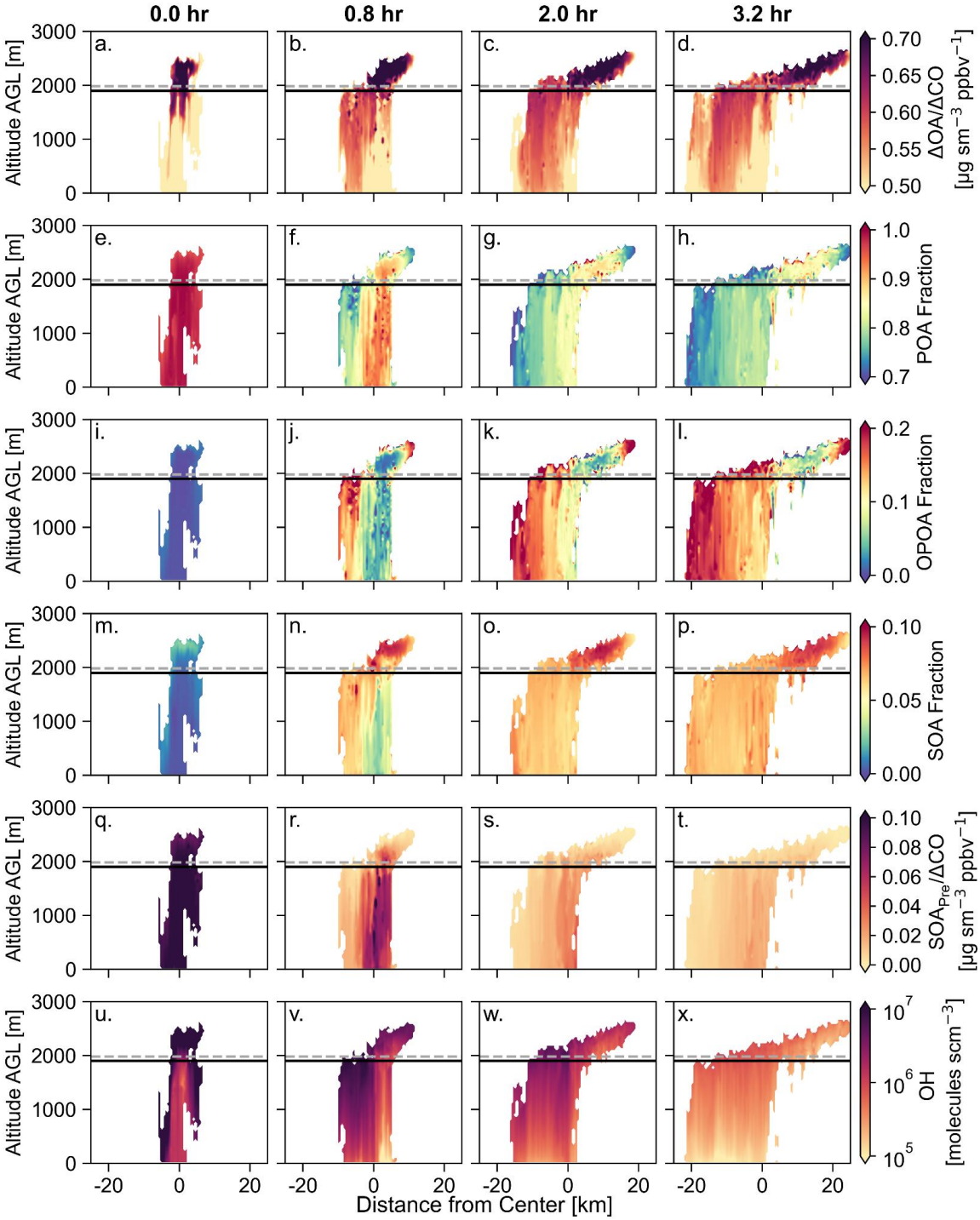

Figure 3.5: Modeled (a.)-(d.) ΔOA/ΔCO, (e.)-(h.) POA fraction, (i.)-(l.) OPOA fraction, (m.)-(p.) SOA fraction, (q.)-(t.) $SOA_{Pre}/\Delta CO$, and (u.)-(x.) OH as a function of distance from center and height at four times downwind. The solid black horizontal line is the height of the PBL. The dashed gray line is the height of the aircraft that sampled the plume. Plume-average vertical profiles of these quantities are located in Figure B.7. The enhancement ratios for POA, OPOA and SOA (rather than fractions) are shown in Figure B.8.

plumes or parts of the plume have higher ΔOA/ΔCO (Akherati et al., 2022; Bian et al., 2017; Hodshire et al., 2019a, 2021; June et al., 2022; Peng et al., 2020). Vertically at 0.8 hr of aging, the ΔOA/ΔCO increases from 0.49 μg sm^{-3} $ppbv^{-1}$ at the surface to 0.62 μg sm^{-3} $ppbv^{-1}$ at the PBL top, while the ΔOA/ΔCO in the FT is around 0.70 ± 0.06 μg sm^{-3} $ppbv^{-1}$. By 3.2 hr of aging, the ΔOA/ΔCO in the PBL ranges from 0.51 μg sm^{-3} $ppbv^{-1}$ at the surface to 0.60 μg sm^{-3} $ppbv^{-1}$ at the PBL top. In the FT at 3.2 hr of aging, the ΔOA/ΔCO has decreased by around 0.05 μg sm^{-3} $ppbv^{-1}$, except for near the top of the plume which experienced close to a net-zero change. The differences in the ΔOA/ΔCO evolution between the PBL and the FT can be explained using differences in dilution, concentration, temperature, and oxidation throughout the plume.

At all altitudes, dilution is contributing to the evaporation of POA (Figure 3.5e-3.5h). Initially, all of the OA mass is POA, at 0.8 hr of aging the POA fraction is 0.86 at the surface, 0.88 at the PBL top, and 0.91 in the FT. Then at 3.2 hr of aging the POA fraction is 0.76 at the surface, 0.78 at the PBL top, and 0.84 in the FT. At 0.0 hr aging, due to faster dilution in the PBL than the FT during emissions, there is a lower ΔPOA/ΔCO ratio in the PBL than in the FT (Figure B.8), explaining the lower initial ΔOA/ΔCO in the PBL. After emissions are complete (and chemistry turns on), slower dilution in the PBL favors slower evaporation of POA in the PBL than in the FT. However, the vertical temperature gradient is also influential in the POA evaporation in the plume. At the surface, the temperature is 300 K, while at the PBL top, the temperature is 280 K. Temperatures in the FT plume range from 280 K to 278 K (Figure B.7e). Within the PBL, where dilution is fairly constant with height, the lower remaining POA fraction at the surface than at the PBL top is explained by the warmer temperature at the surface. The warmer temperature favors more organic matter (OM) partitioning to vapors at the surface. In the FT, the temperature is lower than in the PBL, but dilution (after the initial fast PBL dilution) is

faster, which leads to steady POA evaporation in the FT throughout the simulation. The temperature effect on ΔOA/ΔCO suggested by our modeling work is consistent with an observational study that showed ground measurements having an OA normalized excess mixing ratio that was two-thirds of that measured at aircraft altitudes with this effect being shown for samplings of wildfire smoke and agriculture smoke in multiple field campaigns in the United States (Pagonis et al., 2023). This study also showed substantial evaporation for descending smoke and in an onboard thermal denuder with ~30 K of heating (Pagonis et al., 2023). Additionally, the temperature effect contributing to more evaporation at the surface than at the top of the PBL affects D_{pm}. At each age, the D_{pm} is around 5 to 10% smaller at the surface than at the top of the PBL.

Differences in chemistry within the plume explain the remaining FT/PBL differences in the ΔOA/ΔCO evolution and help to explain the horizontal variability throughout the plume. In the PBL, the OPOA fraction ranges from 0.09 to 0.06 at 0.8 hr, and 0.16 to 0.14 at 3.2 hr. In the FT, the OPOA fraction is 0.005 and 0.08 at 0.8 hr and 3.2 hr respectively (Figure 3.5i-l). The SOA fraction in the PBL is 0.05 at 0.8 hr of aging and 0.06 at 3.2 hr. In the FT, the SOA fraction is 0.09 and 0.08 at 0.8 hr and 3.2 hr respectively (Figure 3.5m-p). In terms of absolute enhancement ratios, the FT tends to have higher ΔSOA/ΔCO at all ages than the PBL, while the PBL tends to have a higher ΔOPOA/ΔCO than the FT due to POA evaporation driving OPOA formation in the PBL (Figure B.8). Prior to the first transect, the SOA formation is faster in the FT than in the PBL due to having more SOA precursors (Figure 3.5q-t). After the first transect, SOA formation slows in the FT (no more SOA precursor), while some SOA precursor remains in the PBL allowing for some additional SOA formation there. However, SOA and OPOA

formation in the PBL is impacted by the concentrated FT plume above resulting in lower OH concentrations in parts of the PBL (Figure 3.5u-x).

Impacts of OH are also seen in the horizontal gradients of OPOA and SOA at each altitude. OH suppression in much of the plume is driven by attenuation of solar radiation, while OH enhancement in dilute parts of the plume results from rapid HONO photolysis being the dominant source of OH in wildfire plumes (Wang et al. 2021). In dilute, sunnier portions of the plume (highest OH concentrations), the OPOA fraction exceeds 20% by the end of the simulation. But in darker parts of the plume (lowest OH), such as the concentrated levels of the FT and the right side of the PBL plume, OPOA formation is slow, with the fraction of OA that is OPOA never exceeding 7% in parts of the FT and just reaching 10% in parts of the PBL. For SOA, the sunnier portions of the PBL have lower concentrations of SOA precursor than the FT and the non-sunny parts of the PBL, limiting the SOA formation. The gradients in light in the plume are evident in the horizontal and vertical gradients of $\Delta O_3/\Delta CO$ and j_{HONO}, where regions of high OH tend to have faster photolysis and faster O_3 formation (Figure B.9). In addition to photolysis gradients due to the concentration of the plume, the plume was oriented west-east, resulting in gradients in photolysis due to the position of the sun. Overall, the concentration and temperature gradients result in a higher SOA fraction in the FT due to the colder temperatures and higher SOA_{Pre}, and a higher OPOA fraction in the PBL due to more POA evaporation as a result of warmer temperatures. The assumed volatility distribution of POA/OPOA and SOA likely influences these results (May et al., 2015; Pagonis et al., 2023); however, the volatility distribution assumed in our study is consistent with prior studies (Jen et al., 2019; May et al., 2013; Shrivastava et al., 2024) and results are in agreement with the observed $\Delta OA/\Delta CO$ at aircraft altitude.

3.4 Conclusions, Implications, and Future Work

In this study we evaluate the SAM-ASP model coupled with TUV at the aircraft altitude and examine differences in free tropospheric and planetary boundary layer evolution seen in the Williams Flats Fire sampled by the FIREX-AQ field campaign on August 3, 2019. At the aircraft altitude, the model explains the observed dilution, coagulation, and net OA evaporation. After 4 hours of aging, the ΔOA/ΔCO at the aircraft altitude is 15% OPOA, 6% SOA and 79% POA; however, nearly all of the SOA formation occurred prior to the first transect (45 minutes downwind). Vertically, in agreement with DIAL-HSRL lidar observations, a significant portion of the plume was present in the FT and PBL, with near equal distribution between the FT and PBL in the model. Generally, there was a lower ΔOA/ΔCO in the PBL as a result of warmer temperatures. Additionally, the lower concentrations throughout the simulation in the PBL leads to slower coagulation. Shading of the PBL due to the concentrated plume above lowers the OH concentration of non-sunny parts of the PBL, slowing the SOA formation there.

There are several implications and needs for future work as a result of the differences in smoke plume evolution between the PBL and FT. The first is coarse global and regional models cannot capture these plume-scale effects, even with current parameterizations. One such parameterization is a parameterization for biomass burning coagulation (Sakamoto et al., 2016). This parameterization can be used in coarse resolution models to increase the size of emitted biomass burning aerosols due to the effects of coagulation (Ramnarine et al., 2019). However, this parameterization calculates one growth rate for a plume. The Sakamoto et al. (2016) parameterization would not capture the faster coagulation in the FT and the slower coagulation in the PBL seen in our study. Additionally, this specific parameterization does not include effects of OA evaporation/condensation on particle size, so it would not capture the evaporation driven size

differences within the PBL. Future versions of parameterizations should include considerations of variability of aging within a plume. For coagulation, this would mean having higher coagulation rates in the core of the plume with slower rates on the edges or in faster diluting regions (e.g., PBL). For subgrid plume processing of OA, we suggest having a temperature dependent parameterization for POA evolution and consideration of vertical gradients in OH for SOA/OPOA formation.

The second implication is effects on air quality due to the temperature driven evaporation of OA near the surface. Since typically, there are higher temperatures at the surface than aloft, this would tend to increase the amount of reactive organic carbon in the gas phase, rather than in the particulate phase. Pagonis et al., (2023) showed that including observationally constrained volatility information in a one-day simulation using High Resolution Rapid Refresh Smoke (HRRR-Smoke) model reduced surface smoke concentrations by 30%.

Overall, these implications suggest the need for more precise plume injection heights (including multiple potential detrainment levels for the same fire) in models as the aging of the plume will be different at different levels. Even if better parameterizations for these subgrid processes such as coagulation, rapid early production, and evaporation are developed, accurately representing plumes in global and regional models requires accurate plume injection heights at multiple potential detrainment levels. The GFAS biomass burning emissions inventory includes estimates of plume injection height (Rémy et al., 2017); however, it includes one estimate per day and may be biased low (Walter et al., 2016), and it does not include multiple peak levels of detrainment. Plume rise models coupled with atmospheric models may allow for better representation of plume dynamics (Walter et al., 2016), but at a higher computational expense, which is likely already increased due to the added parameterizations needed to represent the OA

evaporation/condensation and coagulation processes. Therefore, continued work on improving plume injection height in emission inventories and simulations is needed (Cheeseman et al., 2020; Chen et al., 2021b; Lyapustin et al., 2020).

Finally, to develop the parameterizations that would be needed to represent the differences between FT and PBL smoke plume evolution, additional observational evidence is needed to support the simulated impacts shown in this study and to reduce the limitations induced by the observational uncertainty. At the altitude sampled by the aircraft, our model-observation comparisons are limited in that our model is a Lagrangian model moving with the mean wind speed of the plume injection, while the airplane moved more than two-times faster than this wind speed. Therefore, it is difficult to discern if biases are the result of model biases in emissions or processes, or if it is the result of the observations being influenced by changing fire and environmental conditions. Additionally, we were unable to evaluate the particle size and OA evolution at heights other than the single aircraft altitude located in the FT. From these limitations, we suggest future field campaigns work to remedy these limitations through changes to sampling design through increased use of sampling designs like those used with the Twin Otter aircraft during FIREX-AQ or those used during the California Fire Dynamics Experiment (Carroll et al., 2024; Washenfelder et al., 2022). For example, we recommend having a mobile laboratory with the same instrumentation as the aircraft, and when possible, sample the same fires as the aircraft. Future campaigns should continue to work towards lowering the age of the first transect downind. The first transect used in this study was nearly an hour downwind, sampling late in the plume limits the ability to use OA factors from the AMS to look at the early SOA formation. We also recommend having the aircraft sample at multiple heights (when allowed) at every transect downwind (perhaps lowering the age of the oldest smoke sampled to

keep the same flight time), which would decrease the speed that the aircraft moves downwind, moving closer to Lagrangian sampling, while also improving the quantity of vertical measurements.

3.5 Data Availability

This work is supported by the US NOAA, an Office of Science, Office of Atmospheric Chemistry, Carbon Cycle, and Climate program, under the cooperative agreement award NA21OAR4310128; and the US NSF Atmospheric Chemistry program, under grants AGS-1950327 and AGS-2211153.

All observation data used in this study are publicly available in the NASA FIREX-AQ data archive (FIREX-AQ Science Team, 2019). Version 1.0.0 of SAM-ASP-TUV used in this study, as well as the input files are publicly available (June & Alvarado, 2024).

Chapter 4: Exploring Sulfur Chemistry in the North Atlantic Arctic Spring[3]

4.1 Introduction

Dimethyl sulfide (DMS) and methanethiol (MeSH) are emitted from sea water to the atmosphere (Gros et al., 2023; Kettle et al., 2001; Lana et al., 2011; Novak et al., 2022; Scholz et al., 2023; Zhou et al., 2024). On a global scale, DMS is a dominant natural source of sulfur to the atmosphere (Andreae, 1990; Bates et al., 1992; Carpenter et al., 2012). In the atmosphere, DMS reacts to form sulfur dioxide (SO_2) and methanesulfonic acid (MSA) (Barnes et al., 2006; Chen et al., 2016; Faloona, 2009; Hoffmann et al., 2016; Tashmim et al., 2024). The SO_2 and MSA can then be further oxidized to influence the aerosol size distribution and cloud microphysics (Leaitch et al., 2013; Tashmim et al., 2024; Wollesen de Jonge et al., 2021). As a result of their contribution to marine particles, DMS and MeSH are important contributors to the Earth's radiative budget. Croft et al. (2021) found the May and June average direct radiative effect (DRE) due to DMS over the North Atlantic to be -0.1 W m^{-2} and the aerosol indirect effect (AIE) to be -3.37 W m^{-2}. Wohl et al. (2024) found that MeSH increases the DRE of sulfate aerosol in the Arctic by 5 to 10% and also increases the lifetime of DMS. Therefore, understanding the atmospheric oxidation of DMS and MeSH is important to understanding the contribution of these species to marine sulfate aerosol and cloud condensation nuclei (CCN), which determines their DRE and AIE (Carslaw et al., 2013; Croft et al., 2021; Hodshire et al., 2019c; Quinn et al., 2017; Reddington et al., 2017; Tashmim et al., 2024; Thomas et al., 2010; Wohl et al., 2024).

DMS and MeSH are produced in seawater by dimethylsulfoniopropionate (DMSP), which is synthesized mainly by phytoplankton (McParland and Levine, 2019; Stefels, 2000;

[3] June, N. A., C. Zang, S. E. O'Donnell, B. Croft, R. Y.-W. Chang, J. Kojoj, F. Mattsson, P. Zieger, L. Tashmim, W. C. Porter, S. H. Jathar, M. D. Willis, & J. R. Pierce (in preparation): Exploring Sulfur Chemistry in the North Atlantic Arctic Spring.

Zhang et al., 2019). Oceanic DMS has been extensively observed and has a monthly global climatology with DMS seawater concentrations having a maximum in early summer and a minimum during the winter (Hulswar et al., 2022; Lana et al., 2011). Recent advances have been made in estimating oceanic DMS at finer temporal and spatial scales (Hayashida et al., 2017, 2020; Zhou et al., 2024). Zhou et al. (2024) uses an artificial neural network to estimate daily oceanic DMS at 1°x1°. In the global 20-year annual average, the Zhou et al. (2024) oceanic DMS is 42% lower than the Lana et al. (2011) dataset. Hayashida et al. (2020) uses a sea ice-ocean coupled general circulation to simulate various oceanic variables including DMS for the Arctic, North Atlantic, and North Pacific Oceans at 10-14.5 km horizontal resolution. The Hayashida et al. (2020) estimates oceanic DMS to be approximately 30% lower than Lana et al. (2011) in May and June over the Arctic study area. These new datasets offer the potential to capture interannual variability in oceanic DMS; however, the impact of these new datasets on simulating atmospheric sulfur chemistry in the Arctic has not been examined.

Compared to oceanic DMS, there are less observations of oceanic MeSH leading to additional uncertainties on the importance of MeSH (Gros et al., 2023; Kettle et al., 2001; Leck and Rodhe, 1991; Novak et al., 2022). Oceanic MeSH has been suggested to be on average 20% of oceanic DMS by Kettle et al. (2001) and 10% of oceanic DMS by Leck & Rodhe (1991), although both those studies observed significant variability in DMS-to-MeSH ratios in seawater. Gros et al. (2023) also suggested an average ratio of 20% (but with values up to 50%). Additionally, Gros et al. (2023) showed latitudinal variability in seawater DMS-to-MeSH ratios with higher MeSH percentages in the marginal ice zone. Another study showed the seawater DMS-to-MeSH ratio to be dependent on sea surface temperature (SST) with colder SST resulting

in higher ratios (Wohl et al., 2024). These studies suggest that there is a need to better understand the uncertainties of MeSH emission.

DMS and MeSH are emitted to the atmosphere through gas exchange processes with estimates showing annual DMS flux being between 9 and 35 Tg S y^{-1} depending on the parameterization used for sea-air gas-exchange and oceanic DMS dataset (Hulswar et al., 2022; Kettle et al., 2001; Woodhouse et al., 2010; Zhou et al., 2024). The uncertainty in DMS emission flux from the ocean to the atmosphere is a large contributor to the uncertainty in the aerosol radiative forcing of natural aerosols (Carslaw et al., 2013). In contrast to oceanic DMS concentrations which show a decreasing or zero trend with climate change, the DMS emission fluxes show an increasing trend with climate change due to loss of sea ice and changes in the gas transfer velocity (Hayashida et al., 2017, 2020; Zhou et al., 2024). Wohl et al. (2024) showed MeSH to contribute between 20% to 40% of the volatile marine sulfur emission fluxes with higher values in polar regions. Observations have shown DMS/MeSH can be emitted through cracks, leads, and during melt of sea ice (Hayashida et al., 2017, 2020; Lizotte et al., 2020; Loose et al., 2011; Willis et al., 2023; Wohl et al., 2022). Given evidence that bottom-ice processes produce DMS under the sea-ice (Hayashida et al., 2017, 2020), understanding the emission of DMS through breaks in sea-ice is important; however, most models treat sea ice as a cap to DMS emissions (Willis et al., 2023).

In the atmosphere DMS reacts with OH, NO_3, O_3, and various halogens to primarily form SO_2 and MSA (Barnes et al., 2006; Chen et al., 2016; Faloona, 2009; Hoffmann et al., 2016; Tashmim et al., 2024). Tashmim et al. (2024) found that globally the OH addition and OH abstraction reactions contribute the highest fraction of DMS oxidation at 27.6% and 38.6% respectively. Debromination of sea salt contributes to DMS reacting with BrO to have a larger

fraction of the total DMS oxidation in some marine areas including the Arctic (Tashmim et al., 2024). MeSH has known rate constants with OH, BrO, NO_3 and Cl and can go through a series of reactions to produce SO_2 (Barnes et al., 2006; Butkovskaya and Setser, 1999; Tyndall and Ravishankara, 1989, 1991).

SO_2, H_2SO_4, and MSA are important contributors to the Earth's climate system through both direct and indirect radiative effects (Carslaw et al., 2013; Hodshire et al., 2019c; Quinn et al., 2017; Reddington et al., 2017; Tashmim et al., 2024; Thomas et al., 2010). The low volatility of sulfuric acid in the troposphere allows sulfuric acid to condense onto pre-existing particles and in the presence of vapor molecules of other species (ammonia/amines, low-volatility organics, iodine oxoacids) participate in new particle formation (NPF) (Allan et al., 2015; Baccarini et al., 2020; Bianchi et al., 2019; Dunne et al., 2016; He et al., 2023; Kulmala, 2003; Marti et al., 1997; Napari et al., 2002; Riccobono et al., 2014; Vehkamäki et al., 2002; Zhao et al., 2024). The equilibrium vapor pressure of MSA depends on free ammonia, relative humidity, and temperature (Hodshire et al., 2019c). MSA can grow pre-existing particles through condensation (Hodshire et al., 2019c; Leaitch et al., 2013; Legrand et al., 2017; Preunkert et al., 2008). The role of MSA to participate in nucleation is uncertain but has been suggested to have played a role in observed events near Greenland (Dall´Osto et al., 2018) and investigated in modeling studies (Bork et al., 2014; Hodshire et al., 2019c; Wollesen de Jonge et al., 2021). Recent studies show the uncertainty in DMS emission and oxidation contribute significantly to the uncertainty in the global natural aerosol burden and aerosol radiative forcing (Carslaw et al., 2013; Fung et al., 2022; Novak et al., 2021, 2022; Rosati et al., 2022). Therefore, there is a need to continue to improve the representation of DMS and MeSH oxidation in the atmosphere and understand their influence on atmospheric aerosol.

The evaluation of DMS in atmospheric chemical transport models is the focus of several prior studies (Barnes et al., 2006; Chen et al., 2018; Croft et al., 2021; Fung et al., 2022; Hoffmann et al., 2016, 2021; Tashmim et al., 2024). Croft et al. (2021) evaluated GEOS-Chem-TOMAS with a simplified DMS oxidation mechanism with gas phase reactions of DMS with OH and NO_3 to produce SO_2 and MSA in fixed ratios during the The North Atlantic Aerosol and Marine Ecosystem Study (NAAMES) field campaign. This study found that GEOS-Chem-TOMAS was generally able to simulate the near surface vertical profiles of DMS, and the inclusion of DMS emissions improved the low bias of 0-2 km sulfate aerosol by 30% (Croft et al., 2021). Tashmim et al. (2024) evaluated the implications of an expanded DMS oxidation scheme on GEOS-Chem-TOMAS simulations for two island surface observation sites located at 35°N and 38°S, and for the AToM-4 campaign. The expanded DMS oxidation scheme reduced the biases of DMS, but was unable to evaluate the model biases of dimethyl sulfide oxidized (DMSO), one of the added intermediate compounds of DMS oxidation, due to lack of observations (Tashmim et al., 2024). Additionally, neither of these studies focused on the evaluation of atmospheric DMS in the transition region between pack ice and open ocean: the marginal ice zone.

Previous atmospheric measurements of MeSH are limited compared to measurements of DMS (Gros et al., 2023; Lawson et al., 2020; Novak et al., 2022; Willis et al., 2023). Lawson et al. (2020) measured DMS and MeSH during the Surface Ocean Aerosol Production near New Zealand in austral summer finding campaign average atmospheric DMS concentrations of 208 ppt with a lifetime of 1 d, while MeSH had an average atmospheric concentration of 18 ppt with a lifetime of 0.4 d. Wohl et al. (2024) evaluated the impact of including MeSH emission globally using the Community Atmosphere Model with interactive chemistry (CAM-Chem), but did not

compare the simulated atmospheric MeSH to observations. In that study, MeSH contributed the largest impact on tropospheric sulfate burden over the Southern Ocean (30 to 70%), but also increased the tropospheric sulfate burden over the North Atlantic through the inclusion of MeSH (Wohl et al., 2024). Therefore, there is a need to evaluate the ability of models to simulate the emission and atmospheric oxidation of MeSH particularly in marine polar environments.

Here we aim to reduce some of the uncertainties of emission of DMS/MeSH associated with oceanic DMS inventories and emissions near sea ice, and understand uncertainties atmospheric fates of DMS/MeSH associated with oxidants and deposition in the marine Arctic atmosphere through a modeling study using expanded DMS and MeSH oxidation and measurements from the 2023 Atmospheric Rivers and the onset of sea ice melt (ARTofMELT) field campaign. This modeling study focuses on the important springtime transition period in the Arctic, specifically looking at mid-May to mid-June. In Chapter 4.2, we present an overview of the measurements collected during the ARTofMELT field campaign and detail the configuration of our GEOS-Chem-TOMAS simulations. The measurements taken of sulfur species during ARTofMELT are more detailed than prior studies, along for a more complete evaluation of GEOS-Chem-TOMAS. In Chapter 4.3.1, we evaluate the model-observation agreement of the primary emissions of DMS and MeSH. Then in Chapter 4.3.2 we examine the model simulation of DMS and MeSH atmospheric oxidation, including model-observation comparisons of DMSO and sulfate aerosol. In Chapter 4.3.3, we look at a case study of the elevated atmospheric DMS/MeSH that was observed during the onset of sea ice melt on June 10, 2023. In Chapter 4.4, we summarize our findings and make recommendations for future studies of marine sulfur chemistry in the Arctic.

4.2 Methods

4.2.1 Measurements During the ARTofMELT Field Campaign

The Atmospheric Rivers and the onset of sea ice melt (ARTofMELT) field campaign took place in the Fram Strait from May 9 to June 13, 2023 on the Swedish Icebreaker I/B *Oden* (Figure 4.1b).

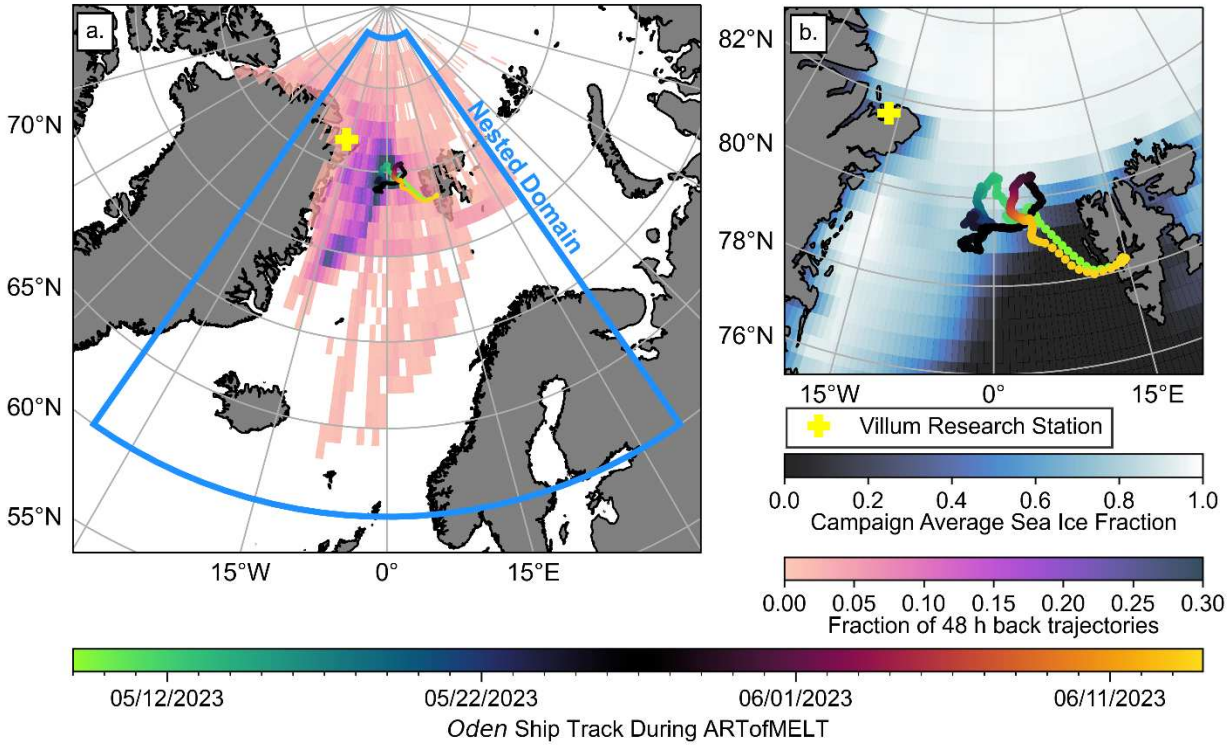

Figure 4.1: (a.) Ship track of *Oden* during ARTofMELT colored by the date. The gridded background shows the frequency of 48 h HYSPLIT back trajectories started from *Oden's* location once per hour during the campaign. The blue outline shows the nested simulation model domain. (b.) A zoomed in view of the ship track of *Oden* during ARTofMELT with the background showing the campaign average sea ice fraction. The yellow plus on both (a.) and (b.) shows the location of Villum Research Station.

We use measurements of atmospheric DMS, MeSH, and DMSO that were collected using the Vocus-CI-ToFMS. The dual-reagent Vocus-CI-ToFMS uses the chemically general proton-transfer ionization (H_3O^+) with adduct-formation ionization (NH_4^+) to measure directly emitted,

less-oxygenated VOCs, and their early-generation oxidation products (Hansel et al., 2018; Mungall et al., 2016; Zang and Willis, 2025; Zaytsev et al., 2019). The limit of detection (LOD) of the instrument varied throughout the campaign, but was generally around 1 ppt for DMS, MeSH, and DMSO (Figure C.1). We use hourly average values for all the analysis, so we adjust the LOD that was calculated at 0.1 Hz by dividing by $360^{0.5}$. Even after the hourly averaging some concentrations in the model and/or observations were still below the LOD, therefore, these values are substituted with 0.5*LOD (Dadashazar et al., 2019; O'Donnell et al., 2023; Polissar et al., 1998, 2001).

We use data of non-refractory aerosol mass smaller than 1 μm collected using a soot particle aerosol mass spectrometer (SP-AMS) (Freitas et al., 2024; Onasch et al., 2012). The SP-AMS alternated between running in laser-on mode to vaporize soot particles and laser-off mode to measure non-refractory particles. In this work we only use the non-size resolved measurements of sulfate particles. Further technical details of the SP-AMS can be found in Onasch et al. (2012), while further details on the data processing and quality control of these data can be found in Freitas et al. (2024).

Both the Vocus-CI-ToFMS and SP-AMS datasets exclude remove time periods when the measurements were influenced by emissions from *Oden*. Additionally, both instruments are missing measurements during additional periods due to issues with the instrumentation.

Additionally, we use some of the meteorological data collected on board the ship to support the analysis. Visibility, precipitation intensity, wind, temperature, relative humidity, cloud cover, and radiation are measured at a weather station on *Oden* located ~25 m above sea level.

4.2.2 GEOS-Chem-TOMAS Model Description

We use the global atmospheric chemistry model (GEOS-Chem) coupled with the TwO-Moment Aerosol Sectional (TOMAS) model v12.9.3 (GC-TOMAS) to simulate the atmospheric DMS (Adams and Seinfeld, 2002; Kodros and Pierce, 2017). The TOMAS aerosol microphysics scheme used in our simulations has 15 size bins from 3 nm to 10 μm. We simulate size-resolved sulfate, sea salt, organic aerosol (OA), black carbon (BC), and dust, and diagnose size-resolved aerosol ammonium, nitrate, and water. Our GC-TOMAS configuration uses 47 vertical layers and is first run at 4°x5° horizontal resolution globally to obtain boundary conditions. We then run a nested simulation for a domain around the ARTofMELT campaign at 0.5°x0.625° horizontal resolution (Figure 4.1a).

The model is run using reanalysis meteorology from MERRA-2 which has fair agreement with the on-ship meteorological observations with the exception of precipitation (Figure C.2). Generally, the precipitation field in the reanalysis meteorology tends to have fewer hours with no precipitation than was actually observed on the ship.

4.2.2.1 Emissions

Anthropogenic and biomass burning emissions are consistent across all simulations in this study. Anthropogenic emissions are from the Community Emissions Data System (CEDS). Biomass burning emissions are from the GFAS inventory. BB emissions come from the Global Fire Assimilation System (GFAS), which assimilates fire radiative power measurements from the Moderate Resolution Imaging Spectroradiometer (MODIS) to make daily estimates of BB emissions for 41 species, burnt dry matter, and fire radiative power (FRP) at 0.5° x 0.5° horizontal resolution globally (Kaiser et al., 2012). For this study, we assume BB emissions to be well-mixed in the PBL. We assume the biomass burning emissions to be lognormally distributed

with a number median diameter of 100 nm and modal width of 2.0 to distribute the emissions across the GC-TOMAS size sections (Janhäll et al., 2010; Ramnarine et al., 2019).

The model includes several natural emissions sources including sea spray, dust, DMS/MeSH, and ammonia from sea birds. The DMS/MeSH emissions are a focus of the sensitivity simulations in our study, and will be discussed further in Chapter 4.2.2.4. Dust emissions follow the Dust Entrainment and Deposition scheme (Fairlie et al., 2007; Zender et al., 2003). Open-ocean sea-salt emissions are a function of wind speed and sea surface temperature (SST) with updates to include the effect of cold waters (SST < 5°C) (Huang and Jaeglé, 2017; Jaeglé et al., 2011). Sea-salt Br^- is emitted assuming a ratio of $2.11x10^{-3}$ kg Br per kg dry sea-salt (Huang et al., 2020; Sander et al., 2003).

Prior studies have shown blowing-snow sea-salt to be important to the aerosol size distribution and BrO in the Arctic during the winter; those updates are included in these simulations (Gong et al., 2023; Huang et al., 2020). The blowing-snow sea-salt emissions are a function of wind-speed, relative humidity, temperature, the age of the snow, and surface snow salinity (Yang et al., 2008, 2010). Assumptions of first-year-ice, multi-year-ice, and snow surface salinity follow Huang et al. (2020). We use a number of sea salt particles produced by each sublimated snow particle of 1, rather than the value of 5 used in Huang et al. (2020) and Gong et al. (2023), as this parameter is highly uncertain and using a value of 1 yields results more consistent with the size-distributions observed during ARTofMELT. The Br^- ratio of the blowing-snow sea-salt is assumed to be a factor of 5 higher than sea-water consistent with prior modeling studies and limited observations (Domine et al., 2004; Huang et al., 2020; Huang and Jaeglé, 2017). The blowing-snow sea-salt is distributed to the GC-TOMAS size bins assuming a gamma distribution following the parameters of Gong et al. (2023).

4.2.2.2 TOMAS Aerosol Microphysics

The TOMAS aerosol microphysics scheme used in our simulations has 15 size bins from 3 nm to 10 μm. All simulations couple MSA to the TOMAS microphysics scheme to include the effects of MSA on aerosol growth (Hodshire et al., 2019c). The size resolved MSA is included in the size resolved sulfate through condensation. All simulations include inorganic new particle formation through the Dunne et al. (2016) mechanism. Organics participate in new particle formation following Riccobono et al. (2014). Both of these updated NPF mechanisms are described in detail in O'Donnell et al. (2025) and in Chapter 5.

Secondary Organic Aerosol (SOA) is treated using the simple SOA scheme that is used in GC-TOMAS (Pai et al., 2020). This scheme uses two SOA classes, a gas-phase SOA precursor, and a SOA tracer that immediately condenses on the preexisting particles. The gas-phase SOA precursor oxidizes to form the immediately condensed SOA tracer on a fixed time scale of 1 day. SOA precursors from non-marine sources associated with terrestrial biogenic, fossil fuel, biofuel, and biomass burning emissions, as well as the uncharacterized Arctic marine source of SOA precursors in the Arctic are included in all simulations. Unlike prior studies which have emitted these precursors as a 50/50 split to the two precursor classes (Croft et al., 2019; Pai et al., 2020), we emit all biogenic sources to the gas-phase precursor class only.

Removal of simulated aerosol mass and number occurs through wet and dry deposition. All simulations include updates for coagulation of interstitial aerosol particles with cloud droplets (Croft et al., 2016; Pierce et al., 2015). Prior modeling studies, primarily focused on the Canadian Arctic, have suggested a need for more vigorous wet removal from Arctic low-level clouds (Browse et al., 2012; Croft et al., 2016). We make modifications to the previous implementation, which introduced a constant "drizzle" rate in low-level clouds in all grid boxes

North of 65°N (Croft et al., 2016), to only include the drizzle rate in low-level clouds North of 65°N and over grid boxes with an ocean fraction greater than 0.8. The drizzle rate is scaled by both the ocean fraction and the cloud fraction.

4.2.2.3 Sulfur Chemical Mechanism

All simulations use the expanded DMS oxidation scheme for GC-TOMAS (Tashmim et al., 2024). We briefly describe the mechanism here, for the full details refer to Figure 1 and Tables 2 to 4 of Tashmim et al. (2024). The oxygenaddition pathway includes gas-phase reactions of DMS with OH and BrO, and an aqueous-phase reaction of DMS with O_3. These reactions lead to the formation of DMSO, which further oxidizes to form MSA. The H-abstraction pathway includes gas-phase reactions of DMS with OH, Cl, and NO_3 leading to the eventual formation (through multiple steps) of either MSA or hydroperoxymethyl thioformate (HPMTF). HPMTF can then react to contribute to SO_2 formation. DMS and O_3 may react in the gas-phase to directly form SO_2. The importance of the different DMS reactions is discussed in Chapter 4.3.2.

Building upon those updates all simulations presented here include MeSH emissions and atmospheric oxidation in GC-TOMAS (Tashmim et al., 2025). The GC-TOMAS MeSH oxidation scheme follows the configuration of Novak et al. (2022). This scheme includes MeSH reactions with OH, BrO, NO_3, and Cl. In the box model case study of Novak et al. (2022), their scheme produced a model yield of SO_2 from MeSH of 0.99, which is similar to another modeling study that obtained a value of 0.98 (Chen et al., 2021a). We include the full MeSH oxidation scheme here as this scheme has not been studied in the Arctic where BrO chemistry may be more influential (Saiz-Lopez et al., 2006, 2008; Tashmim et al., 2024).

We also updated the Henry's law coefficient for DMSO, MSA, and MSIA (Table C.1) for all simulations. These are thermodynamically estimated Henry's law values that are consistent with measurements (Wollesen de Jonge et al., 2021). The updates to the Henry's law coefficient make the wet removal less efficient, which helps to reduce the low bias of DMSO in the model simulations.

4.2.2.4 Oceanic DMS and MeSH

We test three oceanic DMS inventories as inputs to our simulations: the Lana et al. (2011) climatology, an estimate using a biogenic ocean model (Hayashida et al., 2020), and an estimate using the machine learning model developed in Zhou et al. (2024) (Table 4.1). The Lana et al. (2011) DMS climatology is the standard source of oceanic DMS in GC-TOMAS. The Lana et al. (2011) climatology is a monthly climatology of oceanic DMS developed through the use of interpolating and extrapolating world-wide observations. However, as this dataset is a climatology, it cannot be used to capture interannual variability, or capture the potential long-term trends in oceanic DMS (Zhou et al., 2024). The second DMS dataset we use comes from a pan-Arctic sea- ice-ocean physical-biogeochemical model (Hayashida et al., 2020). This model offers higher temporal and spatial resolution than the Lana et al. (2011), as well as being simulated specifically for the time-period of the ARTofMELT field campaign. However, this oceanic data set is limited by its simulation of sea-ice, as it simulates too much sea ice in the Fram Strait near the ARTofMELT field campaign (Figure C.3). Due to this over estimation of sea-ice, the biogenic model likely underestimates oceanic DMS. The final oceanic DMS dataset we use is oceanic DMS estimated using the artificial neural network ensemble model (ANN) developed in Zhou et al. (2024). The ANN uses nine environmental variables as inputs:

chlorophyll-a, SST, sea-surface concentrations of nitrate, phosphate, silicate, and dissolved oxygen, ocean mixed-layer depth, downward shortwave radiation flux, and sea surface salinity.

Table 4.1: Table summarizing oceanic DMS inventories used in this study.

Source	Horizontal Resolution	Temporal Resolution	Data Years
Lana et al. (2011) Climatology	1°x1°	Monthly Climatology	1972-2009
Hayashida et al. (2020) Biogenic Model	0.5°x0.625°	Daily	2023
Zhou et al. (2024) ANN	1°x1°	Daily	2023

Figure C.4 shows the May and June campaign average percent difference for the oceanic DMS in the Hayashida et al. (2020) model and the Zhou et al. (2024) ANN relative to the Lana et al. (2011) monthly climatology. Overall, there is generally a decrease in the oceanic DMS for both the Hayashida et al. (2020) model and Zhou et al. (2024) ANN relative to the Lana et al. (2011) climatology. However, the Hayashida et al. (2020) model has enhancement in oceanic DMS relative to the Lana et al. (2011) along its incorrectly simulated ice edge. Similarly, the ANN has enhanced DMS relative to the Lana et al. (2011) climatology along its ice edge which is in the observed location, due to the use of satellite constrained sea-ice data.

The variability in the relation of oceanic DMS to MeSH is uncertain; however, here we use results of recent observational studies to assume a ratio of MeSH to DMS in the ocean that varies with latitude as described in Table C.1 (Gros et al., 2023; Novak et al., 2022). Our model-observation comparisons are sensitive to this assumption. However, we hope that the importance of MeSH to the sulfur budget shown in this study points to the need to develop oceanic datasets that include both DMS and MeSH.

Sea-air flux in GEOS-Chem is calculated based on Johnson (2010). The emission flux is controlled by the gas transfer velocity, which is a function of wind speed and SST (Johnson, 2010). The standard implementation of this in GEOS-Chem only calculates the sea-air flux of DMS/MeSH if the model gridbox is entirely ocean. One of our simulations (see Chapter 4.2.3) follow the standard implementation, while the rest include updates to the DMS/MeSH emissions to be scaled by the ocean fraction (FO). This scaling allows for emissions throughout the marginal ice zone, which observationally has been shown to have DMS emissions (Hayashida et al., 2017; Lizotte et al., 2020; Loose et al., 2011; Willis et al., 2023; Wohl et al., 2022). However, the influence of marginal ice zone DMS/MeSH emissions on model-observation agreement have not been previously shown.

4.2.3 Summary of GEOS-Chem-TOMAS Simulations

We conduct four primary simulations to test the different DMS inventories and sea-air flux assumptions in GC-TOMAS (Table 4.2). The L11 simulation uses the standard GC-TOMAS seaflux calculation, where no emissions are assumed if there is any sea ice. While the L11*FO, BIO*FO, and ANN*FO simulations include the updates to scale the seaflux by the ocean fraction.

Two additional simulations are used to aid in the discussion of DMSO. The purpose of the $L11_{NODRIZZLE}$ simulation is to show the sensitivity of DMSO (which can be taken up into clouds and lost through wet deposition) to the wet deposition updates for more vigorous wet removal from Arctic low-level clouds implemented in our study. The $L11_{NOSNOW}$ simulation is used to show the influence of BrO from blowing snow on DMS oxidation, and to help to understand if missing bromine is a source of model bias in our study.

Table 4.2: Brief summary of GEOS-Chem-TOMAS simulations used in this study and their corresponding abbreviations. FO is ocean fraction.

Simulation	Description
L11	Uses the monthly temporal resolution Lana et al. oceanic DMS climatology and the standard GC-TOMAS seaflux calculation where seafluxes are assumed to be 0 if FO<1
L11*FO	Uses the monthly temporal resolution Lana et al. oceanic DMS climatology and multiples the seaflux by FO
BIO*FO	Uses the daily temporal resolution oceanic DMS estimate for 2023 from the Hayashida et al. (2020) biogenic ocean model and multiples the seaflux by FO
ANN*FO	Uses the daily temporal resolution oceanic DMS estimate for 2023 from the Zhou et al. (2024) ANN and multiplies the seaflux by FO
$L11_{NODRIZZLE}$	Same as L11, but with the model updates for more vigorous wet removal from Arctic low-level clouds turned off
$L11_{NOSNOW}$	Same as L11, but with the blowing snow emissions turned off

4.2.4 Use of HYSPLIT and Definition of Source Regions

To assess source regions during the campaign, we use the HYbrid Single-Particle Lagrangian Integrated Trajectory (HYSPLIT) model (Rolph et al., 2017; Stein et al., 2015). HYSPLIT represents the forward or backward transport of a particle starting at a point and advects that particle based on the mean of the 3D velocity vectors provided by reanalysis meteorology. We run 48-h HYSPLIT back trajectories for every hour of the campaign using the same MERRA-2 reanalysis that is used in the model. Given that the atmospheric lifetime of DMS/MeSH is on the order of 1 d or less (Kloster et al., 2006; Lawson et al., 2020; Scholz et al., 2023; Wohl et al., 2024), we believe this to be sufficient to access the source region for the purposes of our analysis. Each HYSPLIT back trajectory is initiated at the location of *Oden* and at an altitude of 30 m above sea level (the approximate observation height). In our analysis, we use single HYSPLIT trajectories, rather than ensemble trajectories, which is a limitation. However, the single trajectories assign source region in a manner that is comparable to those assigned with FLEXPART back trajectories during ARTofMELT.

Using the back trajectories, we assign every hour of the campaign a source region as defined in Table 4.3. Currently, the altitude of the back trajectory is not used to further segregate the source region classifications. Figure C.4a shows the time series of the ICE, MIZ, and OCEAN source regions as well as the source region > 66% definition. ICE is the most frequent source region with 436 h. MIZ has 172 h; OCEAN has 82 h; NONE has 174 h.

Table 4.3: Definition of source regions using HYSPLIT back trajectories and the MERRA-2 reanalysis used in GEOS-Chem.

SOURCE REGION > 66%	DEFINITION
ICE	At least 32 h in 48 h back trajectory is over sea ice (sea ice > 80%)
MIZ	At least 32 h in 48 h back trajectory is over the marginal ice zone (sea ice between 10% and 80%)
OCEAN	At least 32 h in 48 h back trajectory is over ocean (sea ice < 10%)
NONE	48 h back trajectory is not over sea ice, the marginal ice zone, or ocean for at least 32 h, meaning no source region is a super majority

4.2.5 Definition of Fog

We also compare DMS oxidation pathways during periods of fog, recent fog and no fog at *Oden* (Figure C.4b). We define fog using observations of visibility and liquid water content (LWC). In our study, we define fog as the observed visibility being less than 1.5 km and the observed LWC being greater than 0.02 kg m^{-3}. Prior studies in the Arctic have found this visibility and LWC threshold to accurately classify fog events (Tjernström et al., 2015). Recent fog is defined as periods with fog in the previous 8 h. We compare this observed definition of fog to the MERRA-2 reanalysis low-cloud fraction (vertically averaged cloud fraction in the five lowest vertical layers). The MERRA-2 reanalysis generally agrees with the model in terms of fog; however, there are times of disagreement (Figure C.5). The reanalysis-observation

disagreement in fog is often in the timing of either the start of the fog, or in the dissipation of the fog. A limitation of this fog classification method is that it only defines fog at the location of the ship, some periods could be influenced by fog upwind of the ship.

4.3 Results

4.3.1 Directly Emitted Species (DMS and MeSH)

The inclusion of emissions from regions with sea ice improves the ability of GC-TOMAS to simulate the atmospheric DMS concentrations during ARTofMELT. The L11 simulation overall has a $\log_{10}$ mean bias (LMB) of -0.88, while the L11*FO simulation has a LMB of 0.24 for hourly averaged DMS during ARTofMELT (Figure 4.2a-b). The L11*FO reduces the LMB for all source regions. For the ICE source region, the L11 simulation underestimates DMS by an order of magnitude, often having values below the LOD (~1 ppt, Figure C.1) of the observation, despite the observed values being above the LOD. In the L11*FO simulation, the simulated DMS is always above the LOD when observations are also above the LOD. For the MIZ source region, the LMB is -0.78 in the L11 simulation and 0.32 in the L11*FO simulation. The reduction of magnitude of the LMB for the ICE and MIZ source regions shows the importance of DMS emissions in regions with sea ice cover.

There is variability in the DMS biases depending on which dataset is used for oceanic DMS (Figure 4.2b-d). The ANN*FO simulation overall has a LMB of -0.47, and the BIO*FO simulation has a LMB of 0.02. Of the three simulations with emissions scaled by ocean fraction, the ANN*FO simulation has the most consistent bias across all source regions, ranging from -0.53 to -0.37 and a best fit slope of 1.04. The ANN dataset was shown to have a low bias compared to observations of oceanic DMS in the Arctic for the years (1998-2017) included in Zhou et al. (2024), but represented the spatial and temporal variability of oceanic DMS, possibly

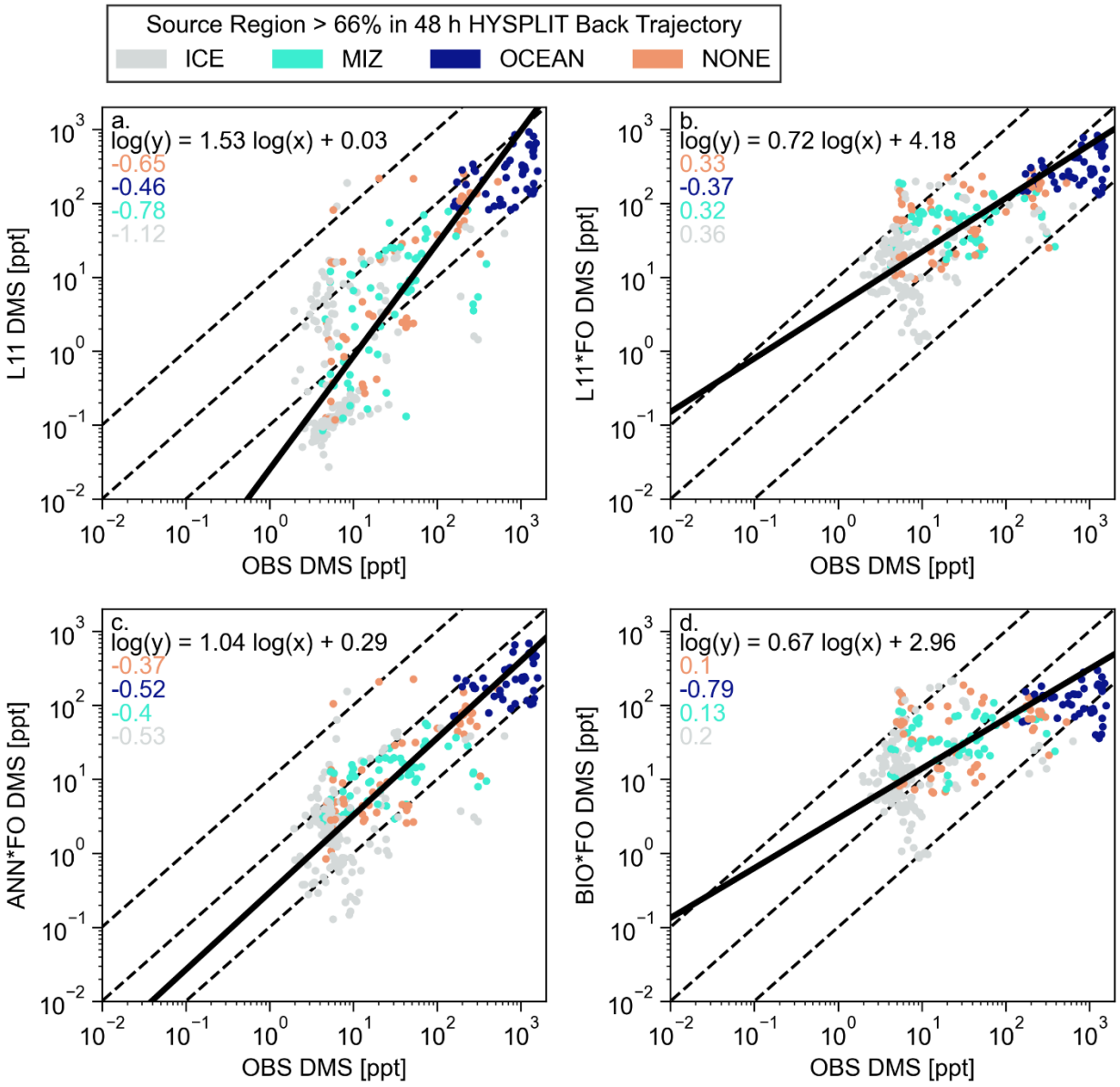

Figure 4.2: Scatter plot comparing the Observed and Modeled DMS from (a.) L11, (b.) L11*FO, (c.) ANN*FO, and (d.) BIO*FO. The dashed black lines are the 10:1, 1:1, and 1:10 lines. The solid black line is the best fit with the equation included in black on each panel. The colored numbers on the panel correspond to the LMB colored by source region. Simulations are defined in Table 4.2, while source regions are defined in Table 4.3.

explaining the low bias present in the atmospheric DMS when using the ANN oceanic DMS dataset. For the BIO*FO simulation, the low bias in atmospheric DMS for the OCEAN source region (LMB of -0.79) is possibly related to the BIO dataset having too much sea ice in the Fram

Strait near ARTofMELT potentially resulting in an underestimate of oceanic DMS in the BIO dataset. The BIO*FO simulation has the lowest magnitude of LMB for the other three source regions. The emissions of DMS in L11*FO, ANN*FO, and BIO*FO may also be influenced by the decision to scale the emissions linearly by the ocean fraction. There are uncertainties in how sea ice influences the gas transfer velocity. One study suggested that the exchange velocity could be either enhanced or diminished depending on the speed of sea ice drift and the effective fetch (Bigdeli et al., 2018).

Similar to DMS, the inclusion of MeSH emissions in oceanic regions with sea ice cover improves the LMB (Figure 4.3a-b). The campaign average LMBs for MeSH are: -0.93 for L11, 0.09 for L11*FO, -0.6 for ANN*FO, and -0.1 for BIO*FO. For all simulations, the slope of the MeSH best fit line is greater than 1 and steeper than the slope for DMS, which suggests possible biases in the assumed latitudinal dependence of the oceanic DMS:MeSH ratio or in the atmospheric lifetime of MeSH. For all simulations, the MeSH LMB for the ICE source region is more negative than that for DMS, suggesting that the oceanic DMS scalar for the higher latitudes could be too small. The biases for the MIZ source region are similar between MeSH and DMS for each respective source region. For the OCEAN source region, the MeSH biases are less negative than those for DMS, suggesting that the oceanic DMS scalar for lower latitudes may be too high. Model biases in the atmospheric lifetime of MeSH could also impact the more negative LMB for the ICE source region. The atmospheric lifetime for MeSH in our simulations is about 0.9 d (Table C.3), which is shorter than the atmospheric lifetime of 1.5 d reported by Wohl et al. (2024), but longer than the 3 h lifetime reported in Novak et al. (2022). Therefore, biases in both the assumed latitudinal dependence of the oceanic DMS:MeSH ratio and the MeSH atmospheric lifetime could contribute to the biases in MeSH during ARTofMELT.

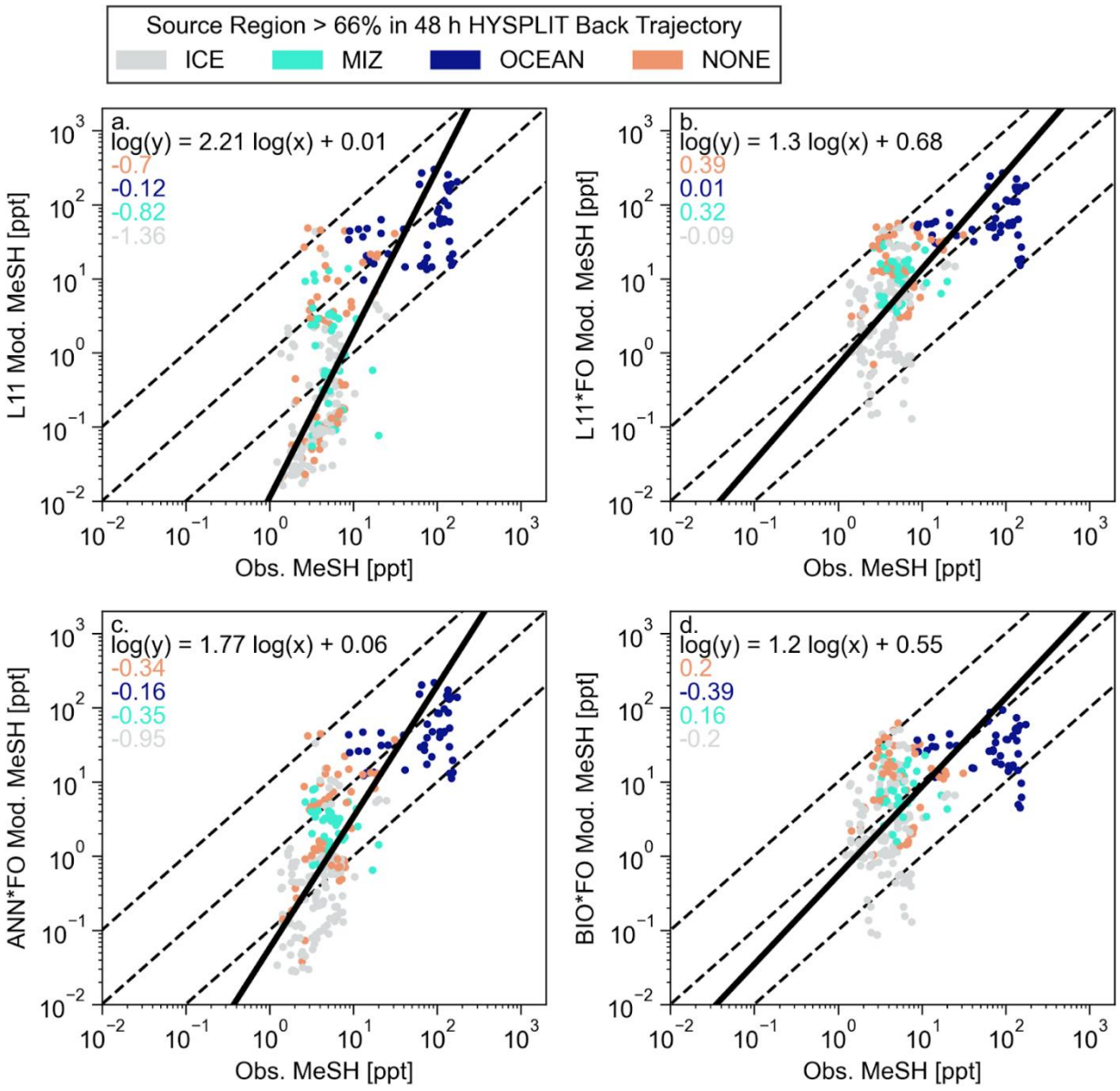

Figure 4.3: Scatter plot comparing the Observed and Modeled MeSH from (a.) L11, (b.) L11*FO, (c.) ANN*FO, and (d.) BIO*FO. The dashed black lines are the 10:1, 1:1, and 1:10 lines. The solid black line is the best fit with the equation included in black on each panel. The colored numbers on the panel correspond to the LMB colored by source region. Simulations are defined in Table 4.2, while source regions are defined in Table 4.3.

4.3.2 Atmospheric Oxidation of DMS and MeSH

In the campaign average, the OH addition pathway is the most dominant DMS oxidation pathway representing approximately 64% of the total DMS oxidation for all simulations (Figure 4.4a-d). The DMS-BrO pathway represents 13%, 6%, and 13% of total DMS oxidation in the

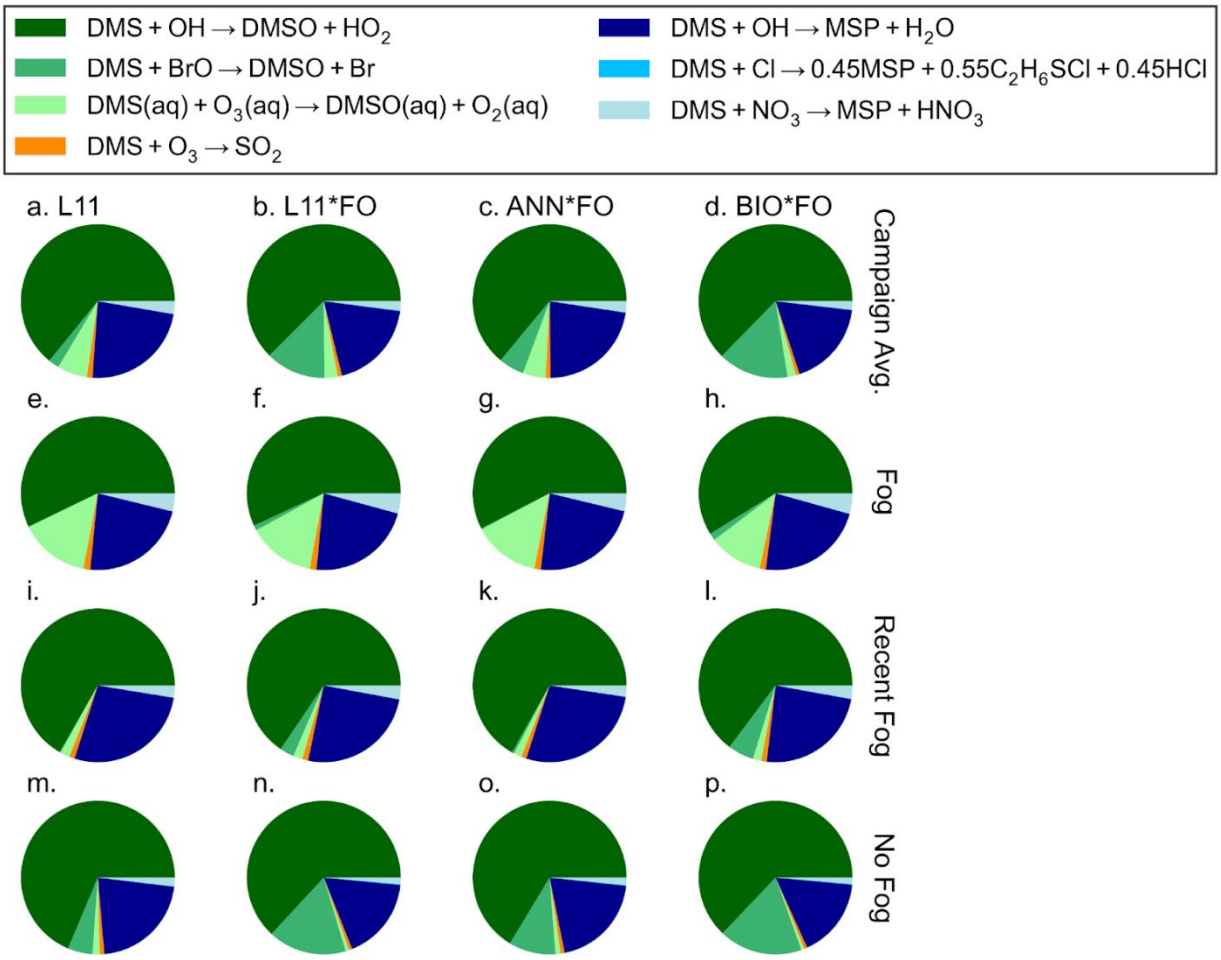

Figure 4.4: Pie chart showing the campaign average DMS oxidation pathways from (a.),(e.),(i.),(m.) L11, (b.),(f.),(j.),(n.) L11*FO, (c.),(g.),(k.),(o.) ANN*FO, and (d.),(h.),(l.),(p.) BIO*FO. (a.) to (d.) represent the campaign average. (e.) to (h.) represent the average during fog. (i.) to (l.) represent the average during hours when fog occurred in the previous 8 h. (m.) to (p.) represent the average during no fog.

L11*FO, ANN*FO, and BIO*FO simulations, compared to 2% in the L11 simulations, suggesting BrO is important to DMS oxidation in regions of partial sea-ice cover. The BrO pathway is important to elevated DMS and DMSO events that occurred earlier in the campaign where there was typically more influence from the ICE source region (Figure C.7). However, our simulations likely underestimate BrO concentrations throughout the campaign, so the importance of the DMS-BrO oxidation pathway is also likely underestimated. In periods of fog, although the

OH addition pathway is still the largest contributor to DMS oxidation (57% during fog), the aqueous phase reaction of DMS with O_3 also becomes important (15% during fog compared to less than 2% outside of fog; Figure 4.4e-h). Periods of recent fog are similar to no fog; however, relative to periods with no fog, the H-abstraction pathway is more important by 6% during periods of recent fog compared to periods with no fog, due to slightly higher temperatures (Figure 4.4i-p).

MeSH oxidation is dominated by the reaction with OH with over 97% of the MeSH oxidation occurring through the MeSH+OH oxidation ppathway (Figure C.8). There is also less variability in the MeSH oxidation pathways between different simulations and different periods of the campaign. The dominance of the OH pathway has been suggested by prior studies (Novak et al., 2022). However, similar to DMS oxidation, the importance of the BrO pathway may be underestimated due to the biases in BrO.

DMSO model-observation agreement is worse than both DMS and MeSH, with an underestimate by more than an order of magnitude in all simulations (Figure 4.5). The DMSO biases are lowest for the OCEAN source region for all simulations. The underestimate of DMSO for the OCEAN source region in all simulations and all source regions in the L11 and ANN*FO simulation is in part due to the underestimate of DMS for those source regions and simulations. However, for the ICE source region the DMSO is always underestimated by more than an order of magnitude for all simulations, even though DMS was overestimated for the ICE source region in the L11*FO and BIO*FO simulations. We hypothesize two potential sources of the additional DMSO bias here: biases in DMSO loss and biases in DMS oxidants that react to form DMSO.

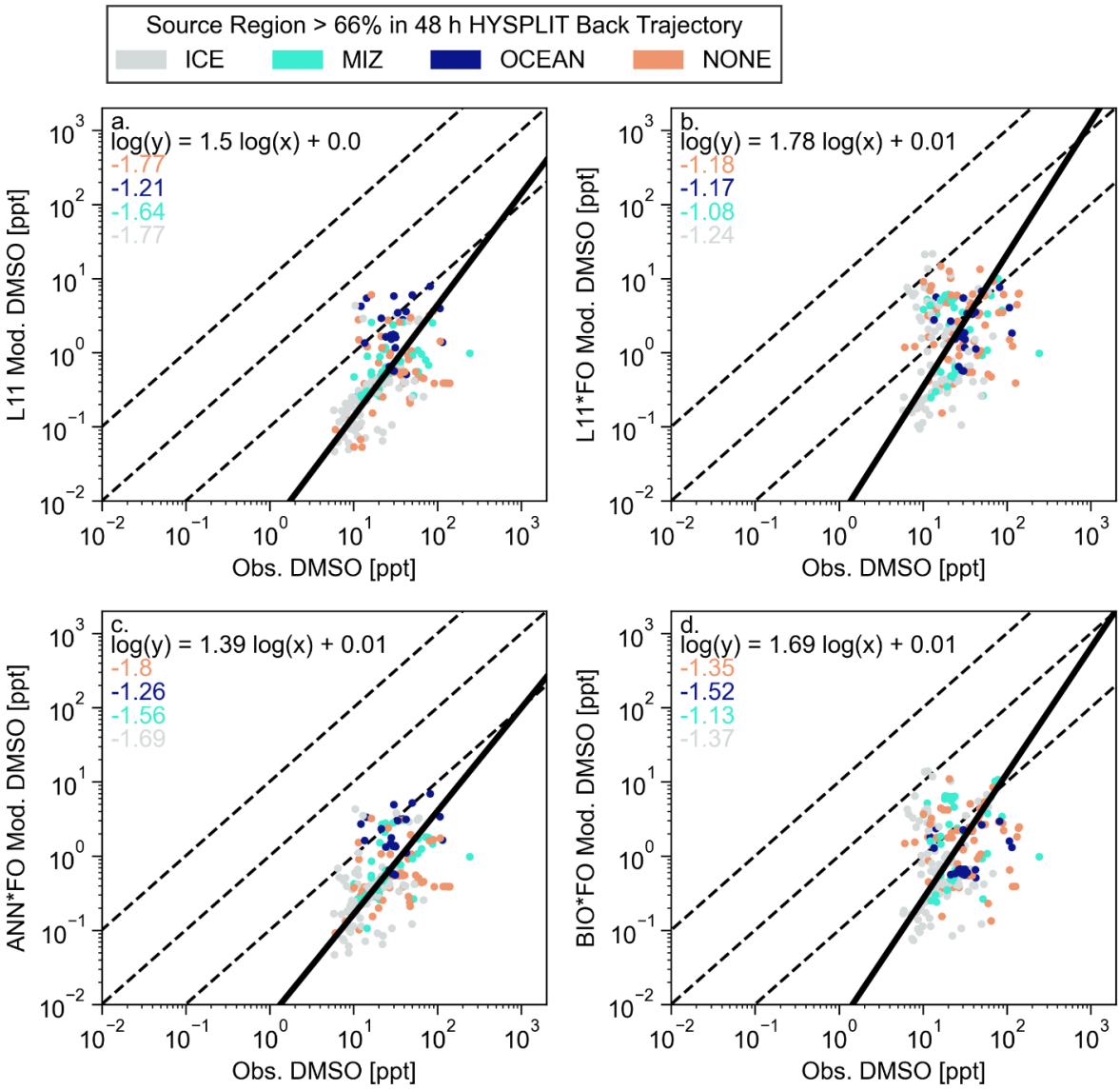

Figure 4.5: Scatter plot comparing the Observed and Modeled DMSO from (a.) L11, (b.) L11*FO, (c.) ANN*FO, and (d.) BIO*FO. The numbers on the panel correspond to the LMB colored by source region.

The DMSO underestimate may be associated with too rapid loss either through chemical reactions or wet removal. In terms of chemical DMSO loss pathways, our study has 84% of DMSO being lost to the $DMSO_{(g)}+OH_{(g)}$ and 16% being lost to the $DMSO_{(aq)}+OH_{(aq)}$ which is comparable to the percentages for this region of the Arctic in Chen et al. (2018). The atmospheric chemical lifetime of DMSO in our simulations is on the order of hours (Table C.3), which is comparable to the lifetime reported by Scholz et al. (2023), but shorter than the 11 h lifetime in

Chen et al. (2018). The inclusion of more vigorous removal through a drizzle parameterization in Arctic low-level clouds may contribute to the underestimate of DMSO in our simulations (Figure C.9a). Turning of the DRIZZLE updates (which have more vigorous removal above 65°N over the open ocean) as is done in the $L11_{NODRIZZLE}$ reduces the LMB to -0.3 for the OCEAN source region compared to the LMB of -1.21 for the L11 simulation. These effects on biases for the OCEAN source region suggest that the assumed drizzle rate is too high for springtime clouds in this region of the Arctic, or potential biases in the low cloud cover, or biases in the aqueous chemistry. For the ICE and MIZ source regions, the $L11_{NODRIZZLE}$ only slightly improves the DMSO LMB (-1.51 and -1.42 respectively for ICE and MIZ for $L11_{NODRIZZLE}$). The differences in the L11 and $L11_{NODRIZZLE}$ simulations make sense as the implementation of the DRIZZLE updates should primarily affect points assigned to the OCEAN source region.

The DMSO underestimate may additionally be associated with biases in the species that react with DMS to form DMSO. The DMSO chemical sources are: DMS+OH (80%), DMS+BrO (16%) and $DMS_{(aq)} + O_{3(aq)}$ (4%). In Chen et al. (2018), the DMS+OH and DMS+BrO pathways were the most dominant sources of DMSO contributing roughly equal percentages. We do not have direct observations of OH or BrO; however, we use prior studies and other observations during ARTofMELT to infer potential biases. There is a positive correlation (R^2 of 0.59) between the simulated OH and the observed downwelling shortwave radiation (Figure C.10a). Although, OH is determined by more than just the presence of shortwave radiation, it has been shown to be correlated (Rohrer and Berresheim, 2006; Souri et al., 2024), so the correlation between OH and shortwave radiation in our study is a positive indicator. Additionally, prior studies have shown GEOS-Chem to simulate OH similar to other chemical transport models and reasonably represent observational estimates of OH (Christian et al., 2017, 2018; Lin et al., 2024). The

correlation of OH with SW radiation and prior studies of GEOS-Chem representation in OH suggest that the production of DMSO through the OH addition pathway should be reasonably estimated.

As mentioned previously, 16% of DMSO in our modeling study forms via the DMS+BrO oxidation pathway, which is lower than the percentages found in this region in prior studies (Chen et al., 2018). An understimate bias in BrO could contribute to both the low bias of DMSO and the underestimate in the importance of the DMS+BrO oxidation pathway. Prior studies have shown elevated BrO leads to surface ozone depletion events in the Arctic spring (Huang et al., 2020; Yang et al., 2010). However, our simulations, despite including the blowing snow emissions of BrO, do not capture the observed ozone during ARTofMELT (Figure C.10b) suggesting biases in halogen chemistry. In Huang et al. (2020), the blowing snow emissions of BrO improved agreement with satellite tropospheric BrO columns and surface ozone in March and April, but were not able to capture ozone depletion events in May (consistent with our simulations; Figure C.11). Huang et al. (2020) hypothesized the lack of ability to capture ozone depletion events in May was related to deposition of bromine on snow enhancing the emission of Br^- later in the spring compared to the assumptions made in the parameterization. Turning off the blowing snow emissions ($L11_{NOSNOW}$) only slightly worsens the LMB of DMSO for all source regions (Figure C.9b), consistent with the slight impacts the blowing snow emissions had on the ozone in our simulations and Huang et al. (2020). Both the ozone and DMSO comparisons with observations suggest a potential underestimate in BrO. Assuming a higher value for the enrichment of Br^- in snow compared to sea water would increase the BrO concentration and also be more consistent with other studies in late spring in the Arctic (Huang et al., 2020; Macdonald et al., 2017; Toom-Sauntry and Barrie, 2002). Additionally, following Huang et al. (2020) we

assumed the salinity of the snow on first-year ice to be 0.1 psu and 0.05 psu on multi-year ice, while measurements during the ARTofMELT campaign measured higher salinities in snow for 6 of the 8 samples (Rush et al., 2024), assuming a higher salinity value would also enhance the BrO. Lastly, there may be unaccounted emissions of bromine directly from now on sea ice in our simulations (Pratt et al., 2013; Swanson et al., 2022; Wales et al., 2023). Swanson et al. (2022) showed that in May the bromine emissions from the sea ice were lower in magnitude than those from blowing snow, but in June the bromine emissions from the sea ice were greater in magnitude than those from blowing snow. Revising the assumptions of the blowing snow parameterization from Huang et al. (2020) to better match conditions during ARTofMELT and including bromine emissions from sea ice could improve the DMSO model-observation agreement by enhancing the production of DMS through the DMS+BrO pathway.

The model observation comparison of sulfate is improved particularly in the MIZ through the inclusion of DMS/MeSH emissions when FO < 1 as shown by the L11*FO and BIO*FO simulation (Figure 4.6a). There is a low bias in sulfate for the ICE source region potentially connected to the DMS oxidation biases discussed previously, as well as missing sulfate sources, biases in deposition, and biases in long range transport in the model.

Additionally, the amount of SO_2 and MSA is increased in the L11*FO and B23*FO simulations (Figure 4.6b-c) consistent with the increase in DMS and MeSH in the L11*FO and BIO*FO simulations. We do not have observations of these species for model validation. The lower SO_2 and MSA concentrations in the ANN*FO simulation is consistent with the lower DMS values in that simulation. The SO_2 and MSA from DMS influence new particle formation and growth as indicated by prior modeling and field campaigns (Croft et al., 2021; Hodshire et al.,

2019c; Park et al., 2021; Tashmim et al., 2024). Aerosol size and composition during ARTofMELT is the focus of Chapter 5.

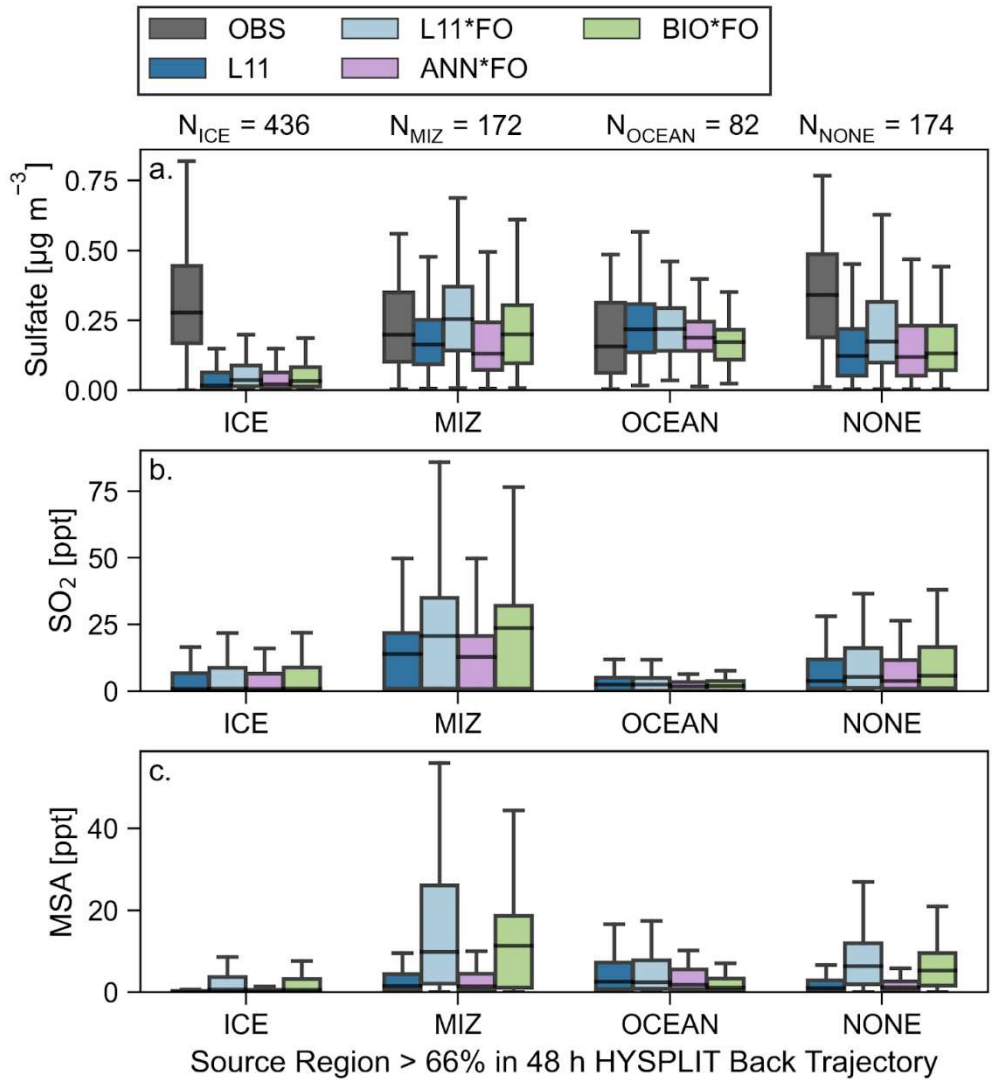

Figure 4.6: (a.) Sulfate grouped by source region for each simulation and the observations. (b.) Simulated SO_2 grouped by source region. (c.) Simulated gas-phase MSA grouped by source region.

4.3.3 Case Study: End of Campaign Warm Period

To further understand the spatial and temporal variability of sulfur chemistry during ARTofMELT, we conduct a case study during a period of elevated DMS near the end of the campaign from 06/10/2023 at 08 UTC to 06/12/2023 at 08 UTC. This period had strong ocean

influence, temperatures above freezing, consistent fog, and marked the onset of sea ice melt for the 2023 season in the region (Figure C.2 & C.5). The back trajectories during this time are all generally from the south with a shift to more southeast influence on June 12 (Figure C.12).

The highest DMS and MeSH concentrations of the campaign in the model and observations occur during this time period from June 10th to 12th (Figure 4.7a-b). For both DMS and MeSH, the peak concentrations in the observations occur on June 11 at 00 UTC and a second maximum at 06 UTC, while the model simulations all have a singular peak at 04 UTC. The timing of the maximum concentrations in the simulations correspond to a minimum in the observations. The biases in the timing of the maximum concentration could be related to biases in advection, or biases in aqueous chemistry. Both the MERRA-2 and observed meteorology suggest the presence of fog on the morning of June 11; however, around 04 UTC (the maxima in DMS/MeSH in the simulations), the MERRA-2 reanalysis has a decrease in the RH that is not present in the observations. The low bias in RH could slow the rate at which DMS is being lost to the aqueous-phase reaction in the model contributing to the increase in modeled DMS concentration. Another possibility is biases in the transport of DMS to the ship. At 04 UTC, the observed wind direction at *Oden* changes to be from the East (whereas the previous hours and hours after are from the south), while the MERRA-2 wind direction is from the South throughout (Figure C.13). Depending on the spatial distribution of DMS concentrations these biases in the timing of the wind direction shifts could contribute to the biases in the timing of the maximum concentration of DMS/MeSH. The peak DMS concentrations in the model are biased low compared to the observations, while the peak MeSH concentrations are biased high for all simulations except BIO*FO. The BIO*FO simulation yields the lowest concentrations of DMS and MeSH of the four simulations as a result of too much sea ice in the biogenic ocean model

(Figure C.14), which lowers its estimation of oceanic DMS. It is possible that the other simulations are also biased low in oceanic DMS; however, spatial variability likely also influences the model biases in the magnitude of the peak concentration during this time period. The biases in MeSH could be the result of the potential biases in MeSH oxidation, or they could be the result of biases in the assumed oceanic DMS:MeSH ratio.

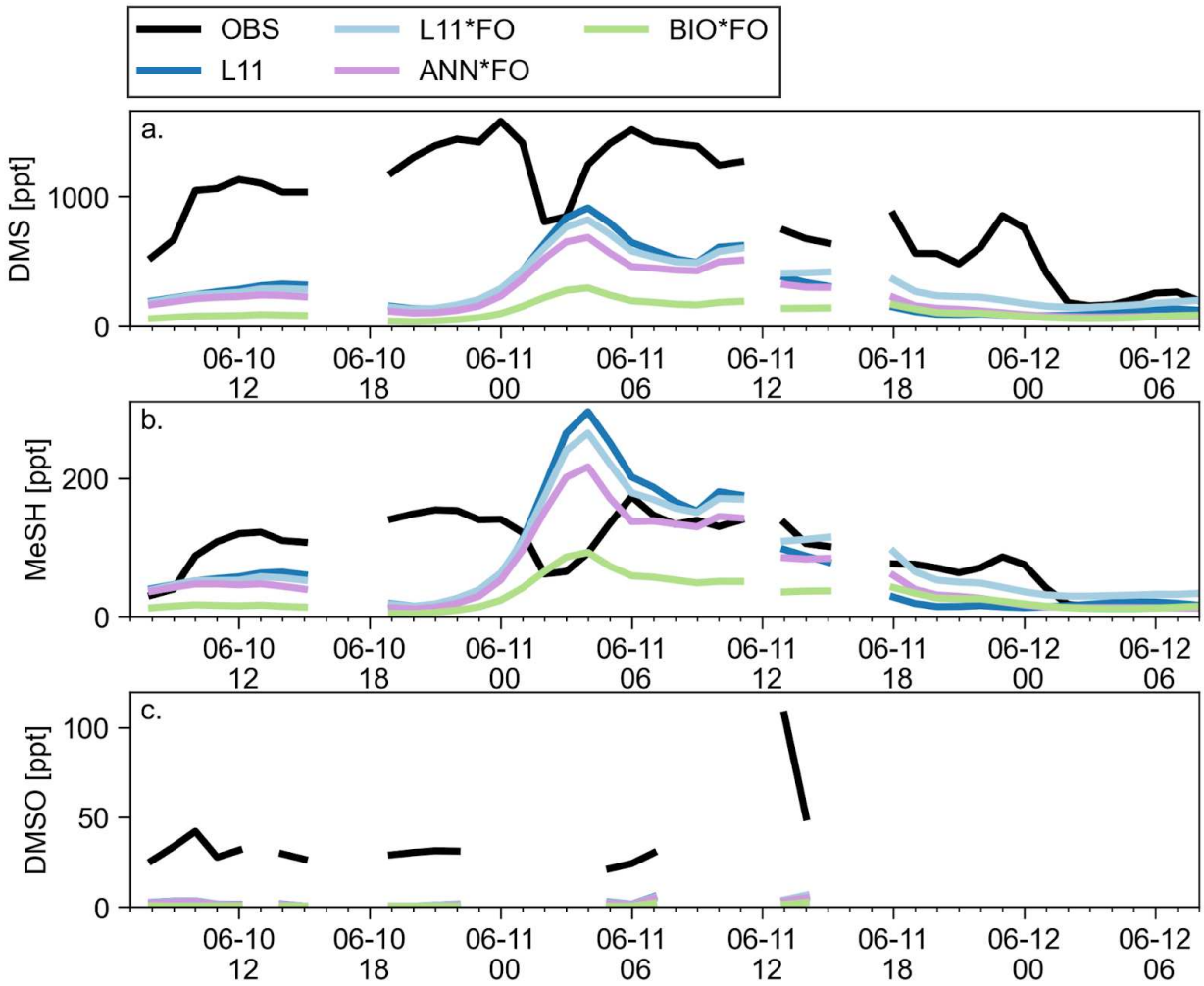

Figure 4.7: Time series of (a.) DMS, (b.) MeSH, and (c.) DMSO for the end of campaign melt onset from June 10 to June 12.

For DMSO, the observations have missing data during this time period; however, the model has a low bias when there are observations available (Figure 4.7c). Since the simulations are biased low in DMS; it is expected that the model would also be biased low in DMSO.

However, biases in DMS oxidation could also contribute to the low bias in DMSO. The O_3 model-observation agreement on 06/10 to 06/12 is better than it is during most of the campaign (Figure C.11), which could potentially result in a better model representation of the DMS oxidation with O_3. At *Oden* and in the surrounding areas, the chemical production of DMSO is larger than the chemical loss of DMSO at this time (Figure C.15e). Due to the presence of fog (both in the model and observations), the aqueous phase reaction is more important during this event relative to the campaign average at *Oden* (Figure C.16). The fog event in the model lasts longer than it did in the observations, which could contribute to the model having too fast DMSO wet deposition from 06/11 at 10 UTC to 06/12 at 03 UTC, which could contribute to the low DMSO bias in the model. The H-abstraction pathway (which doesn't produce DMSO) also has a higher percentage during this time period compared to the rest of the campaign due to the warmer temperatures. On 06/11, the MERRA-2 reanalysis temperatures agree with the observed temperatures, but on 06/12 the MERRA-2 reanalysis has a warm temperature bias (Figure C.2). The temperature biases could contribute to an overestimate in the H-abstraction pathway and an underestimate in DMSO production contributing to the negative DMSO bias of DMSO on 06/12.

The L11*FO, ANN*FO, and BIO*FO simulations have similar spatial gradients of DMS and MeSH to each other with the ship being located on the edge of a gradient with higher concentrations to the north and east, and lower concentrations to the west (Figure 4.8). The spatial patterns of DMS/MeSH in the model seem somewhat connected to the MERRA-2 meteorology around the ship at this time (particularly the low cloud cover; Figure C.17). The previously discussed biases of too fast winds from the South in the MERRA-2 reanalysis could contribute to the simulations having the highest concentrations too far to the north of *Oden*. The biases in atmospheric oxidation/lifetime could contribute to spatial biases in DMS and MeSH,

while the assumed oceanic DMS:MeSH ratio could contribute to MeSH spatial biases. The model may be biased in where it spatially has the highest concentrations of DMS and MeSH concentrations during this case study; however, as we only have observations at *Oden*, we have no way of knowing the actual model biases in the spatial variability

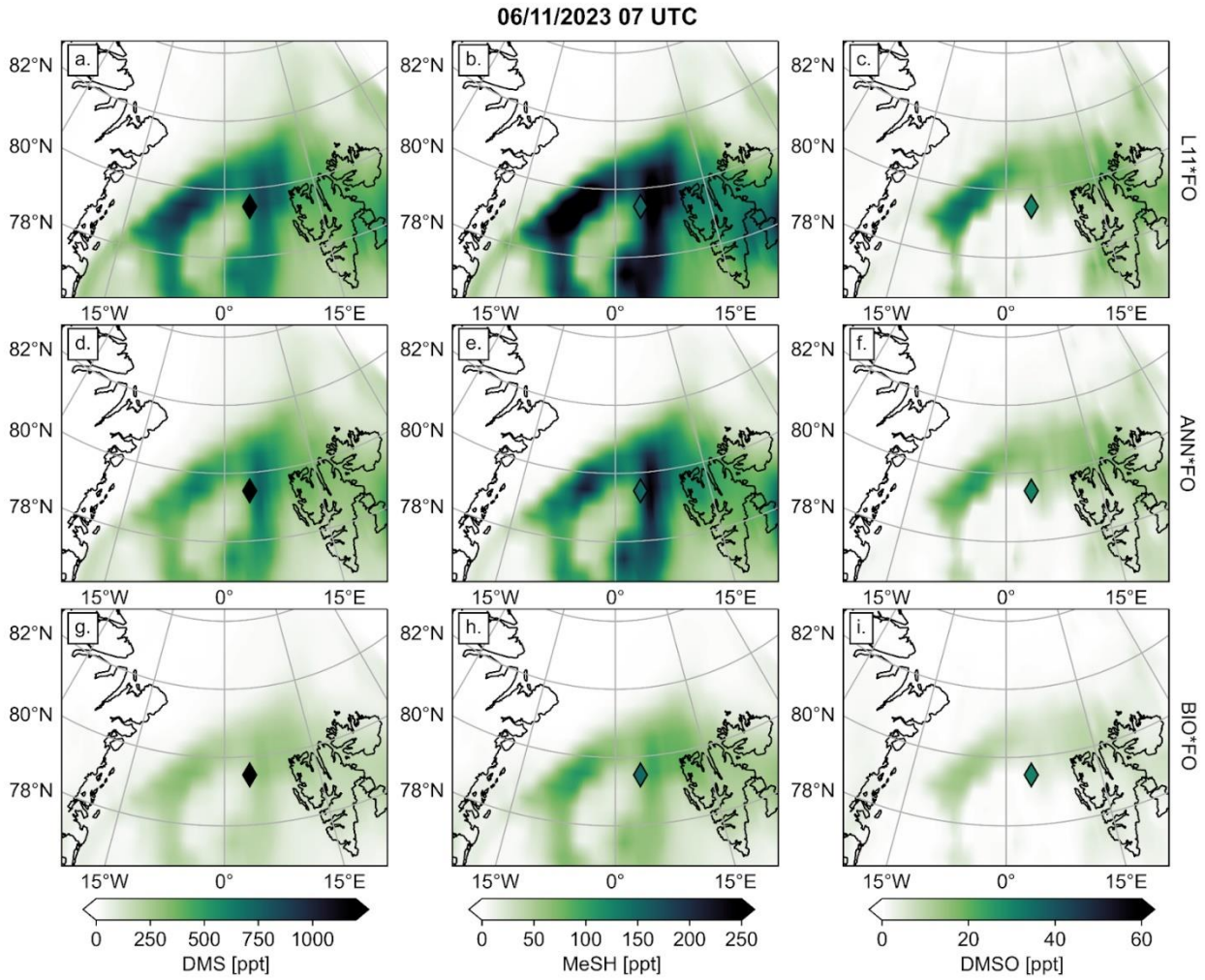

Figure 4.8: Maps of (a.) DMS, (b.) MeSH, and (c.) DMSO from the L11*FO simulation. Maps of (d.) DMS, (e.) MeSH, and (f.) DMSO from the ANN*FO simulation. Maps of (g.) DMS, (h.) MeSH, and (i.) DMSO from the BIO*FO simulation. All maps are from 06/11/2023 07 UTC. The diamond point on each panel is colored by the corresponding observed value from 06/11/2023 07 UTC.

The spatial patterns to the north and west of the ship are similar for DMSO and DMS, but to the south and east of the ship, there is relatively little DMSO (Figure 4.8). In the region to the south and east of the ship, the ratio of DMSO chemical production to chemical loss is higher than

the regional average (Figure C.15e), but also a higher low-cloud fraction and RH (Figure C.17), which results in faster wet deposition of DMSO, lowering the DMSO concentrations. The region of the highest simulated DMSO concentrations to the west of the ship corresponds to high DMS concentrations and DMSO production primarily through the OH-addition pathway (Figure C.15a). Similar to DMS and MeSH, we have no way of knowing the true spatial patterns of DMSO. However, the ability of the model to represent the DMSO spatial patterns is likely connected to DMS, oxidation, and meteorology.

4.4 Conclusions

We used the GC-TOMAS model and the ARTofMELT field campaign data to analyze the marine sulfur chemistry present during the spring-to-summer transition in the Fram Strait. Our main conclusions are as follows:

1. The emission of oceanic DMS/MeSH in grid boxes with ocean fractions less than 1 is important to being able to represent the atmospheric DMS and MeSH concentrations along the ship-track. During periods of mostly sea ice influence these near-ice emissions improve the atmospheric DMS LMB from -1.12 to 0.36 and from -0.78 to 0.32 for times with mostly marginal ice zone influence when using the Lana et al. (2011) oceanic DMS climatology.

2. Using higher spatial and temporal resolution oceanic datasets for the specific year of the campaign offers an opportunity to potentially better capture interannual variability in Arctic sulfur chemistry; however, these datasets come with their own limitations and biases. The simulation using oceanic DMS from the biogenic model and emissions from the sea ice zone has the lowest magnitude of bias for all source regions, except for the ocean where it performs the worst as a result of biases in the biogenic ocean models

representation of sea ice. The ANN with emissions from the sea ice zone simulation has a low bias of DMS for all source regions, but has the most consistent bias over the entirety of the campaign indicative of the ANN oceanic DMS dataset having a low bias of oceanic DMS in the Arctic regions.

3. DMSO is underestimated along the ship track generally by more than an order of magnitude due to both the biases in DMS, and likely biases in DMS oxidation and DMSO wet removal.

4. The OH-addition oxidation pathway of DMS is the most dominant throughout the campaign; however, the aqueous pathway becomes important during periods of fog. The model is also potentially biased low in the importance of the BrO DMS oxidation pathway.

Future work should be done to address the biases of DMSO. The DMSO biases, particularly during sea ice and marginal ice zone influence, are likely connected to the bromine sources from snow and sea ice. Therefore, there should be continued work to improve the bromine emissions and assumptions of present parameterizations in GC-TOMAS. There are also likely biases in the wet deposition of DMSO as a result of the wet deposition scheme in GC-TOMAS needing further refinement to adequately represent the Arctic. Additionally, the value of the Henry's Law Coefficient of DMSO is uncertain.

Additional future work should work on understanding both the emission and oxidation of MeSH. For emissions, a first step could be testing different spatial gradients in the assumed oceanic DMS:MeSH scalar to see if this yields agreement more consistent with the DMS biases.

Beyond the scope of this project, there could also be progress towards developing gridded oceanic MeSH datasets similar to those that exist for oceanic DMS.

4.5 Data Availability

This work was funded by the U.S. National Science Foundation grant number 2211153. This work is part of the ARTofMELT (Atmospheric rivers and the onset of Arctic melt) project. The ARTofMELT expedition was supported and organized by the Swedish Polar Research Secretariat (SPRS) on the Swedish research icebreaker *Oden* in spring under the SWEDARCTIC program. Observation data from *Oden* used in this study will be made available on the Bolin Centre Database once it is finalized (https://bolin.su.se/data/oden-artofmelt-2023/).

Chapter 5: Processes Governing Atmospheric Aerosol in the North Atlantic Arctic Spring[4]

5.1 Introduction

Atmospheric marine particles in the marine and Arctic atmosphere have important impacts on the climate system (Charlson et al., 1987; Croft et al., 2019; Hodshire et al., 2019c; Tashmim et al., 2024; Yang et al., 2014; Yu et al., 2006). These aerosol particles influence the climate directly through scattering (Bond et al., 2013; Charlson et al., 1987, 1991) and indirectly by modifying cloud albedo and lifetime (Albrecht, 1989; Charlson et al., 1987; Twomey, 1974). The scattering and absorption of aerosols is dependent on their size and composition with peak efficiencies generally being between 100 nm and 1 μm in diameter (Bond et al., 2006, 2013; Seinfeld and Pandis, 2016). Aerosols influence cloud properties through acting as cloud condensation nuclei (CCN), and their ability to act as CCN is dependent on size and hygroscopicity (Petters and Kreidenweis, 2007; Twomey, 1974). The radiative effects in the Arctic, as well as global radiative forcing estimates, are very sensitive to aerosols and clouds in the Arctic which have large modeling uncertainties due to complex aerosol feedbacks and strong seasonal cycles (Browse et al., 2012, 2014; Sand et al., 2016; Schmale et al., 2021; Willis et al., 2018). Therefore, improving understanding of aerosol size distributions and composition, and reducing aerosol modeling biases in the Arctic is crucial to the understanding of the overall climate system.

Aerosols in the Arctic have a strong seasonal cycle in concentration, size, and composition (Boyer et al., 2023, 2024; Croft et al., 2016; Schmale et al., 2021; Willis et al., 2023). Measurements of aerosol size distributions at stationary Arctic sites show that the

[4] June, N. A., C. Zang, S. E. O'Donnell, B. Croft, R. Y.-W. Chang, J. Kojoj, F. Mattsson, P. Zieger, D. Fellin, L. Heikkinen, A. Massling, L. Tashmim, W. C. Porter, S. H. Jathar, M. D. Willis, & J. R. Pierce (in preparation): Processes Governing Atmospheric Aerosol in the North Atlantic Arctic Spring.

observed annual cycle has two maxima in aerosol number: one in March-April and one in July (Croft et al., 2016; Engvall et al., 2008; Leaitch et al., 2013; Tunved et al., 2013). The springtime peak tends to be associated with accumulation mode particles due to the presence of Arctic haze, while the summertime peak is associated with less transport from lower latitudes, efficient wet removal, and new particle formation (Croft et al., 2016). The May-June period that is the focus of this study is important to understanding the transition between these two maxima. In this transition period, transport patterns change and wet removal becomes more efficient to limit advection from lower latitudes (Bozem et al., 2019; Garrett et al., 2010; Korhonen et al., 2008; Moschos et al., 2022b, a; Stohl, 2006). As a result, the influence of anthropogenic pollution becomes less common and the importance of local natural aerosols increases (Croft et al., 2016, 2019; Moschos et al., 2022b, a). Additionally, secondary organic aerosol formation and new particle formation are more important in the summer due to emissions from enhanced oceanic biological activity and increased photochemistry (Burkart et al., 2017a, b; Croft et al., 2019; Willis et al., 2017).

Primary sources of particles in the marine Arctic include emissions from sea spray and blowing snow (Gantt and Meskhidze, 2013; Gong et al., 2023; Grythe et al., 2014; Huang et al., 2020; Jaeglé et al., 2011). Sea spray is an important source of CCN in the Arctic system (Gong et al., 2023; Pierce and Adams, 2006). Emissions of sea salt from blowing snow are most important during the winter months, but still contribute roughly equally to the total sea salt emissions as open ocean during the spring-summer transition (Huang and Jaeglé, 2017). Understanding if the sea salt aerosols are from the ocean or from blowing snow is important as the blowing snow emissions tend to contribute to smaller particle sizes (< 1 μm) than those from the open ocean (Gong et al., 2023).

New particle formation (NPF), or the formation of particles from low-volatility vapors is an important source of particle number in the Arctic (Croft et al., 2016; Gordon et al., 2017; Hodshire et al., 2019c; Schmale et al., 2021; Willis et al., 2018). Dimethyl sulfide (DMS) is a contributor to NPF and growth in the Arctic as a result of its oxidation to SO_2 and methanesulfonic acid (MSA) (Croft et al., 2021; Hodshire et al., 2019c; Johnson and Jen, 2023; Tashmim et al., 2024; Thomas et al., 2010). Methanethiol (MeSH) is also emitted from the oceans and oxidizes to SO_2 (Wohl et al., 2024); however, the influence of MeSH on the sulfur budget is less well understood and constrained in models than that of DMS. SO_2 is then further oxidized in the atmosphere to form sulfuric acid (H_2SO_4). In addition to sulfuric acid, other vapors including: amines, MSA, ammonia, iodine, and organics contribute to NPF and growth (Allan et al., 2015; Beck et al., 2021; Croft et al., 2016, 2019, 2021; Hodshire et al., 2019c; Huang et al., 2022; Willis et al., 2018; Zhao et al., 2024). Beck et al. (2021) found through observations that springtime NPF events at Villum, Greenland were driven by iodic acid, but were too weak to facilitate growth to CCN sizes. At Ny-Ålesund, Svalbard nucleation occurred via sulfuric acid and ammonia with growth to CCN sizes facilitated by condensation of MSA and sulfuric acid. Despite the progress in understanding NPF and growth (NPF&G), the ability to simulate these events accurately in models remains difficult due to the representation of mechanisms, precursors, and model resolution.

Secondary organic aerosol (SOA) resulting from a marine origin also contributes to the sub-micron mass in the Arctic (Burkart et al., 2017a, b; Croft et al., 2019; Willis et al., 2017). The oceans are a source of organic vapors that can contribute to SOA formation; however, a lack of speciated volatile organic compound (VOC) measurements in the marine Arctic means the exact source and composition of these SOA precursors are not well characterized (Carpenter et

al., 2012; Carpenter and Nightingale, 2015; Croft et al., 2019, 2021; Kim et al., 2017; Rinaldi et al., 2013). In the North Atlantic and Arctic, organics have been observed and modeled to make a large contribution to the growth of particles to CCN sizes (Burkart et al., 2017a; Croft et al., 2019, 2021; Leaitch et al., 2018; Willis et al., 2017). Part of the goal of this study is to better understand OA and SOA precursors during the springtime Arctic, to potentially reduce model biases in both aerosol mass and size.

Cloud-processing and wet removal of aerosols are also key, but not always well represented in models in the Arctic (Browse et al., 2012; Cesana et al., 2012; Croft et al., 2016; Garrett et al., 2010; Pierce et al., 2015). The inclusion of interstitial coagulation in Arctic clouds in models improves the agreement between observed and simulated aerosol size distributions in the Arctic (Croft et al., 2016; Pierce et al., 2015). Additionally, efficient wet removal in Arctic low-level clouds is important to explaining the observed seasonal cycle of the Aitken and accumulation modes (Browse et al., 2012; Croft et al., 2016). While both Browse et al. (2012) and Croft et al. (2016) identified drizzle as a key contributor to wet removal, they cited the need for continued work on understanding wet deposition in the Arctic due to assumptions in drizzle rate and uncertainties in the low-cloud cover.

Here, we use data from a recent Arctic field campaign and a global chemical transport model coupled with a size-resolved aerosol microphysics model to understand model representation of aerosol composition and the springtime shift in Arctic aerosol size distributions. In Chapter 5.2, we describe our use of measurements from the ARTofMELT field campaign and the simulations we conduct using the atmospheric chemistry model with size resolved aerosol microphysics (GEOS-Chem-TOMAS). In Chapter 5.3, we characterize the model biases by the different source regions that impacted the aerosol composition and size distributions during the

campaign. We also utilize measurements from the Villum Research Station and back trajectories to conduct a case study from a regional perspective when the field campaign was impacted by transport from the North. Finally, we conduct a regional analysis of a time period with strong open ocean influence. In Chapter 5.4, we summarize these findings and make recommendations for future work to further improve parameterization of these Arctic-climate relevant aerosol processes.

5.2 Methods

5.2.1 Measurements During the ARTofMELT Field Campaign

The Atmospheric Rivers and the onset of sea ice melt (ARTofMELT) field campaign took place in the Fram Strait from May 9 to June 13, 2023 on the Swedish Icebreaker *Oden* (See Figure 4.1).

We use data of aerosol mass collected using a soot particle aerosol mass spectrometer (SP-AMS) (Freitas et al., 2024; Onasch et al., 2012). The SP-AMS alternated between running in laser-on mode to vaporize soot particles and laser-off mode to measure non-refractory particles. In this work, we only use the non-size resolved measurements of non-refractory particles. Specifically, we use the data for organics, sulfate, ammonium, and nitrate. Further technical details of the SP-AMS can be found in Onasch et al. (2012), while further details on the data processing and quality control of these data can be found in Freitas et al. (2024). As of the writing of this dissertation, the SP-AMS data are not finalized and are lacking some data corrections including loss correction, collection efficiency, and relative ionization efficiency. These limitations of the SP-AMS data mean that there are likely observational biases in both the concentrations and relative abundances of species measured by the SP-AMS. The SP-AMS data will change prior to publication.

We use measurements of gas phase reactive organic carbon that were collected using the Vocus-CI-ToFMS to aid in the analysis of understanding possible secondary organic aerosol sources in the region. The dual-reagent Vocus-CI-ToFMS uses the chemically general proton-transfer ionization (H_3O^+) with adduct-formation ionization (NH_4^+) to measure directly emitted, less-oxygenated VOCs, and their early-generation oxidation products (Hansel et al., 2018; Mungall et al., 2016; Zang and Willis, 2025; Zaytsev et al., 2019). These data are preliminary.

For the aerosol size distribution, we use a combination of three instruments to cover the size range from 3 nm to 2 μm. The Neutral cluster and Air Ion Spectrometer (NAIS) is used to measure the aerosol size distribution from 2 nm to 40 nm (Mirme and Mirme, 2013). The native temporal resolution of the NAIS data is 10 minutes. The aerosol size distribution from 15 nm to 800 nm is measured using a Differential Mobility Particle Sizer (DMPS) at a 12 minute temporal resolution (Karlsson et al., 2021; Williams et al., 2024). The DMPS data have been loss corrected for diffusional, gravitational, and impaction losses. A Laser Aerosol Spectrometer (LAS) is used for the aerosol size distribution from 0.2 μm to 1.7 μm. The LAS temporal resolution is 10 seconds. The total number concentration is used as a pollution flag to exclude measurements impacted by pollution from *Oden*. This pollution flag is also applied to the SP-AMS and VOCUS-CI-ToFMS data. For this study we re-bin the size distribution data into the 15 bin aerosol size distribution from 3 nm to 10 μm used in GEOS-Chem-TOMAS. For bins that are covered by two of the three instruments a weighted averaging is used to combine the data. The NAIS is known to have a high bias, so its data is weighted less in the overlapping size range with the DMPS data. The pollution flag and some of the loss corrections are preliminary meaning there may be adjustments to the observational data.

Additionally, we use some of the meteorological data collected on board the ship to support the aerosol analysis. Visibility, precipitation intensity, wind, temperature, relative humidity, cloud cover, and radiation are measured at a weather station on *Oden* located ~25 m above sea level.

To further characterize the aerosol size distributions in this region during the spring we use aerosol size distribution data from the Villum Research Station. A Scanning Mobility Particle Sizer (SMPS) measures the aerosol size distribution from 10 nm to 800 nm at Villum (Beck et al., 2021; Dall´Osto et al., 2018; Nguyen et al., 2016; Wang and Flagan, 1990).

We hourly average all observation and model data for our comparisons. Periods with missing observation data either due to pollution or instrument failure are excluded from analysis.

5.2.2 GEOS-Chem-TOMAS Model Description

We use the global atmospheric chemistry model (GEOS-Chem) coupled with the TwO-Moment Aerosol Sectional (TOMAS) model v12.9.3 (GC-TOMAS) to simulate the atmospheric DMS (Adams and Seinfeld, 2002; Kodros and Pierce, 2017). The TOMAS aerosol microphysics scheme used in our simulations has 15 size bins from 3 nm to 10 μm. We simulate size-resolved sulfate, sea salt, organic aerosol (OA), black carbon (BC), and dust, and diagnose size-resolved aerosol ammonium, nitrate, and water. Our GC-TOMAS configuration uses 47 vertical layers and is first run at 4°x5° horizontal resolution globally to obtain boundary conditions. We then run a nested simulation for a domain around the ARTofMELT campaign at 0.5°x0.625° horizontal resolution (Figure 4.1a).

The model is run using reanalysis meteorology from MERRA-2 which has fair agreement with the on-ship meteorological observations with the exception of precipitation (Figure C.1).

Generally, the precipitation field in the reanalysis meteorology tends to have fewer hours with no precipitation than was actually observed on the ship (Figure C.2). This may impact the wet removal.

5.2.2.1 Emissions

The anthropogenic, biomass burning, and non-DMS/MeSH natural emissions are consistent with the configuration of the previous chapter (4.2.2.1). This includes the blowing snow emissions that we will examine the impact of on the aerosol size and composition in this chapter.

For DMS and MeSH emissions, based on the results of the previous chapter, we use the updated sea-air flux calculation. The emission flux is controlled by the gas-transfer velocity, which is a function of wind speed and SST (Johnson, 2010) scaled by the ocean fraction. This scaling allows for emissions throughout the marginal ice zone, which observationally has been shown to have DMS emissions (Hayashida et al., 2017; Lizotte et al., 2020; Loose et al., 2011; Willis et al., 2023; Wohl et al., 2022). The default DMS emissions in GEOS-Chem has no emissions if any ice is in the grid cell. As was described in the previous chapter, including these emissions improved the model-observation agreement of DMS and MeSH, which means it could also be influential on the model-observation agreement of aerosol properties. The oceanic DMS concentrations come from the Lana et al. (2011) dataset because it is the standard source used in GC-TOMAS (Hulswar et al., 2022). The oceanic MeSH is estimated using the same scaling factors described in the previous chapter.

5.2.2.2 TOMAS Aerosol Microphysics

The TOMAS aerosol microphysics scheme used in our simulations has 15 size bins from 3 nm to 10 μm. The updates we make to the TOMAS microphysics are consistent with the previous chapter; however, we will test the sensitivity of these updates here and describe them in greater detail.

All simulations couple MSA to the TOMAS microphysics scheme to include the effects of MSA on aerosol growth (Hodshire et al., 2019c), but we do not allow MSA to participate directly in NPF. We use the parameterization for MSA volatility developed using the E-AIM model in Hodshire et al. (2019). In this parameterization, volatility is calculated based on NH_3, temperature, and relative humidity. MSA can act as non-volatile, semivolatile, or volatile. Figure D.1 shows the volatility of MSA calculated using this parameterization along the ARTofMELT ship track based on the GC-TOMAS output. Very few hours have a classification with free ammonia, and all of those hours fall into the ELVOC-like category based on the parameterization for MSA volatility. The majority of the campaign falls into the no free ammonia category and is split between being treated as VOC-like (RH< 90%) and SVOC-like (RH>90%).

All simulations have updated the inorganic NPF mechanism to Dunne et al. (2016) and the implementation into GC-TOMAS described in O'Donnell et al. (2025). The Dunne et al. (2016) represents binary (sulfuric acid and water) and ternary (sulfuric acid, water, and ammonia) nucleation with ion-mediated and neutral versions of each. For the ion-mediated versions, we use an ion-pair formation rate of 10 pairs cm^{-3} s^{-1}, which is representative of the continental boundary layer. This ion-pair formation rate could be too high for the location of our study: the surface in the marine Arctic (Nieminen et al., 2018; Snow-Kropla et al., 2011). O'Donnell et al. (2025) uses a 10^3 scalar on the inorganic nucleation rates, as the Dunne et al.

(2016) scheme produced too little nucleation at the Southern Great Plains site; we also include that scalar here; however, this scalar may be inappropriate for our study location.

We also allow for organics to participate in NPF following Riccobono et al. (2014) with the implementation into GC-TOMAS described in O'Donnell et al. (2025). The organic nucleation rates are calculated based on sulfuric acid clustering with low-volatility organic species with a temperature dependence (Riccobono et al., 2014; Yu et al., 2017). GC-TOMAS does not explicitly track low-volatility organics, so we assume 1% of condensing SOA has a volatility low enough to participate in NPF. The pseudo-steady state concentration of the low-volatility organics is then calculated using the calculated condensation sink and assumed molecular weight of 200 g mol^{-1} (Pierce and and Adams, 2009). O'Donnell et al. (2025) found that a 10^2 scalar was needed to produce appreciable nucleation from this scheme in GC-TOMAS, and we continue to use that scalar here.

We recognize that there are limitations to our simulation of NPF due to the assumptions and scaling made in the calculations of the nucleation rates. We also realize that we are excluding some NPF mechanisms that may be important. We do not include the NPF mechanism iodine oxoacids, which was shown to be important in the marine boundary layer in Zhao et al. (2024) because GC-TOMAS lacks the chemistry for iodic acid (HIO_3). However, the importance of iodine induced NPF in the Zhao et al. (2024) study rapidly declines above 70°N, where our study is located. Although, based on the MOSAiC field campaign, iodic acid peaks in the Arctic in May, meaning it could be influential at this time of year depending on sea ice conditions (Boyer et al., 2024). However, we cannot say anything about the specific potential importance of iodic acid and the role of iodine in NPF in our study, as the Arctic has variability in conditions

depending on the sea ice conditions, proximity to land, transport patterns, and meteorological condition.

5.2.2.3 Secondary Organic Aerosol Scheme

SOA uses the scheme described in the previous chapter. We also use the updates to the SOA precursor emissions described there. Here we try to advance the characterization of these SOA precursors based on the reactive organic carbon measurements taken on *Oden* during ARTofMELT. In the model sense, we refer to these precursors as Arctic Marine SOA (AMSOA).

5.2.2.4 Wet and Dry Deposition

Removal of simulated aerosol mass and number occurs through wet and dry deposition. All simulations include the updates for interstitial coagulation (Croft et al., 2016; Pierce et al., 2015). Prior modeling studies, primarily focused on the Canadian Arctic, have suggested a need for more vigorous wet removal from Arctic low-level clouds (Browse et al., 2012; Croft et al., 2016). These updates are described in detail in the previous chapter.

5.2.2.5 Sulfur Chemical Mechanism

The DMS and MeSH chemical mechanism is consistent with the description from the previous chapter.

5.2.3 Summary of GEOS-Chem-TOMAS Simulations

Table 5.1 presents the sensitivity simulations used in our study focused on the May-June, 2023 ARTofMELT field campaign. The STAND simulation includes all model updates described in the previous section. The four sensitivity simulations turn off one of the model updates to isolate the impact of these updates. We choose to turn updates off one at a time, since two of these updates have already been shown to have importance in the Arctic region.

Table 5.1: Brief summary of GEOS-Chem-TOMAS simulations used in this study and their corresponding abbreviations.

SIMULATION	DESCRIPTION
STAND	Includes all model updates described in Chapter 5.2.2
NOSNOW	Same as STAND without blowing snow emissions
NOAMSOA	Same as STAND without additional Marine Arctic SOA precursor emissions
NODRIZZLE	Same as STAND without more vigorous wet removal from Arctic (> 66°N) low-level clouds
NORICC	Same as STAND without Organics+Sulfuric acid NPF using Riccobono et al.

5.2.4 Use of HYSPLIT and Definition of Source Regions

Using the same methodology as the previous chapter, we run HYSPLIT back trajectories to define source regions.

HYSPLIT is further used in this chapter through a combination with GC-TOMAS output to extract aerosol size distributions along the Lagrangian back trajectories to understand the evolution of the aerosol size distribution. The methodology of extracting the simulated aerosol size distribution along the back trajectory is described in detail in O'Donnell et al. (2025).

5.3 Results

5.3.1 PM1 Composition During ARTofMELT

OA and sulfate are the largest fraction of particulate matter mass measured by the SP-AMS for ARTofMELT regardless of source region (Figure 5.1). Ammonium and Nitrate make up much smaller fractions and are rarely above the instrument limit of detection. The SP-AMS data typically has an upper size limit of 1 μm and does not include estimates of sea salt. Therefore, to compare to the model, we use the model integration of mass smaller than 1μm and exclude sea salt. In the discussion of Figure 5.1, particulate matter smaller than 1 μm in diameter (PM1) refers to the sum of the OA, sulfate, nitrate, and ammonium concentrations. In terms of absolute PM1 concentration, the model generally has more PM1 than the observations, which is likely the

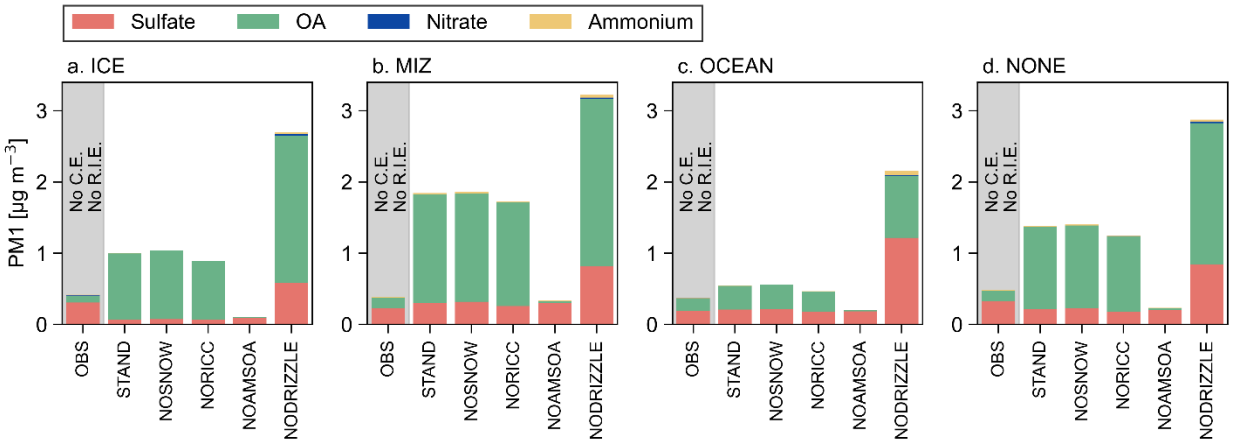

Figure 5.1: Bar chart of the observed and simulated PM concentration and composition for (a.) ICE, (b.) MIZ, (c.) OCEAN, and (d.) NONE source regions. Source region definitions are in Table 4.2. As a reminder, the observational data does not yet have collection efficiency (C.E.) or relative ionization efficiency (R.I.E.) applied to it.

result of biases in both the simulations and observations. For OA, there is hardly any OA simulated for any of the source regions without the inclusion of the AMSOA (NOAMSOA simulation). The AMSOA emissions substantially increase the availability of SOA precursors in the simulations (Figure D.2) resulting in an increase in OA in the STAND simulation relative to the NOAMSOA simulation. The AMSOA emission rate was tuned for the Canadian archipelago in the summer (Croft et al., 2019), and therefore may not be entirely representative of SOA precursors during May-June in the Fram Strait. The AMSOA emission rate will be further refined for this region and time of year once the observational data are finalized. However, the varying biases between source regions (discussed below) suggest that the marine SOA precursor variability could benefit from being modified to be mechanistic rather than a fixed rate scaled by ocean fraction.

For the ICE source region, the campaign average PM1 is 0.43 µg m^{-3} in the observations and 1.00 µg m^{-3} in the STAND simulation (Figure 5.1a). The majority of the PM1 mass for the

ICE source region in the observations is sulfate, while for the STAND simulation most of the PM1 mass is OA. The NOSNOW and NORICC simulations have similar PM1 concentration and composition as the STAND simulation (for the species measured by the SP-AMS) in the ICE source region. The NODRIZZLE simulation has a higher concentration of PM1, despite the DRIZZLE updates not occurring over pack ice or the marginal ice zone, as a result of decreased wet removal close to *Oden*. The NOAMSOA simulation has too little OA compared to the observations, suggesting that there is some uncharacterized source of SOA precursor being emitted in regions with sea ice. The current AMSOA emission rate was tuned for the summer in the Canadian archipelago and is linearly scaled by the ocean fraction (Croft et al., 2019). The high bias of OA in the STAND simulation suggests that the emission rate is too high for regions of mostly sea ice coverage in the Arctic spring. Furthermore, the correlation between the SOA precursor species in the STAND simulation and observed reactive organic carbon species that contribute to SOA is low for the ICE source region relative to those for the OCEAN and MIZ source regions (Figure D.3), potentially suggesting that we are not adequately representing SOA precursor in the ICE source region.

For the MIZ source region, the campaign average PM1 concentration is 0.41 μg m^{-3} and 1.82 μg m^{-3} in the observations and STAND simulation respectively (Figure 5.1b). The observations are 57% sulfate and 40% OA. The STAND PM1 concentrations are 16% sulfate and 83% OA. There is an overestimate in sulfate concentration by 0.08 μg m^{-3} in the STAND simulation for the MIZ source region, meaning most of the bias in the PM1 concentrations for the MIZ source region result from model biases in OA. The MIZ source region averaged OA is 1.50 μg m^{-3} and 0.03 μg m^{-3} for the STAND and NOAMSOA simulations respectively meaning that most of the OA in the STAND simulation at *Oden* coming from the MIZ is a result of the

AMSOA emissions. For the MIZ, the SOA precursors likely have a complex relationship with chlorophyll, melt ponds, and biogenic processes between and underneath the sea ice (Abbatt et al., 2019; Mirrielees et al., 2024).

When the dominant source region is OCEAN, the STAND simulation average PM1 is 0.55 μg m^{-3} and the observed average PM1 is 0.38 μg m^{-3} (Figure 5.1c). In the observations, the composition is 0.17 μg m^{-3} OA and 0.19 μg m^{-3} sulfate. The STAND simulation has 0.21 μg m^{-3} OA and 0.33 μg m^{-3} sulfate. Since the STAND simulation has an underestimate in PM1 mass and the observations are potentially biased low without the needed corrections, it is possible that the assumed drizzle rate is too high for this time and region in the Arctic. The DRIZZLE updates have the largest impact in the OCEAN source region due to the way the updates are implemented resulting in the NODRIZZLE simulation having more than double the PM1 concentration of the STAND simulation for the OCEAN source region. For the OCEAN source region, the PM1 in the NOAMSOA simulation is mostly sulfate with very little OA, meaning the majority of the OA in the STAND simulation comes from the AMSOA simulation. Some of the reactive organic carbon species that are correlated with the AMSOA SOA precursor concentration for the OCEAN source region (Figure D.3b) have previously been shown to be produced from biogenic and ozonolysis processes in the ocean (Kilgour et al., 2024; Kim et al., 2017).

In addition to the STAND simulation biases in OA, the correlations between SOA precursors and DMS also suggest the need for refinement of the AMSOA emission (Figure D.4). The spearman correlation between the measured reactive organic carbon and measured DMS is 0.12, but is as high as 0.26 when using a time-lag of +14 h for the observed DMS. The spearman correlation of the AMSOA SOA precursor with DMS peaks at 0.33 with a time-lag of 0 h. Since the AMSOA emission rate is scaled by ocean fraction, it is unsurprising that it is correlated with

DMS. However, the time-lag in the observed correlation between reactive organic carbon species that represent potential SOA precursors and observed DMS, suggests that in reality the processes contributing to DMS and SOA precursor production in the ocean are not peaking at the same time, likely due to different processes contributing to the production of DMS and SOA precursor species. The correlation results discussed here suggest that using a time lag in the DMS emission flux to represent AMSOA SOA precursor emission flux could help capture more of the observed variability in the SOA precursors (as a relatively simple first step). However, it would also subject the AMSOA SOA precursor to additional biases as a result of the biases in oceanic DMS and sea-to-air flux of DMS discussed in Chapter 4.

5.3.2 Aerosol Size Distributions During ARTofMELT

Table 5.2 shows the ARTofMELT campaign average $\log_{10}$ mean bias (LMB) for each of the simulations for 3 size ranges. For the number of particles between 3 and 15 nm (N_{3to15}), the STAND simulation shows a campaign average LMB of -1.24 (about 50 too few particles cm^{-3} in the STAND simulation). If NAIS observations have a high bias as indicated by prior studies (Mirme and Mirme, 2013), then the bias of the NAIS instrument that provides the N_{3to15} measurements could influence the underestimate of N_{3to15} in the simulations. The STAND simulation better represents the number of particles between 15 and 100 nm ($N_{15to100}$) with a campaign average LMB of 0.51 (about 3x too many particles in the model). $N_{15to100}$ has similar variability in the observation and STAND simulation (Figure D.5b). The LMB in the STAND simulation is 0.58 (about 127 too many particles cm^{-3}) for the number of particles between 100 and 800 nm ($N_{100to800}$). Compared to the other two size modes there is comparatively little variability in $N_{100to800}$ in both the observations and STAND simulation (Figure D.5c). The lack of variability in the accumulation mode could be connected to the presence of Arctic Haze during

ARTofMELT. Arctic haze has been previously observed to be accumulation mode dominated in the Winter and Spring (Boyer et al., 2023; Covert et al., 1996; Croft et al., 2016; Engelmann et al., 2021; Freud et al., 2017; Nguyen et al., 2016). Aerosol process reasons for the biases of each size mode vary by source region (Figure 5.2) and will be discussed in the coming paragraphs.

Table 5.2: Log_{10} mean bias (LMB) during ARTofMELT for N_{3to15}, $N_{15to100}$, $N_{100to800}$. The number of hours with non-nan values for N_{3to15} is 576 h, while for $N_{15to100}$ and $N_{100to800}$ it is 739 h.

Simulation	LMB of N_{3to15}	LMB of $N_{15to100}$	LMB of $N_{100to800}$
STAND	-1.24	0.51	0.58
NOSNOW	-1.21	0.55	0.61
NORICC	-1.81	-0.02	0.36
NOMSOA	0.77	0.77	-0.2
NODRIZZLE	-1.85	-0.33	0.64

For the ICE source region, the STAND simulation underestimates N_{3to15} (LMB of -1.51), slightly overestimates $N_{15to100}$ (LMB of 0.33), and overestimates $N_{100to800}$ (LMB of 0.55) (Figure 5.2). The Aitken ($N_{15to100}$) mode agreement during ICE influence is slightly impacted by the DRIZZLE and RICC updates: turning off either one of these updates changes the sign of the $N_{15to100}$ LMB to be negative. The high bias in the accumulation mode ($N_{100to800}$) for the ICE source region in the STAND simulation is related to too high of an emission rate for the AMSOA precursor. However, the NOAMSOA simulation underestimates $N_{100to800}$ for the ICE source region, so there is the need for some emission of an Arctic SOA precursor flux even in regions with partial ice cover. The STAND N_{3to15} low bias is connected to the high bias in STAND $N_{100to800}$ and STAND $N_{15to100}$ because these high biases connect to a high bias in the coagulation sink for the ICE source region (Figure D.6). The too high coagulation sink in the STAND simulation means that the nucleation mode particles are being lost too quickly through coagulation with larger particles. The condensation sink is increased by the added AMSOA in the ICE source region and at times the STAND simulation overestimates the condensation sink for

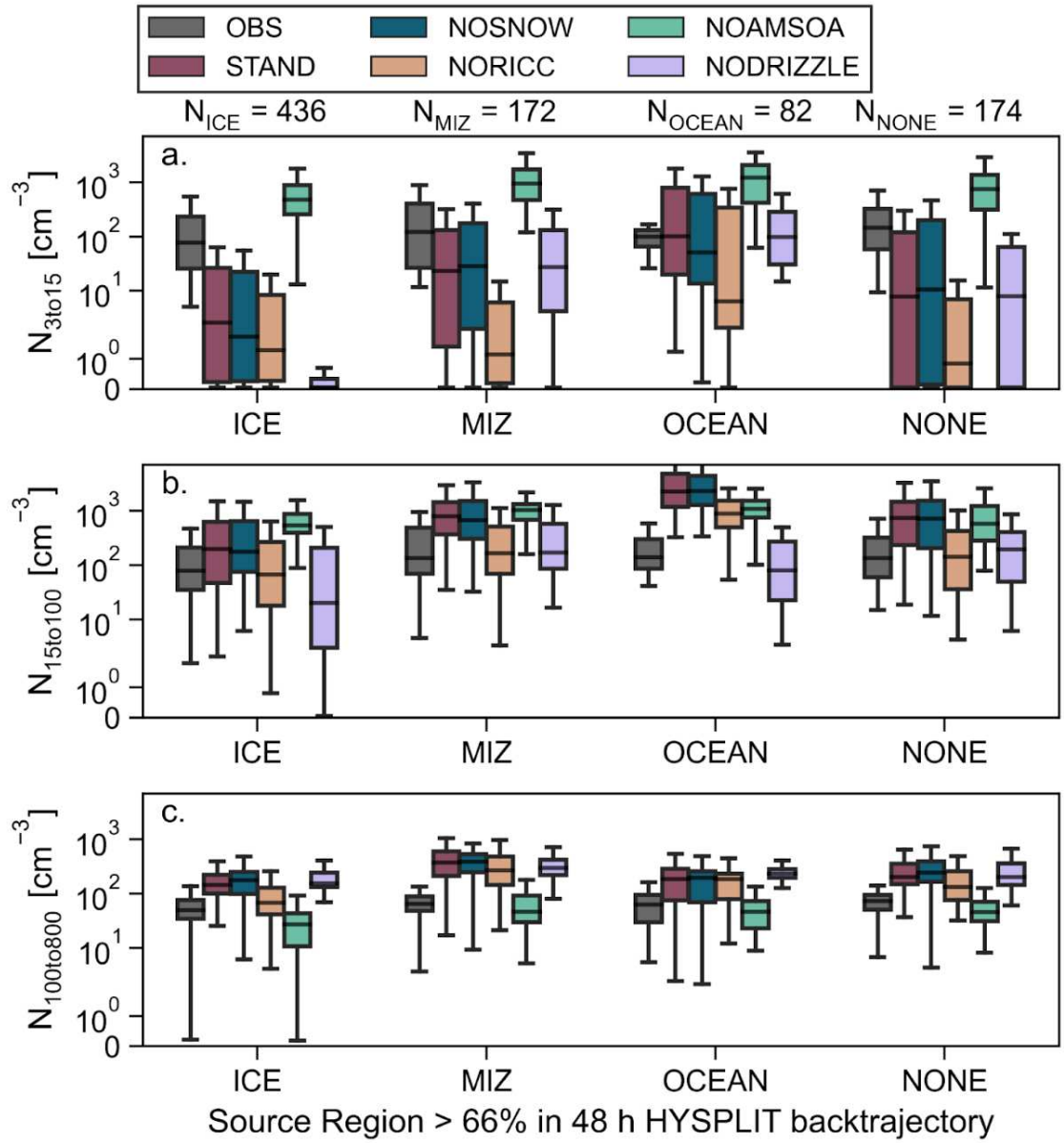

Figure 5.2: (a.) Number concentration between 3 nm and 15 nm (N_{3to15}) along the ARTofMELT ship track grouped by source region. (b.) Number concentration between 15 nm and 100 nm ($N_{15to100}$) grouped by source region along the ARTofMELT ship track. (c.) Number concentration between 100 nm and 800 nm ($N_{100to800}$) grouped by source region along the ARTofMELT ship track.

the ICE source region (Figure D.7). Since nucleation is generally favored in low condensation sink environments (Kecorius et al., 2019; Westervelt et al., 2014), the high bias in the condensation sink could help to explain the low bias in N_{3to15}. We cannot rule out that the low bias in N_{3to15} is due to missing NPF mechanisms in the model. A prior study looking at NPF at

Ny-Ålesund found that sulfuric acid, methane sulfonic acid (MSA) and iodic acid all contributed significantly to the growth below 10 nm in diameter during springtime NPF events (Beck et al., 2021). Iodic acid chemistry is not included in GC-TOMAS, so we do not have the mechanism for iodine to influence NPF. Prior studies have shown photochemical and biological processes in snow and sea ice to influence polar iodine emissions (Gálvez et al., 2016; Hill and Manley, 2009; Raso et al., 2017; Saiz-Lopez et al., 2015), while MOSAiC showed iodic acid concentrations to peak in April-May before declining in June (Boyer et al., 2024). Therefore, there could potentially be the precursors needed for iodine NPF during ARTofMELT when the source is coming from ICE, which would contribute to the N_{3to15} underestimate in the model.

During ARTofMELT, when there is MIZ influence the N_{3to15} LMB is -0.86; the $N_{15to100}$ LMB is 0.59; the $N_{100to800}$ LMB is 0.75 (Figure 5.2). Similar to the ICE source region, the MIZ region has a high bias for the STAND simulation in $N_{100to800}$ as a result of the AMSOA emission and a high bias in $N_{15to100}$ connected to the DRIZZLE and/or RICC updates. In the MIZ region, these $N_{15to100}$ and $N_{100to800}$ high biases result in high biases in both the condensation sink and coagulation sink (Figure D.6), which could contribute to the low bias in N_{3to15}. For the MIZ source region, turning off the RICC updates that allow low-volatility organics to participate in NPF degrades the LMB of N_{3to15} to -1.98 (over an order of magnitude worse in the NORICC relative to the STAND simulation). These results suggest that in the NORICC simulation: the conditions are not right for binary nucleation and there is not enough ammonia for ternary inorganic nucleation. The NOAMSOA simulation has a high bias in N_{3to15} in part due to the improved model-observation agreement of the condensation and coagulation sinks. The connections between the NOAMSOA and NORICC simulations and the STAND simulation seem to indicate that organic NPF is contributing to the observed size distributions and the best

case AMSOA emission is likely in between the current value and being turned off. However, like the ICE source region, we cannot rule out that missing model mechanisms for NPF are contributing to the biases in the model.

During periods with the source region defined as OCEAN the LMBs for the STAND simulation are 0.08, 1.13, 0.47 for N_{3to15}, $N_{15to100}$, and $N_{100to800}$, respectively (Figure 5.2). The N_{3to15} mode seems to be captured in the model as a result of the RICC updates. However, the model also overestimates the relative variability in N_{3to15} during OCEAN influence. As was mentioned in the discussion of Table 5.2, the N_{3to15} observations are missing more data than the other size modes. Many of these missing data points occur during OCEAN influence, limiting our ability to draw conclusions about the performance of our model and the NPF mechanisms. The $N_{15to100}$ high bias seems connected to the RICC, AMSOA, and DRIZZLE updates. The $N_{100to800}$ mean high bias seems connected to the AMSOA emissions being too high, but potentially less of a high bias than the other source regions. The NODRIZZLE simulation has very little relative variability in $N_{100to800}$, whereas in the STAND simulation the variability is more consistent with the observations.

Figure 5.3 shows that the variation in the size resolved aerosol composition throughout the campaign, highlighting the importance of the AMSOA and blowing snow updates at different points in the campaign. The sulfate, nitrate, ammonium, BC and dust species are calculated entirely using the STAND simulation; the OA and AMSOA species are estimated by taking the difference between STAND and NOAMSOA; the sea salt and blowing snow sea salt species are estimated by the difference between STAND and NOSNOW. Similar to Croft et al. (2019), which looked at the Canadian Arctic Archipelago in the summer, AMSOA makes up a large

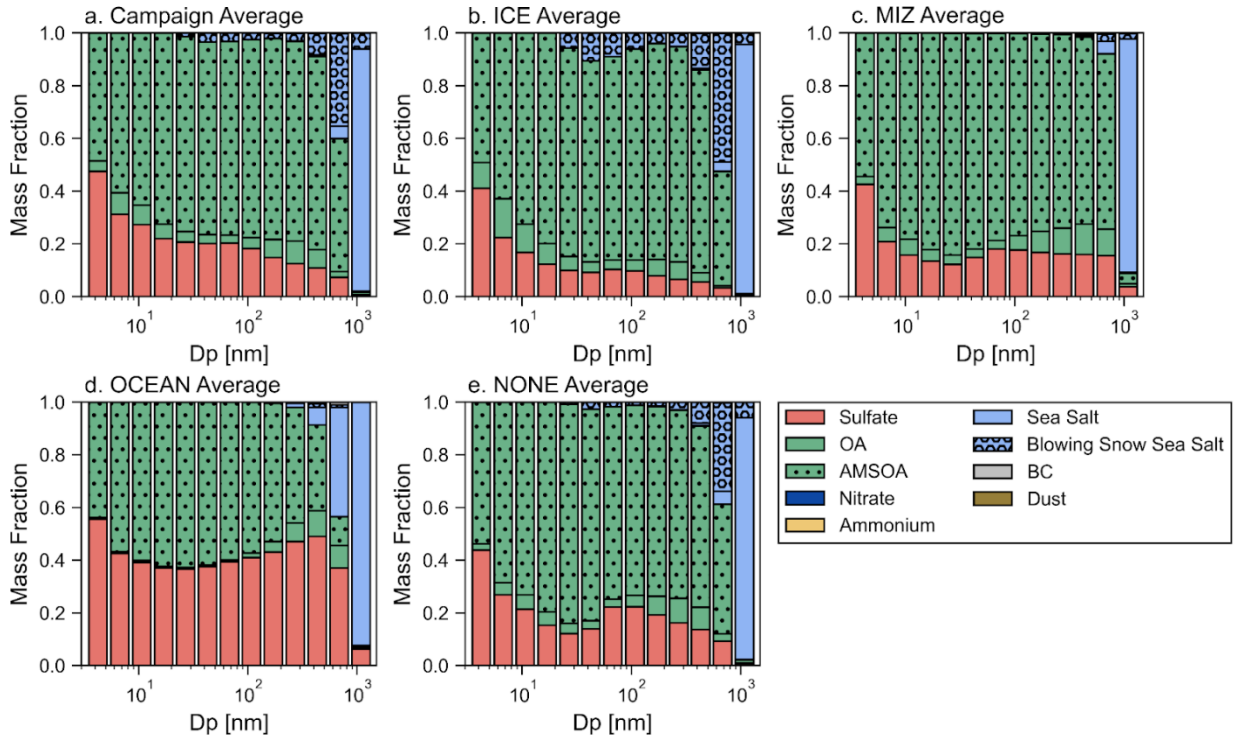

Figure 5.3: Simulated mean size-resolved aerosol composition mass fractions for (a.) the campaign average, (b.) the average during ICE influence, (c.) the average during MIZ influence, (d.) the average during OCEAN influence, and (e.) the average during periods with no dominant source region (NONE).

contribution of the sub-micron mass fraction, reflecting the importance of the marine source of condensable organics. For the ICE source region, the blowing snow emissions contribute mass to both the Aitken and accumulation modes, whereas these updates are not important for the MIZ or OCEAN source regions. The MIZ source region is similar to the ICE source region where AMSOA contributes much of the mass fraction below 800 nm. The OCEAN source region below 300 nm in size is split between AMSOA and sulfate, indicative of both a marine influence on organics and the DMS/MeSH sulfur chemistry. Unlike the other source regions which have a decreasing mass fraction of sulfate with size, the sulfate mass fraction for the OCEAN contributes >40% until 500 nm in diameter. This could indicate that MSA is contributing to the growth of the particles more during OCEAN influence and is consistent with prior studies

looking at the influence of MSA on particle growth (Ghahreman et al., 2019; Hodshire et al., 2019c).

To get a better sense of the bigger picture in the Arctic during ARTofMELT, Figure 5.4 shows the $N_{15to100}$ and $N_{100to800}$ at Villum Research Station. $N_{15to100}$ is represented in the mean, but the STAND simulation does not capture the observed variability in $N_{15to100}$ at Villum. The NOAMSOA simulation has a high bias in $N_{15to100}$ at Villum, but is more variable in the $N_{15to100}$ concentrations. The $N_{15to100}$ bias could also be related to biases in NPF at Villum. Beck et al. (2021) suggested that iodine was a key contributor to springtime NPF at Villum due to the availability of iodic acid being greater than sulfuric acid and MSA. The $N_{100to800}$ is overestimated at Villum in the STAND simulation, which could either be related to the RICC or AMSOA updates. The area around Villum is mostly sea ice, although there are some sea ice fractions below 1, which would allow for AMSOA emissions in the present model configuration. Therefore, the conclusions from the comparisons at *Oden* during ARTofMELT could also apply at Villum, meaning that the AMSOA emissions are too high for what is actually emitted through cracks in sea ice.

5.3.3 Case Study 1: Villum to *Oden*

The first case study we present is for June 6, 2023 at 10 UTC where a back trajectory started at *Oden* passed over Villum Research Station within the PBL 27 hours before reaching the ship (Figure 5.5a). Due to this overpass, we can evaluate the model at a starting point (Villum) and an ending point (*Oden*) and consider the evolution of the aerosol size distribution that may have taken place along that trajectory. The back trajectory was within the boundary layer the entire time between Villum and *Oden* and was over sea ice or the marginal ice zone with enough sea ice influence to fall into the ICE source region. The back trajectories earlier in

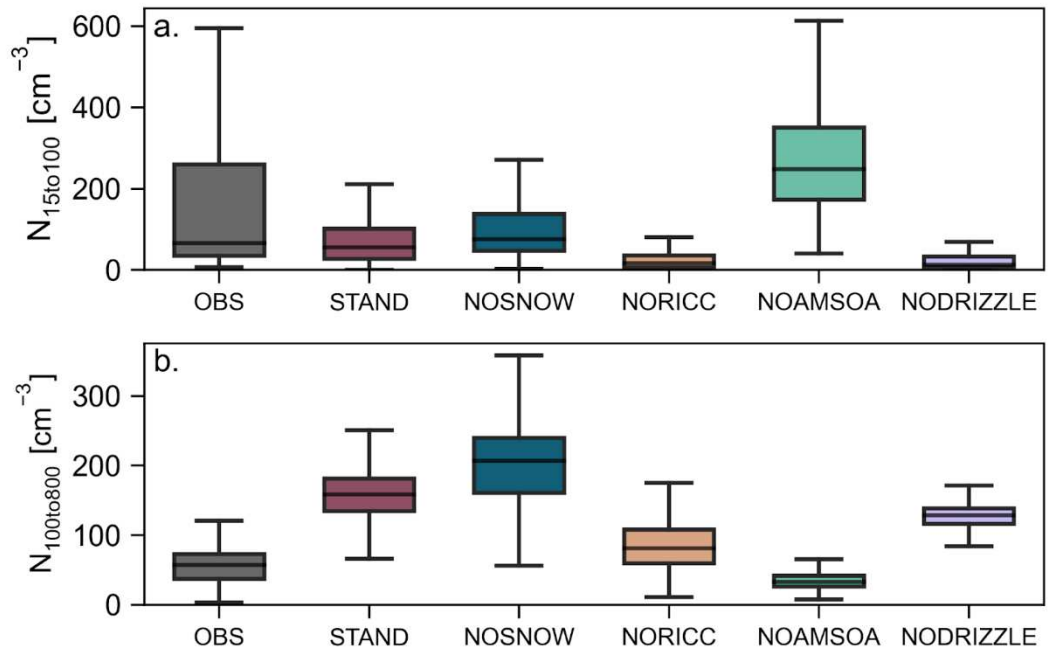

Figure 5.4: (a.) $N_{15to100}$ and (b.) $N_{100to800}$ at Villum Research Station for observations and each of the GC-TOMAS simulations during the ARTofMELT campaign (May 9 to June 13, 2023).

the day than the overpass near Villum came from further North and later in the day they came from further south (Figure D.8).

The back trajectory from the ship at June 6, 2023 at 10 UTC overpasses Villum at June 5, 2023 at 01 UTC; Figure 5.5b shows the aerosol size distribution comparison of the observation and all sensitivity simulations for this time at Villum. The STAND and the observed size distribution have similar number concentration, but the STAND simulation places the particles at too large of a size resulting in an underestimate of the Aitken mode and an overestimate in the accumulation mode. The NOAMSOA simulation shows signs of NPF that are not in the observations and underestimates the Aitken mode, but generally puts the peak of the size distribution at a similar diameter to the observations. The NORICC and NODRIZZLE simulations best capture the accumulation mode, but underestimate the total number

concentration due to the lack of an Aitken mode. To better represent the Villum aerosol size distribution at this time, a reduced AMSOA emission could help as this would suppress NPF relative to NOAMSOA and grow particles less than the STAND simulation.

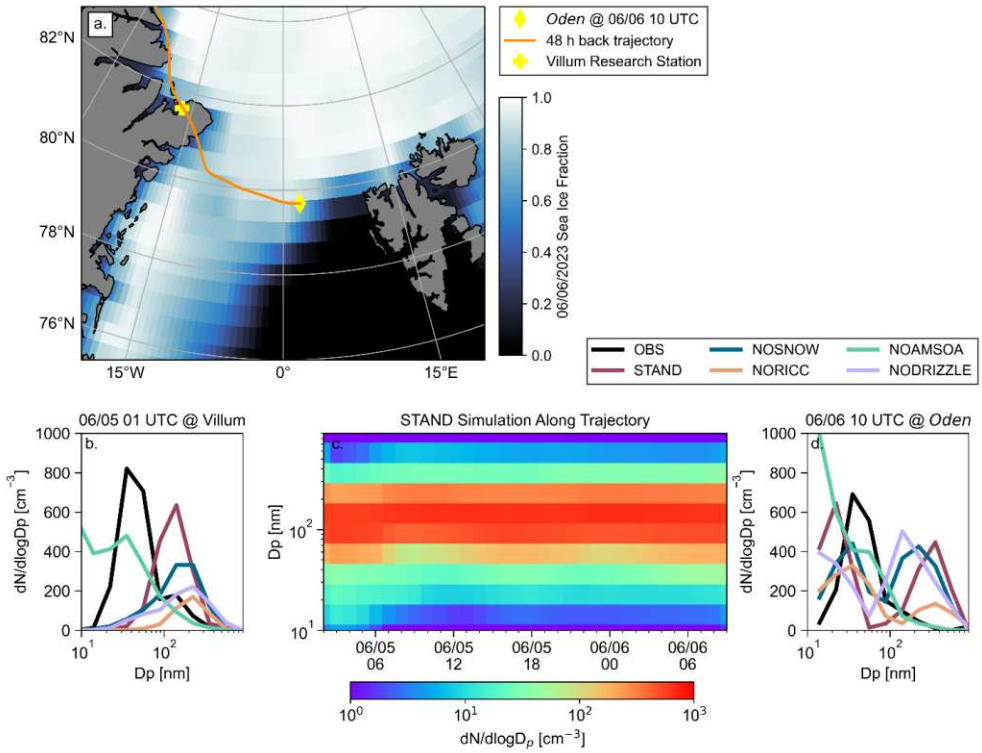

Figure 5.5: (a.) Map showing the back trajectory beginning at *Oden* for 06/06/2023 10 UTC. The background is colored by MERRA-2 sea ice fraction for 06/06/2023. The yellow cross shows the location of Villum and the yellow diamond shows the location of *Oden*. (b.) Observed and simulated aerosol size distribution at Villum at 06/05/2023 01 UTC, a time when a back trajectory started from ARTofMELT passed over the site within the boundary layer. (c.) The aerosol size distribution from the STAND simulation along the back trajectory from Villum to *Oden*. The time series goes from 06/05/2023 02 UTC (one hour after the Villum overpass) to 06/06/2023 09 UTC (one hour before reaching *Oden*). (d.) The observed and simulated aerosol size distribution at 06/06/2023 10 UTC at *Oden*. NAIS observations were unavailable at this time, so the size distributions begin 15 nm.

Along the back trajectory from Villum to *Oden*, the aerosol size distribution in the STAND simulation has a strong and fairly constant accumulation mode (Figure 5.5c). The accumulation mode is consistent with Arctic Haze (Boyer et al. 2023; Croft et al. 2016). The Aitken mode concentration decreases over the first 8 h of the back trajectory and then has a low

concentration until one hour before reaching *Oden* where it begins to increase. There are some slight differences along the back trajectory depending on sensitivity simulation (Figure D.9). The NOAMSOA simulation is constant along the back trajectory with a more concentrated Aitken mode and less concentrated accumulation mode relative to the STAND simulation. The NORICC simulation has fewer particles smaller than 30 nm, suggesting that the Riccobono mechanism contributes to NPF in the STAND simulation during this event.

At *Oden* at 06/06/2023 at 10 UTC, the observed size distribution has a singular peak in the Aitken mode at 40 nm with few particles in the accumulation mode (Figure 5.5d). The STAND simulation has a bimodal distribution with a peak in the Aitken mode at 20 nm and another peak in the accumulation mode at 400 nm. The bias in the accumulation mode is unsurprising, since the Accumulation mode had a high bias at Villum, and the accumulation mode remained constant along the back trajectory. The NORICC and NOSNOW simulations underestimate the concentration of the Aitken mode at this time, but have the peak diameter in the same model size bin as the observations. However, the NORICC and NOSNOW simulations have the same bi-modal structure as the STAND simulation with a second maxima in the size distribution in the accumulation mode. The only simulation without a second maxima in the size distribution in the accumulation mode (as indicated by the observations) is the NOAMSOA simulation. However, the NOAMSOA simulation likely has too much NPF occurring around *Oden*. Similar to the results discussed in Chapters 5.3.1 and 5.3.2, the effects of the AMSOA emission during this case study suggest the need for further refinement of the AMSOA emission.

Figure 5.6 shows the spatial distribution of N_{3to15}, $N_{15to100}$, $N_{100to800}$, and the OA:Sulfate ratio in the STAND simulation. Figure 5.6b and 5.6c at the location of *Oden* are consistent with Figure 5d in that the STAND simulation captures $N_{15to100}$, but overestimates $N_{100to800}$. Spatially,

North of *Oden* there are lower concentrations of N_{3to15} and $N_{15to100}$, but higher concentrations of $N_{100to800}$, potentially suggesting that the particles in that region North of *Oden* have grown more as a result of the AMSOA updates (Figure D.10j-k). The OA:Sulfate ratio shows that the simulations have more OA than sulfate everywhere, except for over Greenland where the land prevents AMSOA emissions. In the same region of the low OA:Sulfate ratio, the $N_{100to800}$ is also lower, suggesting OA is contributing to the high $N_{100to800}$ concentrations regionally in the STAND simulation. Overall, this case study gives a detailed look at a time period of mostly sea ice influence, which is generally when the model biases are highest in magnitude compared during the campaign.

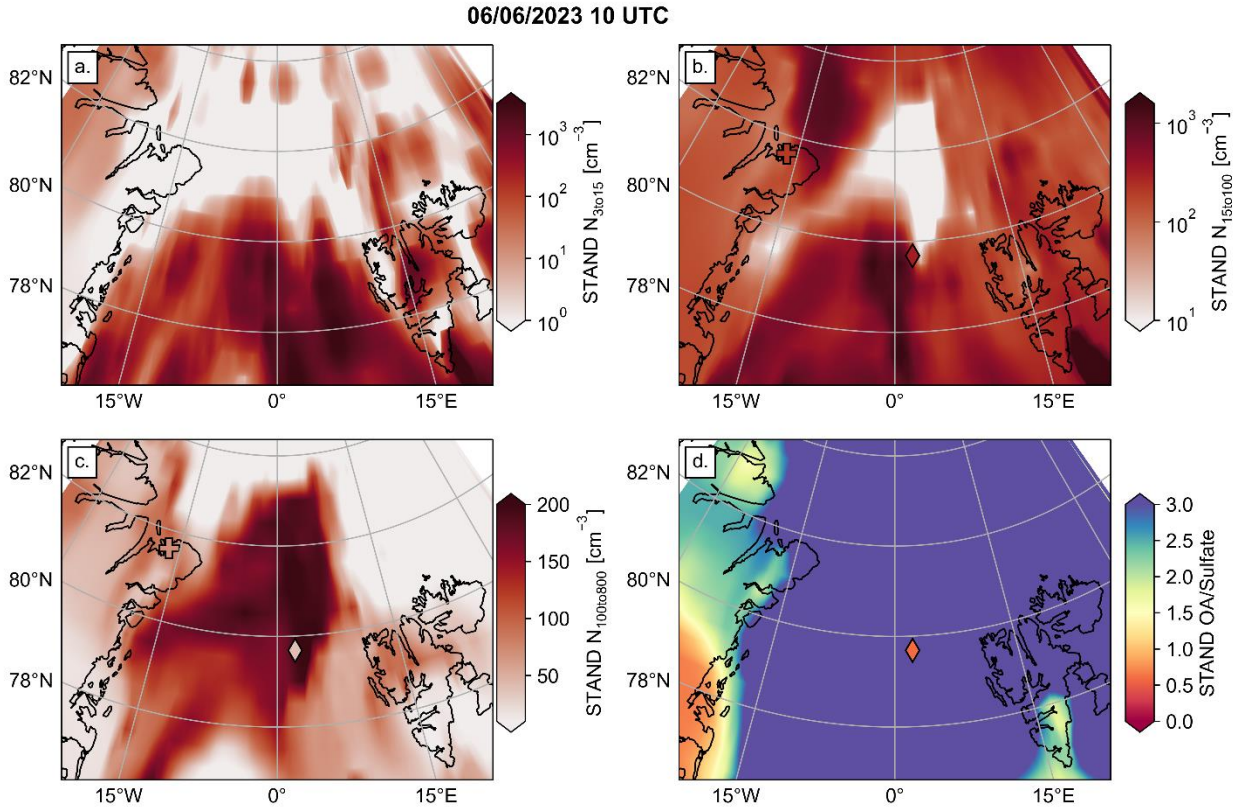

Figure 5.6: Regional maps from the STAND simulation of the (a.) N_{3to15}, (b.) $N_{15to100}$, (c.) $N_{100to800}$ number concentrations, and (d.) OA/Sulfate ratio for 06/06/2023 at 10 UTC. The diamond shows the location of ARTofMELT at this time and is colored by the observed value on the ship at this time. On (b.) and (c.) the plus sign shows the observed $N_{15to100}$ and $N_{100to800}$ at Villum. There were no NAIS observations at this time, so there is no diamond on the (a.) to show the observed N_{3to15}. Figure D.10 shows how these quantities change in sensitivity simulations.

5.3.4 Case Study 2: Marine Influenced New Particle Formation Event

For the second case study, we examine 06/11/2023 at 11 UTC, which was a time when *Oden* was located near the ice edge and the predominant source region was the ocean (Figure D.11). In Chapter 4.3.3, it was discussed that the biases in wind and fog could influence the model representation of DMS on this day. These meteorological biases could also influence the biases in aerosol size distributions on this day; however, here we mostly focus on the influence of the different model updates on the biases in simulated the aerosol size distribution. The STAND simulation at this time overestimates $N_{15to100}$ and underestimates $N_{100to800}$ (Figure 5.7a-b). The NAIS observations were unavailable at this time, however the DMPS observations at 15 nm suggest a weaker influence of nucleation at *Oden* with particles generally showing up grown around 30 nm, while the STAND simulation has NPF&G occurring at the *Oden*. All the sensitivity simulations have NPF&G at *Oden* in the morning to early afternoon of 06/11, but the NORICC and NODRIZZLE simulations have weaker NPF than the STAND simulation. The NODRIZZLE simulation better represents the observed accumulation mode, but due to the suppression of NPF both at the ship and upwind of the ship (Figure 5.8), the NODRIZZLE simulation underestimates the Aitken mode. Since the accumulation mode is most strongly influenced by the AMSOA and DRIZZLE updates, the NORICC simulation has a similar underestimate in the accumulation mode as the STAND simulation. However, the NORICC simulation is closer to showing particles appear as grown at *Oden*. The biases in the simulated aerosol size distribution time series during this potential NPF event, suggest biases in the implementation of the DRIZZLE updates and in the nucleation mechanisms (Figure 5.7). Additionally, the biases in the timing of the fog taking too long to dissipate as discussed in

Chapter 4.3.3, could result in the DRIZZLE updates (which are connected to low-cloud fraction) having too vigorous removal relative to reality in the afternoon of 06/11.

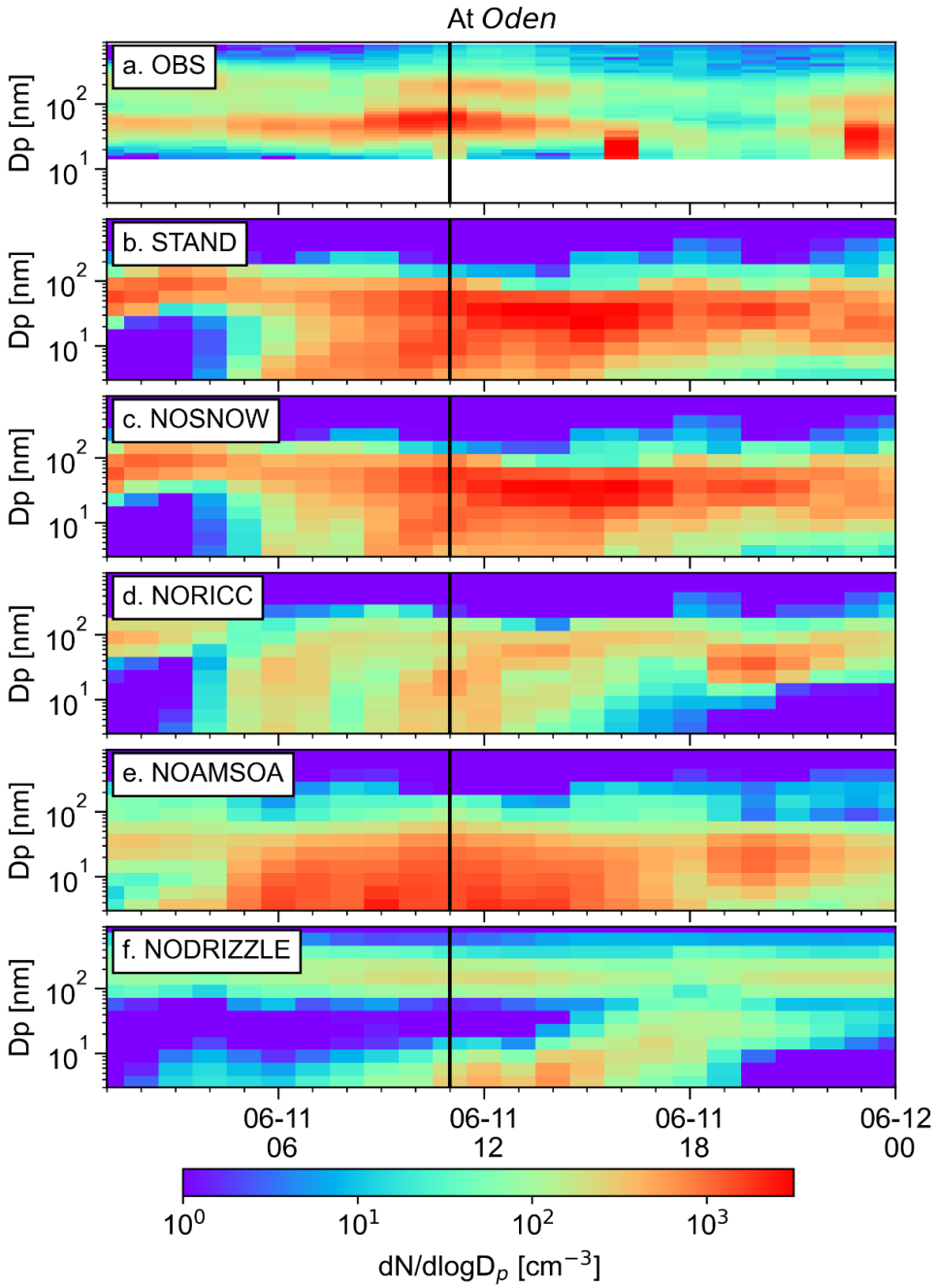

Figure 5.7: (a.) The observed aerosol size distribution measured by the DMPS on *Oden* for 06/11/2023. (b.) The STAND simulated aerosol size distribution for 06/11/2023 at *Oden*. (c.)-(f.) The aerosol size distribution for each of the sensitivity simulations at *Oden* on 06/11/2023. The vertical black line on each panel indicates the time that the back trajectory plotted in Figure 5.8a reached *Oden*.

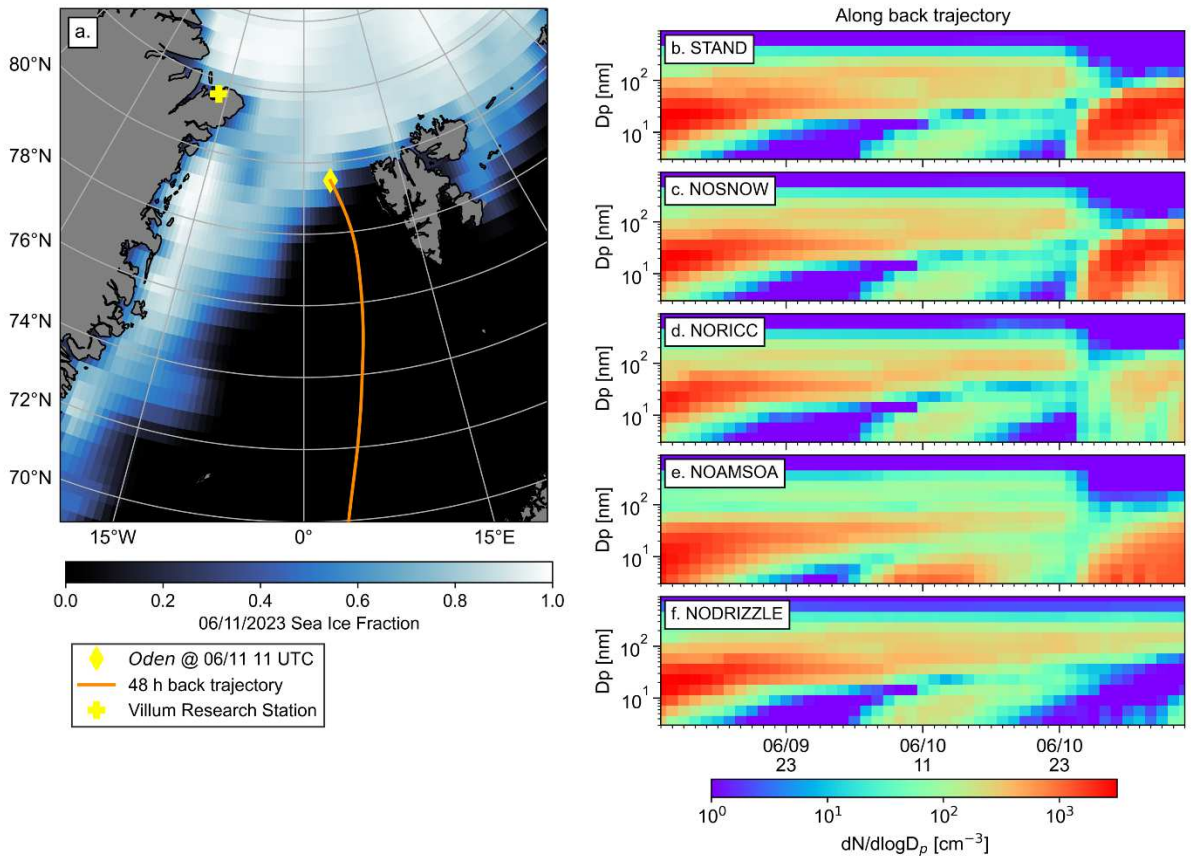

Figure 5.8: (a.) Map of the 48 h back trajectory starting from *Oden* on 06/11/2023 at 11 UTC. The background is the sea ice fraction from MERRA-2 averaged on 06/11/2023. The yellow cross shows the location of Villum and the yellow diamond shows the location of *Oden*. (b.) to (f.) The aerosol size distribution along the back trajectory from 06/09/2023 at 11 UTC (48 h before reaching *Oden*) and ending at 06/09/2023 at 10 UTC (1 h before reaching *Oden*).

Figure 5.8a shows a single back trajectory initiated at *Oden* at 06/11/2023 at 11 UTC, while Figure 5.8b-5.8f shows the aerosol size distribution along this back trajectory for all of the GC-TOMAS simulations. All of the simulations show multiple NPF&G events during the 48 h back trajectory, although the strength and growth in the simulations varies. Suggesting that the NPF&G seen in the STAND simulation is influenced by the RICC, AMSOA, and DRIZZLE updates. The NORICC simulation has weaker NPF than the STAND simulation in the event in the morning of 06/11/2023, suggesting that organics increased the nucleation rate in the STAND simulation. The NOAMSOA simulation has slower growth, suggesting that the marine source of SOA condensed onto the nucleated particles to increase the growth rate. The NPF&G event on

the morning of 06/11/2023 is not present in the NODRIZZLE back trajectory. The NODRIZZLE simulation is the only one with an accumulation mode, suggesting that particles formed in this simulation were quickly lost to coagulation with larger particles.

Regionally, the N_{3to15} concentrations are high suggesting that NPF is occurring around this time (Figure 5.9a). While there is some regional variability in the contribution of different model updates to N_{3to15}, generally it seems that the RICC and DRIZZLE updates contribute to the enhancement of N_{3to15} throughout the region in the morning of 06/11 (Figure D.12e, D.12m). The $N_{15to100}$ concentrations vary more spatially than N_{3to15} with generally higher $N_{15to100}$ concentrations occurring in areas with a higher OA:Sulfate ratio indicating a contribution of OA to growth as a result of the AMSOA updates (Figure 5.9; Figure D.12l). The concentrations of $N_{100to800}$ in the area surrounding *Oden* (Figure 5.9c) are associated with low-level clouds in the region (Figure C.15), which contributes to the DRIZZLE updates removing particles from the accumulation mode across much of the region (Figure D.12o). Overall from this case study, we find that the model representation of wet removal and OA are important to representing the influence of the ocean on NPF&G events.

5.4 Conclusions

We used the GC-TOMAS chemical transport model to investigate processes influencing aerosol observations during the ARTofMELT field campaign. We find that the organic nucleation scheme is important to explaining the observed NPF and Aitken modes due to the limited availability of ammonia limiting inorganic ternary nucleation. We find that AMSOA is an important contributor to the aerosol population during this spring season, but the emission rate of this SOA precursor needs to be refined and potentially correlated with other variables to better capture the variability between the open ocean and marginal ice zone. The importance of

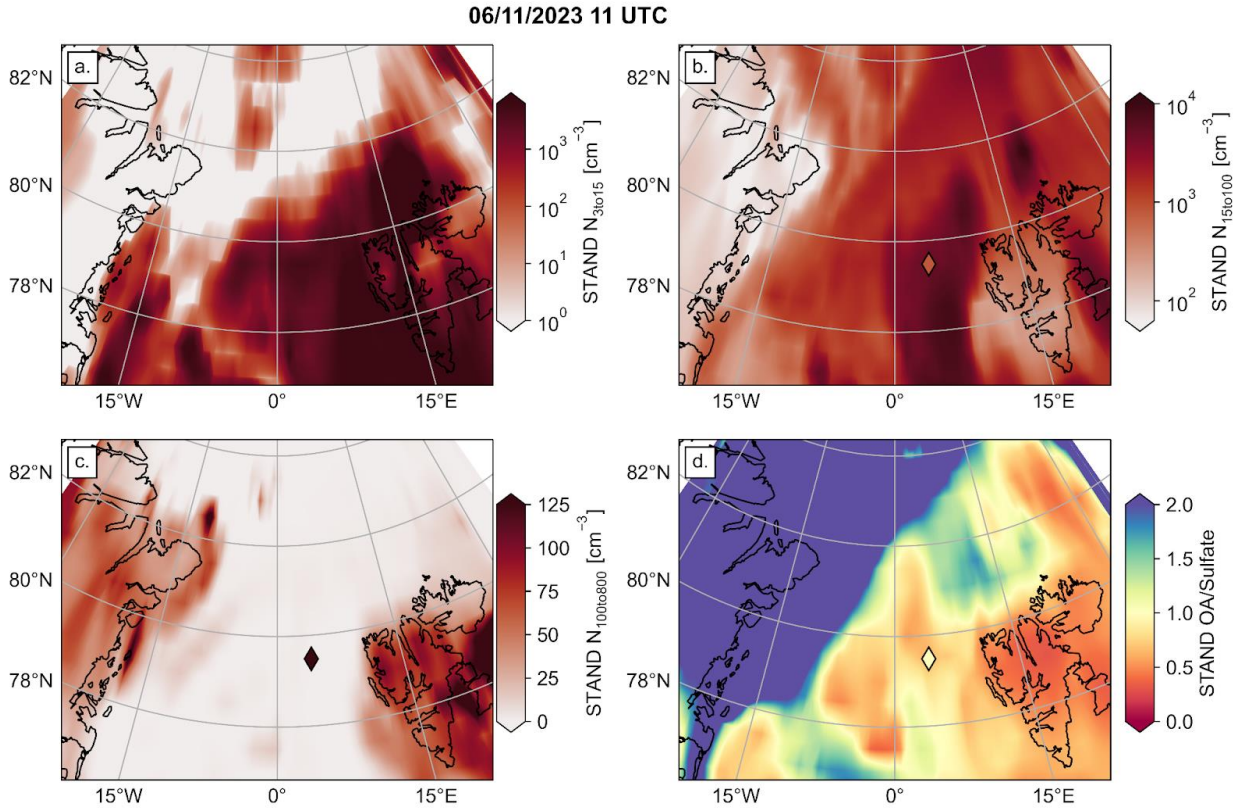

Figure 5.9: Regional maps from the STAND simulation of the (a.) N_{3to15}, (b.) $N_{15to100}$, (c.) $N_{100to800}$ number concentrations, and (d.) OA/Sulfate ratio for 06/11/2023 at 11 UTC. The diamond shows the location of ARTofMELT at this time and is colored by the observed value on the ship at this time. There were no NAIS observations at this time, so there is no diamond on the (a.) to show the observed N_{3to15}. Figure D.12 shows how these quantities change in the sensitivity simulations.

blowing snow is variable, but it makes non-negligible contributions during periods of mostly sea ice influence.

In addition to the limitation of the AMSOA emission, there are several other limitations to our study. The first limitation is that we do not use all possible nucleation mechanisms and the ones we do use have scaling assumptions. The primary nucleation mechanism not included in our study that could be influential is iodine oxoacids. Prior studies have used scaling assumptions for nucleation rates as we do here, but using them limits the ability to say for certain

the importance of different mechanisms and could result in representing NPF&G events accurately for the wrong reasons. An additional limitation is that GC-TOMAS uses the simple SOA scheme. Future updates to better consider the volatility of SOA could better capture NPF&G.

Our results highlight the importance of local emissions, SOA precursors, and NPF on the aerosol size and composition in the springtime Arctic that continue to be poorly constrained in global and regional models. Continued work on reducing biases in aerosols in the Arctic is important to understanding how the relative importance of how different aerosol processes will change in a warming climate and as emission sources change.

Chapter 6: Synthesis and Future Work

6.1 Summary

This dissertation presented an analysis of aerosol microphysics of two different systems: biomass burning and the springtime marine Arctic. Biomass burning is a major source of organic aerosol (OA) to the atmosphere, while the Arctic is a clean environment with comparatively few aerosols. Despite the large difference in concentrations, both have important influences on the role of aerosols in the climate system and represent sources of uncertainty in atmospheric models. For both biomass burning and the Arctic chapters, the representation of aerosol size and composition in the atmosphere are a common theme. OA constitutes a large fraction of the sub-micron mass in both environments; meaning the representation of primary and secondary OA processes is important to accurately simulating both environments. Both biomass burning and the Arctic are influenced by climate change and the changing relative importance of non-anthropogenic sources of aerosols. Therefore, understanding how models represent biomass burning and the marine Arctic in the present climate state is important to understanding how air quality and radiative effects of aerosols may change in the future.

The first half of the dissertation focuses on biomass burning. Chapter 2 presented a global biomass burning plume injection height (BB-PIH) modeling study. Raising the BB-PIH decreases surface $PM_{2.5}$ near biomass burning source regions, while increasing the total atmospheric burden of biomass burning aerosol leading to an increase in the cooling radiative effects of biomass burning on a global scale. On more regional scales, the placement of more smoke above high albedo surfaces, such as clouds and sea-ice, as BB-PIH increases results in an increase in warming due to the biomass burning direct radiative effect. Chapter 3 shows that the aging of wildfire smoke is influenced by the vertical placement and mixing of the smoke in a

case study of a plume sampled during FIREX-AQ using a cloud resolving model. The most concentrated portions of the smoke plume in the free troposphere have the fastest growth due to coagulation. OA evolution shows slow photochemistry and evaporation in the free troposphere are driven by the concentration and temperature gradients within the smoke plume. The results of Chapter 3 motivate the need for continued observational studies to aid in the development of parameterizations for use in models such as GC-TOMAS to represent the sub-grid processes of OA chemistry and evaporation that occur in wildfire plumes. If these parameterizations are developed and implemented into GC-TOMAS, they could alter the simulated effects of BB-PIH on biomass burning air quality and radiative effects that were shown in Chapter 2. For example, a temperature dependent parameterization to represent the slower free tropospheric evaporation of primary OA seen in Chapter 3, would act to increase the atmospheric lifetime of OA, contributing to a larger increase in the aerosol mass as a result of raising the BB-PIH than what was shown in Chapter 2. Overall, the biomass burning chapters show that the vertical distribution of smoke in the atmosphere has important effects on smoke air quality and climate impacts, and smoke plume aging.

The second half of the dissertation focuses on the springtime marine Arctic. Chapter 4 examined sources and chemistry of DMS and MeSH in the Fram Strait in May and June, 2023 during the ARTofMELT campaign. We find that including emissions of DMS/MeSH within the marginal ice zone improves the model-observation agreement atmospheric DMS/MeSH concentrations throughout the campaign. However, the model underestimate in the DMS oxidation product, DMSO, points to biases in the oxidation of DMS in the atmosphere. The biases in DMSO seem connected to model biases bromine emissions related to blowing snow and the model exclusion of snow-pack chemistry as a bromine source. Additionally, wet

deposition of DMSO in the marine low-level clouds may be too fast in the model, contributing to the model underestimate of DMSO. Since DMSO oxidizes to form MSA, which can contribute to the growth of aerosols, DMSO biases could influence the aerosol size distribution and composition that are the focus of the final chapter. The model could also be biased in the formation of SO_2 from DMS and MeSH oxidation, which could contribute to the model representation of new particle formation events discussed in the final chapter. Finally, Chapter 5 discussed the GC-TOMAS representation of aerosol size and composition during the ARTofMELT campaign. The model-observation comparisons of aerosol size and OA suggest a marine and marginal ice zone source of secondary OA (SOA) precursors, but the representation of this source in the model needs further refinement. The model updates for secondary organic aerosol precursor emissions, which were originally developed for other regions of the Arctic to improve model-observation agreement, highlight that while the Arctic is often discussed as one entity, it has variability within it. Wet deposition of aerosols in marine low-level clouds is important to explaining the variability in the accumulation mode number concentrations seen during periods of ocean influence. Throughout the campaign, the participation of low-volatility organics in new particle formation improves the agreement in the nucleation mode number concentrations. Both Arctic studies show uncertainty in wet deposition contributes to the model representation of both marine sulfur chemistry and the aerosol size distribution. Additionally, the marginal ice zone, in addition to the open ocean, is an important source region for precursors to sulfate and organic aerosols.

6.2 Future Work

The studies presented here have improved the understanding of aerosols for both wildfires and the marine Arctic with a focus on how these systems are represented in

atmospheric models. However, there are needs for continued research to further improve the understanding of aerosol sources and microphysics in both wildfire and the marine Arctic environments.

6.2.1 Open Questions About Wildfires

Vertical Variability in Smoke Plume Aging: The results of Chapter 2 showed the importance of the emission height of biomass burning, while the results of Chapter 3 showed that the evolution within a single smoke plume varies both horizontally and vertically as a result of concentration gradients influencing coagulation, SOA precursor availability, and photochemistry. However, present observations have generally focused on the evolution at single altitudes within smoke plumes. During FIREX-AQ and the California Fire Dynamics Experiment the Twin Otter Air Craft was able to sample multiple altitudes and multiple smoke ages (Carroll et al., 2024; Washenfelder et al., 2022). Additionally, we recommend a mobile laboratory with the same instrumentation as the aircraft to sample the surface of the same fires as the aircraft. These sampling methodologies could be used to understand the vertical variability in aerosol microphysics and chemistry in wildfire smoke plumes.

Complex SOA Scheme Impacts on BB-PIH Impacts: The version of GC-TOMAS used in the BB-PIH study in Chapter 2 uses the simple SOA scheme. This limitation in the representation of OA means that even if the model were run at fine enough spatial resolution to capture single plumes or if new parameterizations were developed based on the results of Chapter 3, GC-TOMAS would not be able to capture the vertical influences of temperature on the evaporation of POA and vertical variability of SOA processes within the smoke plume. In the future, updating the SOA scheme to the complex scheme could offer higher quality estimates of the impact of BB-PIH on BB OA lifetime.

Improved Methods for Accurate Plume Injection Height in Models: The impacts of BB-PIH on air quality and biomass burning radiative effects globally shown in Chapter 2 and the vertical variability in smoke aging in a single smoke plume shown in Chapter 3 motivate the need for computationally efficient and accurate estimates of BB-PIH that can be used in regional and global atmospheric models. If a complex SOA scheme is used and parameterizations for subgrid processes like coagulation and OA evaporation are improved, accurate plume injection heights with a diurnal cycle are needed to understand the implications of these updates in regional and global models. The GFAS biomass burning emissions inventory includes daily estimates of plume injection height, but they are generally biased low (Rémy et al., 2017; Walter et al., 2016). Plume rise models coupled with atmospheric models may allow for better representation of plume dynamics (Walter et al., 2016), but at a higher computational expense, which is likely already increased due to the added parameterizations needed to represent the OA evaporation/condensation and coagulation processes. Therefore, continued work on improving plume injection height in emission inventories and simulations is needed (Cheeseman et al., 2020; Chen et al., 2021b; Lyapustin et al., 2020).

6.2.2 Open Questions About the Marine Arctic

SO_2 Observations in the Marine Arctic: Measurements of SO_2 in the Arctic would be beneficial to further understanding model biases discussed in Chapters 4 and 5. SO_2 is one of the primary species formed through the oxidation of DMS and MeSH; therefore, observations of SO_2 would help to further the understanding of the biases of the DMS and MeSH oxidation scheme used in GC-TOMAS. SO_2 is oxidized to form H_2SO_4 and is an important precursor to NPF events in the atmosphere; therefore, SO_2 measurements could help to further understand the role of SO_2 on NPF events in the marine atmosphere. However, currently SO_2 observational detection

limits make it difficult to observe SO_2 in the Arctic. During the MOSAiC expedition from September 2019 to October 2020, SO_2 observations were taken onboard the *Polarstern* ice breaker as it drifted in sea ice in the Arctic Ocean (Angot et al., 2022; Boyer et al., 2024). However, only 0.6% of the SO_2 measurements during MOSAiC were above the 1 ppb detection limit of the instrument and none of the above detection limit values occurred between May and September when the DMS chemistry and NPF are most important (Angot et al., 2022; Boyer et al., 2024; Croft et al., 2016, 2021). Lower detection limit observations of SO_2 would be beneficial to understanding both sulfur chemistry and nucleation in the Arctic.

Characterization of SOA Precursors and Their Emissions: In Chapter 5, we found that there are SOA precursors that are not represented in the current standard emissions of GC-TOMAS. We were able to partially improve the model-observation agreement of OA by adding an additional fixed SOA precursor flux scaled by ocean fraction in the Arctic. The marine SOA precursor from the Arctic was found to be related to various reactive organic carbon species that were observed during ARTofMELT. The reactive organic carbon species that seemed of highest correlation were related to photolytic and biogenic processes in the ocean suggesting that variables such as chlorophyll, shortwave radiation, ocean fraction, and oceanic DMS concentration could be used as starting points to develop a more mechanistic parameterization for the flux of an Arctic marine SOA precursor. In the future, using a more mechanistic scheme for the Arctic marine SOA precursor flux could help to better capture the observed OA variability between periods of ocean, marginal ice zone, and sea ice influence.

Complex SOA Scheme Impacts: Similar to the wildfire studies, the study of aerosols in the marine Arctic would benefit from using a representation of OA that included a volatility basis set. The complex SOA scheme developed for GEOS-Chem is not currently compatible with GC-

TOMAS, but coupling the complex SOA scheme to GC-TOMAS could be done in future work. The representation of volatility of condensing material could help capture evaporation that occurs during some NPF&G events. Additionally, accurate predictions of low-volatility SOA could help to improve the representation of the role of organics in NPF and remove the biases in NPF that could exist in the version of GC-TOMAS used in Chapter 4/5 as the result of assuming a fixed percentage of SOA is low-volatility (O'Donnell et al., 2025).

Importance of Iodine to New Particle Formation: Currently, we do not have a mechanism for iodine to participate in new particle formation in GC-TOMAS. Iodic acid chemistry is not currently included in GC-TOMAS, so adding that chemistry would be the first step (He et al., 2023; Zhao et al., 2024). Once the chemistry to represent the sources and sinks of iodine oxoacids is added, iodine nucleation can be added using the nucleation rate equations for iodine oxoacids neutral and iodine oxoacids ion-induced described in Zhao et al. (2024). Adding iodine nucleation to GC-TOMAS would be beneficial to understanding the relative importance of different NPF in the marine Arctic environment.

Improved Representation of DMS/MeSH Emissions: Biases in the oceanic DMS and oceanic MeSH concentrations cause some of the biases in the representation of atmospheric sulfur chemistry. An interpolated climatology of oceanic MeSH, analogous to the Lana et al. (2011) climatology of oceanic DMS, or model estimates of oceanic MeSH for use in GC-TOMAS could improve the representation of MeSH concentrations in the atmosphere. In our studies, we used the ocean fraction to linearly scale the sea-to-air flux of DMS/MeSH within regions of partial ice cover. However, the actual influence of sea ice on the sea-to-air flux of DMS and MeSH remains uncertain.

References

Abbatt, J. P. D., Leaitch, W. R., Aliabadi, A. A., Bertram, A. K., Blanchet, J.-P., Boivin-Rioux, A., Bozem, H., Burkart, J., Chang, R. Y. W., Charette, J., Chaubey, J. P., Christensen, R. J., Cirisan, A., Collins, D. B., Croft, B., Dionne, J., Evans, G. J., Fletcher, C. G., Galí, M., Ghahreman, R., Girard, E., Gong, W., Gosselin, M., Gourdal, M., Hanna, S. J., Hayashida, H., Herber, A. B., Hesaraki, S., Hoor, P., Huang, L., Hussherr, R., Irish, V. E., Keita, S. A., Kodros, J. K., Köllner, F., Kolonjari, F., Kunkel, D., Ladino, L. A., Law, K., Levasseur, M., Libois, Q., Liggio, J., Lizotte, M., Macdonald, K. M., Mahmood, R., Martin, R. V., Mason, R. H., Miller, L. A., Moravek, A., Mortenson, E., Mungall, E. L., Murphy, J. G., Namazi, M., Norman, A.-L., O'Neill, N. T., Pierce, J. R., Russell, L. M., Schneider, J., Schulz, H., Sharma, S., Si, M., Staebler, R. M., Steiner, N. S., Thomas, J. L., von Salzen, K., Wentzell, J. J. B., Willis, M. D., Wentworth, G. R., Xu, J.-W., and Yakobi-Hancock, J. D.: Overview paper: New insights into aerosol and climate in the Arctic, Atmospheric Chemistry and Physics, 19, 2527–2560, https://doi.org/10.5194/acp-19-2527-2019, 2019.

Abdul-Razzak, H. and Ghan, S. J.: A parameterization of aerosol activation 3. Sectional representation, Journal of Geophysical Research: Atmospheres, 107, AAC 1-1-AAC 1-6, https://doi.org/10.1029/2001JD000483, 2002.

AboEl-Fetouh, Y., O'Neill, N. T., Kodros, J. K., Pierce, J. R., Lu, H., Ranjbar, K., and Xian, P.: Seasonal comparisons of GEOS-Chem-TOMAS (GCT) simulations with AERONET-inversion retrievals over sites in the North American and European Arctic, Atmospheric Environment, 271, 118852, https://doi.org/10.1016/j.atmosenv.2021.118852, 2022.

Adachi, K., Dibb, J. E., Scheuer, E., Katich, J. M., Schwarz, J. P., Perring, A. E., Mediavilla, B., Guo, H., Campuzano-Jost, P., Jimenez, J. L., Crawford, J., Soja, A. J., Oshima, N., Kajino, M., Kinase, T., Kleinman, L., Sedlacek III, A. J., Yokelson, R. J., and Buseck, P. R.: Fine Ash-Bearing Particles as a Major Aerosol Component in Biomass Burning Smoke, Journal of Geophysical Research: Atmospheres, 127, e2021JD035657, https://doi.org/10.1029/2021JD035657, 2022.

Adams, P. J. and Seinfeld, J. H.: Predicting global aerosol size distributions in general circulation models, Journal of Geophysical Research: Atmospheres, 107, AAC 4-1-AAC 4-23, https://doi.org/10.1029/2001JD001010, 2002.

Akagi, S. K., Yokelson, R. J., Wiedinmyer, C., Alvarado, M. J., Reid, J. S., Karl, T., Crounse, J. D., and Wennberg, P. O.: Emission factors for open and domestic biomass burning for use in atmospheric models, Atmospheric Chemistry and Physics, 11, 4039–4072, https://doi.org/10.5194/acp-11-4039-2011, 2011.

Akagi, S. K., Craven, J. S., Taylor, J. W., McMeeking, G. R., Yokelson, R. J., Burling, I. R., Urbanski, S. P., Wold, C. E., Seinfeld, J. H., Coe, H., Alvarado, M. J., and Weise, D. R.: Evolution of trace gases and particles emitted by a chaparral fire in California, Atmospheric Chemistry and Physics, 12, 1397–1421, https://doi.org/10.5194/acp-12-1397-2012, 2012.

Akherati, A., He, Y., Coggon, M. M., Koss, A. R., Hodshire, A. L., Sekimoto, K., Warneke, C., de Gouw, J., Yee, L., Seinfeld, J. H., Onasch, T. B., Herndon, S. C., Knighton, W. B., Cappa, C. D., Kleeman, M. J., Lim, C. Y., Kroll, J. H., Pierce, J. R., and Jathar, S. H.: Oxygenated Aromatic Compounds are Important Precursors of Secondary Organic Aerosol in Biomass-Burning Emissions, Environ. Sci. Technol., 54, 8568–8579, https://doi.org/10.1021/acs.est.0c01345, 2020.

Akherati, A., He, Y., A. Garofalo, L., L. Hodshire, A., K. Farmer, D., M. Kreidenweis, S., Permar, W., Hu, L., V. Fischer, E., N. Jen, C., H. Goldstein, A., T. Levin, E. J., J. DeMott, P., L. Campos, T., Flocke, F., M. Reeves, J., W. Toohey, D., R. Pierce, J., and H. Jathar, S.: Dilution and photooxidation driven processes explain the evolution of organic aerosol in wildfire plumes, Environmental Science: Atmospheres, https://doi.org/10.1039/D1EA00082A, 2022.

Albrecht, B. A.: Aerosols, Cloud Microphysics, and Fractional Cloudiness, Science, https://doi.org/10.1126/science.245.4923.1227, 1989.

Allan, J. D., Williams, P. I., Najera, J., Whitehead, J. D., Flynn, M. J., Taylor, J. W., Liu, D., Darbyshire, E., Carpenter, L. J., Chance, R., Andrews, S. J., Hackenberg, S. C., and McFiggans, G.: Iodine observed in new particle formation events in the Arctic atmosphere during ACCACIA, Atmospheric Chemistry and Physics, 15, 5599–5609, https://doi.org/10.5194/acp-15-5599-2015, 2015.

Alonso-Blanco, E., Calvo, A. I., Pont, V., Mallet, M., Fraile, R., and Castro, A.: Impact of Biomass Burning on Aerosol Size Distribution, Aerosol Optical Properties and Associated Radiative Forcing, Aerosol Air Qual. Res., 14, 708–724, https://doi.org/10.4209/aaqr.2013.05.0163, 2014.

Alvarado, M. J. and Prinn, R. G.: Formation of ozone and growth of aerosols in young smoke plumes from biomass burning: 1. Lagrangian parcel studies, Journal of Geophysical Research: Atmospheres, 114, https://doi.org/10.1029/2008JD011144, 2009.

Alvarado, M. J., Lonsdale, C. R., Yokelson, R. J., Akagi, S. K., Coe, H., Craven, J. S., Fischer, E. V., McMeeking, G. R., Seinfeld, J. H., Soni, T., Taylor, J. W., Weise, D. R., and Wold, C. E.: Investigating the links between ozone and organic aerosol chemistry in a biomass burning plume from a prescribed fire in California chaparral, Atmospheric Chemistry and Physics, 15, 6667–6688, https://doi.org/10.5194/acp-15-6667-2015, 2015.

Alvarado, M. J., Lonsdale, C. R., Macintyre, H. L., Bian, H., Chin, M., Ridley, D. A., Heald, C. L., Thornhill, K. L., Anderson, B. E., Cubison, M. J., Jimenez, J. L., Kondo, Y., Sahu, L. K., Dibb, J. E., and Wang, C.: Evaluating model parameterizations of submicron aerosol scattering and absorption with in situ data from ARCTAS 2008, Atmospheric Chemistry and Physics, 16, 9435–9455, https://doi.org/10.5194/acp-16-9435-2016, 2016.

Andreae, M. O.: Ocean-atmosphere interactions in the global biogeochemical sulfur cycle, Marine Chemistry, 30, 1–29, https://doi.org/10.1016/0304-4203(90)90059-L, 1990.

Andreae, M. O.: Emission of trace gases and aerosols from biomass burning – an updated assessment, Atmospheric Chemistry and Physics, 19, 8523–8546, https://doi.org/10.5194/acp-19-8523-2019, 2019.

Andreae, M. O. and Merlet, P.: Emission of trace gases and aerosols from biomass burning, Global Biogeochemical Cycles, 15, 955–966, https://doi.org/10.1029/2000GB001382, 2001.

Angot, H., Blomquist, B., Howard, D., Archer, S., Bariteau, L., Beck, I., Boyer, M., Crotwell, M., Helmig, D., Hueber, J., Jacobi, H.-W., Jokinen, T., Kulmala, M., Lan, X., Laurila, T., Madronich, M., Neff, D., Petäjä, T., Posman, K., Quéléver, L., Shupe, M. D., Vimont, I., and Schmale, J.: Year-round trace gas measurements in the central Arctic during the MOSAiC expedition, Sci Data, 9, 723, https://doi.org/10.1038/s41597-022-01769-6, 2022.

Baccarini, A., Karlsson, L., Dommen, J., Duplessis, P., Vüllers, J., Brooks, I. M., Saiz-Lopez, A., Salter, M., Tjernström, M., Baltensperger, U., Zieger, P., and Schmale, J.: Frequent new particle formation over the high Arctic pack ice by enhanced iodine emissions, Nat Commun, 11, 4924, https://doi.org/10.1038/s41467-020-18551-0, 2020.

Bahreini, R., Keywood, M. D., Ng, N. L., Varutbangkul, V., Gao, S., Flagan, R. C., Seinfeld, J. H., Worsnop, D. R., and Jimenez, J. L.: Measurements of Secondary Organic Aerosol from Oxidation of Cycloalkenes, Terpenes, and m-Xylene Using an Aerodyne Aerosol Mass Spectrometer, Environ. Sci. Technol., 39, 5674–5688, https://doi.org/10.1021/es048061a, 2005.

Bahreini, R., Ervens, B., Middlebrook, A. M., Warneke, C., de Gouw, J. A., DeCarlo, P. F., Jimenez, J. L., Brock, C. A., Neuman, J. A., Ryerson, T. B., Stark, H., Atlas, E., Brioude, J., Fried, A., Holloway, J. S., Peischl, J., Richter, D., Walega, J., Weibring, P., Wollny, A. G., and Fehsenfeld, F. C.: Organic aerosol formation in urban and industrial plumes near Houston and Dallas, Texas, Journal of Geophysical Research: Atmospheres, 114, https://doi.org/10.1029/2008JD011493, 2009.

Bais, A. F., Madronich, S., Crawford, J., Hall, S. R., Mayer, B., van Weele, M., Lenoble, J., Calvert, J. G., Cantrell, C. A., Shetter, R. E., Hofzumahaus, A., Koepke, P., Monks, P. S., Frost, G., McKenzie, R., Krotkov, N., Kylling, A., Swartz, W. H., Lloyd, S., Pfister, G., Martin, T. J., Roeth, E.-P., Griffioen, E., Ruggaber, A., Krol, M., Kraus, A., Edwards, G. D., Mueller, M., Lefer, B. L., Johnston, P., Schwander, H., Flittner, D., Gardiner, B. G., Barrick, J., and Schmitt, R.: International Photolysis Frequency Measurement and Model Intercomparison (IPMMI): Spectral actinic solar flux measurements and modeling, Journal of Geophysical Research: Atmospheres, 108, https://doi.org/10.1029/2002JD002891, 2003.

Barnes, I., Hjorth, J., and Mihalopoulos, N.: Dimethyl Sulfide and Dimethyl Sulfoxide and Their Oxidation in the Atmosphere, Chem. Rev., 106, 940–975, https://doi.org/10.1021/cr020529+, 2006.

Barrett, T. E., Robinson, E. M., Usenko, S., and Sheesley, R. J.: Source Contributions to Wintertime Elemental and Organic Carbon in the Western Arctic Based on Radiocarbon and Tracer Apportionment, Environ. Sci. Technol., 49, 11631–11639, https://doi.org/10.1021/acs.est.5b03081, 2015.

Bates, T. S., Lamb, B. K., Guenther, A., Dignon, J., and Stoiber, R. E.: Sulfur emissions to the atmosphere from natural sourees, J Atmos Chem, 14, 315–337, https://doi.org/10.1007/BF00115242, 1992.

Beck, L. J., Sarnela, N., Junninen, H., Hoppe, C. J. M., Garmash, O., Bianchi, F., Riva, M., Rose, C., Peräkylä, O., Wimmer, D., Kausiala, O., Jokinen, T., Ahonen, L., Mikkilä, J., Hakala, J., He, X.-C., Kontkanen, J., Wolf, K. K. E., Cappelletti, D., Mazzola, M., Traversi, R., Petroselli, C., Viola, A. P., Vitale, V., Lange, R., Massling, A., Nøjgaard, J. K., Krejci, R., Karlsson, L., Zieger, P., Jang, S., Lee, K., Vakkari, V., Lampilahti, J., Thakur, R. C., Leino, K., Kangasluoma, J., Duplissy, E.-M., Siivola, E., Marbouti, M., Tham, Y. J., Saiz-Lopez, A., Petäjä, T., Ehn, M., Worsnop, D. R., Skov, H., Kulmala, M., Kerminen, V.-M., and Sipilä, M.: Differing Mechanisms of New Particle Formation at Two Arctic Sites, Geophysical Research Letters, 48, e2020GL091334, https://doi.org/10.1029/2020GL091334, 2021.

Bellouin, N., Quaas, J., Gryspeerdt, E., Kinne, S., Stier, P., Watson-Parris, D., Boucher, O., Carslaw, K. S., Christensen, M., Daniau, A.-L., Dufresne, J.-L., Feingold, G., Fiedler, S., Forster, P., Gettelman, A., Haywood, J. M., Lohmann, U., Malavelle, F., Mauritsen, T., McCoy, D. T., Myhre, G., Mülmenstädt, J., Neubauer, D., Possner, A., Rugenstein, M., Sato, Y., Schulz, M., Schwartz, S. E., Sourdeval, O., Storelvmo, T., Toll, V., Winker, D., and Stevens, B.: Bounding Global Aerosol Radiative Forcing of Climate Change, Reviews of Geophysics, 58, e2019RG000660, https://doi.org/10.1029/2019RG000660, 2020.

Bian, Q., Jathar, S. H., Kodros, J. K., Barsanti, K. C., Hatch, L. E., May, A. A., Kreidenweis, S. M., and Pierce, J. R.: Secondary organic aerosol formation in biomass-burning plumes: theoretical analysis of lab studies and ambient plumes, Atmospheric Chemistry and Physics, 17, 5459–5475, https://doi.org/10.5194/acp-17-5459-2017, 2017.

Bianchi, F., Kurtén, T., Riva, M., Mohr, C., Rissanen, M. P., Roldin, P., Berndt, T., Crounse, J. D., Wennberg, P. O., Mentel, T. F., Wildt, J., Junninen, H., Jokinen, T., Kulmala, M., Worsnop, D. R., Thornton, J. A., Donahue, N., Kjaergaard, H. G., and Ehn, M.: Highly Oxygenated Organic Molecules (HOM) from Gas-Phase Autoxidation Involving Peroxy Radicals: A Key Contributor to Atmospheric Aerosol, Chem. Rev., 119, 3472–3509, https://doi.org/10.1021/acs.chemrev.8b00395, 2019.

Bigdeli, A., Hara, T., Loose, B., and Nguyen, A. T.: Wave Attenuation and Gas Exchange Velocity in Marginal Sea Ice Zone, Journal of Geophysical Research: Oceans, 123, 2293–2304, https://doi.org/10.1002/2017JC013380, 2018.

Bilsback, K. R., Kerry, D., Croft, B., Ford, B., Jathar, S. H., Carter, E., Martin, R. V., and Pierce, J. R.: Beyond SOx reductions from shipping: assessing the impact of NOx and

carbonaceous-particle controls on human health and climate, Environ. Res. Lett., 15, 124046, https://doi.org/10.1088/1748-9326/abc718, 2020a.

Bilsback, K. R., Baumgartner, J., Cheeseman, M., Ford, B., Kodros, J. K., Li, X., Ramnarine, E., Tao, S., Zhang, Y., Carter, E., and Pierce, J. R.: Estimated Aerosol Health and Radiative Effects of the Residential Coal Ban in the Beijing-Tianjin-Hebei Region of China, Aerosol Air Qual. Res., 20, 2332–2346, https://doi.org/10.4209/aaqr.2019.11.0565, 2020b.

Bilsback, K. R., He, Y., Cappa, C. D., Chang, R. Y.-W., Croft, B., Martin, R. V., Ng, N. L., Seinfeld, J. H., Pierce, J. R., and Jathar, S. H.: Vapors Are Lost to Walls, Not to Particles on the Wall: Artifact-Corrected Parameters from Chamber Experiments and Implications for Global Secondary Organic Aerosol, Environ. Sci. Technol., 57, 53–63, https://doi.org/10.1021/acs.est.2c03967, 2023.

Bohren, C. F. and Huffman, D. R.: Absorption and Scattering of Light by Small Particles, John Wiley & Sons, 547 pp., 2008.

Bond, T. C., Habib, G., and Bergstrom, R. W.: Limitations in the enhancement of visible light absorption due to mixing state, Journal of Geophysical Research: Atmospheres, 111, https://doi.org/10.1029/2006JD007315, 2006.

Bond, T. C., Doherty, S. J., Fahey, D. W., Forster, P. M., Berntsen, T., DeAngelo, B. J., Flanner, M. G., Ghan, S., Kärcher, B., Koch, D., Kinne, S., Kondo, Y., Quinn, P. K., Sarofim, M. C., Schultz, M. G., Schulz, M., Venkataraman, C., Zhang, H., Zhang, S., Bellouin, N., Guttikunda, S. K., Hopke, P. K., Jacobson, M. Z., Kaiser, J. W., Klimont, Z., Lohmann, U., Schwarz, J. P., Shindell, D., Storelvmo, T., Warren, S. G., and Zender, C. S.: Bounding the role of black carbon in the climate system: A scientific assessment, Journal of Geophysical Research: Atmospheres, 118, 5380–5552, https://doi.org/10.1002/jgrd.50171, 2013.

Bork, N., Elm, J., Olenius, T., and Vehkamäki, H.: Methane sulfonic acid-enhanced formation of molecular clusters of sulfuric acid and dimethyl amine, Atmospheric Chemistry and Physics, 14, 12023–12030, https://doi.org/10.5194/acp-14-12023-2014, 2014.

Boucher, O., Randall, D. A., Artaxo, P., Bretherton, C., Feingold, G., Foster, P., Kerminen, V.-M., Kondo, Y., Liao, H., Rasch, P. J., Satheesh, S. K., Sherwood, S., Stevens, B., and Zhang, X. Y.: Clouds and Aerosols, in: Climate Change 2013 – The Physical Science Basis. Contribution of Working Group I to the Fifth Assessment Report of the Intergovernmental Panel on Climate Change, Cambridge University Press, 571–657, 2013.

Bourgeois, I., Peischl, J., Neuman, J. A., Brown, S. S., Allen, H. M., Campuzano-Jost, P., Coggon, M. M., DiGangi, J. P., Diskin, G. S., Gilman, J. B., Gkatzelis, G. I., Guo, H., Halliday, H. A., Hanisco, T. F., Holmes, C. D., Huey, L. G., Jimenez, J. L., Lamplugh, A. D., Lee, Y. R., Lindaas, J., Moore, R. H., Nault, B. A., Nowak, J. B., Pagonis, D., Rickly, P. S., Robinson, M. A., Rollins, A. W., Selimovic, V., St. Clair, J. M., Tanner, D., Vasquez, K. T., Veres, P. R., Warneke, C., Wennberg, P. O., Washenfelder, R. A., Wiggins, E. B.,

Womack, C. C., Xu, L., Zarzana, K. J., and Ryerson, T. B.: Comparison of airborne measurements of NO, NO_2, HONO, NO_y, and CO during FIREX-AQ, Atmospheric Measurement Techniques, 15, 4901–4930, https://doi.org/10.5194/amt-15-4901-2022, 2022.

Boy, J., Rollenbeck, R., Valarezo, C., and Wilcke, W.: Amazonian biomass burning-derived acid and nutrient deposition in the north Andean montane forest of Ecuador, Global Biogeochemical Cycles, 22, https://doi.org/10.1029/2007GB003158, 2008.

Boyer, M., Aliaga, D., Pernov, J. B., Angot, H., Quéléver, L. L. J., Dada, L., Heutte, B., Dall'Osto, M., Beddows, D. C. S., Brasseur, Z., Beck, I., Bucci, S., Duetsch, M., Stohl, A., Laurila, T., Asmi, E., Massling, A., Thomas, D. C., Nøjgaard, J. K., Chan, T., Sharma, S., Tunved, P., Krejci, R., Hansson, H. C., Bianchi, F., Lehtipalo, K., Wiedensohler, A., Weinhold, K., Kulmala, M., Petäjä, T., Sipilä, M., Schmale, J., and Jokinen, T.: A full year of aerosol size distribution data from the central Arctic under an extreme positive Arctic Oscillation: insights from the Multidisciplinary drifting Observatory for the Study of Arctic Climate (MOSAiC) expedition, Atmospheric Chemistry and Physics, 23, 389–415, https://doi.org/10.5194/acp-23-389-2023, 2023.

Boyer, M., Aliaga, D., Quéléver, L. L. J., Bucci, S., Angot, H., Dada, L., Heutte, B., Beck, L., Duetsch, M., Stohl, A., Beck, I., Laurila, T., Sarnela, N., Thakur, R. C., Miljevic, B., Kulmala, M., Petäjä, T., Sipilä, M., Schmale, J., and Jokinen, T.: The annual cycle and sources of relevant aerosol precursor vapors in the central Arctic during the MOSAiC expedition, Atmospheric Chemistry and Physics, 24, 12595–12621, https://doi.org/10.5194/acp-24-12595-2024, 2024.

Bozem, H., Hoor, P., Kunkel, D., Köllner, F., Schneider, J., Herber, A., Schulz, H., Leaitch, W. R., Aliabadi, A. A., Willis, M. D., Burkart, J., and Abbatt, J. P. D.: Characterization of transport regimes and the polar dome during Arctic spring and summer using in situ aircraft measurements, Atmospheric Chemistry and Physics, 19, 15049–15071, https://doi.org/10.5194/acp-19-15049-2019, 2019.

Browse, J., Carslaw, K. S., Arnold, S. R., Pringle, K., and Boucher, O.: The scavenging processes controlling the seasonal cycle in Arctic sulphate and black carbon aerosol, Atmospheric Chemistry and Physics, 12, 6775–6798, https://doi.org/10.5194/acp-12-6775-2012, 2012.

Browse, J., Carslaw, K. S., Mann, G. W., Birch, C. E., Arnold, S. R., and Leck, C.: The complex response of Arctic aerosol to sea-ice retreat, Atmospheric Chemistry and Physics, 14, 7543–7557, https://doi.org/10.5194/acp-14-7543-2014, 2014.

Burkart, J., Hodshire, A. L., Mungall, E. L., Pierce, J. R., Collins, D. B., Ladino, L. A., Lee, A. K. Y., Irish, V., Wentzell, J. J. B., Liggio, J., Papakyriakou, T., Murphy, J., and Abbatt, J.: Organic Condensation and Particle Growth to CCN Sizes in the Summertime Marine Arctic Is Driven by Materials More Semivolatile Than at Continental Sites, Geophysical Research Letters, 44, 10,725-10,734, https://doi.org/10.1002/2017GL075671, 2017a.

Burkart, J., Willis, M. D., Bozem, H., Thomas, J. L., Law, K., Hoor, P., Aliabadi, A. A., Köllner, F., Schneider, J., Herber, A., Abbatt, J. P. D., and Leaitch, W. R.: Summertime

observations of elevated levels of ultrafine particles in the high Arctic marine boundary layer, Atmospheric Chemistry and Physics, 17, 5515–5535, https://doi.org/10.5194/acp-17-5515-2017, 2017b.

Burke, M., Childs, M. L., de la Cuesta, B., Qiu, M., Li, J., Gould, C. F., Heft-Neal, S., and Wara, M.: The contribution of wildfire to PM2.5 trends in the USA, Nature, 622, 761–766, https://doi.org/10.1038/s41586-023-06522-6, 2023.

Butkovskaya, N. I. and Setser, D. W.: Product Branching Fractions and Kinetic Isotope Effects for the Reactions of OH and OD Radicals with CH3SH and CH3SD, J. Phys. Chem. A, 103, 6921–6929, https://doi.org/10.1021/jp9914828, 1999.

Capes, G., Johnson, B., McFiggans, G., Williams, P. I., Haywood, J., and Coe, H.: Aging of biomass burning aerosols over West Africa: Aircraft measurements of chemical composition, microphysical properties, and emission ratios, Journal of Geophysical Research: Atmospheres, 113, https://doi.org/10.1029/2008JD009845, 2008.

Carpenter, L. J. and Nightingale, P. D.: Chemistry and Release of Gases from the Surface Ocean, Chem. Rev., 115, 4015–4034, https://doi.org/10.1021/cr5007123, 2015.

Carpenter, L. J., Archer, S. D., and Beale, R.: Ocean-atmosphere trace gas exchange, Chem. Soc. Rev., 41, 6473–6506, https://doi.org/10.1039/C2CS35121H, 2012.

Carrico, C. M., Petters, M. D., Kreidenweis, S. M., Collett Jr., J. L., Engling, G., and Malm, W. C.: Aerosol hygroscopicity and cloud droplet activation of extracts of filters from biomass burning experiments, Journal of Geophysical Research: Atmospheres, 113, https://doi.org/10.1029/2007JD009274, 2008.

Carroll, B. J., Brewer, W. A., Strobach, E., Lareau, N., Brown, S. S., Valero, M. M., Kochanski, A., Clements, C. B., Kahn, R., Noyes, K. T. J., Makowiecki, A., Holloway, M. W., Zucker, M., Clough, K., Drucker, J., Zuraski, K., Peischl, J., McCarty, B., Marchbanks, R., Sandberg, S., Baidar, S., Pichugina, Y. L., Banta, R. M., Wang, S., Klofas, A., Winters, B., and Salas, T.: Measuring Coupled Fire–Atmosphere Dynamics: The California Fire Dynamics Experiment (CalFiDE), https://doi.org/10.1175/BAMS-D-23-0012.1, 2024.

Carslaw, K. S., Lee, L. A., Reddington, C. L., Pringle, K. J., Rap, A., Forster, P. M., Mann, G. W., Spracklen, D. V., Woodhouse, M. T., Regayre, L. A., and Pierce, J. R.: Large contribution of natural aerosols to uncertainty in indirect forcing, Nature, 503, 67–71, https://doi.org/10.1038/nature12674, 2013.

Cascio, W. E.: Wildland fire smoke and human health, Science of The Total Environment, 624, 586–595, https://doi.org/10.1016/j.scitotenv.2017.12.086, 2018.

Cesana, G., Kay, J. E., Chepfer, H., English, J. M., and de Boer, G.: Ubiquitous low-level liquid-containing Arctic clouds: New observations and climate model constraints from CALIPSO-GOCCP, Geophysical Research Letters, 39, https://doi.org/10.1029/2012GL053385, 2012.

Chang, D. Y., Yoon, J., Lelieveld, J., Park, S. K., Yum, S. S., Kim, J., and Jeong, S.: Direct radiative forcing of biomass burning aerosols from the extensive Australian wildfires in 2019–2020, Environ. Res. Lett., 16, 044041, https://doi.org/10.1088/1748-9326/abecfe, 2021.

Charan, S. M., Huang, Y., and Seinfeld, J. H.: Computational Simulation of Secondary Organic Aerosol Formation in Laboratory Chambers, Chem. Rev., 119, 11912–11944, https://doi.org/10.1021/acs.chemrev.9b00358, 2019.

Charlson, R. J., Lovelock, J. E., Andreae, M. O., and Warren, S. G.: Oceanic phytoplankton, atmospheric sulphur, cloud albedo and climate, Nature, 326, 655–661, https://doi.org/10.1038/326655a0, 1987.

Charlson, R. J., Langner, J., Rodhe, H., Leovy, C. B., and Warren, S. G.: Perturbation of the northern hemisphere radiative balance by backscattering from anthropogenic sulfate aerosols, Tellus A: Dynamic Meteorology and Oceanography, 43, 152–163, https://doi.org/10.3402/tellusa.v43i4.11944, 1991.

Cheeseman, M., Ford, B., Volckens, J., Lyapustin, A., and Pierce, J. R.: The Relationship Between MAIAC Smoke Plume Heights and Surface PM, Geophysical Research Letters, 47, e2020GL088949, https://doi.org/10.1029/2020GL088949, 2020.

Chen, J., Li, C., Ristovski, Z., Milic, A., Gu, Y., Islam, M. S., Wang, S., Hao, J., Zhang, H., He, C., Guo, H., Fu, H., Miljevic, B., Morawska, L., Thai, P., Lam, Y. F., Pereira, G., Ding, A., Huang, X., and Dumka, U. C.: A review of biomass burning: Emissions and impacts on air quality, health and climate in China, Science of The Total Environment, 579, 1000–1034, https://doi.org/10.1016/j.scitotenv.2016.11.025, 2017.

Chen, J., Berndt, T., Møller, K. H., Lane, J. R., and Kjaergaard, H. G.: Atmospheric Fate of the CH3SOO Radical from the CH3S + O2 Equilibrium, J. Phys. Chem. A, 125, 8933–8941, https://doi.org/10.1021/acs.jpca.1c06900, 2021a.

Chen, Q., Geng, L., Schmidt, J. A., Xie, Z., Kang, H., Dachs, J., Cole-Dai, J., Schauer, A. J., Camp, M. G., and Alexander, B.: Isotopic constraints on the role of hypohalous acids in sulfate aerosol formation in the remote marine boundary layer, Atmospheric Chemistry and Physics, 16, 11433–11450, https://doi.org/10.5194/acp-16-11433-2016, 2016.

Chen, Q., Sherwen, T., Evans, M., and Alexander, B.: DMS oxidation and sulfur aerosol formation in the marine troposphere: a focus on reactive halogen and multiphase chemistry, Atmospheric Chemistry and Physics, 18, 13617–13637, https://doi.org/10.5194/acp-18-13617-2018, 2018.

Chen, X., Wang, J., Xu, X., Zhou, M., Zhang, H., Castro Garcia, L., Colarco, P. R., Janz, S. J., Yorks, J., McGill, M., Reid, J. S., de Graaf, M., and Kondragunta, S.: First retrieval of absorbing aerosol height over dark target using TROPOMI oxygen B band: Algorithm development and application for surface particulate matter estimates, Remote Sensing of Environment, 265, 112674, https://doi.org/10.1016/j.rse.2021.112674, 2021b.

Childs, M. L., Li, J., Wen, J., Heft-Neal, S., Driscoll, A., Wang, S., Gould, C. F., Qiu, M., Burney, J., and Burke, M.: Daily Local-Level Estimates of Ambient Wildfire Smoke PM2.5 for the Contiguous US, Environ. Sci. Technol., 56, 13607–13621, https://doi.org/10.1021/acs.est.2c02934, 2022.

Christian, K. E., Brune, W. H., and Mao, J.: Global sensitivity analysis of the GEOS-Chem chemical transport model: ozone and hydrogen oxides during ARCTAS (2008), Atmospheric Chemistry and Physics, 17, 3769–3784, https://doi.org/10.5194/acp-17-3769-2017, 2017.

Christian, K. E., Brune, W. H., Mao, J., and Ren, X.: Global sensitivity analysis of GEOS-Chem modeled ozone and hydrogen oxides during the INTEX campaigns, Atmospheric Chemistry and Physics, 18, 2443–2460, https://doi.org/10.5194/acp-18-2443-2018, 2018.

Clement, A. C., Burgman, R., and Norris, J. R.: Observational and Model Evidence for Positive Low-Level Cloud Feedback, Science, 325, 460–464, https://doi.org/10.1126/science.1171255, 2009.

Covert, D. S., Wiedensohler ,Alfred, Aalto ,Pasi, Heintzenberg ,Jost, Mcmurry ,Peter H., and and Leck, C.: Aerosol number size distributions from 3 to 500 nm diameter in the arctic marine boundary layer during summer and autumn, Tellus B: Chemical and Physical Meteorology, 48, 197–212, https://doi.org/10.3402/tellusb.v48i2.15886, 1996.

Croft, B., Martin, R. V., Leaitch, W. R., Tunved, P., Breider, T. J., D'Andrea, S. D., and Pierce, J. R.: Processes controlling the annual cycle of Arctic aerosol number and size distributions, Atmospheric Chemistry and Physics, 16, 3665–3682, https://doi.org/10.5194/acp-16-3665-2016, 2016.

Croft, B., Martin, R. V., Leaitch, W. R., Burkart, J., Chang, R. Y.-W., Collins, D. B., Hayes, P. L., Hodshire, A. L., Huang, L., Kodros, J. K., Moravek, A., Mungall, E. L., Murphy, J. G., Sharma, S., Tremblay, S., Wentworth, G. R., Willis, M. D., Abbatt, J. P. D., and Pierce, J. R.: Arctic marine secondary organic aerosol contributes significantly to summertime particle size distributions in the Canadian Arctic Archipelago, Atmospheric Chemistry and Physics, 19, 2787–2812, https://doi.org/10.5194/acp-19-2787-2019, 2019.

Croft, B., Martin, R. V., Moore, R. H., Ziemba, L. D., Crosbie, E. C., Liu, H., Russell, L. M., Saliba, G., Wisthaler, A., Müller, M., Schiller, A., Galí, M., Chang, R. Y.-W., McDuffie, E. E., Bilsback, K. R., and Pierce, J. R.: Factors controlling marine aerosol size distributions and their climate effects over the northwest Atlantic Ocean region, Atmospheric Chemistry and Physics, 21, 1889–1916, https://doi.org/10.5194/acp-21-1889-2021, 2021.

Cubison, M. J., Ortega, A. M., Hayes, P. L., Farmer, D. K., Day, D., Lechner, M. J., Brune, W. H., Apel, E., Diskin, G. S., Fisher, J. A., Fuelberg, H. E., Hecobian, A., Knapp, D. J., Mikoviny, T., Riemer, D., Sachse, G. W., Sessions, W., Weber, R. J., Weinheimer, A. J., Wisthaler, A., and Jimenez, J. L.: Effects of aging on organic aerosol from open biomass burning smoke in aircraft and laboratory studies, Atmospheric Chemistry and Physics, 11, 12049–12064, https://doi.org/10.5194/acp-11-12049-2011, 2011.

Dadashazar, H., Ma, L., and Sorooshian, A.: Sources of pollution and interrelationships between aerosol and precipitation chemistry at a central California site, Science of The Total Environment, 651, 1776–1787, https://doi.org/10.1016/j.scitotenv.2018.10.086, 2019.

Dall´Osto, M., Simo, R., Harrison, R. M., Beddows, D. C. S., Saiz-Lopez, A., Lange, R., Skov, H., Nøjgaard, J. K., Nielsen, I. E., and Massling, A.: Abiotic and biotic sources influencing spring new particle formation in North East Greenland, Atmospheric Environment, 190, 126–134, https://doi.org/10.1016/j.atmosenv.2018.07.019, 2018.

Damoah, R., Spichtinger, N., Forster, C., James, P., Mattis, I., Wandinger, U., Beirle, S., Wagner, T., and Stohl, A.: Around the world in 17 days - hemispheric-scale transport of forest fire smoke from Russia in May 2003, Atmospheric Chemistry and Physics, 4, 1311–1321, https://doi.org/10.5194/acp-4-1311-2004, 2004.

Daniau, A.-L., Bartlein, P. J., Harrison, S. P., Prentice, I. C., Brewer, S., Friedlingstein, P., Harrison-Prentice, T. I., Inoue, J., Izumi, K., Marlon, J. R., Mooney, S., Power, M. J., Stevenson, J., Tinner, W., Andrič, M., Atanassova, J., Behling, H., Black, M., Blarquez, O., Brown, K. J., Carcaillet, C., Colhoun, E. A., Colombaroli, D., Davis, B. a. S., D'Costa, D., Dodson, J., Dupont, L., Eshetu, Z., Gavin, D. G., Genries, A., Haberle, S., Hallett, D. J., Hope, G., Horn, S. P., Kassa, T. G., Katamura, F., Kennedy, L. M., Kershaw, P., Krivonogov, S., Long, C., Magri, D., Marinova, E., McKenzie, G. M., Moreno, P. I., Moss, P., Neumann, F. H., Norström, E., Paitre, C., Rius, D., Roberts, N., Robinson, G. S., Sasaki, N., Scott, L., Takahara, H., Terwilliger, V., Thevenon, F., Turner, R., Valsecchi, V. G., Vannière, B., Walsh, M., Williams, N., and Zhang, Y.: Predictability of biomass burning in response to climate changes, Global Biogeochemical Cycles, 26, https://doi.org/10.1029/2011GB004249, 2012.

Decker, Z. C. J., Wang, S., Bourgeois, I., Campuzano Jost, P., Coggon, M. M., DiGangi, J. P., Diskin, G. S., Flocke, F. M., Franchin, A., Fredrickson, C. D., Gkatzelis, G. I., Hall, S. R., Halliday, H., Hayden, K., Holmes, C. D., Huey, L. G., Jimenez, J. L., Lee, Y. R., Lindaas, J., Middlebrook, A. M., Montzka, D. D., Neuman, J. A., Nowak, J. B., Pagonis, D., Palm, B. B., Peischl, J., Piel, F., Rickly, P. S., Robinson, M. A., Rollins, A. W., Ryerson, T. B., Sekimoto, K., Thornton, J. A., Tyndall, G. S., Ullmann, K., Veres, P. R., Warneke, C., Washenfelder, R. A., Weinheimer, A. J., Wisthaler, A., Womack, C., and Brown, S. S.: Novel Analysis to Quantify Plume Crosswind Heterogeneity Applied to Biomass Burning Smoke, Environ. Sci. Technol., 55, 15646–15657, https://doi.org/10.1021/acs.est.1c03803, 2021.

Dennison, P. E., Brewer, S. C., Arnold, J. D., and Moritz, M. A.: Large wildfire trends in the western United States, 1984–2011, Geophysical Research Letters, 41, 2928–2933, https://doi.org/10.1002/2014GL059576, 2014.

Di Virgilio, G., Evans, J. P., Blake, S. A. P., Armstrong, M., Dowdy, A. J., Sharples, J., and McRae, R.: Climate Change Increases the Potential for Extreme Wildfires, Geophysical Research Letters, 46, 8517–8526, https://doi.org/10.1029/2019GL083699, 2019.

Domine, F., Sparapani, R., Ianniello, A., and Beine, H. J.: The origin of sea salt in snow on Arctic sea ice and in coastal regions, Atmospheric Chemistry and Physics, 4, 2259–2271, https://doi.org/10.5194/acp-4-2259-2004, 2004.

Donahue, N. M., Robinson, A. L., Stanier, C. O., and Pandis, S. N.: Coupled Partitioning, Dilution, and Chemical Aging of Semivolatile Organics, Environ. Sci. Technol., 40, 2635–2643, https://doi.org/10.1021/es052297c, 2006.

van Donkelaar, A., Hammer, M. S., Bindle, L., Brauer, M., Brook, J. R., Garay, M. J., Hsu, N. C., Kalashnikova, O. V., Kahn, R. A., Lee, C., Levy, R. C., Lyapustin, A., Sayer, A. M., and Martin, R. V.: Monthly Global Estimates of Fine Particulate Matter and Their Uncertainty, Environ. Sci. Technol., 55, 15287–15300, https://doi.org/10.1021/acs.est.1c05309, 2021.

Dowdy, A. J., Ye, H., Pepler, A., Thatcher, M., Osbrough, S. L., Evans, J. P., Di Virgilio, G., and McCarthy, N.: Future changes in extreme weather and pyroconvection risk factors for Australian wildfires, Sci Rep, 9, 10073, https://doi.org/10.1038/s41598-019-46362-x, 2019.

Dunne, E. M., Gordon, H., Kürten, A., Almeida, J., Duplissy, J., Williamson, C., Ortega, I. K., Pringle, K. J., Adamov, A., Baltensperger, U., Barmet, P., Benduhn, F., Bianchi, F., Breitenlechner, M., Clarke, A., Curtius, J., Dommen, J., Donahue, N. M., Ehrhart, S., Flagan, R. C., Franchin, A., Guida, R., Hakala, J., Hansel, A., Heinritzi, M., Jokinen, T., Kangasluoma, J., Kirkby, J., Kulmala, M., Kupc, A., Lawler, M. J., Lehtipalo, K., Makhmutov, V., Mann, G., Mathot, S., Merikanto, J., Miettinen, P., Nenes, A., Onnela, A., Rap, A., Reddington, C. L. S., Riccobono, F., Richards, N. A. D., Rissanen, M. P., Rondo, L., Sarnela, N., Schobesberger, S., Sengupta, K., Simon, M., Sipilä, M., Smith, J. N., Stozkhov, Y., Tomé, A., Tröstl, J., Wagner, P. E., Wimmer, D., Winkler, P. M., Worsnop, D. R., and Carslaw, K. S.: Global atmospheric particle formation from CERN CLOUD measurements, Science, 354, 1119–1124, https://doi.org/10.1126/science.aaf2649, 2016.

Dzepina, K., Volkamer, R. M., Madronich, S., Tulet, P., Ulbrich, I. M., Zhang, Q., Cappa, C. D., Ziemann, P. J., and Jimenez, J. L.: Evaluation of recently-proposed secondary organic aerosol models for a case study in Mexico City, Atmospheric Chemistry and Physics, 9, 5681–5709, https://doi.org/10.5194/acp-9-5681-2009, 2009.

Engelmann, R., Ansmann, A., Ohneiser, K., Griesche, H., Radenz, M., Hofer, J., Althausen, D., Dahlke, S., Maturilli, M., Veselovskii, I., Jimenez, C., Wiesen, R., Baars, H., Bühl, J., Gebauer, H., Haarig, M., Seifert, P., Wandinger, U., and Macke, A.: Wildfire smoke, Arctic haze, and aerosol effects on mixed-phase and cirrus clouds over the North Pole region during MOSAiC: an introduction, Atmospheric Chemistry and Physics, 21, 13397–13423, https://doi.org/10.5194/acp-21-13397-2021, 2021.

Engvall, A.-C., Krejci, R., Ström, J., Treffeisen, R., Scheele, R., Hermansen, O., and Paatero, J.: Changes in aerosol properties during spring-summer period in the Arctic troposphere,

Atmospheric Chemistry and Physics, 8, 445–462, https://doi.org/10.5194/acp-8-445-2008, 2008.

Fairlie, T. D., Jacob, D. J., and Park, R. J.: The impact of transpacific transport of mineral dust in the United States, Atmospheric Environment, 41, 1251–1266, https://doi.org/10.1016/j.atmosenv.2006.09.048, 2007.

Faloona, I.: Sulfur processing in the marine atmospheric boundary layer: A review and critical assessment of modeling uncertainties, Atmospheric Environment, 43, 2841–2854, https://doi.org/10.1016/j.atmosenv.2009.02.043, 2009.

Fanourgakis, G. S., Kanakidou, M., Nenes, A., Bauer, S. E., Bergman, T., Carslaw, K. S., Grini, A., Hamilton, D. S., Johnson, J. S., Karydis, V. A., Kirkevåg, A., Kodros, J. K., Lohmann, U., Luo, G., Makkonen, R., Matsui, H., Neubauer, D., Pierce, J. R., Schmale, J., Stier, P., Tsigaridis, K., van Noije, T., Wang, H., Watson-Parris, D., Westervelt, D. M., Yang, Y., Yoshioka, M., Daskalakis, N., Decesari, S., Gysel-Beer, M., Kalivitis, N., Liu, X., Mahowald, N. M., Myriokefalitakis, S., Schrödner, R., Sfakianaki, M., Tsimpidi, A. P., Wu, M., and Yu, F.: Evaluation of global simulations of aerosol particle and cloud condensation nuclei number, with implications for cloud droplet formation, Atmospheric Chemistry and Physics, 19, 8591–8617, https://doi.org/10.5194/acp-19-8591-2019, 2019.

Feng, X., Mickley, L. J., Bell, M. L., Liu, T., Fisher, J. A., and Val Martin, M.: Improved estimates of smoke exposure during Australia fire seasons: importance of quantifying plume injection heights, Atmospheric Chemistry and Physics, 24, 2985–3007, https://doi.org/10.5194/acp-24-2985-2024, 2024.

Ford, B. and Heald, C. L.: An A-train and model perspective on the vertical distribution of aerosols and CO in the Northern Hemisphere, Journal of Geophysical Research: Atmospheres, 117, https://doi.org/10.1029/2011JD016977, 2012.

Ford, B. and Heald, C. L.: Aerosol loading in the Southeastern United States: reconciling surface and satellite observations, Atmospheric Chemistry and Physics, 13, 9269–9283, https://doi.org/10.5194/acp-13-9269-2013, 2013.

Ford, B., Val Martin, M., Zelasky, S. E., Fischer, E. V., Anenberg, S. C., Heald, C. L., and Pierce, J. R.: Future Fire Impacts on Smoke Concentrations, Visibility, and Health in the Contiguous United States, GeoHealth, 2, 229–247, https://doi.org/10.1029/2018GH000144, 2018.

Forster, C., Wandinger, U., Wotawa, G., James, P., Mattis, I., Althausen, D., Simmonds, P., O'Doherty, S., Jennings, S. G., Kleefeld, C., Schneider, J., Trickl, T., Kreipl, S., Jäger, H., and Stohl, A.: Transport of boreal forest fire emissions from Canada to Europe, Journal of Geophysical Research: Atmospheres, 106, 22887–22906, https://doi.org/10.1029/2001JD900115, 2001.

Freitas, G. P., Kojoj, J., Mavis, C., Creamean, J., Mattsson, F., Nilsson, L., Spicker Schmidt, J., Adachi, K., Šantl-Temkiv, T., Ahlberg, E., Mohr, C., Riipinen, I., and Zieger, P.: A

comprehensive characterisation of natural aerosol sources in the high Arctic during the onset of sea ice melt, Faraday Discussions, https://doi.org/10.1039/D4FD00162A, 2024.

Freitas, S. R., Longo, K. M., and Andreae, M. O.: Impact of including the plume rise of vegetation fires in numerical simulations of associated atmospheric pollutants, Geophysical Research Letters, 33, https://doi.org/10.1029/2006GL026608, 2006.

Freitas, S. R., Longo, K. M., Chatfield, R., Latham, D., Silva Dias, M. a. F., Andreae, M. O., Prins, E., Santos, J. C., Gielow, R., and Carvalho, J. A. J.: Including the sub-grid scale plume rise of vegetation fires in low resolution atmospheric transport models, Atmospheric Chemistry and Physics, 7, 3385–3398, https://doi.org/10.5194/acp-7-3385-2007, 2007.

Freitas, S. R., Longo, K. M., Trentmann, J., and Latham, D.: Technical Note: Sensitivity of 1-D smoke plume rise models to the inclusion of environmental wind drag, Atmospheric Chemistry and Physics, 10, 585–594, https://doi.org/10.5194/acp-10-585-2010, 2010.

Freud, E., Krejci, R., Tunved, P., Leaitch, R., Nguyen, Q. T., Massling, A., Skov, H., and Barrie, L.: Pan-Arctic aerosol number size distributions: seasonality and transport patterns, Atmospheric Chemistry and Physics, 17, 8101–8128, https://doi.org/10.5194/acp-17-8101-2017, 2017.

Frossard, A. A., Shaw, P. M., Russell, L. M., Kroll, J. H., Canagaratna, M. R., Worsnop, D. R., Quinn, P. K., and Bates, T. S.: Springtime Arctic haze contributions of submicron organic particles from European and Asian combustion sources, Journal of Geophysical Research: Atmospheres, 116, https://doi.org/10.1029/2010JD015178, 2011.

Fung, K. M., Heald, C. L., Kroll, J. H., Wang, S., Jo, D. S., Gettelman, A., Lu, Z., Liu, X., Zaveri, R. A., Apel, E. C., Blake, D. R., Jimenez, J.-L., Campuzano-Jost, P., Veres, P. R., Bates, T. S., Shilling, J. E., and Zawadowicz, M.: Exploring dimethyl sulfide (DMS) oxidation and implications for global aerosol radiative forcing, Atmospheric Chemistry and Physics, 22, 1549–1573, https://doi.org/10.5194/acp-22-1549-2022, 2022.

Gálvez, Ó., Baeza-Romero, M. T., Sanz, M., and Saiz-Lopez, A.: Photolysis of frozen iodate salts as a source of active iodine in the polar environment, Atmospheric Chemistry and Physics, 16, 12703–12713, https://doi.org/10.5194/acp-16-12703-2016, 2016.

Gan, R. W., Ford, B., Lassman, W., Pfister, G., Vaidyanathan, A., Fischer, E., Volckens, J., Pierce, J. R., and Magzamen, S.: Comparison of wildfire smoke estimation methods and associations with cardiopulmonary-related hospital admissions, GeoHealth, 1, 122–136, https://doi.org/10.1002/2017GH000073, 2017.

Gantt, B. and Meskhidze, N.: The physical and chemical characteristics of marine primary organic aerosol: a review, Atmospheric Chemistry and Physics, 13, 3979–3996, https://doi.org/10.5194/acp-13-3979-2013, 2013.

Garofalo, L. A., Pothier, M. A., Levin, E. J. T., Campos, T., Kreidenweis, S. M., and Farmer, D. K.: Emission and Evolution of Submicron Organic Aerosol in Smoke from Wildfires in

the Western United States, ACS Earth Space Chem., 3, 1237–1247, https://doi.org/10.1021/acsearthspacechem.9b00125, 2019.

Garrett, T. J., Zhao, C., and Novelli, P. C.: Assessing the relative contributions of transport efficiency and scavenging to seasonal variability in Arctic aerosol, Tellus B: Chemical and Physical Meteorology, 62, 2010.

Generoso, S., Bey, I., Labonne, M., and Bréon, F.-M.: Aerosol vertical distribution in dust outflow over the Atlantic: Comparisons between GEOS-Chem and Cloud-Aerosol Lidar and Infrared Pathfinder Satellite Observation (CALIPSO), Journal of Geophysical Research: Atmospheres, 113, https://doi.org/10.1029/2008JD010154, 2008.

Ghahreman, R., Gong, W., Galí, M., Norman, A.-L., Beagley, S. R., Akingunola, A., Zheng, Q., Lupu, A., Lizotte, M., Levasseur, M., and Leaitch, W. R.: Dimethyl sulfide and its role in aerosol formation and growth in the Arctic summer – a modelling study, Atmospheric Chemistry and Physics, 19, 14455–14476, https://doi.org/10.5194/acp-19-14455-2019, 2019.

Gkatzelis, G. I., Coggon, M. M., Stockwell, C. E., Hornbrook, R. S., Allen, H., Apel, E. C., Bela, M. M., Blake, D. R., Bourgeois, I., Brown, S. S., Campuzano-Jost, P., St. Clair, J. M., Crawford, J. H., Crounse, J. D., Day, D. A., DiGangi, J. P., Diskin, G. S., Fried, A., Gilman, J. B., Guo, H., Hair, J. W., Halliday, H. S., Hanisco, T. F., Hannun, R., Hills, A., Huey, L. G., Jimenez, J. L., Katich, J. M., Lamplugh, A., Lee, Y. R., Liao, J., Lindaas, J., McKeen, S. A., Mikoviny, T., Nault, B. A., Neuman, J. A., Nowak, J. B., Pagonis, D., Peischl, J., Perring, A. E., Piel, F., Rickly, P. S., Robinson, M. A., Rollins, A. W., Ryerson, T. B., Schueneman, M. K., Schwantes, R. H., Schwarz, J. P., Sekimoto, K., Selimovic, V., Shingler, T., Tanner, D. J., Tomsche, L., Vasquez, K. T., Veres, P. R., Washenfelder, R., Weibring, P., Wennberg, P. O., Wisthaler, A., Wolfe, G. M., Womack, C. C., Xu, L., Ball, K., Yokelson, R. J., and Warneke, C.: Parameterizations of US wildfire and prescribed fire emission ratios and emission factors based on FIREX-AQ aircraft measurements, Atmospheric Chemistry and Physics, 24, 929–956, https://doi.org/10.5194/acp-24-929-2024, 2024.

Gong, X., Zhang, J., Croft, B., Yang, X., Frey, M. M., Bergner, N., Chang, R. Y.-W., Creamean, J. M., Kuang, C., Martin, R. V., Ranjithkumar, A., Sedlacek, A. J., Uin, J., Willmes, S., Zawadowicz, M. A., Pierce, J. R., Shupe, M. D., Schmale, J., and Wang, J.: Arctic warming by abundant fine sea salt aerosols from blowing snow, Nat. Geosci., 16, 768–774, https://doi.org/10.1038/s41561-023-01254-8, 2023.

Gordon, H., Kirkby, J., Baltensperger, U., Bianchi, F., Breitenlechner, M., Curtius, J., Dias, A., Dommen, J., Donahue, N. M., Dunne, E. M., Duplissy, J., Ehrhart, S., Flagan, R. C., Frege, C., Fuchs, C., Hansel, A., Hoyle, C. R., Kulmala, M., Kürten, A., Lehtipalo, K., Makhmutov, V., Molteni, U., Rissanen, M. P., Stozkhov, Y., Tröstl, J., Tsagkogeorgas, G., Wagner, R., Williamson, C., Wimmer, D., Winkler, P. M., Yan, C., and Carslaw, K. S.: Causes and importance of new particle formation in the present-day and preindustrial atmospheres, Journal of Geophysical Research: Atmospheres, 122, 8739–8760, https://doi.org/10.1002/2017JD026844, 2017.

Gordon, J. N. D., Bilsback, K. R., Fiddler, M. N., Pokhrel, R. P., Fischer, E. V., Pierce, J. R., and Bililign, S.: The Effects of Trash, Residential Biofuel, and Open Biomass Burning Emissions on Local and Transported PM2.5 and Its Attributed Mortality in Africa, GeoHealth, 7, e2022GH000673, https://doi.org/10.1029/2022GH000673, 2023.

Granier, C., Bessagnet, B., Bond, T., D'Angiola, A., Denier van der Gon, H., Frost, G. J., Heil, A., Kaiser, J. W., Kinne, S., Klimont, Z., Kloster, S., Lamarque, J.-F., Liousse, C., Masui, T., Meleux, F., Mieville, A., Ohara, T., Raut, J.-C., Riahi, K., Schultz, M. G., Smith, S. J., Thompson, A., van Aardenne, J., van der Werf, G. R., and van Vuuren, D. P.: Evolution of anthropogenic and biomass burning emissions of air pollutants at global and regional scales during the 1980–2010 period, Climatic Change, 109, 163, https://doi.org/10.1007/s10584-011-0154-1, 2011.

Gros, V., Bonsang, B., Sarda-Estève, R., Nikolopoulos, A., Metfies, K., Wietz, M., and Peeken, I.: Concentrations of dissolved dimethyl sulfide (DMS), methanethiol and other trace gases in context of microbial communities from the temperate Atlantic to the Arctic Ocean, Biogeosciences, 20, 851–867, https://doi.org/10.5194/bg-20-851-2023, 2023.

Gryspeerdt, E., Stier, P., and Partridge, D. G.: Satellite observations of cloud regime development: the role of aerosol processes, Atmospheric Chemistry and Physics, 14, 1141–1158, https://doi.org/10.5194/acp-14-1141-2014, 2014.

Grythe, H., Ström, J., Krejci, R., Quinn, P., and Stohl, A.: A review of sea-spray aerosol source functions using a large global set of sea salt aerosol concentration measurements, Atmospheric Chemistry and Physics, 14, 1277–1297, https://doi.org/10.5194/acp-14-1277-2014, 2014.

Guo, H., Campuzano-Jost, P., Nault, B. A., Day, D. A., Schroder, J. C., Kim, D., Dibb, J. E., Dollner, M., Weinzierl, B., and Jimenez, J. L.: The importance of size ranges in aerosol instrument intercomparisons: a case study for the Atmospheric Tomography Mission, Atmospheric Measurement Techniques, 14, 3631–3655, https://doi.org/10.5194/amt-14-3631-2021, 2021.

Hansel, A., Scholz, W., Mentler, B., Fischer, L., and Berndt, T.: Detection of RO2 radicals and other products from cyclohexene ozonolysis with NH4+ and acetate chemical ionization mass spectrometry, Atmospheric Environment, 186, 248–255, https://doi.org/10.1016/j.atmosenv.2018.04.023, 2018.

Hatch, L. E., Luo, W., Pankow, J. F., Yokelson, R. J., Stockwell, C. E., and Barsanti, K. C.: Identification and quantification of gaseous organic compounds emitted from biomass burning using two-dimensional gas chromatography–time-of-flight mass spectrometry, Atmospheric Chemistry and Physics, 15, 1865–1899, https://doi.org/10.5194/acp-15-1865-2015, 2015.

Hatch, L. E., Yokelson, R. J., Stockwell, C. E., Veres, P. R., Simpson, I. J., Blake, D. R., Orlando, J. J., and Barsanti, K. C.: Multi-instrument comparison and compilation of non-methane organic gas emissions from biomass burning and implications for smoke-derived

secondary organic aerosol precursors, Atmospheric Chemistry and Physics, 17, 1471–1489, https://doi.org/10.5194/acp-17-1471-2017, 2017.

Hatch, L. E., Rivas-Ubach, A., Jen, C. N., Lipton, M., Goldstein, A. H., and Barsanti, K. C.: Measurements of I/SVOCs in biomass-burning smoke using solid-phase extraction disks and two-dimensional gas chromatography, Atmospheric Chemistry and Physics, 18, 17801–17817, https://doi.org/10.5194/acp-18-17801-2018, 2018.

Hayashida, H., Steiner, N., Monahan, A., Galindo, V., Lizotte, M., and Levasseur, M.: Implications of sea-ice biogeochemistry for oceanic production and emissions of dimethyl sulfide in the Arctic, Biogeosciences, 14, 3129–3155, https://doi.org/10.5194/bg-14-3129-2017, 2017.

Hayashida, H., Carnat, G., Galí, M., Monahan, A. H., Mortenson, E., Sou, T., and Steiner, N. S.: Spatiotemporal Variability in Modeled Bottom Ice and Sea Surface Dimethylsulfide Concentrations and Fluxes in the Arctic During 1979–2015, Global Biogeochemical Cycles, 34, e2019GB006456, https://doi.org/10.1029/2019GB006456, 2020.

Haywood, J. and Boucher, O.: Estimates of the direct and indirect radiative forcing due to tropospheric aerosols: A review, Reviews of Geophysics, 38, 513–543, https://doi.org/10.1029/1999RG000078, 2000.

He, X.-C., Simon, M., Iyer, S., Xie, H.-B., Rörup, B., Shen, J., Finkenzeller, H., Stolzenburg, D., Zhang, R., Baccarini, A., Tham, Y. J., Wang, M., Amanatidis, S., Piedehierro, A. A., Amorim, A., Baalbaki, R., Brasseur, Z., Caudillo, L., Chu, B., Dada, L., Duplissy, J., El Haddad, I., Flagan, R. C., Granzin, M., Hansel, A., Heinritzi, M., Hofbauer, V., Jokinen, T., Kemppainen, D., Kong, W., Krechmer, J., Kürten, A., Lamkaddam, H., Lopez, B., Ma, F., Mahfouz, N. G. A., Makhmutov, V., Manninen, H. E., Marie, G., Marten, R., Massabò, D., Mauldin, R. L., Mentler, B., Onnela, A., Petäjä, T., Pfeifer, J., Philippov, M., Ranjithkumar, A., Rissanen, M. P., Schobesberger, S., Scholz, W., Schulze, B., Surdu, M., Thakur, R. C., Tomé, A., Wagner, A. C., Wang, D., Wang, Y., Weber, S. K., Welti, A., Winkler, P. M., Zauner-Wieczorek, M., Baltensperger, U., Curtius, J., Kurtén, T., Worsnop, D. R., Volkamer, R., Lehtipalo, K., Kirkby, J., Donahue, N. M., Sipilä, M., and Kulmala, M.: Iodine oxoacids enhance nucleation of sulfuric acid particles in the atmosphere, Science, 382, 1308–1314, https://doi.org/10.1126/science.adh2526, 2023.

Hecobian, A., Liu, Z., Hennigan, C. J., Huey, L. G., Jimenez, J. L., Cubison, M. J., Vay, S., Diskin, G. S., Sachse, G. W., Wisthaler, A., Mikoviny, T., Weinheimer, A. J., Liao, J., Knapp, D. J., Wennberg, P. O., Kürten, A., Crounse, J. D., Clair, J. S., Wang, Y., and Weber, R. J.: Comparison of chemical characteristics of 495 biomass burning plumes intercepted by the NASA DC-8 aircraft during the ARCTAS/CARB-2008 field campaign, Atmospheric Chemistry and Physics, 11, 13325–13337, https://doi.org/10.5194/acp-11-13325-2011, 2011.

Heinold, B., Baars, H., Barja, B., Christensen, M., Kubin, A., Ohneiser, K., Schepanski, K., Schutgens, N., Senf, F., Schrödner, R., Villanueva, D., and Tegen, I.: Important role of stratospheric injection height for the distribution and radiative forcing of smoke aerosol

from the 2019–2020 Australian wildfires, Atmospheric Chemistry and Physics, 22, 9969–9985, https://doi.org/10.5194/acp-22-9969-2022, 2022.

Hennigan, C. J., Sullivan, A. P., Collett Jr., J. L., and Robinson, A. L.: Levoglucosan stability in biomass burning particles exposed to hydroxyl radicals, Geophysical Research Letters, 37, https://doi.org/10.1029/2010GL043088, 2010.

Hill, V. L. and Manley, S. L.: Release of reactive bromine and iodine from diatoms and its possible role in halogen transfer in polar and tropical oceans, Limnology and Oceanography, 54, 812–822, https://doi.org/10.4319/lo.2009.54.3.0812, 2009.

Hinds, W. C.: Aerosol Technology: Properties, Behavior, and Measurement of Airborne Particles, Wiley, 512 pp., 1999.

Hobbs, P. V., Reid, J. S., Kotchenruther, R. A., Ferek, R. J., and Weiss, R.: Direct Radiative Forcing by Smoke from Biomass Burning, Science, 275, 1777–1778, https://doi.org/10.1126/science.275.5307.1777, 1997.

Hobbs, P. V., Sinha, P., Yokelson, R. J., Christian, T. J., Blake, D. R., Gao, S., Kirchstetter, T. W., Novakov, T., and Pilewskie, P.: Evolution of gases and particles from a savanna fire in South Africa, Journal of Geophysical Research: Atmospheres, 108, https://doi.org/10.1029/2002JD002352, 2003.

Hodshire, A. L., Akherati, A., Alvarado, M. J., Brown-Steiner, B., Jathar, S. H., Jimenez, J. L., Kreidenweis, S. M., Lonsdale, C. R., Onasch, T. B., Ortega, A. M., and Pierce, J. R.: Aging Effects on Biomass Burning Aerosol Mass and Composition: A Critical Review of Field and Laboratory Studies, Environ. Sci. Technol., 53, 10007–10022, https://doi.org/10.1021/acs.est.9b02588, 2019a.

Hodshire, A. L., Bian, Q., Ramnarine, E., Lonsdale, C. R., Alvarado, M. J., Kreidenweis, S. M., Jathar, S. H., and Pierce, J. R.: More Than Emissions and Chemistry: Fire Size, Dilution, and Background Aerosol Also Greatly Influence Near-Field Biomass Burning Aerosol Aging, Journal of Geophysical Research: Atmospheres, 124, 5589–5611, https://doi.org/10.1029/2018JD029674, 2019b.

Hodshire, A. L., Campuzano-Jost, P., Kodros, J. K., Croft, B., Nault, B. A., Schroder, J. C., Jimenez, J. L., and Pierce, J. R.: The potential role of methanesulfonic acid (MSA) in aerosol formation and growth and the associated radiative forcings, Atmospheric Chemistry and Physics, 19, 3137–3160, https://doi.org/10.5194/acp-19-3137-2019, 2019c.

Hodshire, A. L., Ramnarine, E., Akherati, A., Alvarado, M. L., Farmer, D. K., Jathar, S. H., Kreidenweis, S. M., Lonsdale, C. R., Onasch, T. B., Springston, S. R., Wang, J., Wang, Y., Kleinman, L. I., Sedlacek III, A. J., and Pierce, J. R.: Dilution impacts on smoke aging: evidence in Biomass Burning Observation Project (BBOP) data, Atmospheric Chemistry and Physics, 21, 6839–6855, https://doi.org/10.5194/acp-21-6839-2021, 2021.

Hoffmann, E. H., Tilgner, A., Schrödner, R., Bräuer, P., Wolke, R., and Herrmann, H.: An advanced modeling study on the impacts and atmospheric implications of multiphase dimethyl sulfide chemistry, Proceedings of the National Academy of Sciences, 113, 11776–11781, https://doi.org/10.1073/pnas.1606320113, 2016.

Hoffmann, E. H., Heinold, B., Kubin, A., Tegen, I., and Herrmann, H.: The Importance of the Representation of DMS Oxidation in Global Chemistry-Climate Simulations, Geophysical Research Letters, 48, e2021GL094068, https://doi.org/10.1029/2021GL094068, 2021.

Holland, M. M. and Bitz, C. M.: Polar amplification of climate change in coupled models, Climate Dynamics, 21, 221–232, https://doi.org/10.1007/s00382-003-0332-6, 2003.

Huang, J. and Jaeglé, L.: Wintertime enhancements of sea salt aerosol in polar regions consistent with a sea ice source from blowing snow, Atmospheric Chemistry and Physics, 17, 3699–3712, https://doi.org/10.5194/acp-17-3699-2017, 2017.

Huang, J., Jaeglé, L., Chen, Q., Alexander, B., Sherwen, T., Evans, M. J., Theys, N., and Choi, S.: Evaluating the impact of blowing-snow sea salt aerosol on springtime BrO and O_3 in the Arctic, Atmospheric Chemistry and Physics, 20, 7335–7358, https://doi.org/10.5194/acp-20-7335-2020, 2020.

Huang, R.-J., Hoffmann, T., Ovadnevaite, J., Laaksonen, A., Kokkola, H., Xu, W., Xu, W., Ceburnis, D., Zhang, R., Seinfeld, J. H., and O'Dowd, C.: Heterogeneous iodine-organic chemistry fast-tracks marine new particle formation, Proceedings of the National Academy of Sciences, 119, e2201729119, https://doi.org/10.1073/pnas.2201729119, 2022.

Huffman, J. A., Docherty, K. S., Aiken, A. C., Cubison, M. J., Ulbrich, I. M., DeCarlo, P. F., Sueper, D., Jayne, J. T., Worsnop, D. R., Ziemann, P. J., and Jimenez, J. L.: Chemically-resolved aerosol volatility measurements from two megacity field studies, Atmospheric Chemistry and Physics, 9, 7161–7182, https://doi.org/10.5194/acp-9-7161-2009, 2009.

Hulswar, S., Simó, R., Galí, M., Bell, T. G., Lana, A., Inamdar, S., Halloran, P. R., Manville, G., and Mahajan, A. S.: Third revision of the global surface seawater dimethyl sulfide climatology (DMS-Rev3), Earth System Science Data, 14, 2963–2987, https://doi.org/10.5194/essd-14-2963-2022, 2022.

Jacobson, M. Z.: Strong radiative heating due to the mixing state of black carbon in atmospheric aerosols, Nature, 409, 695–697, https://doi.org/10.1038/35055518, 2001.

Jaeglé, L., Quinn, P. K., Bates, T. S., Alexander, B., and Lin, J.-T.: Global distribution of sea salt aerosols: new constraints from in situ and remote sensing observations, Atmospheric Chemistry and Physics, 11, 3137–3157, https://doi.org/10.5194/acp-11-3137-2011, 2011.

Jalava, P. I., Salonen, R. O., Hälinen, A. I., Penttinen, P., Pennanen, A. S., Sillanpää, M., Sandell, E., Hillamo, R., and Hirvonen, M.-R.: In vitro inflammatory and cytotoxic effects of size-segregated particulate samples collected during long-range transport of wildfire smoke to

Helsinki, Toxicology and Applied Pharmacology, 215, 341–353, https://doi.org/10.1016/j.taap.2006.03.007, 2006.

Janhäll, S., Andreae, M. O., and Pöschl, U.: Biomass burning aerosol emissions from vegetation fires: particle number and mass emission factors and size distributions, Atmospheric Chemistry and Physics, 10, 1427–1439, https://doi.org/10.5194/acp-10-1427-2010, 2010.

Jathar, S. H., Gordon, T. D., Hennigan, C. J., Pye, H. O. T., Pouliot, G., Adams, P. J., Donahue, N. M., and Robinson, A. L.: Unspeciated organic emissions from combustion sources and their influence on the secondary organic aerosol budget in the United States, Proceedings of the National Academy of Sciences, 111, 10473–10478, https://doi.org/10.1073/pnas.1323740111, 2014.

Jen, C. N., Hatch, L. E., Selimovic, V., Yokelson, R. J., Weber, R., Fernandez, A. E., Kreisberg, N. M., Barsanti, K. C., and Goldstein, A. H.: Speciated and total emission factors of particulate organics from burning western US wildland fuels and their dependence on combustion efficiency, Atmospheric Chemistry and Physics, 19, 1013–1026, https://doi.org/10.5194/acp-19-1013-2019, 2019.

Jian, Y. and Fu, T.-M.: Injection heights of springtime biomass-burning plumes over peninsular Southeast Asia and their impacts on long-range pollutant transport, Atmospheric Chemistry and Physics, 14, 3977–3989, https://doi.org/10.5194/acp-14-3977-2014, 2014.

Jimenez, J. L., Canagaratna, M. R., Donahue, N. M., Prevot, A. S. H., Zhang, Q., Kroll, J. H., DeCarlo, P. F., Allan, J. D., Coe, H., Ng, N. L., Aiken, A. C., Docherty, K. S., Ulbrich, I. M., Grieshop, A. P., Robinson, A. L., Duplissy, J., Smith, J. D., Wilson, K. R., Lanz, V. A., Hueglin, C., Sun, Y. L., Tian, J., Laaksonen, A., Raatikainen, T., Rautiainen, J., Vaattovaara, P., Ehn, M., Kulmala, M., Tomlinson, J. M., Collins, D. R., Cubison, M. J., E, Dunlea, J., Huffman, J. A., Onasch, T. B., Alfarra, M. R., Williams, P. I., Bower, K., Kondo, Y., Schneider, J., Drewnick, F., Borrmann, S., Weimer, S., Demerjian, K., Salcedo, D., Cottrell, L., Griffin, R., Takami, A., Miyoshi, T., Hatakeyama, S., Shimono, A., Sun, J. Y., Zhang, Y. M., Dzepina, K., Kimmel, J. R., Sueper, D., Jayne, J. T., Herndon, S. C., Trimborn, A. M., Williams, L. R., Wood, E. C., Middlebrook, A. M., Kolb, C. E., Baltensperger, U., and Worsnop, D. R.: Evolution of Organic Aerosols in the Atmosphere, Science, https://doi.org/10.1126/science.1180353, 2009.

Johnson, J. S. and Jen, C. N.: Role of Methanesulfonic Acid in Sulfuric Acid–Amine and Ammonia New Particle Formation, ACS Earth Space Chem., 7, 653–660, https://doi.org/10.1021/acsearthspacechem.3c00017, 2023.

Johnson, M. T.: A numerical scheme to calculate temperature and salinity dependent air-water transfer velocities for any gas, Ocean Science, 6, 913–932, https://doi.org/10.5194/os-6-913-2010, 2010.

Johnston, H. J., Mueller, W., Steinle, S., Vardoulakis, S., Tantrakarnapa, K., Loh, M., and Cherrie, J. W.: How Harmful Is Particulate Matter Emitted from Biomass Burning? A Thailand Perspective, Curr Pollution Rep, 5, 353–377, https://doi.org/10.1007/s40726-019-00125-4, 2019.

Jolleys, M. D., Coe, H., McFiggans, G., Taylor, J. W., O'Shea, S. J., Le Breton, M., Bauguitte, S. J.-B., Moller, S., Di Carlo, P., Aruffo, E., Palmer, P. I., Lee, J. D., Percival, C. J., and Gallagher, M. W.: Properties and evolution of biomass burning organic aerosol from Canadian boreal forest fires, Atmospheric Chemistry and Physics, 15, 3077–3095, https://doi.org/10.5194/acp-15-3077-2015, 2015.

Jolly, W. M., Cochrane, M. A., Freeborn, P. H., Holden, Z. A., Brown, T. J., Williamson, G. J., and Bowman, D. M. J. S.: Climate-induced variations in global wildfire danger from 1979 to 2013, Nat Commun, 6, 7537, https://doi.org/10.1038/ncomms8537, 2015.

June, N. A., Hodshire, A. L., Wiggins, E. B., Winstead, E. L., Robinson, C. E., Thornhill, K. L., Sanchez, K. J., Moore, R. H., Pagonis, D., Guo, H., Campuzano-Jost, P., Jimenez, J. L., Coggon, M. M., Dean-Day, J. M., Bui, T. P., Peischl, J., Yokelson, R. J., Alvarado, M. J., Kreidenweis, S. M., Jathar, S. H., and Pierce, J. R.: Aerosol size distribution changes in FIREX-AQ biomass burning plumes: the impact of plume concentration on coagulation and OA condensation/evaporation, Atmospheric Chemistry and Physics, 22, 12803–12825, https://doi.org/10.5194/acp-22-12803-2022, 2022.

Kahn, R. A., Li, W.-H., Moroney, C., Diner, D. J., Martonchik, J. V., and Fishbein, E.: Aerosol source plume physical characteristics from space-based multiangle imaging, Journal of Geophysical Research: Atmospheres, 112, https://doi.org/10.1029/2006JD007647, 2007.

Kaiser, J. W., Heil, A., Andreae, M. O., Benedetti, A., Chubarova, N., Jones, L., Morcrette, J.-J., Razinger, M., Schultz, M. G., Suttie, M., and van der Werf, G. R.: Biomass burning emissions estimated with a global fire assimilation system based on observed fire radiative power, Biogeosciences, 9, 527–554, https://doi.org/10.5194/bg-9-527-2012, 2012.

Karlsson, L., Krejci, R., Koike, M., Ebell, K., and Zieger, P.: A long-term study of cloud residuals from low-level Arctic clouds, Atmospheric Chemistry and Physics, 21, 8933–8959, https://doi.org/10.5194/acp-21-8933-2021, 2021.

Kecorius, S., Vogl, T., Paasonen, P., Lampilahti, J., Rothenberg, D., Wex, H., Zeppenfeld, S., van Pinxteren, M., Hartmann, M., Henning, S., Gong, X., Welti, A., Kulmala, M., Stratmann, F., Herrmann, H., and Wiedensohler, A.: New particle formation and its effect on cloud condensation nuclei abundance in the summer Arctic: a case study in the Fram Strait and Barents Sea, Atmospheric Chemistry and Physics, 19, 14339–14364, https://doi.org/10.5194/acp-19-14339-2019, 2019.

Kettle, A. J., Rhee, T. S., von Hobe, M., Poulton, A., Aiken, J., and Andreae, M. O.: Assessing the flux of different volatile sulfur gases from the ocean to the atmosphere, Journal of Geophysical Research: Atmospheres, 106, 12193–12209, https://doi.org/10.1029/2000JD900630, 2001.

Keywood, M., Kanakidou, M., Stohl, A., Dentener, F., Grassi, G., Meyer, C. P., Torseth, K., Edwards, D., Thompson, A. M., Lohmann, U., and Burrows, J.: Fire in the Air: Biomass Burning Impacts in a Changing Climate, Critical Reviews in Environmental Science and Technology, 43, 40–83, https://doi.org/10.1080/10643389.2011.604248, 2013.

Keywood, M., Cope, M., Meyer, C. P. M., Iinuma, Y., and Emmerson, K.: When smoke comes to town: The impact of biomass burning smoke on air quality, Atmospheric Environment, 121, 13–21, https://doi.org/10.1016/j.atmosenv.2015.03.050, 2015.

Kilgour, D. B., Novak, G. A., Claflin, M. S., Lerner, B. M., and Bertram, T. H.: Production of oxygenated volatile organic compounds from the ozonolysis of coastal seawater, Atmospheric Chemistry and Physics, 24, 3729–3742, https://doi.org/10.5194/acp-24-3729-2024, 2024.

Kim, M. J., Novak, G. A., Zoerb, M. C., Yang, M., Blomquist, B. W., Huebert, B. J., Cappa, C. D., and Bertram, T. H.: Air-Sea exchange of biogenic volatile organic compounds and the impact on aerosol particle size distributions, Geophysical Research Letters, 44, 3887–3896, https://doi.org/10.1002/2017GL072975, 2017.

Kim, M.-H., Omar, A. H., Tackett, J. L., Vaughan, M. A., Winker, D. M., Trepte, C. R., Hu, Y., Liu, Z., Poole, L. R., Pitts, M. C., Kar, J., and Magill, B. E.: The CALIPSO version 4 automated aerosol classification and lidar ratio selection algorithm, Atmospheric Measurement Techniques, 11, 6107–6135, https://doi.org/10.5194/amt-11-6107-2018, 2018.

Kloster, S., Feichter, J., Maier-Reimer, E., Six, K. D., Stier, P., and Wetzel, P.: DMS cycle in the marine ocean-atmosphere system – a global model study, Biogeosciences, 3, 29–51, https://doi.org/10.5194/bg-3-29-2006, 2006.

Kodros, J. K. and Pierce, J. R.: Important global and regional differences in aerosol cloud-albedo effect estimates between simulations with and without prognostic aerosol microphysics, Journal of Geophysical Research: Atmospheres, 122, 4003–4018, https://doi.org/10.1002/2016JD025886, 2017.

Kodros, J. K., Scott, C. E., Farina, S. C., Lee, Y. H., L'Orange, C., Volckens, J., and Pierce, J. R.: Uncertainties in global aerosols and climate effects due to biofuel emissions, Atmospheric Chemistry and Physics, 15, 8577–8596, https://doi.org/10.5194/acp-15-8577-2015, 2015.

Kodros, J. K., Cucinotta, R., Ridley, D. A., Wiedinmyer, C., and Pierce, J. R.: The aerosol radiative effects of uncontrolled combustion of domestic waste, Atmospheric Chemistry and Physics, 16, 6771–6784, https://doi.org/10.5194/acp-16-6771-2016, 2016.

Kodros, J. K., Volckens, J., Jathar, S. H., and Pierce, J. R.: Ambient Particulate Matter Size Distributions Drive Regional and Global Variability in Particle Deposition in the Respiratory Tract, GeoHealth, 2, 298–312, https://doi.org/10.1029/2018GH000145, 2018a.

Kodros, J. K., Hanna, S. J., Bertram, A. K., Leaitch, W. R., Schulz, H., Herber, A. B., Zanatta, M., Burkart, J., Willis, M. D., Abbatt, J. P. D., and Pierce, J. R.: Size-resolved mixing state of black carbon in the Canadian high Arctic and implications for simulated direct radiative effect, Atmospheric Chemistry and Physics, 18, 11345–11361, https://doi.org/10.5194/acp-18-11345-2018, 2018b.

Korhonen, H., Carslaw, K. S., Spracklen, D. V., Ridley, D. A., and Ström, J.: A global model study of processes controlling aerosol size distributions in the Arctic spring and summer, Journal of Geophysical Research: Atmospheres, 113, https://doi.org/10.1029/2007JD009114, 2008.

Koss, A. R., Sekimoto, K., Gilman, J. B., Selimovic, V., Coggon, M. M., Zarzana, K. J., Yuan, B., Lerner, B. M., Brown, S. S., Jimenez, J. L., Krechmer, J., Roberts, J. M., Warneke, C., Yokelson, R. J., and de Gouw, J.: Non-methane organic gas emissions from biomass burning: identification, quantification, and emission factors from PTR-ToF during the FIREX 2016 laboratory experiment, Atmospheric Chemistry and Physics, 18, 3299–3319, https://doi.org/10.5194/acp-18-3299-2018, 2018.

Kulmala, M.: How Particles Nucleate and Grow, Science, 302, 1000–1001, https://doi.org/10.1126/science.1090848, 2003.

Kulmala, M. and Kerminen, V.-M.: On the formation and growth of atmospheric nanoparticles, Atmospheric Research, 90, 132–150, https://doi.org/10.1016/j.atmosres.2008.01.005, 2008.

Lamarque, J.-F., Bond, T. C., Eyring, V., Granier, C., Heil, A., Klimont, Z., Lee, D., Liousse, C., Mieville, A., Owen, B., Schultz, M. G., Shindell, D., Smith, S. J., Stehfest, E., Van Aardenne, J., Cooper, O. R., Kainuma, M., Mahowald, N., McConnell, J. R., Naik, V., Riahi, K., and van Vuuren, D. P.: Historical (1850–2000) gridded anthropogenic and biomass burning emissions of reactive gases and aerosols: methodology and application, Atmospheric Chemistry and Physics, 10, 7017–7039, https://doi.org/10.5194/acp-10-7017-2010, 2010.

Lana, A., Bell, T. G., Simó, R., Vallina, S. M., Ballabrera-Poy, J., Kettle, A. J., Dachs, J., Bopp, L., Saltzman, E. S., Stefels, J., Johnson, J. E., and Liss, P. S.: An updated climatology of surface dimethlysulfide concentrations and emission fluxes in the global ocean, Global Biogeochemical Cycles, 25, https://doi.org/10.1029/2010GB003850, 2011.

Lawson, S. J., Law, C. S., Harvey, M. J., Bell, T. G., Walker, C. F., de Bruyn, W. J., and Saltzman, E. S.: Methanethiol, dimethyl sulfide and acetone over biologically productive waters in the southwest Pacific Ocean, Atmospheric Chemistry and Physics, 20, 3061–3078, https://doi.org/10.5194/acp-20-3061-2020, 2020.

Leaitch, W. R., Sharma, S., Huang, L., Toom-Sauntry, D., Chivulescu, A., Macdonald, A. M., von Salzen, K., Pierce, J. R., Bertram, A. K., Schroder, J. C., Shantz, N. C., Chang, R. Y.-W., and Norman, A.-L.: Dimethyl sulfide control of the clean summertime Arctic aerosol and cloud, Elementa: Science of the Anthropocene, 1, 000017, https://doi.org/10.12952/journal.elementa.000017, 2013.

Leaitch, W. R., Russell, L. M., Liu, J., Kolonjari, F., Toom, D., Huang, L., Sharma, S., Chivulescu, A., Veber, D., and Zhang, W.: Organic functional groups in the submicron aerosol at 82.5° N, 62.5° W from 2012 to 2014, Atmospheric Chemistry and Physics, 18, 3269–3287, https://doi.org/10.5194/acp-18-3269-2018, 2018.

Leck, C. and Rodhe, H.: Emissions of marine biogenic sulfur to the atmosphere of northern Europe, J Atmos Chem, 12, 63–86, https://doi.org/10.1007/BF00053934, 1991.

Lee, L. A., Pringle, K. J., Reddington, C. L., Mann, G. W., Stier, P., Spracklen, D. V., Pierce, J. R., and Carslaw, K. S.: The magnitude and causes of uncertainty in global model simulations of cloud condensation nuclei, Atmospheric Chemistry and Physics, 13, 8879–8914, https://doi.org/10.5194/acp-13-8879-2013, 2013.

Lee, S.-H., Gordon, H., Yu, H., Lehtipalo, K., Haley, R., Li, Y., and Zhang, R.: New Particle Formation in the Atmosphere: From Molecular Clusters to Global Climate, Journal of Geophysical Research: Atmospheres, 124, 7098–7146, https://doi.org/10.1029/2018JD029356, 2019.

Legrand, M., Preunkert, S., Weller, R., Zipf, L., Elsässer, C., Merchel, S., Rugel, G., and Wagenbach, D.: Year-round record of bulk and size-segregated aerosol composition in central Antarctica (Concordia site) – Part 2: Biogenic sulfur (sulfate and methanesulfonate) aerosol, Atmospheric Chemistry and Physics, 17, 14055–14073, https://doi.org/10.5194/acp-17-14055-2017, 2017.

Leonard, S. S., Castranova, V., Chen, B. T., Schwegler-Berry, D., Hoover, M., Piacitelli, C., and Gaughan, D. M.: Particle size-dependent radical generation from wildland fire smoke, Toxicology, 236, 103–113, https://doi.org/10.1016/j.tox.2007.04.008, 2007.

Leung, F.-Y. T., Logan, J. A., Park, R., Hyer, E., Kasischke, E., Streets, D., and Yurganov, L.: Impacts of enhanced biomass burning in the boreal forests in 1998 on tropospheric chemistry and the sensitivity of model results to the injection height of emissions, Journal of Geophysical Research: Atmospheres, 112, https://doi.org/10.1029/2006JD008132, 2007.

Li, J., Han, Z., Surapipith, V., Fan, W., Thongboonchoo, N., Wu, J., Li, J., Tao, J., Wu, Y., Macatangay, R., Bran, S. H., Yu, E., Zhang, A., Liang, L., and Zhang, R.: Direct and indirect effects and feedbacks of biomass burning aerosols over Mainland Southeast Asia and South China in springtime, Science of The Total Environment, 842, 156949, https://doi.org/10.1016/j.scitotenv.2022.156949, 2022.

Li, S., Zhang, L., Cai, K., Ge, W., and Zhang, X.: Comparisons of the vertical distributions of aerosols in the CALIPSO and GEOS-Chem datasets in China, Atmospheric Environment: X, 3, 100036, https://doi.org/10.1016/j.aeaoa.2019.100036, 2019.

Li, Y., Tong, D., Ma, S., Freitas, S. R., Ahmadov, R., Sofiev, M., Zhang, X., Kondragunta, S., Kahn, R., Tang, Y., Baker, B., Campbell, P., Saylor, R., Grell, G., and Li, F.: Impacts of estimated plume rise on $PM_{2.5}$ exceedance prediction during extreme wildfire events: a comparison of three schemes (Briggs, Freitas, and Sofiev), Atmospheric Chemistry and Physics, 23, 3083–3101, https://doi.org/10.5194/acp-23-3083-2023, 2023.

Lin, H., Emmons, L. K., Lundgren, E. W., Yang, L. H., Feng, X., Dang, R., Zhai, S., Tang, Y., Kelp, M. M., Colombi, N. K., Eastham, S. D., Fritz, T. M., and Jacob, D. J.: Intercomparison of GEOS-Chem and CAM-chem tropospheric oxidant chemistry within

the Community Earth System Model version 2 (CESM2), Atmospheric Chemistry and Physics, 24, 8607–8624, https://doi.org/10.5194/acp-24-8607-2024, 2024.

Liu, J. C., Pereira, G., Uhl, S. A., Bravo, M. A., and Bell, M. L.: A systematic review of the physical health impacts from non-occupational exposure to wildfire smoke, Environmental Research, 136, 120–132, https://doi.org/10.1016/j.envres.2014.10.015, 2015.

Lizotte, M., Levasseur, M., Galindo, V., Gourdal, M., Gosselin, M., Tremblay, J.-É., Blais, M., Charette, J., and Hussherr, R.: Phytoplankton and dimethylsulfide dynamics at two contrasting Arctic ice edges, Biogeosciences, 17, 1557–1581, https://doi.org/10.5194/bg-17-1557-2020, 2020.

Lonsdale, C. R., Alvarado, M. J., Hodshire, A. L., Ramnarine, E., and Pierce, J. R.: Simulating the forest fire plume dispersion, chemistry, and aerosol formation using SAM-ASP version 1.0, Geoscientific Model Development, 13, 4579–4593, https://doi.org/10.5194/gmd-13-4579-2020, 2020.

Loose, B., Schlosser, P., Perovich, D., Ringelberg, D., Ho, D. T., Takahashi, T., Richter-Menge, J., Reynolds, C. M., Mcgillis, W. R., and Tison, J.-L.: Gas diffusion through columnar laboratory sea ice: implications for mixed-layer ventilation of CO2 in the seasonal ice zone, Tellus B: Chemical and Physical Meteorology, 63, 2011.

Lu, Z., Liu, X., Ke, Z., Zhang, K., Ma, P.-L., and Fan, J.: Incorporating an Interactive Fire Plume-Rise Model in the DOE's Energy Exascale Earth System Model Version 1 (E3SMv1) and Examining Aerosol Radiative Effect, Journal of Advances in Modeling Earth Systems, 16, e2023MS003818, https://doi.org/10.1029/2023MS003818, 2024.

Lyapustin, A., Wang, Y., Korkin, S., Kahn, R., and Winker, D.: MAIAC Thermal Technique for Smoke Injection Height From MODIS, IEEE Geoscience and Remote Sensing Letters, 17, 730–734, https://doi.org/10.1109/LGRS.2019.2936332, 2020.

Ma, C., Ni, R., Su, H., and Cheng, Y.: Enhancing Global Simulation of Smoke Injection Height for Intense Pyro-Convection Through Coupling an Improved One-Dimensional Plume Rise Model in CAM-chem, Journal of Advances in Modeling Earth Systems, 16, e2023MS004127, https://doi.org/10.1029/2023MS004127, 2024.

Ma, X. and Yu, F.: Seasonal and spatial variations of global aerosol optical depth: multi-year modelling with GEOS-Chem-APM and comparisons with multiple-platform observations, Tellus B: Chemical and Physical Meteorology, 67, 25115, https://doi.org/10.3402/tellusb.v67.25115, 2015.

Macdonald, K. M., Sharma, S., Toom, D., Chivulescu, A., Hanna, S., Bertram, A. K., Platt, A., Elsasser, M., Huang, L., Tarasick, D., Chellman, N., McConnell, J. R., Bozem, H., Kunkel, D., Lei, Y. D., Evans, G. J., and Abbatt, J. P. D.: Observations of atmospheric chemical deposition to high Arctic snow, Atmospheric Chemistry and Physics, 17, 5775–5788, https://doi.org/10.5194/acp-17-5775-2017, 2017.

Mardi, A. H., Dadashazar, H., MacDonald, A. B., Braun, R. A., Crosbie, E., Xian, P., Thorsen, T. J., Coggon, M. M., Fenn, M. A., Ferrare, R. A., Hair, J. W., Woods, R. K., Jonsson, H. H., Flagan, R. C., Seinfeld, J. H., and Sorooshian, A.: Biomass Burning Plumes in the Vicinity of the California Coast: Airborne Characterization of Physicochemical Properties, Heating Rates, and Spatiotemporal Features, Journal of Geophysical Research: Atmospheres, 123, 13,560-13,582, https://doi.org/10.1029/2018JD029134, 2018.

Marlon, J. R., Bartlein, P. J., Carcaillet, C., Gavin, D. G., Harrison, S. P., Higuera, P. E., Joos, F., Power, M. J., and Prentice, I. C.: Climate and human influences on global biomass burning over the past two millennia, Nature Geosci, 1, 697–702, https://doi.org/10.1038/ngeo313, 2008.

Marti, J. J., Jefferson, A., Cai, X. P., Richert, C., McMurry, P. H., and Eisele, F.: H2SO4 vapor pressure of sulfuric acid and ammonium sulfate solutions, Journal of Geophysical Research: Atmospheres, 102, 3725–3735, https://doi.org/10.1029/96JD03064, 1997.

May, A. A., Levin, E. J. T., Hennigan, C. J., Riipinen, I., Lee, T., Collett Jr., J. L., Jimenez, J. L., Kreidenweis, S. M., and Robinson, A. L.: Gas-particle partitioning of primary organic aerosol emissions: 3. Biomass burning, Journal of Geophysical Research: Atmospheres, 118, 11,327-11,338, https://doi.org/10.1002/jgrd.50828, 2013.

May, A. A., Lee, T., McMeeking, G. R., Akagi, S., Sullivan, A. P., Urbanski, S., Yokelson, R. J., and Kreidenweis, S. M.: Observations and analysis of organic aerosol evolution in some prescribed fire smoke plumes, Atmospheric Chemistry and Physics, 15, 6323–6335, https://doi.org/10.5194/acp-15-6323-2015, 2015.

McClure, C. D., Lim, C. Y., Hagan, D. H., Kroll, J. H., and Cappa, C. D.: Biomass-burning-derived particles from a wide variety of fuels – Part 1: Properties of primary particles, Atmospheric Chemistry and Physics, 20, 1531–1547, https://doi.org/10.5194/acp-20-1531-2020, 2020.

McParland, E. L. and Levine, N. M.: The role of differential DMSP production and community composition in predicting variability of global surface DMSP concentrations, Limnology and Oceanography, 64, 757–773, https://doi.org/10.1002/lno.11076, 2019.

Menut, L., Flamant, C., Turquety, S., Deroubaix, A., Chazette, P., and Meynadier, R.: Impact of biomass burning on pollutant surface concentrations in megacities of the Gulf of Guinea, Atmospheric Chemistry and Physics, 18, 2687–2707, https://doi.org/10.5194/acp-18-2687-2018, 2018.

Mims, S. R., Kahn, R. A., Moroney, C. M., Gaitley, B. J., Nelson, D. L., and Garay, M. J.: MISR Stereo Heights of Grassland Fire Smoke Plumes in Australia, IEEE Transactions on Geoscience and Remote Sensing, 48, 25–35, https://doi.org/10.1109/TGRS.2009.2027114, 2010.

Mirme, S. and Mirme, A.: The mathematical principles and design of the NAIS – a spectrometer for the measurement of cluster ion and nanometer aerosol size distributions, Atmospheric Measurement Techniques, 6, 1061–1071, https://doi.org/10.5194/amt-6-1061-2013, 2013.

Mirrielees, J. A., Kirpes, R. M., Costa, E. J., Porter, G. C. E., Murray, B. J., Lata, N. N., Boschi, V., China, S., Grannas, A. M., Ault, A. P., Matrai, P. A., and Pratt, K. A.: Marine aerosol generation experiments in the High Arctic during summertime, Elementa: Science of the Anthropocene, 12, 00134, https://doi.org/10.1525/elementa.2023.00134, 2024.

Moore, R. H., Wiggins, E. B., Ahern, A. T., Zimmerman, S., Montgomery, L., Campuzano Jost, P., Robinson, C. E., Ziemba, L. D., Winstead, E. L., Anderson, B. E., Brock, C. A., Brown, M. D., Chen, G., Crosbie, E. C., Guo, H., Jimenez, J. L., Jordan, C. E., Lyu, M., Nault, B. A., Rothfuss, N. E., Sanchez, K. J., Schueneman, M., Shingler, T. J., Shook, M. A., Thornhill, K. L., Wagner, N. L., and Wang, J.: Sizing response of the Ultra-High Sensitivity Aerosol Spectrometer (UHSAS) and Laser Aerosol Spectrometer (LAS) to changes in submicron aerosol composition and refractive index, Atmospheric Measurement Techniques, 14, 4517–4542, https://doi.org/10.5194/amt-14-4517-2021, 2021.

Moritz, M. A., Parisien, M.-A., Batllori, E., Krawchuk, M. A., Van Dorn, J., Ganz, D. J., and Hayhoe, K.: Climate change and disruptions to global fire activity, Ecosphere, 3, art49, https://doi.org/10.1890/ES11-00345.1, 2012.

Moschos, V., Schmale, J., Aas, W., Becagli, S., Calzolai, G., Eleftheriadis, K., Moffett, C. E., Schnelle-Kreis, J., Severi, M., Sharma, S., Skov, H., Vestenius, M., Zhang, W., Hakola, H., Hellén, H., Huang, L., Jaffrezo, J.-L., Massling, A., Nøjgaard, J. K., Petäjä, T., Popovicheva, O., Sheesley, R. J., Traversi, R., Yttri, K. E., Prévôt, A. S. H., Baltensperger, U., and El Haddad, I.: Elucidating the present-day chemical composition, seasonality and source regions of climate-relevant aerosols across the Arctic land surface, Environ. Res. Lett., 17, 034032, https://doi.org/10.1088/1748-9326/ac444b, 2022a.

Moschos, V., Dzepina, K., Bhattu, D., Lamkaddam, H., Casotto, R., Daellenbach, K. R., Canonaco, F., Rai, P., Aas, W., Becagli, S., Calzolai, G., Eleftheriadis, K., Moffett, C. E., Schnelle-Kreis, J., Severi, M., Sharma, S., Skov, H., Vestenius, M., Zhang, W., Hakola, H., Hellén, H., Huang, L., Jaffrezo, J.-L., Massling, A., Nøjgaard, J. K., Petäjä, T., Popovicheva, O., Sheesley, R. J., Traversi, R., Yttri, K. E., Schmale, J., Prévôt, A. S. H., Baltensperger, U., and El Haddad, I.: Equal abundance of summertime natural and wintertime anthropogenic Arctic organic aerosols, Nat. Geosci., 15, 196–202, https://doi.org/10.1038/s41561-021-00891-1, 2022b.

Mungall, E. L., Croft, B., Lizotte, M., Thomas, J. L., Murphy, J. G., Levasseur, M., Martin, R. V., Wentzell, J. J. B., Liggio, J., and Abbatt, J. P. D.: Dimethyl sulfide in the summertime Arctic atmosphere: measurements and source sensitivity simulations, Atmospheric Chemistry and Physics, 16, 6665–6680, https://doi.org/10.5194/acp-16-6665-2016, 2016.

Napari, I., Noppel, M., Vehkamäki, H., and Kulmala, M.: Parametrization of ternary nucleation rates for H2SO4-NH3-H2O vapors, Journal of Geophysical Research: Atmospheres, 107, AAC 6-1-AAC 6-6, https://doi.org/10.1029/2002JD002132, 2002.

Nguyen, Q. T., Glasius, M., Sørensen, L. L., Jensen, B., Skov, H., Birmili, W., Wiedensohler, A., Kristensson, A., Nøjgaard, J. K., and Massling, A.: Seasonal variation of atmospheric particle number concentrations, new particle formation and atmospheric oxidation capacity at the high Arctic site Villum Research Station, Station Nord, Atmospheric Chemistry and Physics, 16, 11319–11336, https://doi.org/10.5194/acp-16-11319-2016, 2016.

Nieminen, T., Kerminen, V.-M., Petäjä, T., Aalto, P. P., Arshinov, M., Asmi, E., Baltensperger, U., Beddows, D. C. S., Beukes, J. P., Collins, D., Ding, A., Harrison, R. M., Henzing, B., Hooda, R., Hu, M., Hõrrak, U., Kivekäs, N., Komsaare, K., Krejci, R., Kristensson, A., Laakso, L., Laaksonen, A., Leaitch, W. R., Lihavainen, H., Mihalopoulos, N., Németh, Z., Nie, W., O'Dowd, C., Salma, I., Sellegri, K., Svenningsson, B., Swietlicki, E., Tunved, P., Ulevicius, V., Vakkari, V., Vana, M., Wiedensohler, A., Wu, Z., Virtanen, A., and Kulmala, M.: Global analysis of continental boundary layer new particle formation based on long-term measurements, Atmospheric Chemistry and Physics, 18, 14737–14756, https://doi.org/10.5194/acp-18-14737-2018, 2018.

Novak, G. A., Fite, C. H., Holmes, C. D., Veres, P. R., Neuman, J. A., Faloona, I., Thornton, J. A., Wolfe, G. M., Vermeuel, M. P., Jernigan, C. M., Peischl, J., Ryerson, T. B., Thompson, C. R., Bourgeois, I., Warneke, C., Gkatzelis, G. I., Coggon, M. M., Sekimoto, K., Bui, T. P., Dean-Day, J., Diskin, G. S., DiGangi, J. P., Nowak, J. B., Moore, R. H., Wiggins, E. B., Winstead, E. L., Robinson, C., Thornhill, K. L., Sanchez, K. J., Hall, S. R., Ullmann, K., Dollner, M., Weinzierl, B., Blake, D. R., and Bertram, T. H.: Rapid cloud removal of dimethyl sulfide oxidation products limits SO2 and cloud condensation nuclei production in the marine atmosphere, Proceedings of the National Academy of Sciences, 118, e2110472118, https://doi.org/10.1073/pnas.2110472118, 2021.

Novak, G. A., Kilgour, D. B., Jernigan, C. M., Vermeuel, M. P., and Bertram, T. H.: Oceanic emissions of dimethyl sulfide and methanethiol and their contribution to sulfur dioxide production in the marine atmosphere, Atmospheric Chemistry and Physics, 22, 6309–6325, https://doi.org/10.5194/acp-22-6309-2022, 2022.

O'Dell, K., Ford, B., Fischer, E. V., and Pierce, J. R.: Contribution of Wildland-Fire Smoke to US PM2.5 and Its Influence on Recent Trends, Environ. Sci. Technol., 53, 1797–1804, https://doi.org/10.1021/acs.est.8b05430, 2019.

O'Dell, K., Bilsback, K., Ford, B., Martenies, S. E., Magzamen, S., Fischer, E. V., and Pierce, J. R.: Estimated Mortality and Morbidity Attributable to Smoke Plumes in the United States: Not Just a Western US Problem, GeoHealth, 5, e2021GH000457, https://doi.org/10.1029/2021GH000457, 2021.

O'Donnell, S. E., Akherati, A., He, Y., Hodshire, A. L., Shilling, J. E., Kuang, C., Fast, J. D., Mei, F., Schobesberger, S., Thornton, J. A., Smith, J. N., Jathar, S. H., and Pierce, J. R.:

Look Up: Probing the Vertical Profile of New Particle Formation and Growth in the Planetary Boundary Layer With Models and Observations, Journal of Geophysical Research: Atmospheres, 128, e2022JD037525, https://doi.org/10.1029/2022JD037525, 2023.

Omar, A. H., Winker, D. M., Vaughan, M. A., Hu, Y., Trepte, C. R., Ferrare, R. A., Lee, K.-P., Hostetler, C. A., Kittaka, C., Rogers, R. R., Kuehn, R. E., and Liu, Z.: The CALIPSO Automated Aerosol Classification and Lidar Ratio Selection Algorithm, Journal of Atmospheric and Oceanic Technology, 26, 1994–2014, https://doi.org/10.1175/2009JTECHA1231.1, 2009.

Onasch, T. B., Trimborn, A., Fortner, E. C., Jayne, J. T., Kok, G. L., Williams, L. R., Davidovits, P., and Worsnop, D. R.: Soot Particle Aerosol Mass Spectrometer: Development, Validation, and Initial Application, Aerosol Science and Technology, 46, 804–817, https://doi.org/10.1080/02786826.2012.663948, 2012.

Ooi, M. C.-G., Chuang, M.-T., Fu, J. S., Kong, S. S., Huang, W.-S., Wang, S.-H., Pimonsree, S., Chan, A., Pani, S. K., and Lin, N.-H.: Improving prediction of trans-boundary biomass burning plume dispersion: from northern peninsular Southeast Asia to downwind western North Pacific Ocean, Atmospheric Chemistry and Physics, 21, 12521–12541, https://doi.org/10.5194/acp-21-12521-2021, 2021.

Pagonis, D., Campuzano-Jost, P., Guo, H., Day, D. A., Schueneman, M. K., Brown, W. L., Nault, B. A., Stark, H., Siemens, K., Laskin, A., Piel, F., Tomsche, L., Wisthaler, A., Coggon, M. M., Gkatzelis, G. I., Halliday, H. S., Krechmer, J. E., Moore, R. H., Thomson, D. S., Warneke, C., Wiggins, E. B., and Jimenez, J. L.: Airborne extractive electrospray mass spectrometry measurements of the chemical composition of organic aerosol, Atmospheric Measurement Techniques, 14, 1545–1559, https://doi.org/10.5194/amt-14-1545-2021, 2021.

Pagonis, D., Selimovic, V., Campuzano-Jost, P., Guo, H., Day, D. A., Schueneman, M. K., Nault, B. A., Coggon, M. M., DiGangi, J. P., Diskin, G. S., Fortner, E. C., Gargulinski, E. M., Gkatzelis, G. I., Hair, J. W., Herndon, S. C., Holmes, C. D., Katich, J. M., Nowak, J. B., Perring, A. E., Saide, P., Shingler, T. J., Soja, A. J., Thapa, L. H., Warneke, C., Wiggins, E. B., Wisthaler, A., Yacovitch, T. I., Yokelson, R. J., and Jimenez, J. L.: Impact of Biomass Burning Organic Aerosol Volatility on Smoke Concentrations Downwind of Fires, Environ. Sci. Technol., 57, 17011–17021, https://doi.org/10.1021/acs.est.3c05017, 2023.

Pai, S. J., Heald, C. L., Pierce, J. R., Farina, S. C., Marais, E. A., Jimenez, J. L., Campuzano-Jost, P., Nault, B. A., Middlebrook, A. M., Coe, H., Shilling, J. E., Bahreini, R., Dingle, J. H., and Vu, K.: An evaluation of global organic aerosol schemes using airborne observations, Atmospheric Chemistry and Physics, 20, 2637–2665, https://doi.org/10.5194/acp-20-2637-2020, 2020.

Palm, B. B., Peng, Q., Fredrickson, C. D., Lee, B. H., Garofalo, L. A., Pothier, M. A., Kreidenweis, S. M., Farmer, D. K., Pokhrel, R. P., Shen, Y., Murphy, S. M., Permar, W.,

Hu, L., Campos, T. L., Hall, S. R., Ullmann, K., Zhang, X., Flocke, F., Fischer, E. V., and Thornton, J. A.: Quantification of organic aerosol and brown carbon evolution in fresh wildfire plumes, PNAS, 117, 29469–29477, https://doi.org/10.1073/pnas.2012218117, 2020.

Palm, B. B., Peng, Q., Hall, S. R., Ullmann, K., Campos, T. L., Weinheimer, A., Montzka, D., Tyndall, G., Permar, W., Hu, L., Flocke, F., Fischer, E. V., and Thornton, J. A.: Spatially Resolved Photochemistry Impacts Emissions Estimates in Fresh Wildfire Plumes, Geophysical Research Letters, 48, e2021GL095443, https://doi.org/10.1029/2021GL095443, 2021.

Park, K.-T., Yoon, Y. J., Lee, K., Tunved, P., Krejci, R., Ström, J., Jang, E., Kang, H. J., Jang, S., Park, J., Lee, B. Y., Traversi, R., Becagli, S., and Hermansen, O.: Dimethyl Sulfide-Induced Increase in Cloud Condensation Nuclei in the Arctic Atmosphere, Global Biogeochemical Cycles, 35, e2021GB006969, https://doi.org/10.1029/2021GB006969, 2021.

Paugam, R., Wooster, M., Atherton, J., Freitas, S. R., Schultz, M. G., and Kaiser, J. W.: Development and optimization of a wildfire plume rise model based on remote sensing data inputs – Part 2, Atmospheric Chemistry and Physics Discussions, 15, 9815–9895, https://doi.org/10.5194/acpd-15-9815-2015, 2015.

Paugam, R., Wooster, M., Freitas, S., and Val Martin, M.: A review of approaches to estimate wildfire plume injection height within large-scale atmospheric chemical transport models, Atmospheric Chemistry and Physics, 16, 907–925, https://doi.org/10.5194/acp-16-907-2016, 2016.

Peng, Q., Palm, B. B., Melander, K. E., Lee, B. H., Hall, S. R., Ullmann, K., Campos, T., Weinheimer, A. J., Apel, E. C., Hornbrook, R. S., Hills, A. J., Montzka, D. D., Flocke, F., Hu, L., Permar, W., Wielgasz, C., Lindaas, J., Pollack, I. B., Fischer, E. V., Bertram, T. H., and Thornton, J. A.: HONO Emissions from Western U.S. Wildfires Provide Dominant Radical Source in Fresh Wildfire Smoke, Environ. Sci. Technol., 54, 5954–5963, https://doi.org/10.1021/acs.est.0c00126, 2020.

Peterson, D. A., Campbell, J. R., Hyer, E. J., Fromm, M. D., Kablick, G. P., Cossuth, J. H., and DeLand, M. T.: Wildfire-driven thunderstorms cause a volcano-like stratospheric injection of smoke, npj Clim Atmos Sci, 1, 1–8, https://doi.org/10.1038/s41612-018-0039-3, 2018.

Petters, M. D. and Kreidenweis, S. M.: A single parameter representation of hygroscopic growth and cloud condensation nucleus activity, Atmospheric Chemistry and Physics, 7, 1961–1971, https://doi.org/10.5194/acp-7-1961-2007, 2007.

Petters, M. D., Carrico, C. M., Kreidenweis, S. M., Prenni, A. J., DeMott, P. J., Collett Jr., J. L., and Moosmüller, H.: Cloud condensation nucleation activity of biomass burning aerosol, Journal of Geophysical Research: Atmospheres, 114, https://doi.org/10.1029/2009JD012353, 2009.

Philip, S., Martin, R. V., Pierce, J. R., Jimenez, J. L., Zhang, Q., Canagaratna, M. R., Spracklen, D. V., Nowlan, C. R., Lamsal, L. N., Cooper, M. J., and Krotkov, N. A.: Spatially and seasonally resolved estimate of the ratio of organic mass to organic carbon, Atmospheric Environment, 87, 34–40, https://doi.org/10.1016/j.atmosenv.2013.11.065, 2014.

Pierce, J. R. and Adams, P. J.: Global evaluation of CCN formation by direct emission of sea salt and growth of ultrafine sea salt, Journal of Geophysical Research: Atmospheres, 111, https://doi.org/10.1029/2005JD006186, 2006.

Pierce, J. R. and Adams, P. J.: Efficiency of cloud condensation nuclei formation from ultrafine particles, Atmospheric Chemistry and Physics, 7, 1367–1379, https://doi.org/10.5194/acp-7-1367-2007, 2007.

Pierce, J. R. and and Adams, P. J.: A Computationally Efficient Aerosol Nucleation/ Condensation Method: Pseudo-Steady-State Sulfuric Acid, Aerosol Science and Technology, 43, 216–226, https://doi.org/10.1080/02786820802587896, 2009.

Pierce, J. R., Chen, K., and Adams, P. J.: Contribution of primary carbonaceous aerosol to cloud condensation nuclei: processes and uncertainties evaluated with a global aerosol microphysics model, Atmospheric Chemistry and Physics, 7, 5447–5466, https://doi.org/10.5194/acp-7-5447-2007, 2007.

Pierce, J. R., Riipinen, I., Kulmala, M., Ehn, M., Petäjä, T., Junninen, H., Worsnop, D. R., and Donahue, N. M.: Quantification of the volatility of secondary organic compounds in ultrafine particles during nucleation events, Atmospheric Chemistry and Physics, 11, 9019–9036, https://doi.org/10.5194/acp-11-9019-2011, 2011.

Pierce, J. R., Croft, B., Kodros, J. K., D'Andrea, S. D., and Martin, R. V.: The importance of interstitial particle scavenging by cloud droplets in shaping the remote aerosol size distribution and global aerosol-climate effects, Atmospheric Chemistry and Physics, 15, 6147–6158, https://doi.org/10.5194/acp-15-6147-2015, 2015.

Polissar, A. V., Hopke, P. K., Paatero, P., Malm, W. C., and Sisler, J. F.: Atmospheric aerosol over Alaska: 2. Elemental composition and sources, Journal of Geophysical Research: Atmospheres, 103, 19045–19057, https://doi.org/10.1029/98JD01212, 1998.

Polissar, A. V., Hopke, P. K., and Harris, J. M.: Source Regions for Atmospheric Aerosol Measured at Barrow, Alaska, Environ. Sci. Technol., 35, 4214–4226, https://doi.org/10.1021/es0107529, 2001.

Pratt, K. A., Custard, K. D., Shepson, P. B., Douglas, T. A., Pöhler, D., General, S., Zielcke, J., Simpson, W. R., Platt, U., Tanner, D. J., Gregory Huey, L., Carlsen, M., and Stirm, B. H.: Photochemical production of molecular bromine in Arctic surface snowpacks, Nature Geosci, 6, 351–356, https://doi.org/10.1038/ngeo1779, 2013.

Preunkert, S., Jourdain, B., Legrand, M., Udisti, R., Becagli, S., and Cerri, O.: Seasonality of sulfur species (dimethyl sulfide, sulfate, and methanesulfonate) in Antarctica: Inland

versus coastal regions, Journal of Geophysical Research: Atmospheres, 113, https://doi.org/10.1029/2008JD009937, 2008.

Quinn, P. K., Coffman, D. J., Johnson, J. E., Upchurch, L. M., and Bates, T. S.: Small fraction of marine cloud condensation nuclei made up of sea spray aerosol, Nature Geosci, 10, 674–679, https://doi.org/10.1038/ngeo3003, 2017.

Ramnarine, E., Kodros, J. K., Hodshire, A. L., Lonsdale, C. R., Alvarado, M. J., and Pierce, J. R.: Effects of near-source coagulation of biomass burning aerosols on global predictions of aerosol size distributions and implications for aerosol radiative effects, Atmospheric Chemistry and Physics, 19, 6561–6577, https://doi.org/10.5194/acp-19-6561-2019, 2019.

Raso, A. R. W., Custard, K. D., May, N. W., Tanner, D., Newburn, M. K., Walker, L., Moore, R. J., Huey, L. G., Alexander, L., Shepson, P. B., and Pratt, K. A.: Active molecular iodine photochemistry in the Arctic, Proceedings of the National Academy of Sciences, 114, 10053–10058, https://doi.org/10.1073/pnas.1702803114, 2017.

Reddington, C. L., Carslaw, K. S., Stier, P., Schutgens, N., Coe, H., Liu, D., Allan, J., Browse, J., Pringle, K. J., Lee, L. A., Yoshioka, M., Johnson, J. S., Regayre, L. A., Spracklen, D. V., Mann, G. W., Clarke, A., Hermann, M., Henning, S., Wex, H., Kristensen, T. B., Leaitch, W. R., Pöschl, U., Rose, D., Andreae, M. O., Schmale, J., Kondo, Y., Oshima, N., Schwarz, J. P., Nenes, A., Anderson, B., Roberts, G. C., Snider, J. R., Leck, C., Quinn, P. K., Chi, X., Ding, A., Jimenez, J. L., and Zhang, Q.: The Global Aerosol Synthesis and Science Project (GASSP): Measurements and Modeling to Reduce Uncertainty, https://doi.org/10.1175/BAMS-D-15-00317.1, 2017.

Reid, C. E., Brauer, M., Johnston, F. H., Jerrett, M., Balmes, J. R., and Elliott, C. T.: Critical Review of Health Impacts of Wildfire Smoke Exposure, Environmental Health Perspectives, 124, 1334–1343, https://doi.org/10.1289/ehp.1409277, 2016.

Reid, J. S. and Hobbs, P. V.: Physical and optical properties of young smoke from individual biomass fires in Brazil, Journal of Geophysical Research: Atmospheres, 103, 32013–32030, https://doi.org/10.1029/98JD00159, 1998.

Reid, J. S., Koppmann, R., Eck, T. F., and Eleuterio, D. P.: A review of biomass burning emissions part II: intensive physical properties of biomass burning particles, Atmos. Chem. Phys., 27, 2005a.

Reid, J. S., Eck, T. F., Christopher, S. A., Koppmann, R., Dubovik, O., Eleuterio, D. P., Holben, B. N., Reid, E. A., and Zhang, J.: A review of biomass burning emissions part III: intensive optical properties of biomass burning particles, Atmospheric Chemistry and Physics, 5, 827–849, https://doi.org/10.5194/acp-5-827-2005, 2005b.

Rémy, S., Veira, A., Paugam, R., Sofiev, M., Kaiser, J. W., Marenco, F., Burton, S. P., Benedetti, A., Engelen, R. J., Ferrare, R., and Hair, J. W.: Two global data sets of daily fire emission injection heights since 2003, Atmospheric Chemistry and Physics, 17, 2921–2942, https://doi.org/10.5194/acp-17-2921-2017, 2017.

Riccobono, F., Schobesberger, S., Scott, C. E., Dommen, J., Ortega, I. K., Rondo, L., Almeida, J., Amorim, A., Bianchi, F., Breitenlechner, M., David, A., Downard, A., Dunne, E. M., Duplissy, J., Ehrhart, S., Flagan, R. C., Franchin, A., Hansel, A., Junninen, H., Kajos, M., Keskinen, H., Kupc, A., Kürten, A., Kvashin, A. N., Laaksonen, A., Lehtipalo, K., Makhmutov, V., Mathot, S., Nieminen, T., Onnela, A., Petäjä, T., Praplan, A. P., Santos, F. D., Schallhart, S., Seinfeld, J. H., Sipilä, M., Spracklen, D. V., Stozhkov, Y., Stratmann, F., Tomé, A., Tsagkogeorgas, G., Vaattovaara, P., Viisanen, Y., Vrtala, A., Wagner, P. E., Weingartner, E., Wex, H., Wimmer, D., Carslaw, K. S., Curtius, J., Donahue, N. M., Kirkby, J., Kulmala, M., Worsnop, D. R., and Baltensperger, U.: Oxidation Products of Biogenic Emissions Contribute to Nucleation of Atmospheric Particles, Science, 344, 717–721, https://doi.org/10.1126/science.1243527, 2014.

Rinaldi, M., Fuzzi, S., Decesari, S., Marullo, S., Santoleri, R., Provenzale, A., von Hardenberg, J., Ceburnis, D., Vaishya, A., O'Dowd, C. D., and Facchini, M. C.: Is chlorophyll-a the best surrogate for organic matter enrichment in submicron primary marine aerosol?, Journal of Geophysical Research: Atmospheres, 118, 4964–4973, https://doi.org/10.1002/jgrd.50417, 2013.

Robinson, A. L., Donahue, N. M., Shrivastava, M. K., Weitkamp, E. A., Sage, A. M., Grieshop, A. P., Lane, T. E., Pierce, J. R., and Pandis, S. N.: Rethinking Organic Aerosols: Semivolatile Emissions and Photochemical Aging, Science, https://doi.org/10.1126/science.1133061, 2007.

Rohrer, F. and Berresheim, H.: Strong correlation between levels of tropospheric hydroxyl radicals and solar ultraviolet radiation, Nature, 442, 184–187, https://doi.org/10.1038/nature04924, 2006.

Rolph, G., Stein, A., and Stunder, B.: Real-time Environmental Applications and Display sYstem: READY, Environmental Modelling & Software, 95, 210–228, https://doi.org/10.1016/j.envsoft.2017.06.025, 2017.

Rosati, B., Isokääntä, S., Christiansen, S., Jensen, M. M., Moosakutty, S. P., Wollesen de Jonge, R., Massling, A., Glasius, M., Elm, J., Virtanen, A., and Bilde, M.: Hygroscopicity and CCN potential of DMS-derived aerosol particles, Atmospheric Chemistry and Physics, 22, 13449–13466, https://doi.org/10.5194/acp-22-13449-2022, 2022.

Rush, S., Vlahos, P., Lee, C.-H., Lee, K., and Barrett, L. J.: Boron to salinity ratios in the Fram Strait entering the Central Arctic: The role of sea ice formation and future predictions, Marine Chemistry, 267, 104463, https://doi.org/10.1016/j.marchem.2024.104463, 2024.

Ryerson, T. B., Williams, E. J., and Fehsenfeld, F. C.: An efficient photolysis system for fast-response NO2 measurements, Journal of Geophysical Research: Atmospheres, 105, 26447–26461, https://doi.org/10.1029/2000JD900389, 2000.

Saiz-Lopez, A., Shillito, J. A., Coe, H., and Plane, J. M. C.: Measurements and modelling of I_2, IO, OIO, BrO and NO_3 in the mid-latitude marine boundary layer, Atmospheric Chemistry and Physics, 6, 1513–1528, https://doi.org/10.5194/acp-6-1513-2006, 2006.

Saiz-Lopez, A., Plane, J. M. C., Mahajan, A. S., Anderson, P. S., Bauguitte, S. J.-B., Jones, A. E., Roscoe, H. K., Salmon, R. A., Bloss, W. J., Lee, J. D., and Heard, D. E.: On the vertical distribution of boundary layer halogens over coastal Antarctica: implications for O_3, HO_x, NO_x and the Hg lifetime, Atmospheric Chemistry and Physics, 8, 887–900, https://doi.org/10.5194/acp-8-887-2008, 2008.

Saiz-Lopez, A., Blaszczak-Boxe, C. S., and Carpenter, L. J.: A mechanism for biologically induced iodine emissions from sea ice, Atmospheric Chemistry and Physics, 15, 9731–9746, https://doi.org/10.5194/acp-15-9731-2015, 2015.

Sakamoto, K. M., Allan, J. D., Coe, H., Taylor, J. W., Duck, T. J., and Pierce, J. R.: Aged boreal biomass-burning aerosol size distributions from BORTAS 2011, Atmospheric Chemistry and Physics, 15, 1633–1646, https://doi.org/10.5194/acp-15-1633-2015, 2015.

Sakamoto, K. M., Laing, J. R., Stevens, R. G., Jaffe, D. A., and Pierce, J. R.: The evolution of biomass-burning aerosol size distributions due to coagulation: dependence on fire and meteorological details and parameterization, Atmospheric Chemistry and Physics, 16, 7709–7724, https://doi.org/10.5194/acp-16-7709-2016, 2016.

Saleh, R., Robinson, E. S., Tkacik, D. S., Ahern, A. T., Liu, S., Aiken, A. C., Sullivan, R. C., Presto, A. A., Dubey, M. K., Yokelson, R. J., Donahue, N. M., and Robinson, A. L.: Brownness of organics in aerosols from biomass burning linked to their black carbon content, Nature Geosci, 7, 647–650, https://doi.org/10.1038/ngeo2220, 2014.

Samset, B. H. and Myhre, G.: Vertical dependence of black carbon, sulphate and biomass burning aerosol radiative forcing, Geophysical Research Letters, 38, https://doi.org/10.1029/2011GL049697, 2011.

Sand, M., Berntsen, T. K., von Salzen, K., Flanner, M. G., Langner, J., and Victor, D. G.: Response of Arctic temperature to changes in emissions of short-lived climate forcers, Nature Clim Change, 6, 286–289, https://doi.org/10.1038/nclimate2880, 2016.

Sander, R., Keene, W. C., Pszenny, A. a. P., Arimoto, R., Ayers, G. P., Baboukas, E., Cainey, J. M., Crutzen, P. J., Duce, R. A., Hönninger, G., Huebert, B. J., Maenhaut, W., Mihalopoulos, N., Turekian, V. C., and Van Dingenen, R.: Inorganic bromine in the marine boundary layer: a critical review, Atmospheric Chemistry and Physics, 3, 1301–1336, https://doi.org/10.5194/acp-3-1301-2003, 2003.

Schill, G. P., Froyd, K. D., Bian, H., Kupc, A., Williamson, C., Brock, C. A., Ray, E., Hornbrook, R. S., Hills, A. J., Apel, E. C., Chin, M., Colarco, P. R., and Murphy, D. M.: Widespread biomass burning smoke throughout the remote troposphere, Nat. Geosci., 13, 422–427, https://doi.org/10.1038/s41561-020-0586-1, 2020.

Schmale, J., Zieger, P., and Ekman, A. M. L.: Aerosols in current and future Arctic climate, Nat. Clim. Chang., 11, 95–105, https://doi.org/10.1038/s41558-020-00969-5, 2021.

Scholz, W., Shen, J., Aliaga, D., Wu, C., Carbone, S., Moreno, I., Zha, Q., Huang, W., Heikkinen, L., Jaffrezo, J. L., Uzu, G., Partoll, E., Leiminger, M., Velarde, F., Laj, P., Ginot, P.,

Artaxo, P., Wiedensohler, A., Kulmala, M., Mohr, C., Andrade, M., Sinclair, V., Bianchi, F., and Hansel, A.: Measurement report: Long-range transport and the fate of dimethyl sulfide oxidation products in the free troposphere derived from observations at the high-altitude research station Chacaltaya (5240 m a.s.l.) in the Bolivian Andes, Atmospheric Chemistry and Physics, 23, 895–920, https://doi.org/10.5194/acp-23-895-2023, 2023.

Seinfeld, J. H. and Pandis, S. N.: Atmospheric Chemistry and Physics: From Air Pollution to Climate Change, John Wiley & Sons, Incorporated, New York, UNITED STATES, 2016.

Sekimoto, K., Koss, A. R., Gilman, J. B., Selimovic, V., Coggon, M. M., Zarzana, K. J., Yuan, B., Lerner, B. M., Brown, S. S., Warneke, C., Yokelson, R. J., Roberts, J. M., and de Gouw, J.: High- and low-temperature pyrolysis profiles describe volatile organic compound emissions from western US wildfire fuels, Atmospheric Chemistry and Physics, 18, 9263–9281, https://doi.org/10.5194/acp-18-9263-2018, 2018.

Sellitto, P., Belhadji, R., Kloss, C., and Legras, B.: Radiative impacts of the Australian bushfires 2019–2020 – Part 1: Large-scale radiative forcing, Atmospheric Chemistry and Physics, 22, 9299–9311, https://doi.org/10.5194/acp-22-9299-2022, 2022.

Shetter, R. E. and Müller, M.: Photolysis frequency measurements using actinic flux spectroradiometry during the PEM-Tropics mission: Instrumentation description and some results, Journal of Geophysical Research: Atmospheres, 104, 5647–5661, https://doi.org/10.1029/98JD01381, 1999.

Shrivastava, M., Cappa, C. D., Fan, J., Goldstein, A. H., Guenther, A. B., Jimenez, J. L., Kuang, C., Laskin, A., Martin, S. T., Ng, N. L., Petaja, T., Pierce, J. R., Rasch, P. J., Roldin, P., Seinfeld, J. H., Shilling, J., Smith, J. N., Thornton, J. A., Volkamer, R., Wang, J., Worsnop, D. R., Zaveri, R. A., Zelenyuk, A., and Zhang, Q.: Recent advances in understanding secondary organic aerosol: Implications for global climate forcing, Reviews of Geophysics, 55, 509–559, https://doi.org/10.1002/2016RG000540, 2017.

Shrivastava, M., Fan, J., Zhang, Y., Rasool, Q. Z., Zhao, B., Shen, J., Pierce, J. R., Jathar, S. H., Akherati, A., Zhang, J., Zaveri, R. A., Gaudet, B., Liu, Y., Andreae, M. O., Pöhlker, M. L., Donahue, N. M., Wang, Y., and Seinfeld, J. H.: Intense formation of secondary ultrafine particles from Amazonian vegetation fires and their invigoration of deep clouds and precipitation, One Earth, 7, 1029–1043, https://doi.org/10.1016/j.oneear.2024.05.015, 2024.

Sillanpää, M., Hillamo, R., Saarikoski, S., Frey, A., Pennanen, A., Makkonen, U., Spolnik, Z., Van Grieken, R., Braniš, M., Brunekreef, B., Chalbot, M.-C., Kuhlbusch, T., Sunyer, J., Kerminen, V.-M., Kulmala, M., and Salonen, R. O.: Chemical composition and mass closure of particulate matter at six urban sites in Europe, Atmospheric Environment, 40, 212–223, https://doi.org/10.1016/j.atmosenv.2006.01.063, 2006.

Smith, J. D., Sio, V., Yu, L., Zhang, Q., and Anastasio, C.: Secondary Organic Aerosol Production from Aqueous Reactions of Atmospheric Phenols with an Organic Triplet

Excited State, Environ. Sci. Technol., 48, 1049–1057, https://doi.org/10.1021/es4045715, 2014.

Snow-Kropla, E. J., Pierce, J. R., Westervelt, D. M., and Trivitayanurak, W.: Cosmic rays, aerosol formation and cloud-condensation nuclei: sensitivities to model uncertainties, Atmospheric Chemistry and Physics, 11, 4001–4013, https://doi.org/10.5194/acp-11-4001-2011, 2011.

Souri, A. H., Duncan, B. N., Strode, S. A., Anderson, D. C., Manyin, M. E., Liu, J., Oman, L. D., Zhang, Z., and Weir, B.: Enhancing long-term trend simulation of the global tropospheric hydroxyl (TOH) and its drivers from 2005 to 2019: a synergistic integration of model simulations and satellite observations, Atmospheric Chemistry and Physics, 24, 8677–8701, https://doi.org/10.5194/acp-24-8677-2024, 2024.

Spracklen, D. V., Mickley, L. J., Logan, J. A., Hudman, R. C., Yevich, R., Flannigan, M. D., and Westerling, A. L.: Impacts of climate change from 2000 to 2050 on wildfire activity and carbonaceous aerosol concentrations in the western United States, Journal of Geophysical Research: Atmospheres, 114, https://doi.org/10.1029/2008JD010966, 2009.

Spracklen, D. V., Carslaw, K. S., Pöschl, U., Rap, A., and Forster, P. M.: Global cloud condensation nuclei influenced by carbonaceous combustion aerosol, Atmospheric Chemistry and Physics, 11, 9067–9087, https://doi.org/10.5194/acp-11-9067-2011, 2011.

Stefels, J.: Physiological aspects of the production and conversion of DMSP in marine algae and higher plants, Journal of Sea Research, 43, 183–197, https://doi.org/10.1016/S1385-1101(00)00030-7, 2000.

Stein, A. F., Draxler, R. R., Rolph, G. D., Stunder, B. J. B., Cohen, M. D., and Ngan, F.: NOAA's HYSPLIT Atmospheric Transport and Dispersion Modeling System, https://doi.org/10.1175/BAMS-D-14-00110.1, 2015.

Stockwell, C. E., Veres, P. R., Williams, J., and Yokelson, R. J.: Characterization of biomass burning emissions from cooking fires, peat, crop residue, and other fuels with high-resolution proton-transfer-reaction time-of-flight mass spectrometry, Atmospheric Chemistry and Physics, 15, 845–865, https://doi.org/10.5194/acp-15-845-2015, 2015.

Stohl, A.: Characteristics of atmospheric transport into the Arctic troposphere, Journal of Geophysical Research: Atmospheres, 111, https://doi.org/10.1029/2005JD006888, 2006.

Swanson, W. F., Holmes, C. D., Simpson, W. R., Confer, K., Marelle, L., Thomas, J. L., Jaeglé, L., Alexander, B., Zhai, S., Chen, Q., Wang, X., and Sherwen, T.: Comparison of model and ground observations finds snowpack and blowing snow aerosols both contribute to Arctic tropospheric reactive bromine, Atmospheric Chemistry and Physics, 22, 14467–14488, https://doi.org/10.5194/acp-22-14467-2022, 2022.

Tackett, J. L., Winker, D. M., Getzewich, B. J., Vaughan, M. A., Young, S. A., and Kar, J.: CALIPSO lidar level 3 aerosol profile product: version 3 algorithm design, Atmospheric

Measurement Techniques, 11, 4129–4152, https://doi.org/10.5194/amt-11-4129-2018, 2018.

Tashmim, L., Porter, W. C., Chen, Q., Alexander, B., Fite, C. H., Holmes, C. D., Pierce, J. R., Croft, B., and Ishino, S.: Contribution of expanded marine sulfur chemistry to the seasonal variability of dimethyl sulfide oxidation products and size-resolved sulfate aerosol, Atmospheric Chemistry and Physics, 24, 3379–3403, https://doi.org/10.5194/acp-24-3379-2024, 2024.

Thomas, M. A., Suntharalingam, P., Pozzoli, L., Rast, S., Devasthale, A., Kloster, S., Feichter, J., and Lenton, T. M.: Quantification of DMS aerosol-cloud-climate interactions using the ECHAM5-HAMMOZ model in a current climate scenario, Atmospheric Chemistry and Physics, 10, 7425–7438, https://doi.org/10.5194/acp-10-7425-2010, 2010.

Tjernström, M., Shupe, M. D., Brooks, I. M., Persson, P. O. G., Prytherch, J., Salisbury, D. J., Sedlar, J., Achtert, P., Brooks, B. J., Johnston, P. E., Sotiropoulou, G., and Wolfe, D.: Warm-air advection, air mass transformation and fog causes rapid ice melt, Geophysical Research Letters, 42, 5594–5602, https://doi.org/10.1002/2015GL064373, 2015.

Toom-Sauntry, D. and Barrie, L. A.: Chemical composition of snowfall in the high Arctic: 1990–1994, Atmospheric Environment, 36, 2683–2693, https://doi.org/10.1016/S1352-2310(02)00115-2, 2002.

Tosca, M. G., Randerson, J. T., Zender, C. S., Nelson, D. L., Diner, D. J., and Logan, J. A.: Dynamics of fire plumes and smoke clouds associated with peat and deforestation fires in Indonesia, Journal of Geophysical Research: Atmospheres, 116, https://doi.org/10.1029/2010JD015148, 2011.

Trentmann, J., Luderer, G., Winterrath, T., Fromm, M. D., Servranckx, R., Textor, C., Herzog, M., Graf, H.-F., and Andreae, M. O.: Modeling of biomass smoke injection into the lower stratosphere by a large forest fire (Part I): reference simulation, Atmospheric Chemistry and Physics, 6, 5247–5260, https://doi.org/10.5194/acp-6-5247-2006, 2006.

Tunved, P., Ström, J., and Krejci, R.: Arctic aerosol life cycle: linking aerosol size distributions observed between 2000 and 2010 with air mass transport and precipitation at Zeppelin station, Ny-Ålesund, Svalbard, Atmospheric Chemistry and Physics, 13, 3643–3660, https://doi.org/10.5194/acp-13-3643-2013, 2013.

Twomey, S.: Pollution and the planetary albedo, Atmospheric Environment (1967), 8, 1251–1256, https://doi.org/10.1016/0004-6981(74)90004-3, 1974.

Tyndall, G. S. and Ravishankara, A. R.: Kinetics of the reaction of the methylthio radical with ozone at 298 K, J. Phys. Chem., 93, 4707–4710, https://doi.org/10.1021/j100349a006, 1989.

Tyndall, G. S. and Ravishankara, A. R.: Atmospheric oxidation of reduced sulfur species, International Journal of Chemical Kinetics, 23, 483–527, https://doi.org/10.1002/kin.550230604, 1991.

Vakkari, V., Kerminen, V.-M., Beukes, J. P., Tiitta, P., van Zyl, P. G., Josipovic, M., Venter, A. D., Jaars, K., Worsnop, D. R., Kulmala, M., and Laakso, L.: Rapid changes in biomass burning aerosols by atmospheric oxidation, Geophysical Research Letters, 41, 2644–2651, https://doi.org/10.1002/2014GL059396, 2014.

Val Martin, M., Logan, J. A., Kahn, R. A., Leung, F.-Y., Nelson, D. L., and Diner, D. J.: Smoke injection heights from fires in North America: analysis of 5 years of satellite observations, Atmospheric Chemistry and Physics, 10, 1491–1510, https://doi.org/10.5194/acp-10-1491-2010, 2010.

Val Martin, M., Kahn, R. A., and Tosca, M. G.: A Global Analysis of Wildfire Smoke Injection Heights Derived from Space-Based Multi-Angle Imaging, Remote Sensing, 10, 1609, https://doi.org/10.3390/rs10101609, 2018.

Vehkamäki, H., Kulmala, M., Napari, I., Lehtinen, K. E. J., Timmreck, C., Noppel, M., and Laaksonen, A.: An improved parameterization for sulfuric acid–water nucleation rates for tropospheric and stratospheric conditions, Journal of Geophysical Research: Atmospheres, 107, AAC 3-1-AAC 3-10, https://doi.org/10.1029/2002JD002184, 2002.

Wales, P. A., Keller, C. A., Knowland, K. E., Pawson, S., Choi, S., Hendrick, F., Van Roozendael, M., Salawitch, R. J., Sulieman, R., and Swanson, W. F.: Application of Satellite-Based Detections of Arctic Bromine Explosion Events Within GEOS-Chem, Journal of Advances in Modeling Earth Systems, 15, e2022MS003465, https://doi.org/10.1029/2022MS003465, 2023.

Wallace, J. M. and Hobbs, P. V.: Atmospheric Science: An Introductory Survey, Elsevier, 507 pp., 2006.

Walter, C., Freitas, S. R., Kottmeier, C., Kraut, I., Rieger, D., Vogel, H., and Vogel, B.: The importance of plume rise on the concentrations and atmospheric impacts of biomass burning aerosol, Atmospheric Chemistry and Physics, 16, 9201–9219, https://doi.org/10.5194/acp-16-9201-2016, 2016.

Wang, M., Kong, W., Marten, R., He, X.-C., Chen, D., Pfeifer, J., Heitto, A., Kontkanen, J., Dada, L., Kürten, A., Yli-Juuti, T., Manninen, H. E., Amanatidis, S., Amorim, A., Baalbaki, R., Baccarini, A., Bell, D. M., Bertozzi, B., Bräkling, S., Brilke, S., Murillo, L. C., Chiu, R., Chu, B., De Menezes, L.-P., Duplissy, J., Finkenzeller, H., Carracedo, L. G., Granzin, M., Guida, R., Hansel, A., Hofbauer, V., Krechmer, J., Lehtipalo, K., Lamkaddam, H., Lampimäki, M., Lee, C. P., Makhmutov, V., Marie, G., Mathot, S., Mauldin, R. L., Mentler, B., Müller, T., Onnela, A., Partoll, E., Petäjä, T., Philippov, M., Pospisilova, V., Ranjithkumar, A., Rissanen, M., Rörup, B., Scholz, W., Shen, J., Simon, M., Sipilä, M., Steiner, G., Stolzenburg, D., Tham, Y. J., Tomé, A., Wagner, A. C., Wang, D. S., Wang, Y., Weber, S. K., Winkler, P. M., Wlasits, P. J., Wu, Y., Xiao, M., Ye, Q., Zauner-Wieczorek, M., Zhou, X., Volkamer, R., Riipinen, I., Dommen, J., Curtius, J., Baltensperger, U., Kulmala, M., Worsnop, D. R., Kirkby, J., Seinfeld, J. H., El-Haddad, I., Flagan, R. C., and Donahue, N. M.: Rapid growth of new atmospheric particles by

nitric acid and ammonia condensation, Nature, 581, 184–189, https://doi.org/10.1038/s41586-020-2270-4, 2020.

Wang, S., Coggon, M. M., Gkatzelis, G. I., Warneke, C., Bourgeois, I., Ryerson, T., Peischl, J., Veres, P. R., Neuman, J. A., Hair, J., Shingler, T., Fenn, M., Diskin, G., Huey, L. G., Lee, Y. R., Apel, E. C., Hornbrook, R. S., Hills, A. J., Hall, S. R., Ullmann, K., Bela, M. M., Trainer, M. K., Kumar, R., Orlando, J. J., Flocke, F. M., and Emmons, L. K.: Chemical Tomography in a Fresh Wildland Fire Plume: A Large Eddy Simulation (LES) Study, Journal of Geophysical Research: Atmospheres, 126, e2021JD035203, https://doi.org/10.1029/2021JD035203, 2021.

Wang, S. C. and Flagan, R. C.: Scanning Electrical Mobility Spectrometer, Aerosol Science and Technology, https://doi.org/10.1080/02786829008959441, 1990.

Warneke, C., Schwarz, J. P., Dibb, J., Kalashnikova, O., Frost, G., Al-Saad, J., Brown, S. S., Brewer, Wm. A., Soja, A., Seidel, F. C., Washenfelder, R. A., Wiggins, E. B., Moore, R. H., Anderson, B. E., Jordan, C., Yacovitch, T. I., Herndon, S. C., Liu, S., Kuwayama, T., Jaffe, D., Johnston, N., Selimovic, V., Yokelson, R., Giles, D. M., Holben, B. N., Goloub, P., Popovici, I., Trainer, M., Kumar, A., Pierce, R. B., Fahey, D., Roberts, J., Gargulinski, E. M., Peterson, D. A., Ye, X., Thapa, L. H., Saide, P. E., Fite, C. H., Holmes, C. D., Wang, S., Coggon, M. M., Decker, Z. C. J., Stockwell, C. E., Xu, L., Gkatzelis, G., Aikin, K., Lefer, B., Kaspari, J., Griffin, D., Zeng, L., Weber, R., Hastings, M., Chai, J., Wolfe, G. M., Hanisco, T. F., Liao, J., Campuzano Jost, P., Guo, H., Jimenez, J. L., Crawford, J., and Team, T. F.-A. S.: Fire Influence on Regional to Global Environments and Air Quality (FIREX-AQ), Journal of Geophysical Research: Atmospheres, 128, e2022JD037758, https://doi.org/10.1029/2022JD037758, 2023.

Washenfelder, R. A., Azzarello, L., Ball, K., Brown, S. S., Decker, Z. C. J., Franchin, A., Fredrickson, C. D., Hayden, K., Holmes, C. D., Middlebrook, A. M., Palm, B. B., Pierce, R. B., Price, D. J., Roberts, J. M., Robinson, M. A., Thornton, J. A., Womack, C. C., and Young, C. J.: Complexity in the Evolution, Composition, and Spectroscopy of Brown Carbon in Aircraft Measurements of Wildfire Plumes, Geophysical Research Letters, 49, e2022GL098951, https://doi.org/10.1029/2022GL098951, 2022.

Westervelt, D. M., Pierce, J. R., and Adams, P. J.: Analysis of feedbacks between nucleation rate, survival probability and cloud condensation nuclei formation, Atmospheric Chemistry and Physics, 14, 5577–5597, https://doi.org/10.5194/acp-14-5577-2014, 2014.

Wiedinmyer, C., Akagi, S. K., Yokelson, R. J., Emmons, L. K., Al-Saadi, J. A., Orlando, J. J., and Soja, A. J.: The Fire INventory from NCAR (FINN): a high resolution global model to estimate the emissions from open burning, Geoscientific Model Development, 4, 625–641, https://doi.org/10.5194/gmd-4-625-2011, 2011.

Wilkins, J. L., de Foy, B., Thompson, A. M., Peterson, D. A., Hyer, E. J., Graves, C., Fishman, J., and Morris, G. A.: Evaluation of Stratospheric Intrusions and Biomass Burning Plumes on the Vertical Distribution of Tropospheric Ozone Over the Midwestern United States,

Journal of Geophysical Research: Atmospheres, 125, e2020JD032454, https://doi.org/10.1029/2020JD032454, 2020.

Williams, A. S., Dedrick, J. L., Russell, L. M., Tornow, F., Silber, I., Fridlind, A. M., Swanson, B., DeMott, P. J., Zieger, P., and Krejci, R.: Aerosol size distribution properties associated with cold-air outbreaks in the Norwegian Arctic, Atmospheric Chemistry and Physics, 24, 11791–11805, https://doi.org/10.5194/acp-24-11791-2024, 2024.

Willis, M. D., Köllner, F., Burkart, J., Bozem, H., Thomas, J. L., Schneider, J., Aliabadi, A. A., Hoor, P. M., Schulz, H., Herber, A. B., Leaitch, W. R., and Abbatt, J. P. D.: Evidence for marine biogenic influence on summertime Arctic aerosol, Geophysical Research Letters, 44, 6460–6470, https://doi.org/10.1002/2017GL073359, 2017.

Willis, M. D., Leaitch, W. R., and Abbatt, J. P. D.: Processes Controlling the Composition and Abundance of Arctic Aerosol, Reviews of Geophysics, 56, 621–671, https://doi.org/10.1029/2018RG000602, 2018.

Willis, M. D., Lannuzel, D., Else, B., Angot, H., Campbell, K., Crabeck, O., Delille, B., Hayashida, H., Lizotte, M., Loose, B., Meiners, K. M., Miller, L., Moreau, S., Nomura, D., Prytherch, J., Schmale, J., Steiner, N., Tedesco, L., and Thomas, J.: Polar oceans and sea ice in a changing climate, Elementa: Science of the Anthropocene, 11, 00056, https://doi.org/10.1525/elementa.2023.00056, 2023.

Wilmot, T. Y., Mallia, D. V., Hallar, A. G., and Lin, J. C.: Wildfire plumes in the Western US are reaching greater heights and injecting more aerosols aloft as wildfire activity intensifies, Sci Rep, 12, 12400, https://doi.org/10.1038/s41598-022-16607-3, 2022.

Wohl, C., Jones, A. E., Sturges, W. T., Nightingale, P. D., Else, B., Butterworth, B. J., and Yang, M.: Sea ice concentration impacts dissolved organic gases in the Canadian Arctic, Biogeosciences, 19, 1021–1045, https://doi.org/10.5194/bg-19-1021-2022, 2022.

Wohl, C., Villamayor, J., Galí, M., Mahajan, A. S., Fernández, R. P., Cuevas, C. A., Bossolasco, A., Li, Q., Kettle, A. J., Williams, T., Sarda-Esteve, R., Gros, V., Simó, R., and Saiz-Lopez, A.: Marine emissions of methanethiol increase aerosol cooling in the Southern Ocean, Science Advances, 10, eadq2465, https://doi.org/10.1126/sciadv.adq2465, 2024.

Wollesen de Jonge, R., Elm, J., Rosati, B., Christiansen, S., Hyttinen, N., Lüdemann, D., Bilde, M., and Roldin, P.: Secondary aerosol formation from dimethyl sulfide – improved mechanistic understanding based on smog chamber experiments and modelling, Atmospheric Chemistry and Physics, 21, 9955–9976, https://doi.org/10.5194/acp-21-9955-2021, 2021.

Woodhouse, M. T., Carslaw, K. S., Mann, G. W., Vallina, S. M., Vogt, M., Halloran, P. R., and Boucher, O.: Low sensitivity of cloud condensation nuclei to changes in the sea-air flux of dimethyl-sulphide, Atmospheric Chemistry and Physics, 10, 7545–7559, https://doi.org/10.5194/acp-10-7545-2010, 2010.

Wu, Y., Han, Y., Voulgarakis, A., Wang, T., Li, M., Wang, Y., Xie, M., Zhuang, B., and Li, S.: An agricultural biomass burning episode in eastern China: Transport, optical properties, and impacts on regional air quality, Journal of Geophysical Research: Atmospheres, 122, 2304–2324, https://doi.org/10.1002/2016JD025319, 2017.

Xu, L., Crounse, J. D., Vasquez, K. T., Allen, H., Wennberg, P. O., Bourgeois, I., Brown, S. S., Campuzano-Jost, P., Coggon, M. M., Crawford, J. H., DiGangi, J. P., Diskin, G. S., Fried, A., Gargulinski, E. M., Gilman, J. B., Gkatzelis, G. I., Guo, H., Hair, J. W., Hall, S. R., Halliday, H. A., Hanisco, T. F., Hannun, R. A., Holmes, C. D., Huey, L. G., Jimenez, J. L., Lamplugh, A., Lee, Y. R., Liao, J., Lindaas, J., Neuman, J. A., Nowak, J. B., Peischl, J., Peterson, D. A., Piel, F., Richter, D., Rickly, P. S., Robinson, M. A., Rollins, A. W., Ryerson, T. B., Sekimoto, K., Selimovic, V., Shingler, T., Soja, A. J., St. Clair, J. M., Tanner, D. J., Ullmann, K., Veres, P. R., Walega, J., Warneke, C., Washenfelder, R. A., Weibring, P., Wisthaler, A., Wolfe, G. M., Womack, C. C., and Yokelson, R. J.: Ozone chemistry in western U.S. wildfire plumes, Science Advances, 7, eabl3648, https://doi.org/10.1126/sciadv.abl3648, 2021.

Yang, Q., Bitz, C. M., and Doherty, S. J.: Offsetting effects of aerosols on Arctic and global climate in the late 20th century, Atmospheric Chemistry and Physics, 14, 3969–3975, https://doi.org/10.5194/acp-14-3969-2014, 2014.

Yang, X., Pyle, J. A., and Cox, R. A.: Sea salt aerosol production and bromine release: Role of snow on sea ice, Geophysical Research Letters, 35, https://doi.org/10.1029/2008GL034536, 2008.

Yang, X., Pyle, J. A., Cox, R. A., Theys, N., and Van Roozendael, M.: Snow-sourced bromine and its implications for polar tropospheric ozone, Atmospheric Chemistry and Physics, 10, 7763–7773, https://doi.org/10.5194/acp-10-7763-2010, 2010.

Ye, X., Saide, P. E., Hair, J., Fenn, M., Shingler, T., Soja, A., Gargulinski, E., and Wiggins, E.: Assessing Vertical Allocation of Wildfire Smoke Emissions Using Observational Constraints From Airborne Lidar in the Western U.S., Journal of Geophysical Research: Atmospheres, 127, e2022JD036808, https://doi.org/10.1029/2022JD036808, 2022.

Yokelson, R. J., Crounse, J. D., DeCarlo, P. F., Karl, T., Urbanski, S., Atlas, E., Campos, T., Shinozuka, Y., Kapustin, V., Clarke, A. D., Weinheimer, A., Knapp, D. J., Montzka, D. D., Holloway, J., Weibring, P., Flocke, F., Zheng, W., Toohey, D., Wennberg, P. O., Wiedinmyer, C., Mauldin, L., Fried, A., Richter, D., Walega, J., Jimenez, J. L., Adachi, K., Buseck, P. R., Hall, S. R., and Shetter, R.: Emissions from biomass burning in the Yucatan, Atmospheric Chemistry and Physics, 9, 5785–5812, https://doi.org/10.5194/acp-9-5785-2009, 2009.

Yu, F., Luo, G., Nadykto, A. B., and Herb, J.: Impact of temperature dependence on the possible contribution of organics to new particle formation in the atmosphere, Atmospheric Chemistry and Physics, 17, 4997–5005, https://doi.org/10.5194/acp-17-4997-2017, 2017.

Yu, H., Kaufman, Y. J., Chin, M., Feingold, G., Remer, L. A., Anderson, T. L., Balkanski, Y., Bellouin, N., Boucher, O., Christopher, S., DeCola, P., Kahn, R., Koch, D., Loeb, N.,

Reddy, M. S., Schulz, M., Takemura, T., and Zhou, M.: A review of measurement-based assessments of the aerosol direct radiative effect and forcing, Atmospheric Chemistry and Physics, 6, 613–666, https://doi.org/10.5194/acp-6-613-2006, 2006.

Yu, K., Keller, C. A., Jacob, D. J., Molod, A. M., Eastham, S. D., and Long, M. S.: Errors and improvements in the use of archived meteorological data for chemical transport modeling: an analysis using GEOS-Chem v11-01 driven by GEOS-5 meteorology, Geoscientific Model Development, 11, 305–319, https://doi.org/10.5194/gmd-11-305-2018, 2018.

Yu, Y., Mao, J., Wullschleger, S. D., Chen, A., Shi, X., Wang, Y., Hoffman, F. M., Zhang, Y., and Pierce, E.: Machine learning–based observation-constrained projections reveal elevated global socioeconomic risks from wildfire, Nat Commun, 13, 1250, https://doi.org/10.1038/s41467-022-28853-0, 2022.

Yue, X., Mickley, L. J., Logan, J. A., and Kaplan, J. O.: Ensemble projections of wildfire activity and carbonaceous aerosol concentrations over the western United States in the mid-21st century, Atmospheric Environment, 77, 767–780, https://doi.org/10.1016/j.atmosenv.2013.06.003, 2013.

Zang, C. L. and Willis, M. D.: Deployment and evaluation of an NH_4^+/ H_3O^+ reagent ion switching chemical ionization mass spectrometer for the detection of reduced and oxygenated gas-phase organic compounds, Atmospheric Measurement Techniques, 18, 17–35, https://doi.org/10.5194/amt-18-17-2025, 2025.

Zaytsev, A., Breitenlechner, M., Koss, A. R., Lim, C. Y., Rowe, J. C., Kroll, J. H., and Keutsch, F. N.: Using collision-induced dissociation to constrain sensitivity of ammonia chemical ionization mass spectrometry (NH_4^+ CIMS) to oxygenated volatile organic compounds, Atmospheric Measurement Techniques, 12, 1861–1870, https://doi.org/10.5194/amt-12-1861-2019, 2019.

Zender, C. S., Bian, H., and Newman, D.: Mineral Dust Entrainment and Deposition (DEAD) model: Description and 1990s dust climatology, Journal of Geophysical Research: Atmospheres, 108, https://doi.org/10.1029/2002JD002775, 2003.

Zhai, S., Jacob, D. J., Brewer, J. F., Li, K., Moch, J. M., Kim, J., Lee, S., Lim, H., Lee, H. C., Kuk, S. K., Park, R. J., Jeong, J. I., Wang, X., Liu, P., Luo, G., Yu, F., Meng, J., Martin, R. V., Travis, K. R., Hair, J. W., Anderson, B. E., Dibb, J. E., Jimenez, J. L., Campuzano-Jost, P., Nault, B. A., Woo, J.-H., Kim, Y., Zhang, Q., and Liao, H.: Relating geostationary satellite measurements of aerosol optical depth (AOD) over East Asia to fine particulate matter ($PM_{2.5}$): insights from the KORUS-AQ aircraft campaign and GEOS-Chem model simulations, Atmospheric Chemistry and Physics, 21, 16775–16791, https://doi.org/10.5194/acp-21-16775-2021, 2021.

Zhang, X.-H., Liu, J., Liu, J., Yang, G., Xue, C.-X., Curson, A. R. J., and Todd, J. D.: Biogenic production of DMSP and its degradation to DMS—their roles in the global sulfur cycle, Sci. China Life Sci., 62, 1296–1319, https://doi.org/10.1007/s11427-018-9524-y, 2019.

Zhao, B., Donahue, N. M., Zhang, K., Mao, L., Shrivastava, M., Ma, P.-L., Shen, J., Wang, S., Sun, J., Gordon, H., Tang, S., Fast, J., Wang, M., Gao, Y., Yan, C., Singh, B., Li, Z., Huang, L., Lou, S., Lin, G., Wang, H., Jiang, J., Ding, A., Nie, W., Qi, X., Chi, X., and Wang, L.: Global variability in atmospheric new particle formation mechanisms, Nature, 631, 98–105, https://doi.org/10.1038/s41586-024-07547-1, 2024.

Zhou, S., Collier, S., Jaffe, D. A., Briggs, N. L., Hee, J., Sedlacek III, A. J., Kleinman, L., Onasch, T. B., and Zhang, Q.: Regional influence of wildfires on aerosol chemistry in the western US and insights into atmospheric aging of biomass burning organic aerosol, Atmospheric Chemistry and Physics, 17, 2477–2493, https://doi.org/10.5194/acp-17-2477-2017, 2017.

Zhou, S., Chen, Y., Huang, S., Gong, X., Yang, G., Zhang, H., Herrmann, H., Wiedensohler, A., Poulain, L., Zhang, Y., Wang, F., Xu, Z., and Yan, K.: A 20-year (1998–2017) global sea surface dimethyl sulfide gridded dataset with daily resolution, Earth System Science Data, 16, 4267–4290, https://doi.org/10.5194/essd-16-4267-2024, 2024.

Zhu, L., Val Martin, M., Gatti, L. V., Kahn, R., Hecobian, A., and Fischer, E. V.: Development and implementation of a new biomass burning emissions injection height scheme (BBEIH v1.0) for the GEOS-Chem model (v9-01-01), Geoscientific Model Development, 11, 4103–4116, https://doi.org/10.5194/gmd-11-4103-2018, 2018.

Appendix A: Supplement to Inclusion of Biomass Burning Plume Injection Height in GEOS-Chem-TOMAS: Global-Scale Implications for Atmospheric Aerosols and Radiative Forcing

Appendix A Text 1: AERONET AOD and $PM_{2.5}$ Comparisons

During periods of smoke, there are slight improvements in the NMB and normalized mean error (NME) between AERONET AOD at 440 nm and the BB-PIH simulations relative to that for the PBL simulation (Figure A.6a-A.6c). The NMB and NME for AOD improve in magnitude by about 2% in the HIGHER simulation compared to the PBL simulation during periods designated as smoke-impacted using the PBL simulation. The NMB and NME in HIGHER compared to PBL improve by 3% when using the HIGHER simulation to designate times as smoke-impacted. The low biases we see in AERONET AOD are comparable to those seen in prior studies using GEOS-Chem (AboEl-Fetouh et al., 2022; Kodros et al., 2016; Ma and Yu, 2015; Zhai et al., 2021). In all BB simulations, the AOD at 440 nm is generally within an order of magnitude of the AERONET AOD at 440 nm. Globally and regionally the simulations capture the seasonal cycle of AOD well (Figure A.7). Larger improvements in the AERONET to modeled AOD agreement are found for some regions and seasons. For example, during the BB season in Boreal NA there is a larger improvement in NMB as a result of the higher frequency of above PBL BB emissions in this region (Figure A.7c). As Chapter 2.3.2.2 shows, elevation of the BB-PIH has strong impacts on global-mean BB-DRE.

During periods of smoke, all BB simulations, regardless of BB-PIH, agree within an order of magnitude with the van Donkelaar et al. 2021 surface total $PM_{2.5}$ (Figure A.6d-A.6f). Part of the purpose of the van Donkelaar $PM_{2.5}$ product is GEOS-Chem does not accurately represent surface $PM_{2.5}$ concentrations; therefore by doing this comparison we can understand if we are closer to best estimates of surface $PM_{2.5}$ or if there are likely other sources of bias that

satellite products are still needed to correct. For months designated as smoke-impacted, the NMB of surface $PM_{2.5}$ is -49% in the PBL simulation and -54% in the HIGHER, compared to a NMB of -69% in the NBB simulation. When considering the entire 2-year simulation, NMB is -62% for the NBB simulation and -60% for all BB simulations for total $PM_{2.5}$ relative to the van Donkelarr et al. (2021) dataset. Hence, the model is biased low for total $PM_{2.5}$ likely due to reasons well beyond BB aerosol. The sign and magnitude of the biases between van Donkelaar et al. 2021 surface total $PM_{2.5}$ and the GEOS-Chem-TOMAS simulated surface total $PM_{2.5}$ were similar to previous studies using GEOS-Chem-TOMAS and a similar $PM_{2.5}$ product (Bilsback et al., 2020a; Gordon et al., 2023).

In most regions, the model captures the seasonal cycle of surface total $PM_{2.5}$ (Figure A.8). Even during months with little increase in surface total $PM_{2.5}$ due to BB, the simulations still have an underprediction, suggesting an underestimate in $PM_{2.5}$ from other sources in addition to BB. In boreal North America, changes due to the BB-PIH are evident during the 2019 BB season from April to August, where there was an increase in the low bias as BB-PIH increased. In boreal Asia, increases in low bias as BB-PIH were seen during both the 2019 and 2020 BB season. The 2019-2020 Australian bushfires showed increases in low bias during January 2020, but slight improvements in agreement during December 2019 and February 2020. Overall, the change in the total $PM_{2.5}$ biases due to raising the BB-PIH are smaller than the total $PM_{2.5}$ biases of the standard model (PBL).

In the CONUS, comparisons with van Donkelaar et al. (2021) total $PM_{2.5}$ indicate low bias in total $PM_{2.5}$ in all months and simulations with a two-year average NMB of -32 % in all BB simulations. In the two-year average, over the CONUS, the simulated total $PM_{2.5}$ NMB in the van Donkelaar et al. and O'Dell et al. comparisons have similar seasonal patterns (Figure A.9).

There are slight improvements in agreement in the southwestern and the eastern US. In comparison to the O'Dell et al. smoke-attributed $PM_{2.5}$ and modeled BB $PM_{2.5}$, raising the BB-PIH reduces bias in the Midwest and the eastern US. On a monthly basis, all BB-PIH simulations underestimate total surface $PM_{2.5}$ during the 2020 Western US wildfire season (August and September 2020) in comparison to both van Donkelaar et al. and O'Dell et al. total $PM_{2.5}$ (Figure A.9). In the comparisons with O'Dell et al., this low bias in total $PM_{2.5}$ over the CONUS is mostly due to underestimation of $PM_{2.5}$ due to BB during the 2020 Western US wildfire season in addition to low biases in non-smoke $PM_{2.5}$. In the western US, particularly California, there is an overestimate in BB $PM_{2.5}$ during the 2020 western US wildfire season, which is reduced by raising the BB-PIH, as this places the smoke away from the surface. Outside of these months, it appears that the model tends to underestimate non-smoke $PM_{2.5}$.

Appendix A Tables

Table A.1: Model Simulation Names and Descriptions

Simulation	Biomass Burning Plume Injection Height Scenario
NBB	N/A
PBL	Surface layer, instantaneously well-mixed into the planetary boundary layer
STANDARD	Normally distributed from GFAS altitude of plume bottom to GFAS altitude of plume top (standard)
HIGHER	Normally distributed from GFAS altitude of plume top to GFAS altitude of plume top plus the plume depth (shifted up)

Appendix A Figures

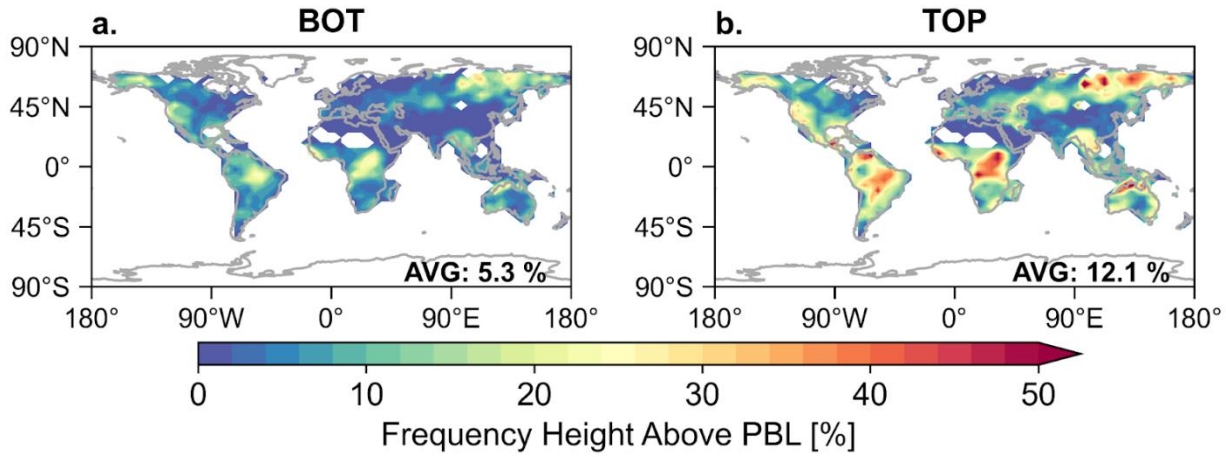

Figure A.1: Frequency the GFAS plume heights are above the PBL height for (a.) altitude of plume bottom (BOT), and (b.) altitude of plume top (TOP).

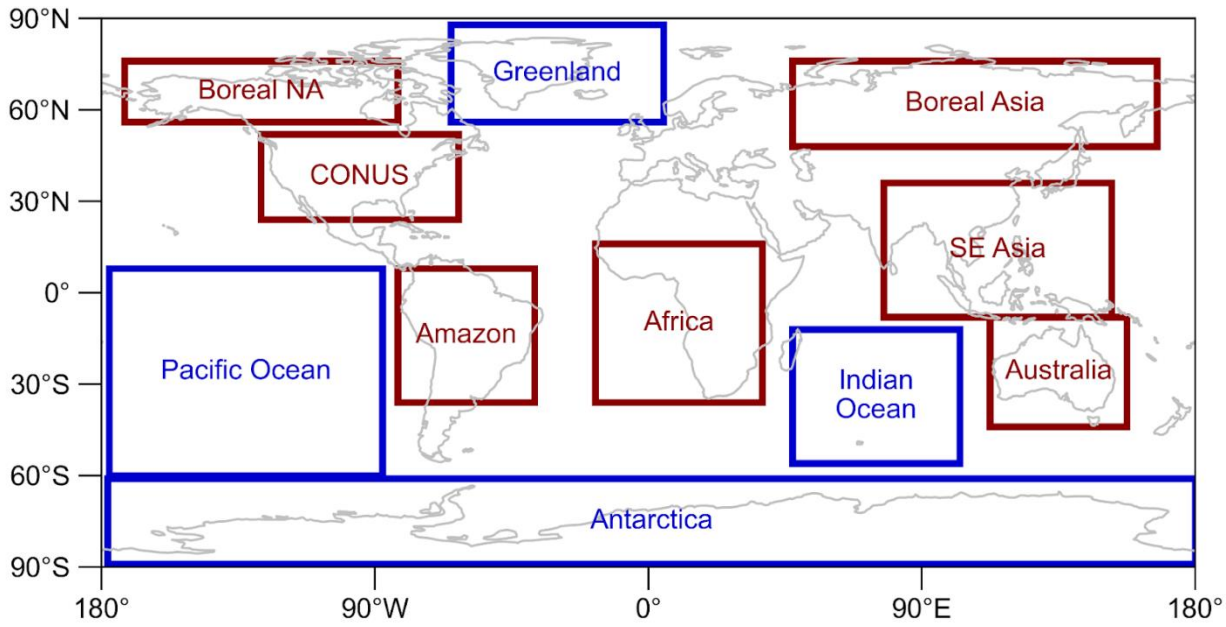

Figure A.2: Map of the biomass burning regions (red) and remote regions (blue) of interest in this study.

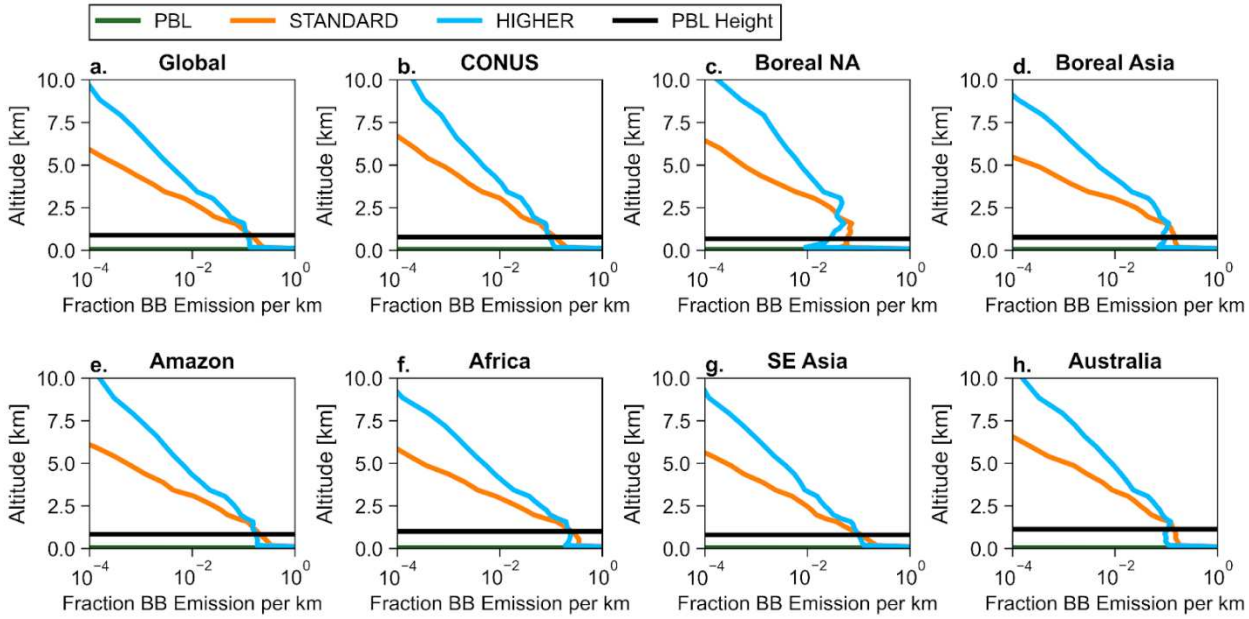

Figure A.3: Regional two-year mean (2019 to 2020) fraction of biomass burning emissions per km as a function of altitude in each source region (regions in Figure A.2). Each line represents a different plume injection height (PIH) scenario: PBL (green, all at surface then well-mixed in PBL), STANDARD (orange), and HIGHER (blue). For all simulations, emissions in the PBL are well-mixed between the surface and top of the PBL. Simulation acronyms are defined in Figure 2.1. For a reference point, the two-year average PBL height for each region is shown in black.

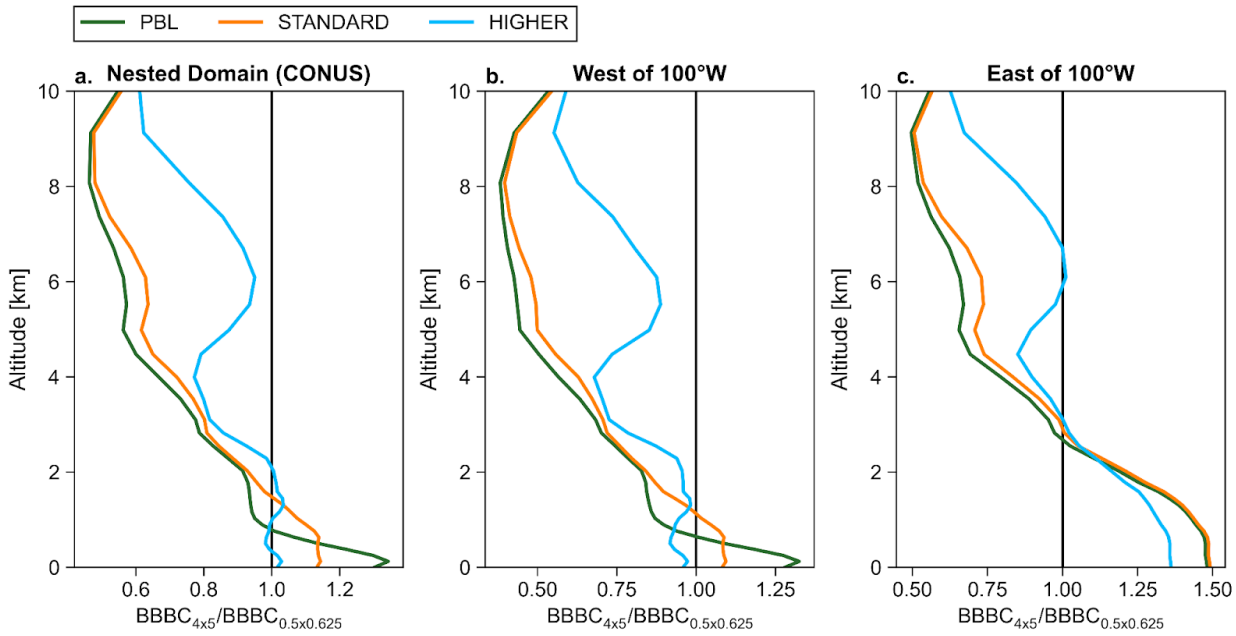

Figure A.4: Ratio of BB BC mass at 4°x5° ($BBBC_{4x5}$) to BB BC mass at 0.5°x0.625° ($BBBC_{0.5x0.625}$) during August and September 2020 in (a.) the nested simulation domain, (b.) the western portion of the nested domain, and (c.) the eastern portion of the nested domain as a function of altitude. Each line represents a different plume injection height (PIH) scenario: PBL (green), STANDARD (orange), and HIGHER (blue). Simulation acronyms are defined in Figure 2.1.

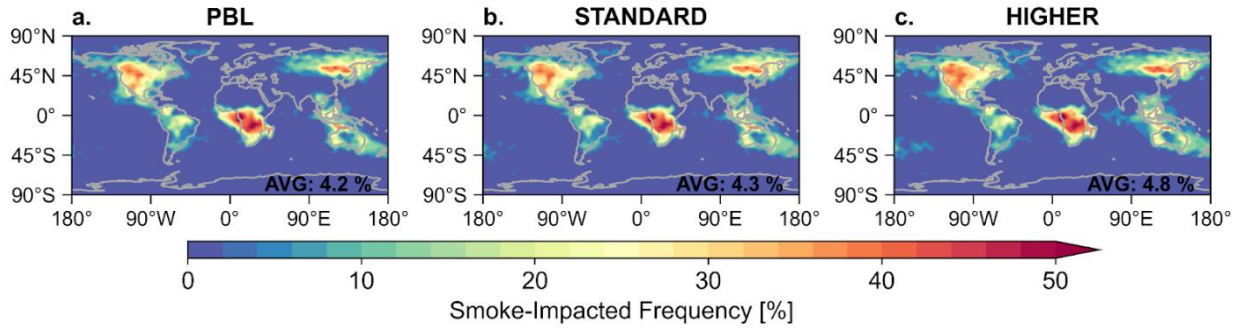

Figure A.5: Two-year (2019 to 2020) frequency of days with greater than a 50% increase in AOD at 440 nm due to BB, which are designated as smoke-impacted days by comparing the PBL simulation relative to the NBB simulation. Simulation acronyms are defined in Figure 2.1.

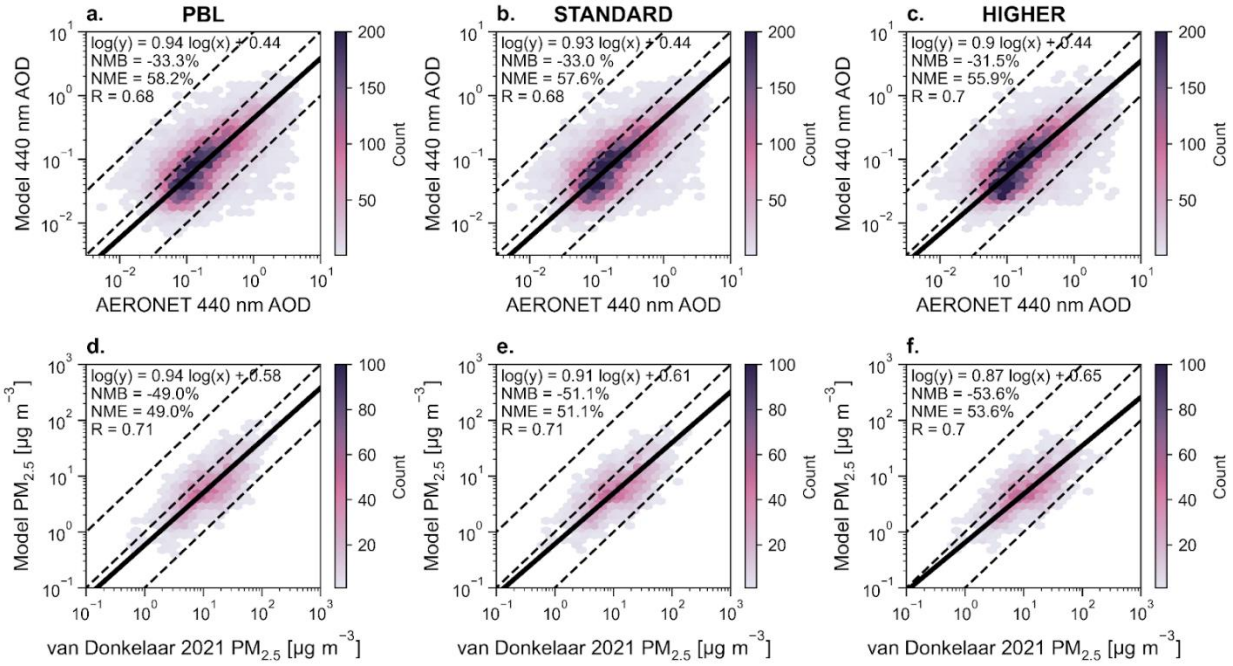

Figure A.6: 2D histograms of (a.)-(c.) AERONET AOD at 440 nm vs. Model AOD at 440 nm, (d.)-(f.) van Donkelaar et al. 2021 surface $PM_{2.5}$ vs. Model surface total $PM_{2.5}$. The data points on this figure are limited to smoky periods, defined as times when the model AOD at 440 nm increased by more than 50% between the NBB and PBL simulation at each location. On each panel is the best fit between the model and observations in solid black, the dashed lines are the 10:1, 1:1, and 1:10 lines. The equation for the best fit line, the normalized mean bias, normalized mean error, and the logspace Pearson correlation coefficient are shown on each panel.

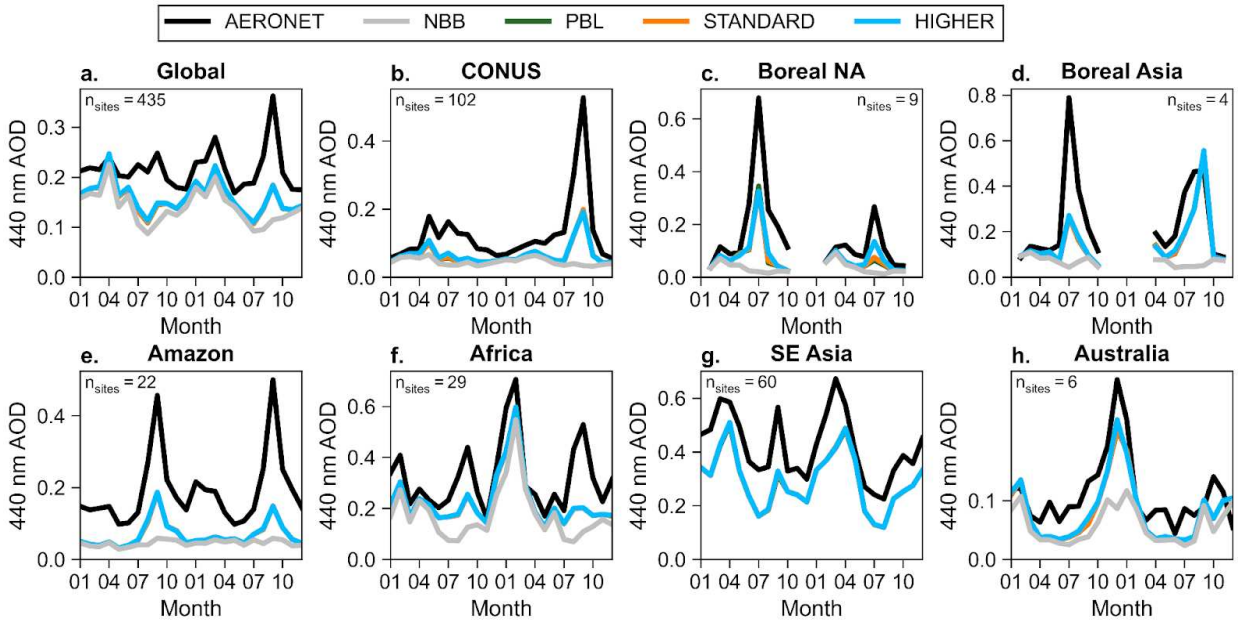

Figure A.7: Monthly averaged AOD at 440 nm at locations of AERONET sites by source region (regions in Figure A.2) for January 2019 to December 2020. The AERONET observations are in black. Model simulations are collocated to time and location of AERONET observations and are in different colors for each BB PIH scenario: PBL (green), STANDARD (orange), and HIGHER (blue). The simulation with biomass burning turned off (NBB) is shown in gray. Simulation acronyms are defined in Figure 2.1.

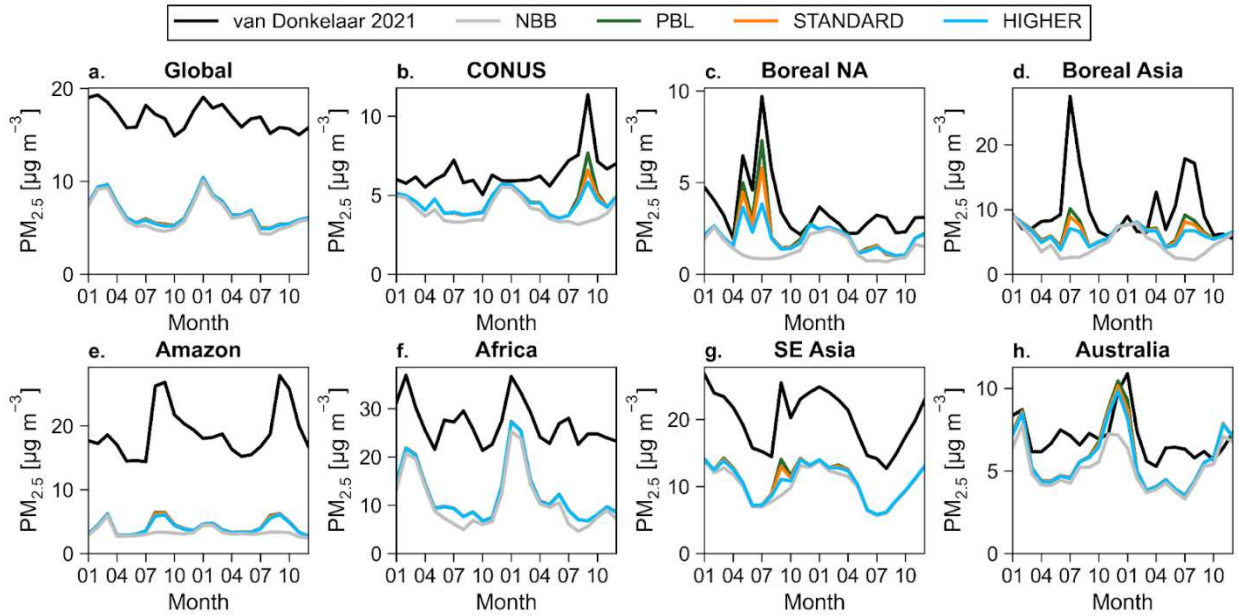

Figure A.8: Monthly averaged surface $PM_{2.5}$ by source region (regions in Figure A.2). The van Donkelaar et al. 2021 $PM_{2.5}$ concentrations are in black. Model simulations are in different colors for each BB-PIH scenario: PBL (green), STANDARD (orange), and HIGHER (blue). The simulation with biomass burning turned off (NBB) is shown in gray. Simulation acronyms are defined in Figure 2.1.

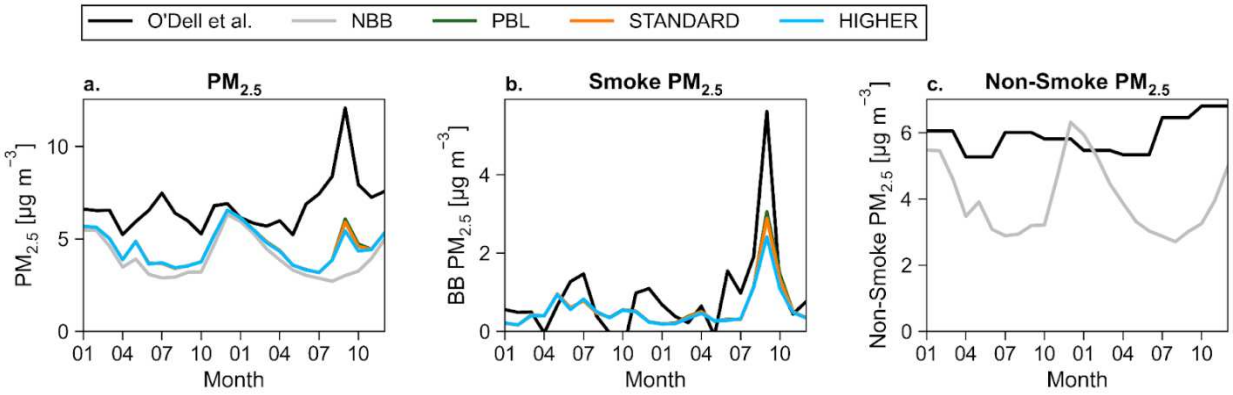

Figure A.9: Monthly averaged surface $PM_{2.5}$ over CONUS land areas for (a.) total surface $PM_{2.5}$, (b.) surface $PM_{2.5}$ attributed to smoke, and (c.) non-smoke attributed smoke $PM_{2.5}$ for January 2019 to December 2020. The $PM_{2.5}$ product from O'Dell et al. 2018 is shown in black. Model simulations are in different colors for each BB-PIH scenario: PBL (green), STANDARD (orange), and HIGHER (blue). The simulation with biomass burning turned off (NBB) is shown in gray. Simulation acronyms are defined in Figure 2.1.

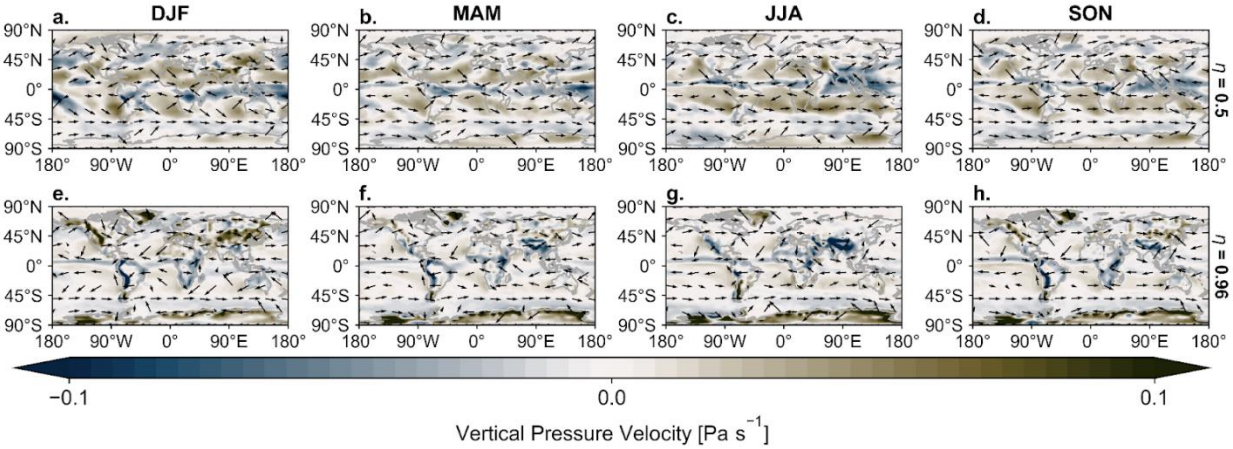

Figure A.10: Seasonally averaged vertical pressure velocity (colored) and horizontal winds (arrows) for heights of (a.)-(d.) η=0.5 (mid-troposphere), and (e.)-(h.) η=0.96 (planetary boundary layer) using the 2019 and 2020 MERRA-2 Reanalysis. η is a terrain-following coordinate that is used to define the vertical grid in modeling; it describes the fraction of the atmosphere between that layer and the pressure at the model top (0.01 hPa).

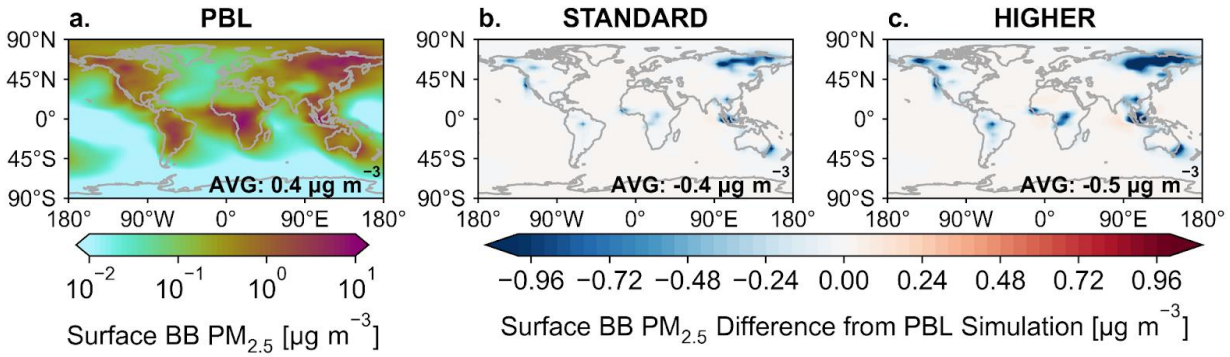

Figure A.11: (a.) Average Surface $PM_{2.5}$ from biomass burning (BB $PM_{2.5}$) for 2019 and 2020 in the PBL simulation. Difference in surface average BB $PM_{2.5}$ from for 2019 and 2020 relative to the PBL simulation for (b.) STANDARD, (c.) HIGHER.

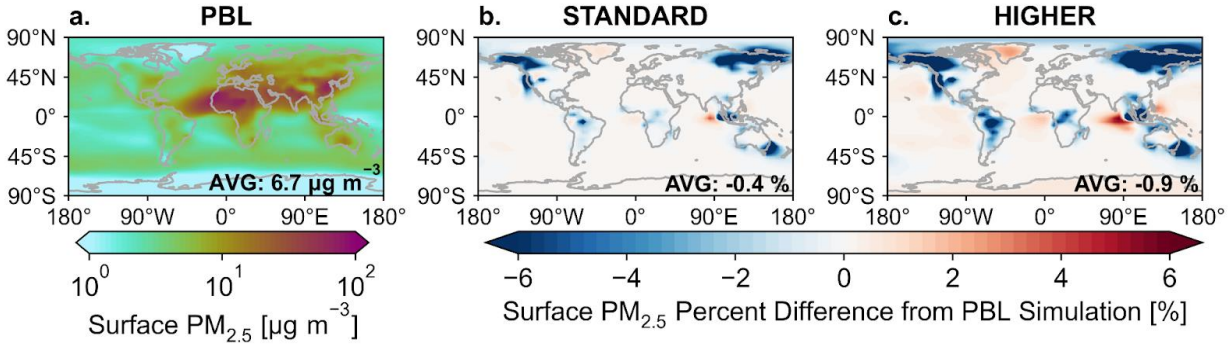

Figure A.12: (a.) Average Surface $PM_{2.5}$ for 2019 and 2020 in the PBL simulation. Percent difference in surface average $PM_{2.5}$ from for 2019 and 2020 relative to the PBL simulation for (b.) STANDARD, and (c.) HIGHER. Simulation acronyms are defined in Figure 2.1.

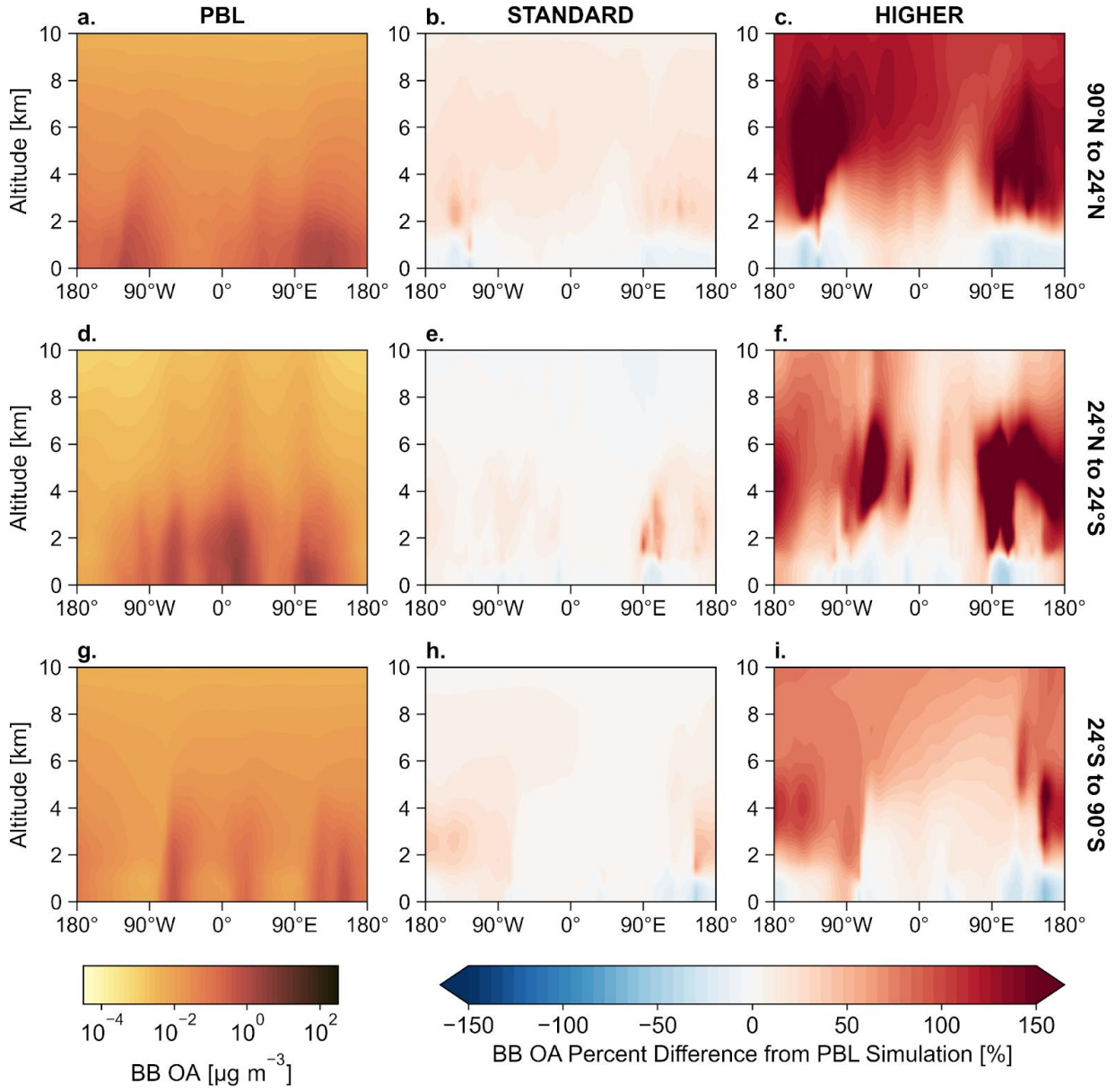

Figure A.13: Average OA from BB in 2019 and 2020 as a function of longitude and altitude in the PBL BB PIH scenario in the (a.) Northern Hemisphere Extratropics (24°N to 90°N), (d.) Tropics (24°S to 24°N), and (g.) Southern Hemisphere Extratropics (90°S to 24°S). Percent difference in OA from BB relative to the PBL simulation in the Northern Hemisphere Extratropics for each of the BB PIH scenarios (b.) STANDARD and (c.) HIGHER. Percent difference in OA from BB relative to the PBL simulation in the Tropics for each of the BB PIH scenarios (e.) STANDARD and (f.) HIGHER. Percent difference in OA from BB relative to the PBL simulation in the Southern Hemisphere Extratropics for each of the BB PIH scenarios (h.) STANDARD and (i.) HIGHER. Simulation acronyms are defined in Figure 2.1.

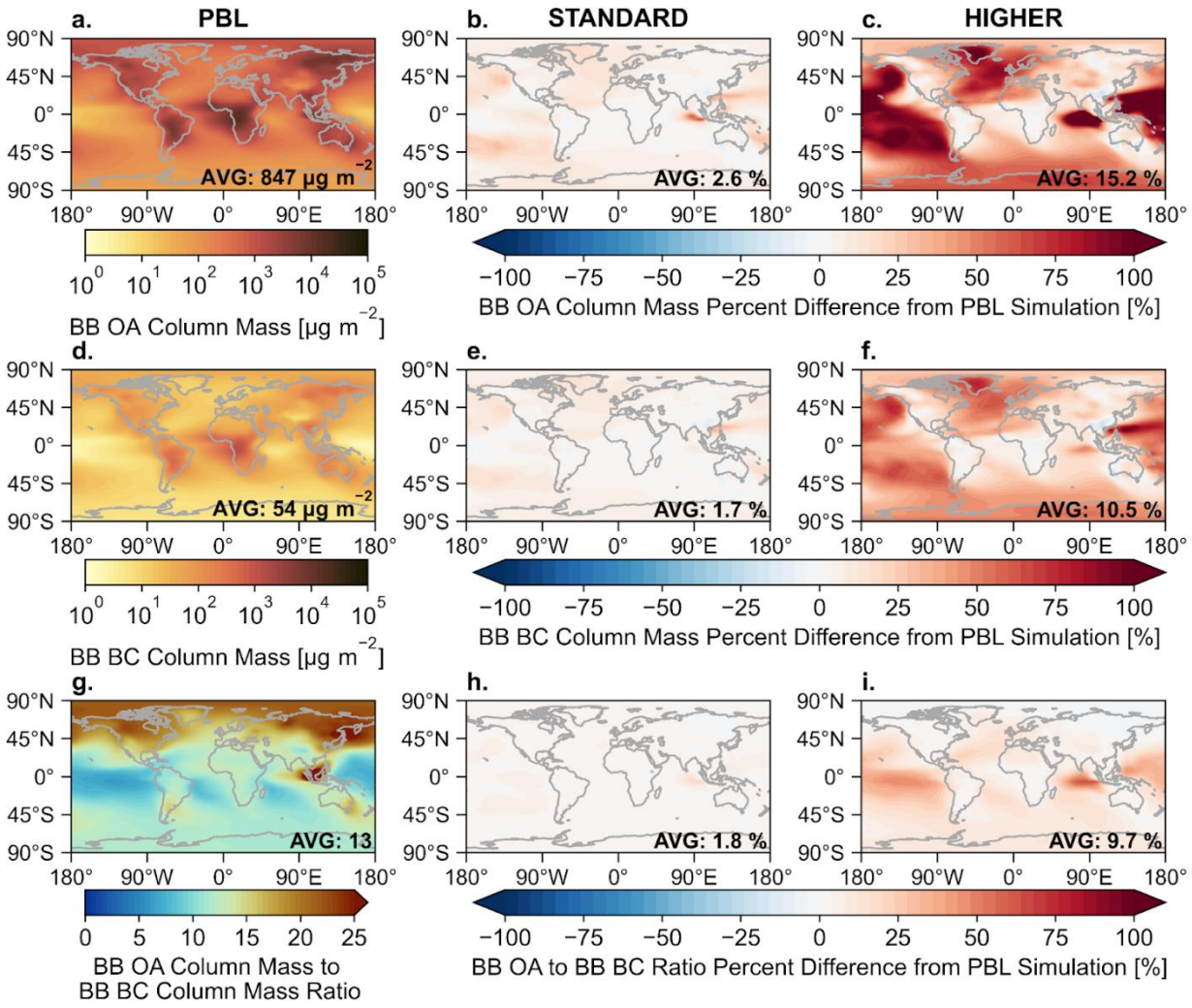

Figure A.14: (a.) Average column-integrated OA mass from BB in the PBL simulation for 2019 and 2020. Percent difference in average column integrated OA mass from BB in 2019 and 2020 relative to the PBL simulation for (b.) STANDARD and (c.) HIGHER. (d.) Average column integrated BC mass in the PBL simulation for 2019 and 2020. Percent difference in average column integrated BC mass in 2019 and 2020 relative to the PBL simulation for (e.) STANDARD and (f.) HIGHER. (g.) The two-year average (2019 and 2020) ratio of BB OA column mass to BB BC column mass for the PBL simulation. (h.)-(i.) The two-year average percent difference in the ratios of BB OA to BB BC column mass ratio in the BB-PIH scenarios relative to the PBL simulation. The two-year global average values are shown on each panel. Simulation acronyms are defined in Figure 2.1.

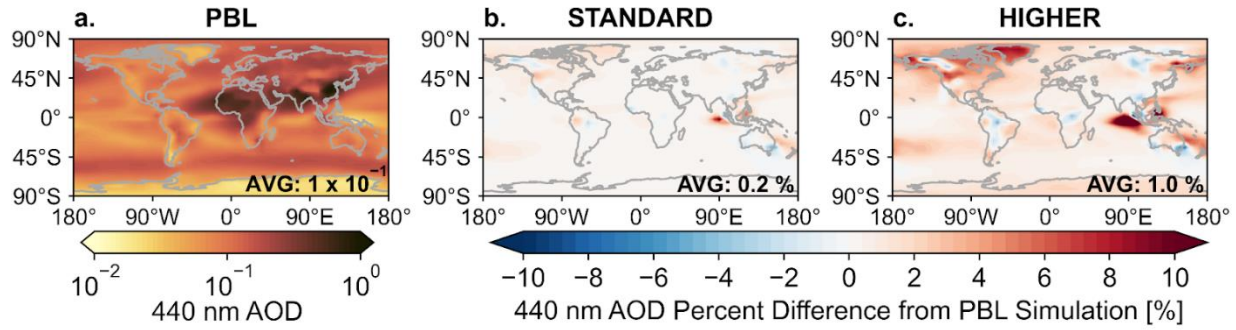

Figure A.15: (a.) Average AOD for 2019 and 2020 in the PBL simulation. Percent difference in surface average AOD from for 2019 and 2020 relative to the PBL simulation for (b.) STANDARD and (c.) HIGHER. Simulation acronyms are defined in Figure 2.1.

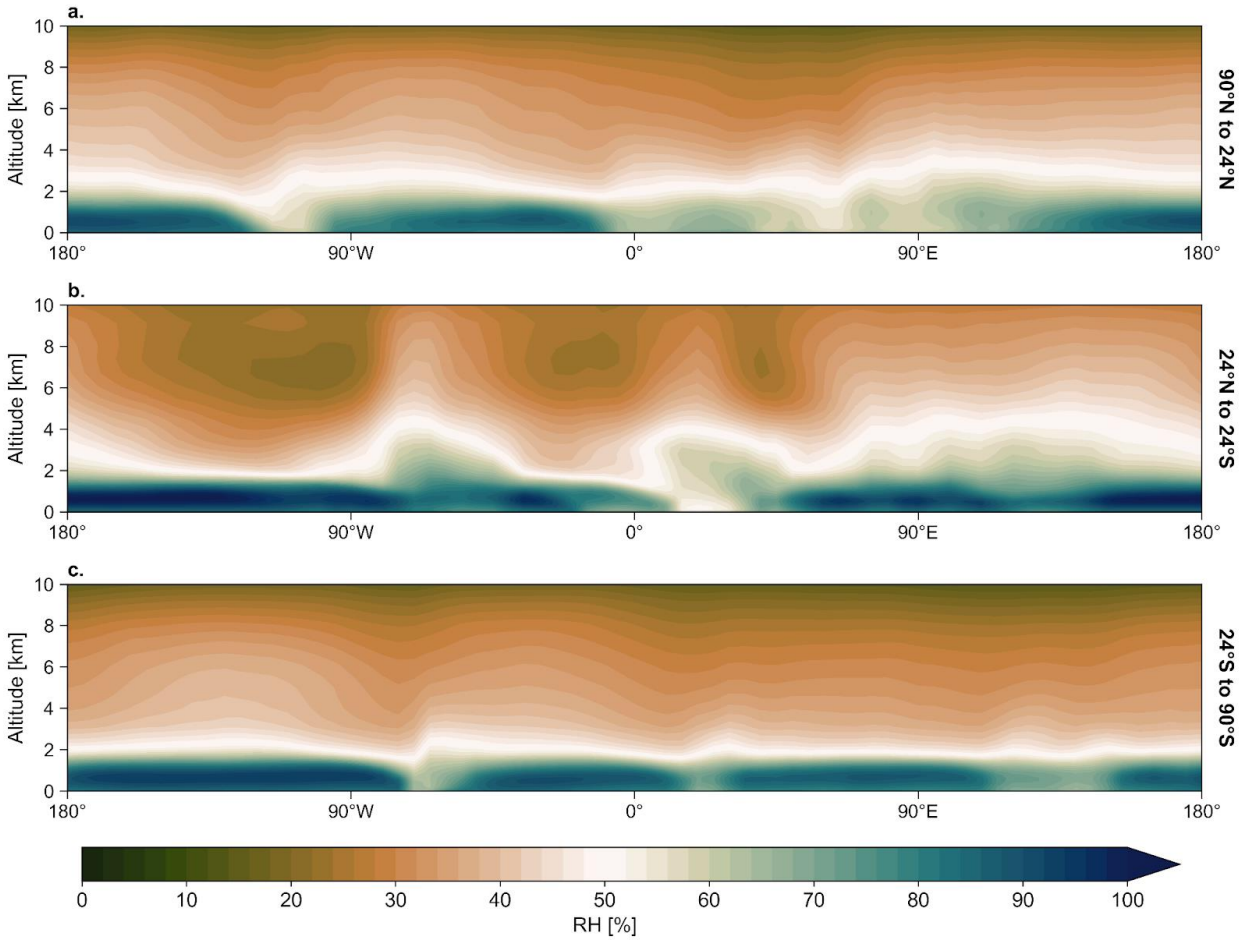

Figure A.16: The average relative humidity (RH) based on MERRA-2 Reanalysis during 2019 and 2020 as a function of altitude in the (a.) Northern Hemisphere Extratropics (24°N to 90°N), (e.) Tropics (24°S to 24°N), and (i.) Southern Hemisphere Extratropics (90°S to 24°S).

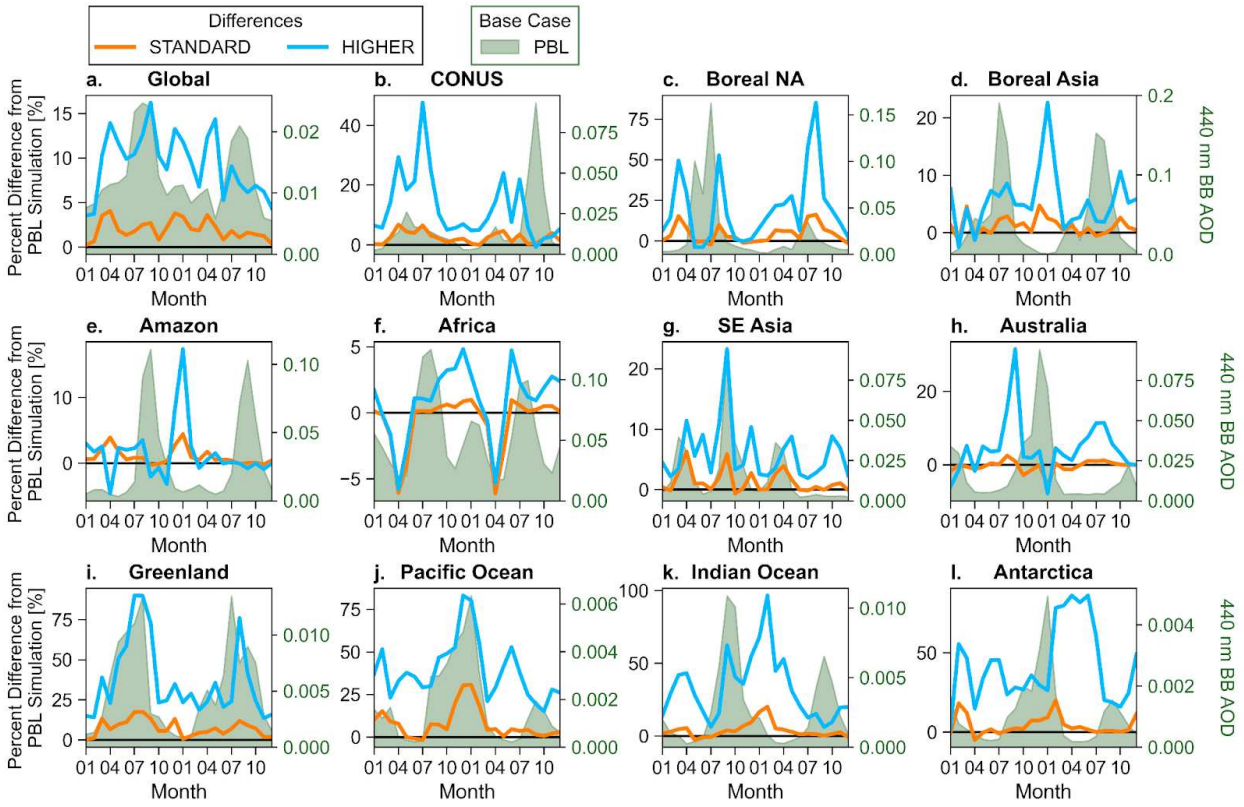

Figure A.17: The monthly percent difference in BB AOD at 440 nm (January 2019 to December 2020) relative to the PBL BB-PIH scenario for the STANDARD BB-PIH scenario(orange) and HIGHER BB-PIH scenario (blue) refer to black vertical axis. The BB AOD at 440 nm for the PBL simulation as context for the amount of BB aerosol present is shown in green (refer to the green vertical axis). Each panel corresponds to a different biomass burning region (a-h) or transport region (i-l) as shown in Figure A.2.

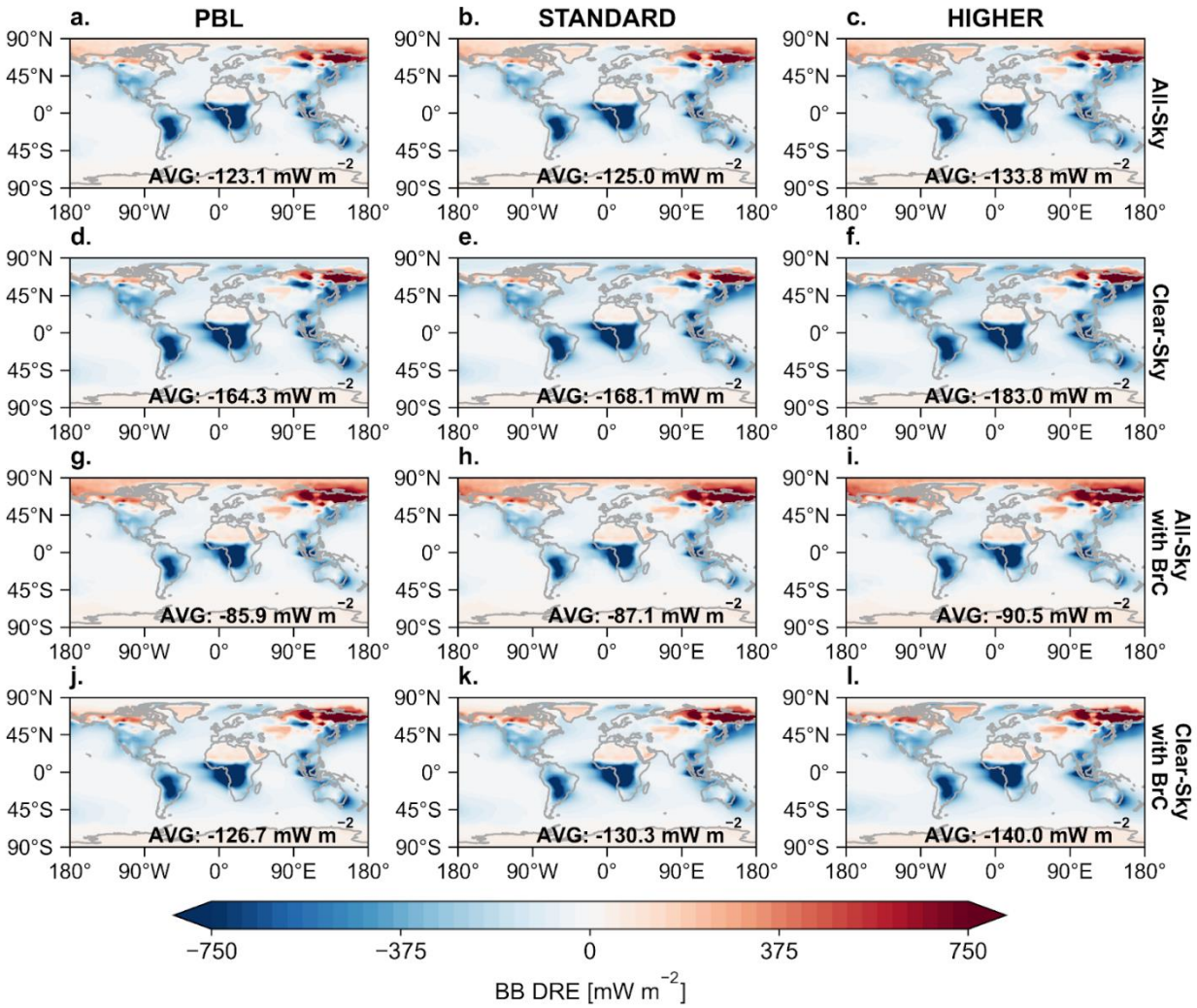

Figure A.18: Average all-sky BB-DRE for 2019 and 2020 for the simulations (a.) PBL, (b.) STANDARD and (c.) HIGHER. Average clear-sky BB-DRE for 2019 and 2020 for the simulations (d.) PBL, (e.) STANDARD and (f.) HIGHER. Average all-sky BB-DRE including BrC for 2019 and 2020 for the simulations (g.) PBL, (h.) STANDARD and (i.) HIGHER. Average clear-sky BB-DRE including BrC for 2019 and 2020 for the simulations (j) PBL, (k.) STANDARD and (l.) HIGHER. Simulation acronyms are defined in Figure 2.1.

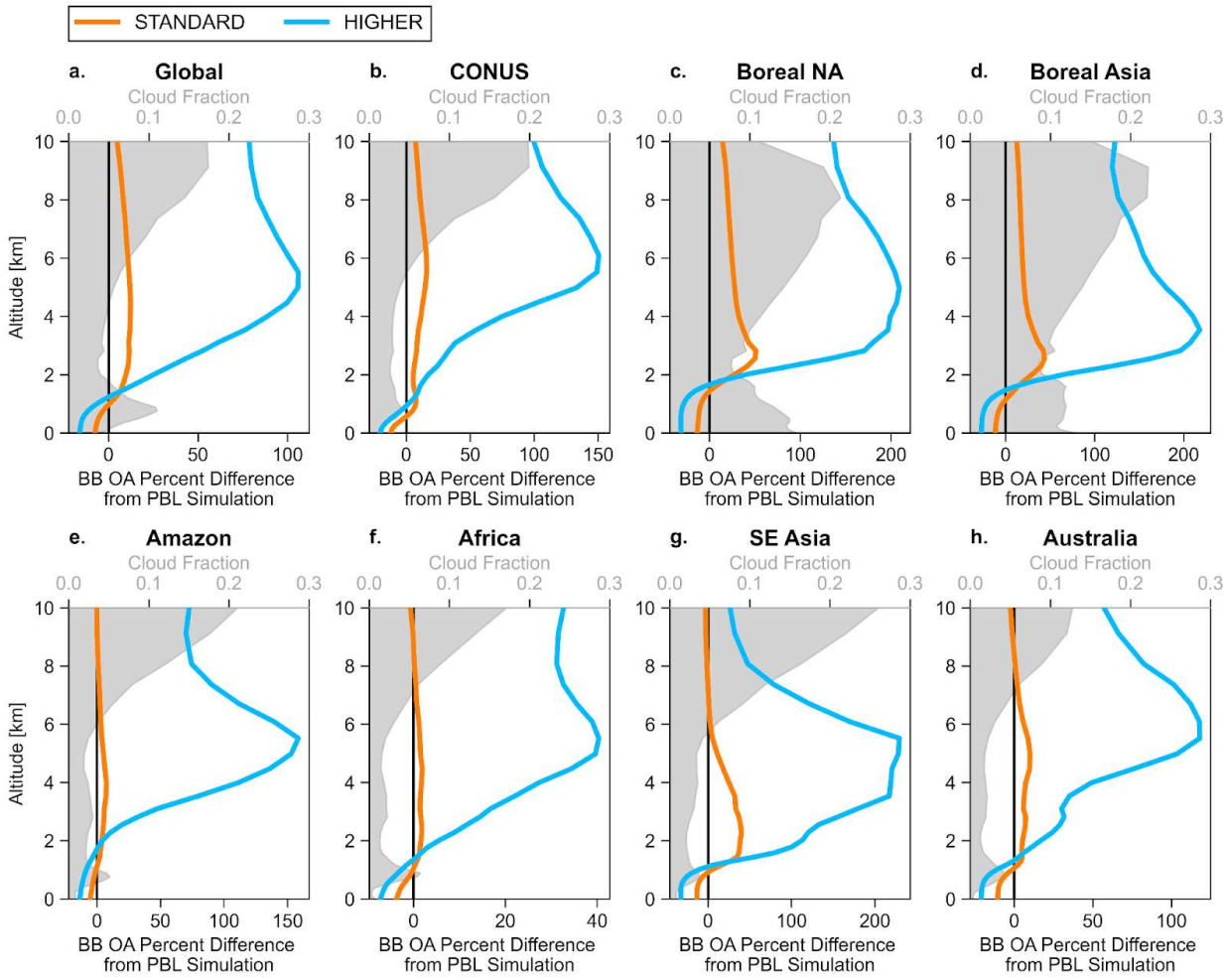

Figure A.19: Percent difference in BB OA as a function of altitude for STANDARD (orange) and HIGHER (blue), all relative to the PBL simulation (refer to the bottom x-axis). Cloud fraction as a function of altitude in gray (refer to top x-axis). Each panel is a different region indicated by the text in black bold font above each panel (regions in Figure A.2). Simulation acronyms are defined in Figure 2.1.

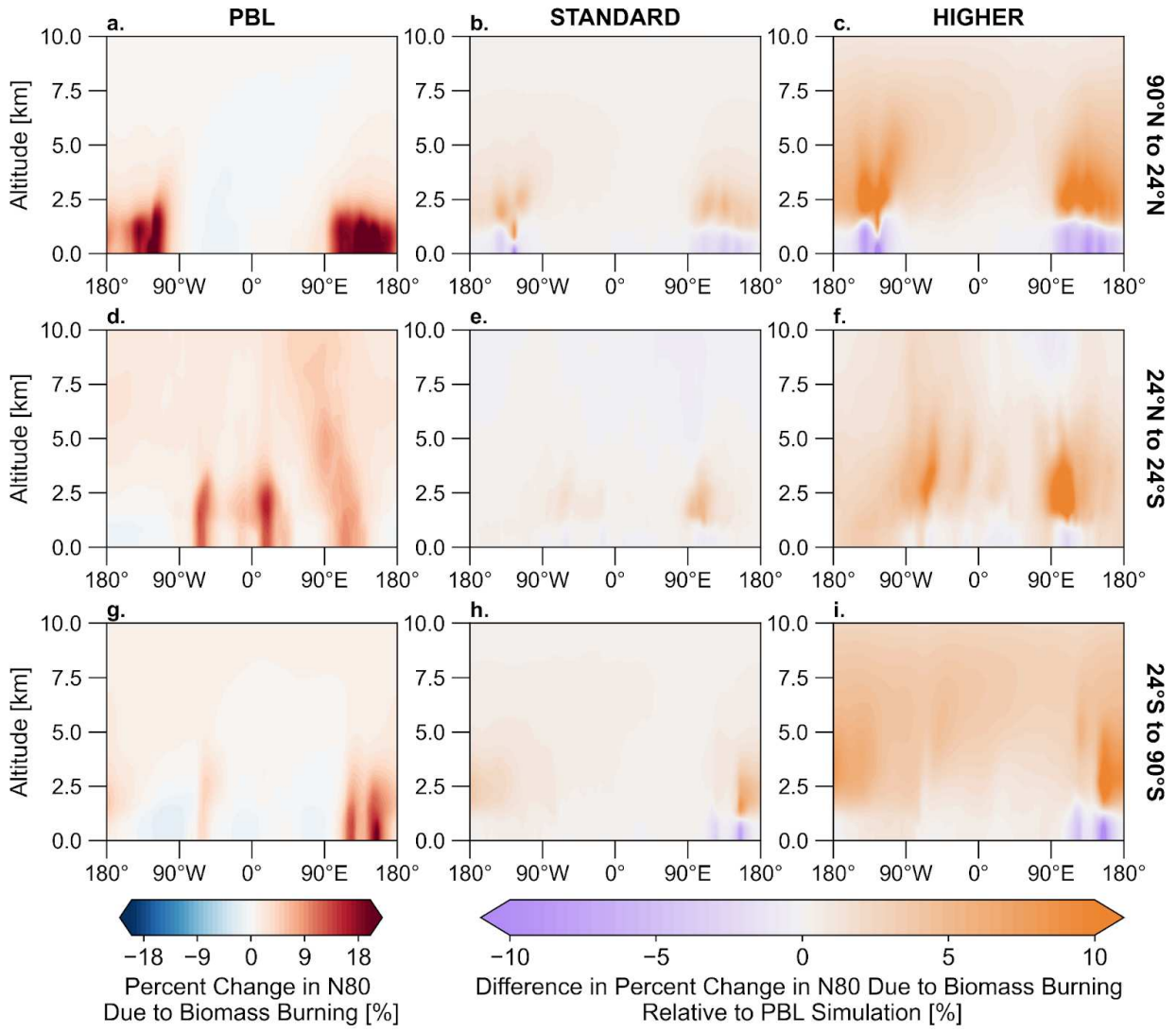

Figure A.20: Two-year mean (2019-2020) N80 concentration as a function of longitude and altitude for the PBL BB PIH scenario in the (a.) Northern Hemisphere Extratropics (24°N to 90°N), (d.) Tropics (24°S to 24°N), and (g.) Southern Hemisphere Extratropics (90°S to 24°S). Percent difference in N80 from the PBL simulation in the Northern Hemisphere Extratropics for each of the BB PIH scenarios (b.) STANDARD and (c.) HIGHER. (e.) and (f.), and (h.) and (i.) are similar to (b.) and (c.) but for the Tropics and Southern Hemisphere Extratropics respectively. Simulation acronyms are defined in Figure 2.1.

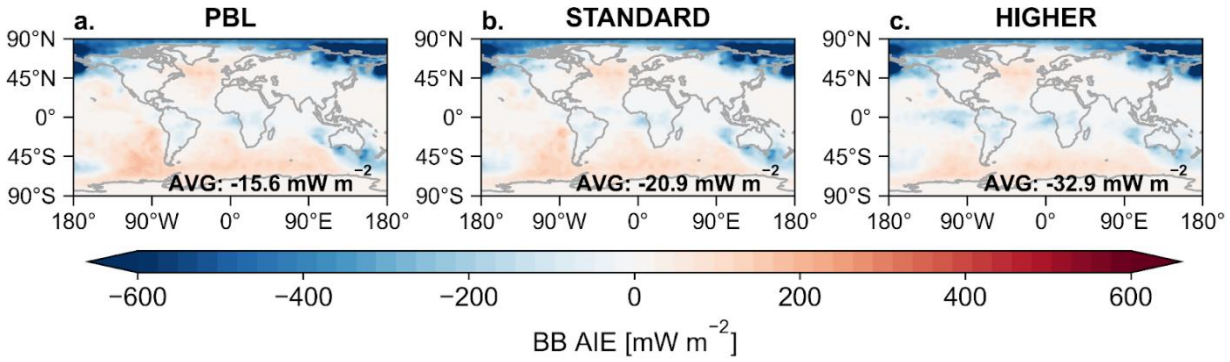

Figure A.21: Two-year mean (2019-2020) BB-AIE for the simulations of (a.) PBL, (b.) STANDARD, and (c.) HIGHER. Simulation acronyms are defined in Figure 2.1.

Appendix B: Supplement to Look Within: Intraplume Differences on Smoke Aerosol Aging Driven by Concentration Gradients

Appendix B Tables

Table B.1: The photolysis reactions with rates calculated by TUV in the SAM-ASP-TUV v1.0.0 model.

Photolysis Reaction
RXN 1: $O_2 + h\nu \rightarrow O + O$
RXN 2: $O_3 + h\nu \rightarrow O_2 + O(^1D)$
RXN 3: $O_3 + h\nu \rightarrow O_2 + O(^3P)$
RXN 4: $HO_2 + h\nu \rightarrow OH + O$
RXN 5: $H_2O_2 + h\nu \rightarrow 2OH$
RXN 6: $NO_2 + h\nu \rightarrow NO + O(^3P)$
RXN 7: $NO_3 + h\nu \rightarrow NO + O_2$
RXN 8: $NO_3 + h\nu \rightarrow NO_2 + O(^3P)$
RXN 9: $N_2O_5 + h\nu \rightarrow NO_3 + NO + O(^3P)$
RXN 10: $N_2O_5 + h\nu \rightarrow NO_3 + NO_2$
RXN 11: $N_2O + h\nu \rightarrow N_2 + O(^1D)$
RXN 12: $HNO_2 + h\nu \rightarrow OH + NO$
RXN 13: $HNO_3 + h\nu \rightarrow OH + NO_2$
RXN 14: $HNO_4 + h\nu \rightarrow HO_2 + NO_2$
RXN 15: $NO_3^-{}_{(aq)} + h\nu \rightarrow NO_{2\,(aq)} + O^-$
RXN 16: $NO_3^-{}_{(aq)} + h\nu \rightarrow NO_2^-{}_{(aq)} + O(^3P)$
RXN 17: $CH_2O + h\nu \rightarrow H + HCO$
RXN 18: $CH_2O + h\nu \rightarrow H_2 + CO$
RXN 19: $CH_3CHO + h\nu \rightarrow CH_3 + HCO$
RXN 20: $CH_3CHO + h\nu \rightarrow CH_4 + CO$
RXN 21: $CH_3CHO + h\nu \rightarrow CH_3CO + H$
RXN 22 $C_2H_5CHO + h\nu \rightarrow C_2H_5 + HCO$
RXN 23: $CH_2(OH)CHO + h\nu \rightarrow$ Products
RXN 24: $CH_2CHCHO + h\nu \rightarrow$ Products
RXN 25: $CH_2C(CH_3)CHO + h\nu \rightarrow$ Products
RXN 26: $CH_3COCH_3 + h\nu \rightarrow CH_3CO + CH_3$
RXN 27: $CH_3COCHCH_2 + h\nu \rightarrow$ Products
RXN 28: $CH_3COCH_2CH_3 + h\nu \rightarrow CH_3CO + CH_3$
RXN 29: $CH_2(OH)COCH_3 + h\nu \rightarrow CH_3CO + CH_2(OH)$
RXN 30: $CH_2(OH)COCH_3 + h\nu \rightarrow CH_2(OH)CO + CH_3$
RXN 31: $CH_3OOH + h\nu \rightarrow CH_3O + OH$
RXN 32: $HOCH_2OOH + h\nu \rightarrow HOCH_2O + OH$
RXN 33: $CH_3CO(OOH) + h\nu \rightarrow$ Products
RXN 34: $CH_3ONO_2 + h\nu \rightarrow CH_3O + NO_2$
RXN 35: $CH_3CH_2ONO_2 + h\nu \rightarrow CH_3CH_2O + NO_2$
RXN 36: $CH_3CHONO_2CH_3 + h\nu \rightarrow CH_3CHOCH_3 + NO_2$

RXN 37: $CH_2(OH)CH_2(ONO_2) + h\nu \rightarrow CH_2(OH)CH_2(O.) + NO_2$
RXN 38: $CH_3COCH_2(ONO_2) + h\nu \rightarrow CH_3COCH_2(O.) + NO_2$
RXN 39: $C(CH_3)_3(ONO_2) + h\nu \rightarrow C(CH_3)_3(O.) + NO_2$
RXN 40: $CH_3CO(OONO_2) + h\nu \rightarrow CH_3CO(OO) + NO_2$
RXN 41: $CH_3CO(OONO_2) + h\nu \rightarrow CH_3CO(O) + NO_3$
RXN 42: $CH_3CH_2CO(OONO_2) + h\nu \rightarrow CH_3CH_2CO(OO) + NO_2$
RXN 43: $CH_3CH_2CO(OONO_2) + h\nu \rightarrow CH_3CH_2CO(O) + NO_3$
RXN 44: $CHOCHO + h\nu \rightarrow HCO + HCO$
RXN 45: $CHOCHO + h\nu \rightarrow CH_2O + CO$
RXN 46: $CH_3COCHO + h\nu \rightarrow CH_3CO + CO$
RXN 47: $CH_3COCOCH_3 + h\nu \rightarrow$ Products
RXN 48: $CH_3COCO(OH) + h\nu \rightarrow$ Products

Table B.2: Description of the different POA aging schemes tested. The reactions follow this form for each of the POA volatility bins: $IVOC_n + OH \rightarrow A(IVOC_{n-1}) + F(IVOC_{n+1})$ with an oxidation rate of $1.0*10^{-11}$ cm^3 $molec^{-1}$ s^{-1}. The simulations are done twice, once with base case SOA_{Pre} Emissions and once with a doubling of SOA_{Pre} Emissions. The sum of A and F is always 1.075 following Ahmadov et al. (2012) and Robinson et al. (2007) except for the OPOA off sensitivity simulations. The main simulation in Chapter 3 is always the A = 0.825, F = 0.25 simulation.

Model Sensitivity Simulation	Functionalization Coefficient (A)	Fragmentation Coefficient (F)
A = 0.5375, F = 0.5375	0.5375	0.5375
A = 0.825, F = 0.25 (Main)	0.825	0.25
A = 0.975, F = 0.1	0.975	0.1
A = 1.075, F = 0.0	1.075	0.0
OPOA Off	0.0	0.0

Appendix B Figures

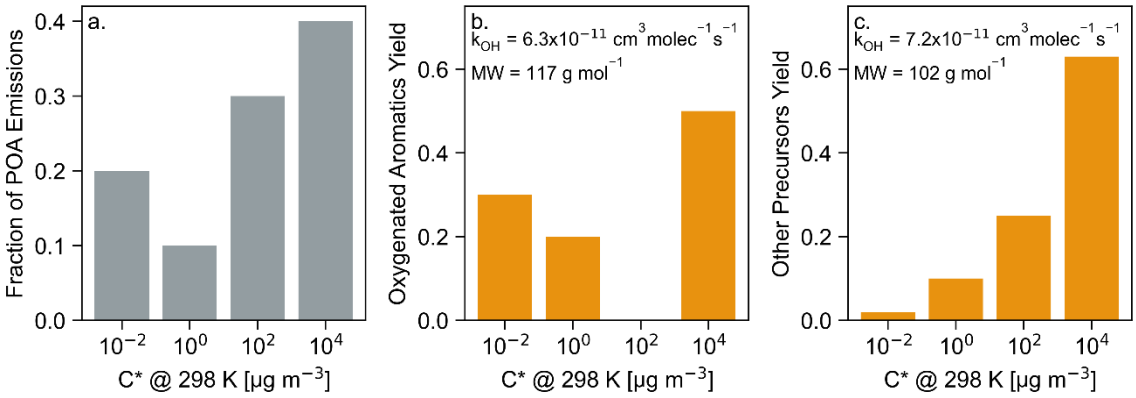

Figure B.1: (a.) Volatility distribution for the POA biomass burning emissions. (b.) The yield into the volatility distribution for the oxygenated aromatics SOA precursor class. (c.) The yield into the volatility distribution for the other SOA precursor class.

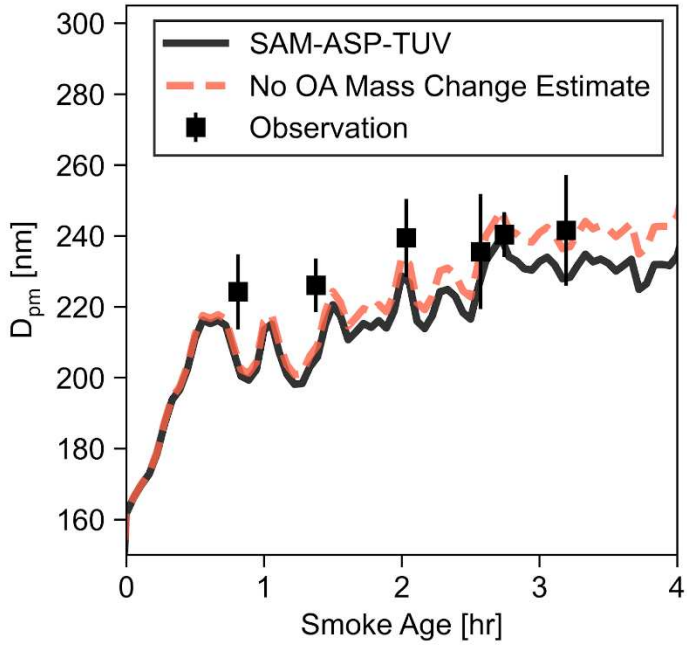

Figure B.2: D_{pm} evolution for the aircraft observations (points), SAM-ASP-TUV at aircraft altitude (black line), and estimate of the impact of OA condensation/evaporation on SAM-ASP-TUV D_{pm} using equation 6 of June et al. (2022) with the modeled ordinary least squares best fit of ΔOA/ΔCO.

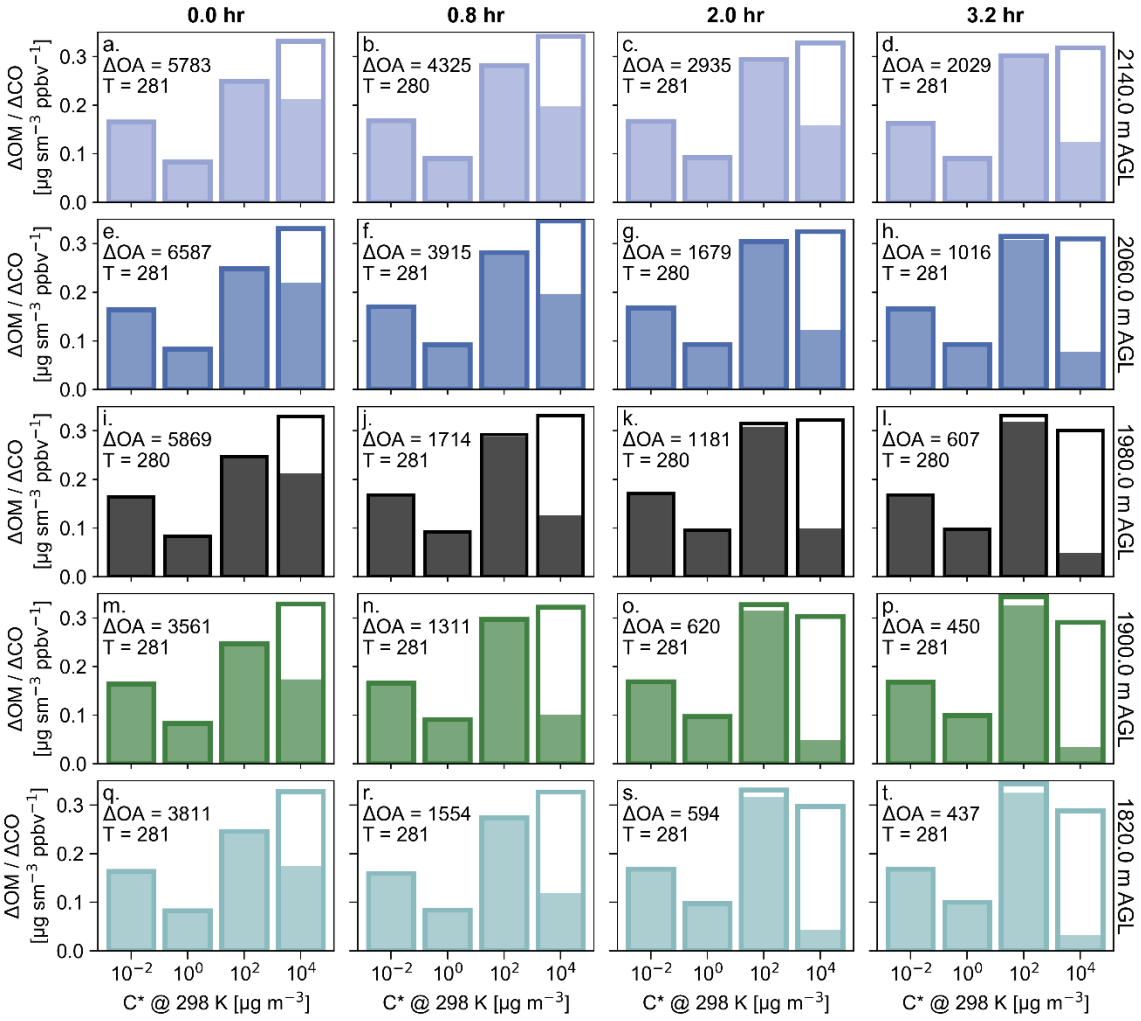

Figure B.3: Plume average volatility distribution from the model at 5 heights (rows), colored to match the vertical height lines used in Figure 3.2. Height 1980.0 m (black) is closest to the aircraft observations. The shaded area represents organic mass in the particulate phase in each volatility bin, while the white area within the bar represents organic mass in the gas phase in each volatility bin. Each column is a different time downwind with increasing smoke age from 0.0 h to 3.2 h from left to right.

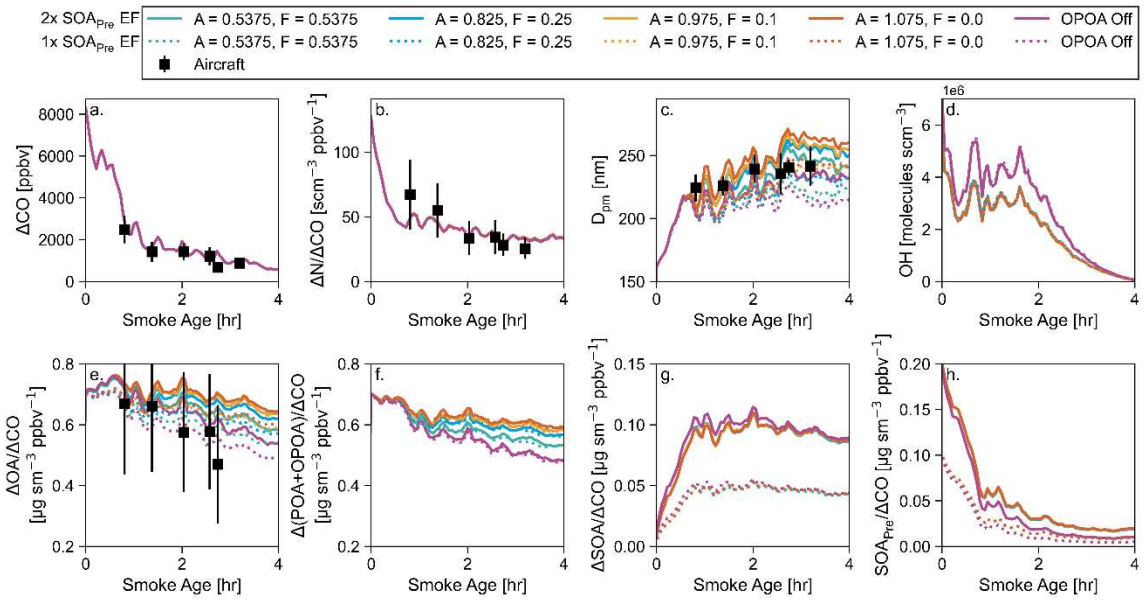

Figure B.4: Sensitivity of the OA aging scheme to the evolution of (a.) ΔCO, (b.) ΔN/ΔCO, (c.) D_{pm}, (d.) OH, (e.) ΔOA/ΔCO, (f.) Δ(POA+OPOA)/ΔCO, (g.) ΔSOA/ΔCO, (h.) SOA_{Pre}/ΔCO. The transect-average aircraft observations for the August 3, 2019, sampling of the Williams Flats Fire are shown as black squares for panels (a.)-(d.), with the error bars showing the standard deviation of the measurements. Each line represents one of the simulations described in Table B.2.

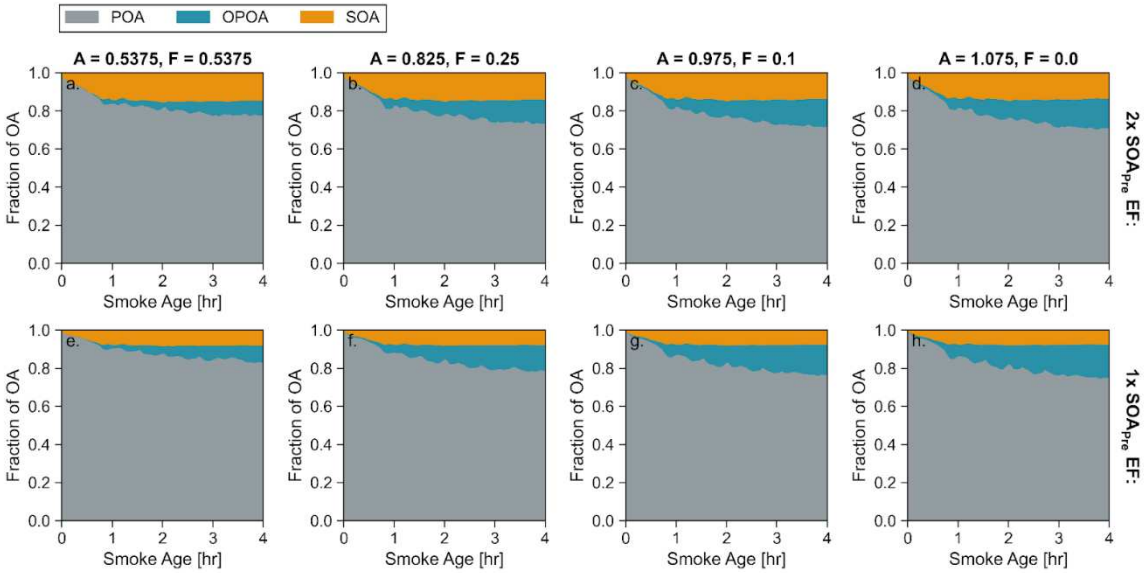

Figure B.5: The evolution of the fraction of OA that is POA, OPOA, and SOA for each of the simulations described in Table B.2 at the altitude of the aircraft. (a.)-(d.) are the simulations with 2x SOA_{Pre} emissions and (e.)-(h.) are the simulations with the base case SOA_{Pre} emissions.

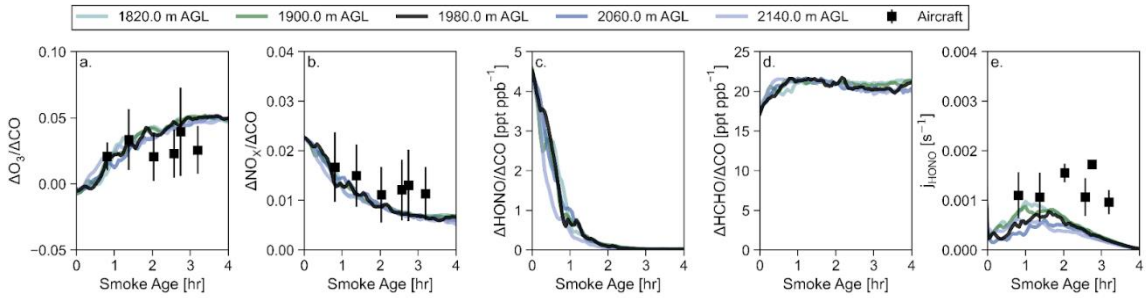

Figure B.6: The transect average evolution of (a.) $\Delta O_3/\Delta CO$, (b.) $\Delta NO_X/\Delta CO$, (c.) $\Delta HONO/\Delta CO$, (d.) $\Delta HCHO/\Delta CO$, and (e.) j_{HONO}. The solid-colored lines are the model plume average at five heights with the 1980.0 m line being the altitude closest to the height of the aircraft. The transect-average aircraft observations for the August 3, 2019, sampling of the Williams Flats Fire are shown as black squares.

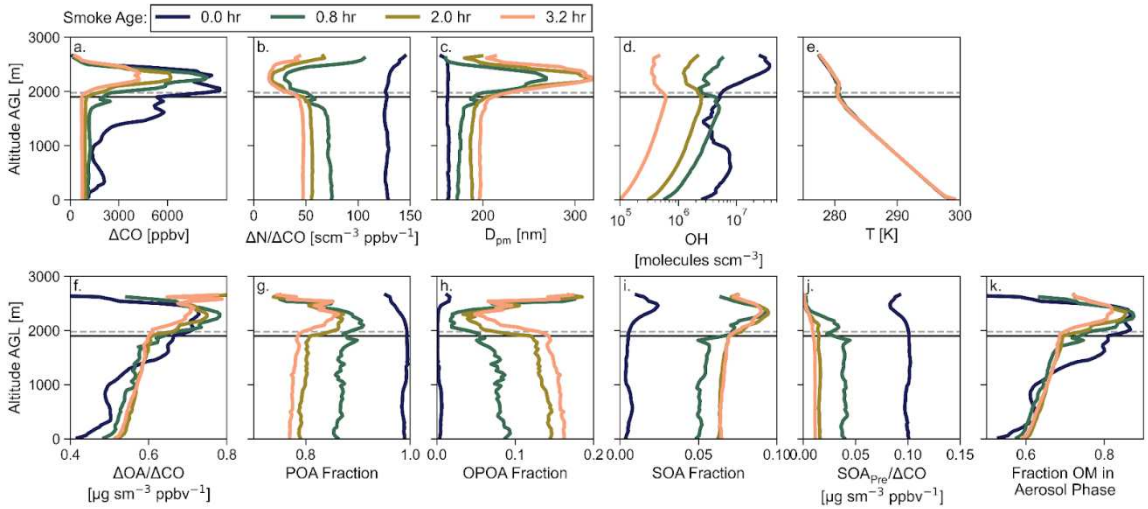

Figure B.7: Plume-average vertical profiles at four times downwind for (a.) ΔCO, (b.) ΔN/ΔCO, (c.) D_{pm}, (d.) OH, (e.) temperature (T), (f.) OAER, (g.) POA fraction, (h.) OPOA fraction, (i.) SOA fraction, (j.) $SOA_{Pre}/\Delta CO$, and (k.) Fraction of organic matter (OM) in aerosol phase. Each colored line is a different smoke age. The solid black horizontal line is the height of the PBL. The dashed gray line is the height of the aircraft that sampled the plume.

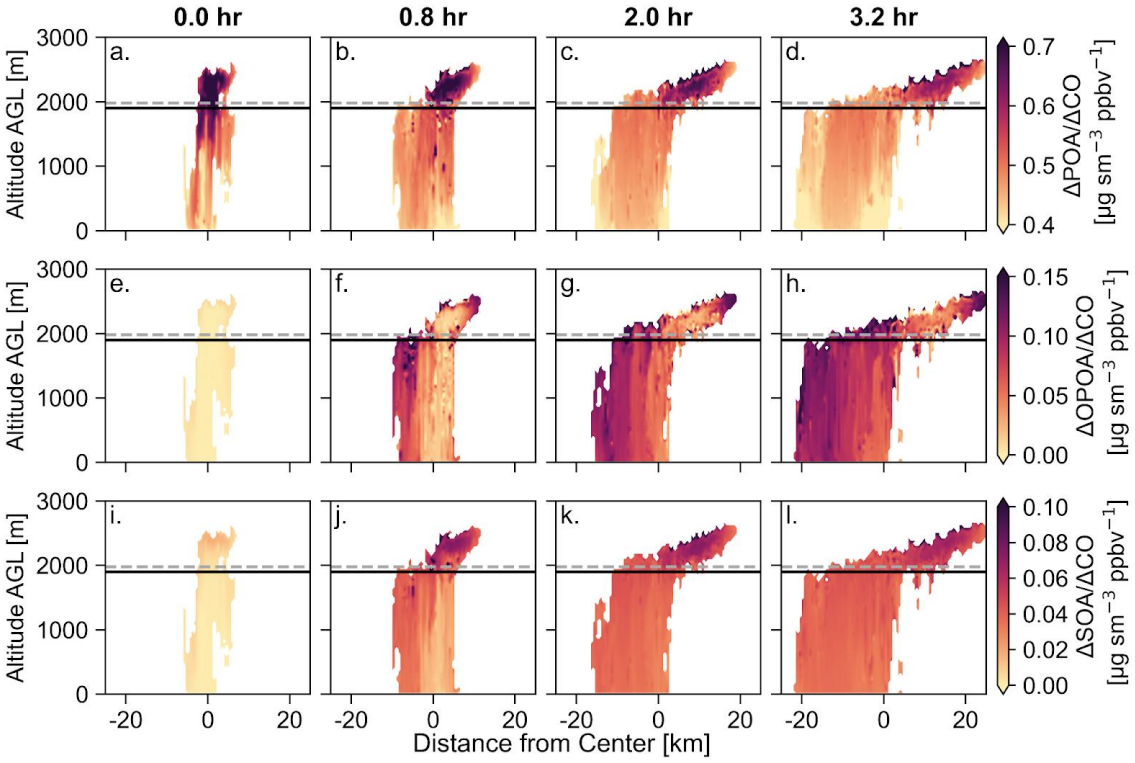

Figure B.8: Modeled (a.)-(d.) ΔPOA/ΔCO, (e.)-(h.) ΔOPOA/ΔCO, (i.)-(l.) ΔSOA/ΔCO as a function of distance from center and height at four times downwind. The solid black horizontal line is the height of the PBL. The dashed gray line is the height of the aircraft that sampled the plume.

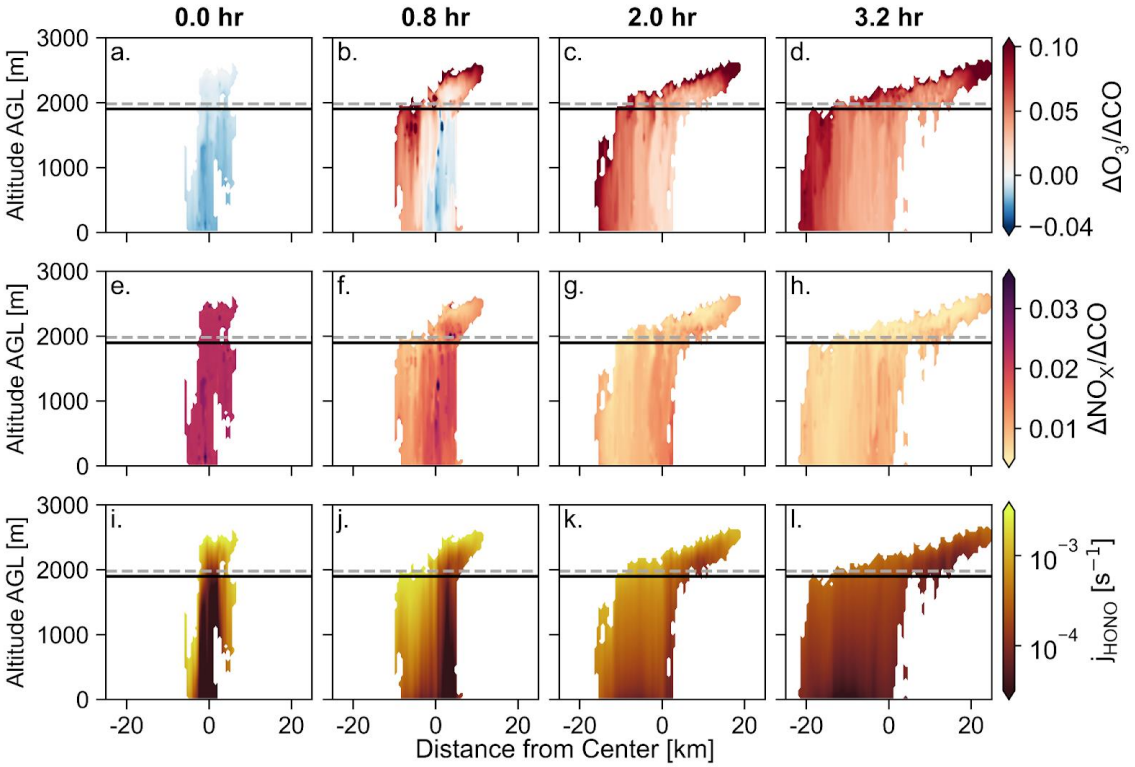

Figure B.9: Modeled (a.)-(d.) $\Delta O_3/\Delta CO$, (e.)-(h.) $\Delta NO_X/\Delta CO$, (i.)-(l.) j_{HONO} as a function of distance from center and height at four times downwind. The solid black horizontal line is the height of the PBL. The dashed gray line is the height of the aircraft that sampled the plume.

Appendix C: Supplement to Exploring Sulfur Chemistry in the North Atlantic Arctic Spring

Appendix C Tables

Table C.1: The old Henry's law coefficients used in GC-TOMAS and the revised Henry's law coefficients for sulfur chemistry species. The revised Henry's Law values are from Wollesen de Jonge et al. (2021).

Species	New Henry's Law [mol atm^{-1} kg^{-1}]	Old Henry's Law [mol atm^{-1} kg^{-1}]
DMSO	2×10^5	1×10^7
MSA	1×10^8	1×10^9
MSIA	1.7×10^6	1×10^8

Table C.2: Oceanic DMS scalar to get oceanic MeSH for each latitude band within our nested model domain based on Gros et al. (2023).

Latitude Band [°N]	Scalar
> 80	0.14
75 to 80	0.25
70 to 75	0.28
65 to 70	0.18
60 to 65	0.13

Table C.3: Campaign average atmospheric lifetime of DMS, MeSH, and DMSO.

Simulation	DMS Lifetime [d]	MeSH Lifetime [d]	DMSO Lifetime [d]
L11	1.7	0.9	0.1
L11*FO	1.4	0.9	0.2
ANN*FO	1.6	0.9	0.1
BIO*FO	1.2	0.8	0.2

Appendix C Figures

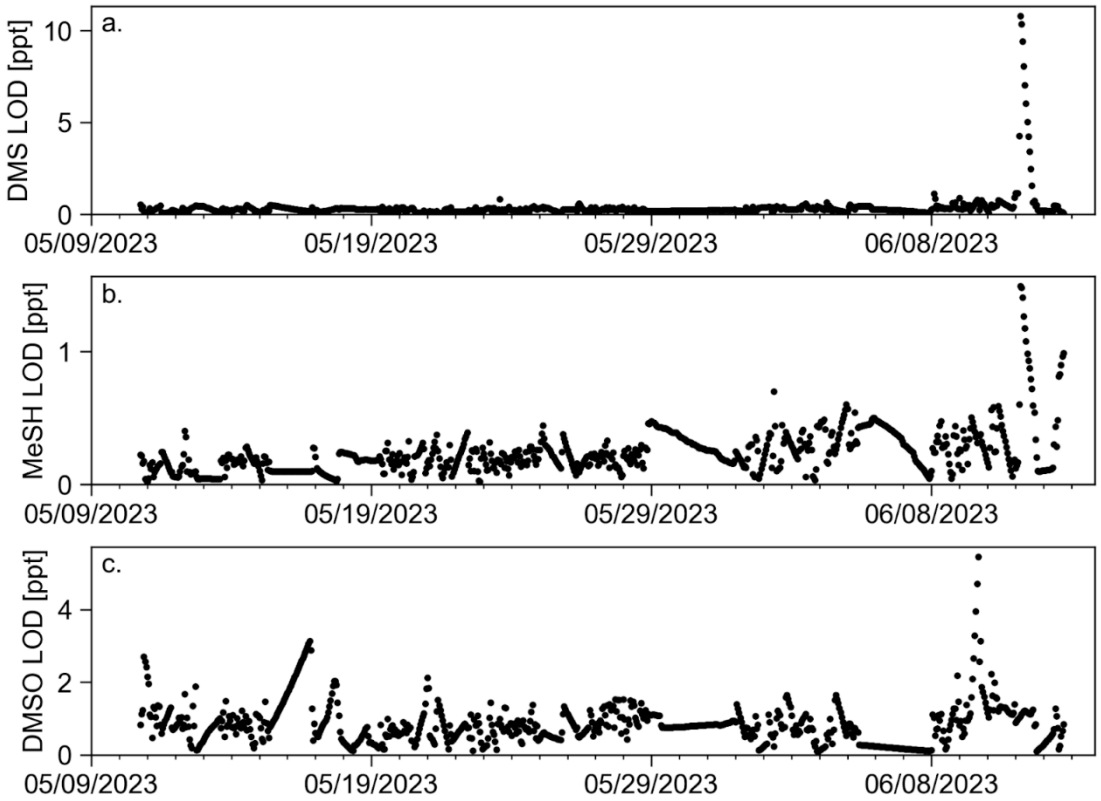

Figure C.1: Time series of the observational limit of detection (LOD) for (a.) DMS, (b.) MeSH, and (c.) DMSO.

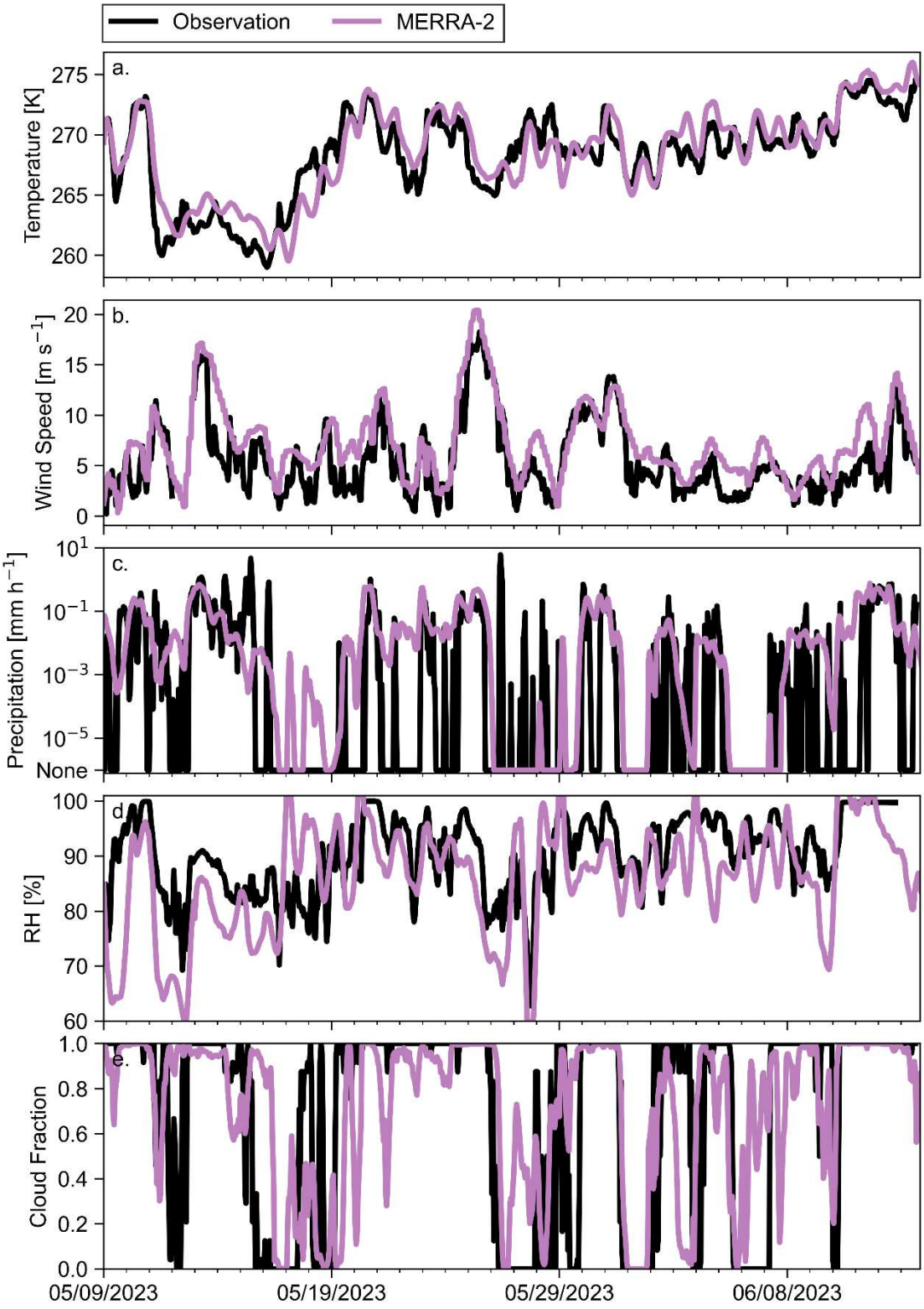

Figure C.2: Time series of observed and MERRA-2 reanalysis meteorological variables during the ARTofMELT field campaign for (a.) temperature, (b.) wind speed, (c.) precipitation, (d.) RH, and (e.) cloud fraction.

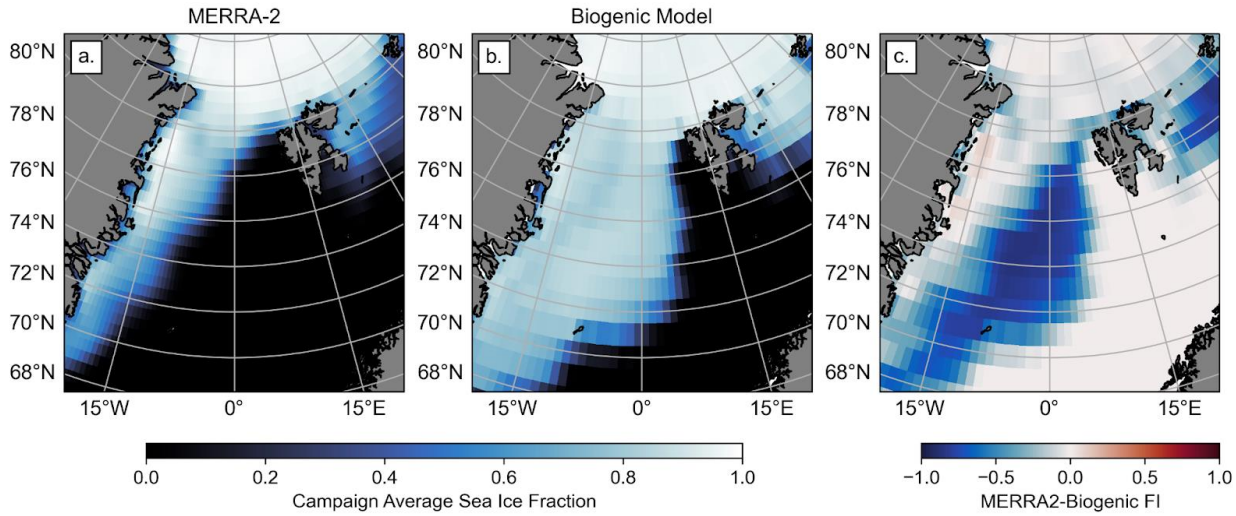

Figure C.3: (a.) MERRA-2 sea ice fraction averaged during the ARTofMELT campaign. (b.) Sea ice fraction from the biogenic ocean model averaged during the ARTofMELT campaign. (c.) Difference between MERRA-2 and the biogenic sea ice fractions averaged during the ARTofMELT campaign.

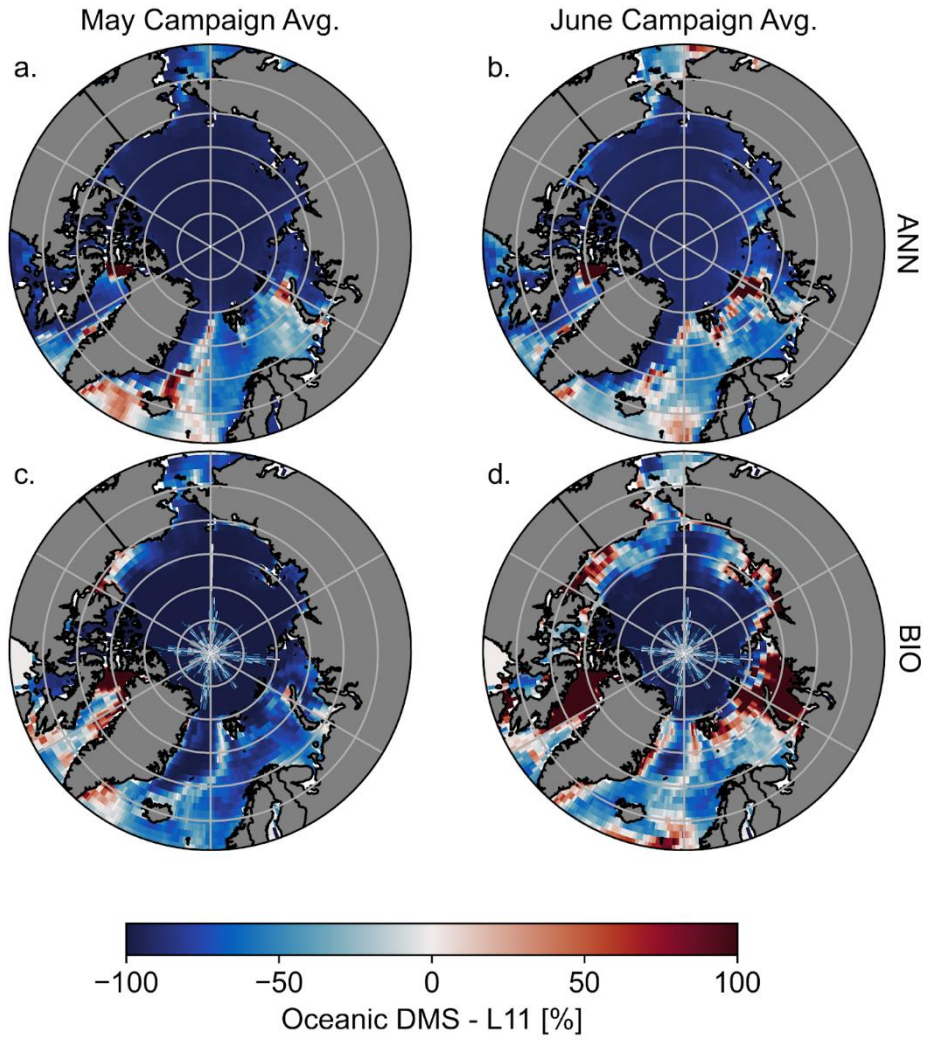

Figure C.4: The May campaign average (May 9 to May 31) percent difference between Lana et al. climatology oceanic DMS with oceanic DMS in the (a.) ANN dataset and (c.) the BIO dataset. The June campaign average (June 1 to June 14) percent difference between Lana et al. climatology oceanic DMS with oceanic DMS in the (b.) ANN dataset and (d.) the BIO dataset.

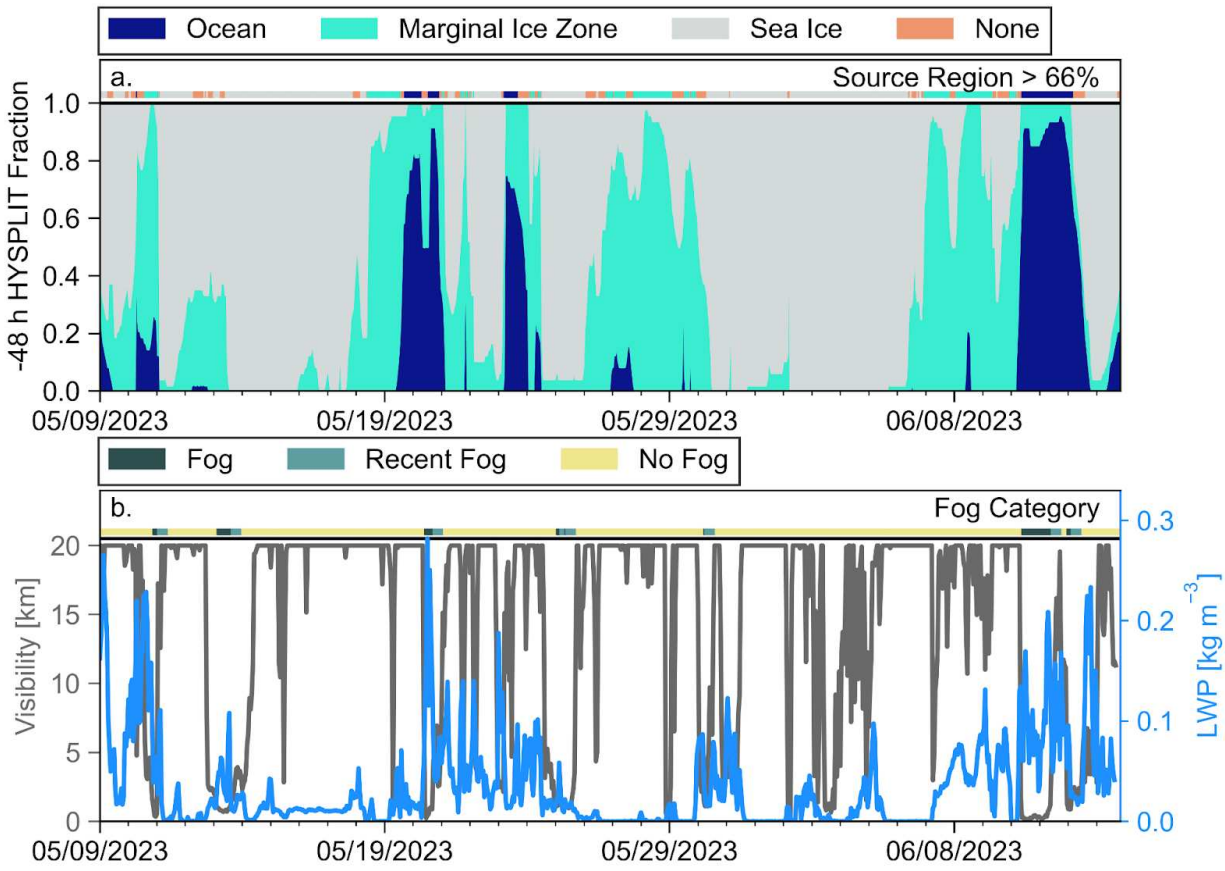

Figure C.5: (a.) Time series of the fraction of time each 48 h back trajectory spent over ocean, marginal ice zone, or sea ice. The top row of points shows the source region defined using Table 2. (b.) Observations of visibility (left y-axis) and liquid water path (LWP; right y-axis). The top row of points shows the periods of fog, recent fog and no fog using the definitions described in Chapter 4.2.6.

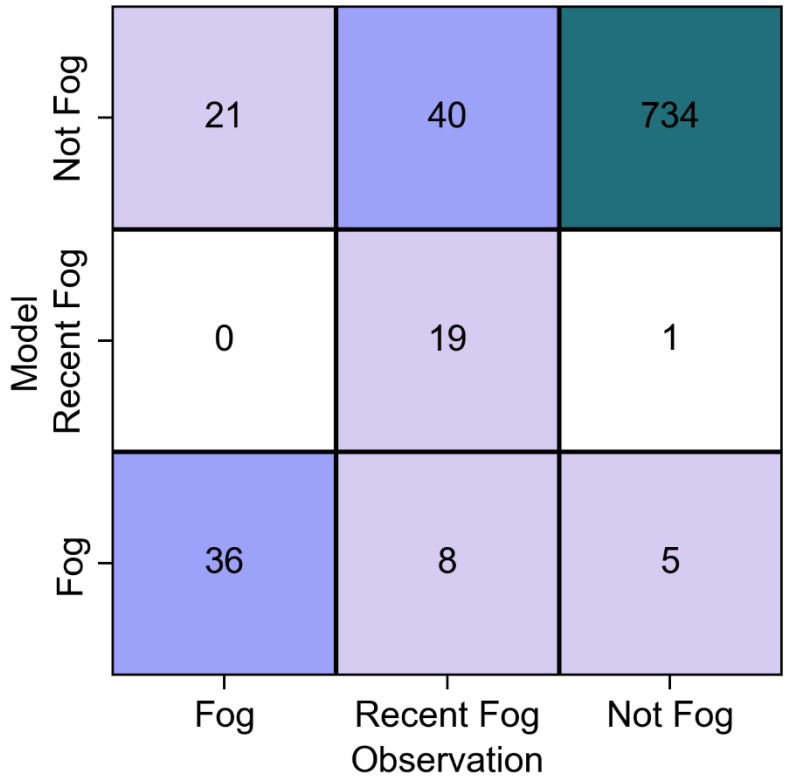

Figure C.6: The fog category determined using MERRA-2 and the observations. The number in each box is the number of hours spent in that box during the ARTofMelt campaign. The color of the box gets darker as the number of hours increases.

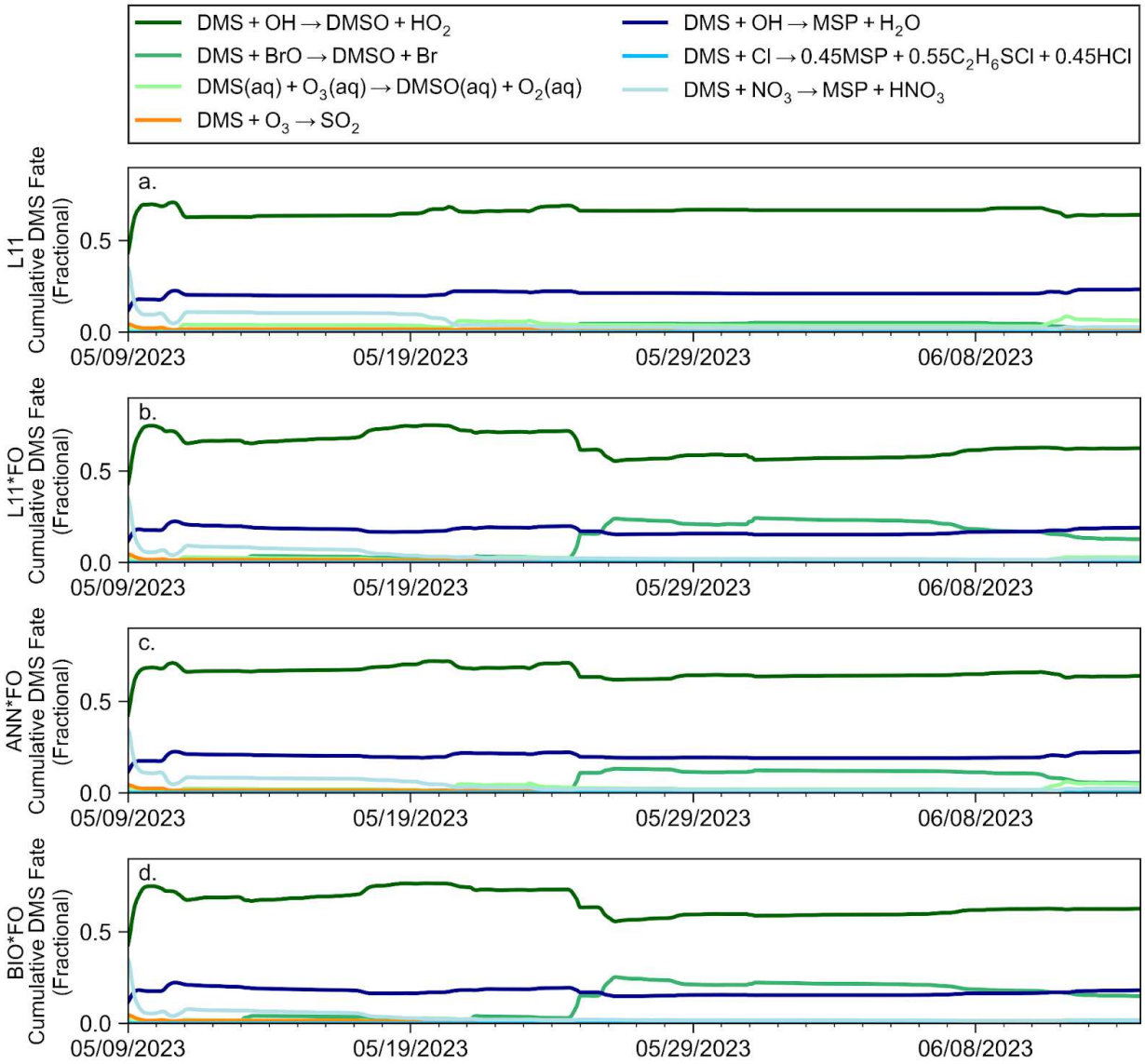

Figure C.7: Time series of the cumulative DMS oxidation pathway fractions starting on May 9, 2023 through the end of the ARTofMELT field campaign for the (a.) L11, (b.) L11*FO, (c.) B23, (d.) B23*FO simulations.

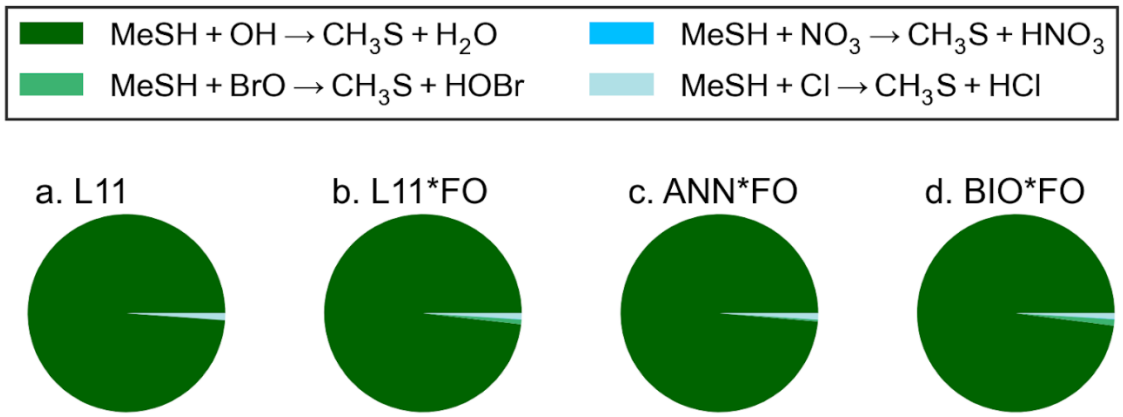

Figure C.8: MeSH oxidation pathways for the campaign average for (a.) L11, (b.) L11*FO, (c.) B23, and (d.) B23*FO.

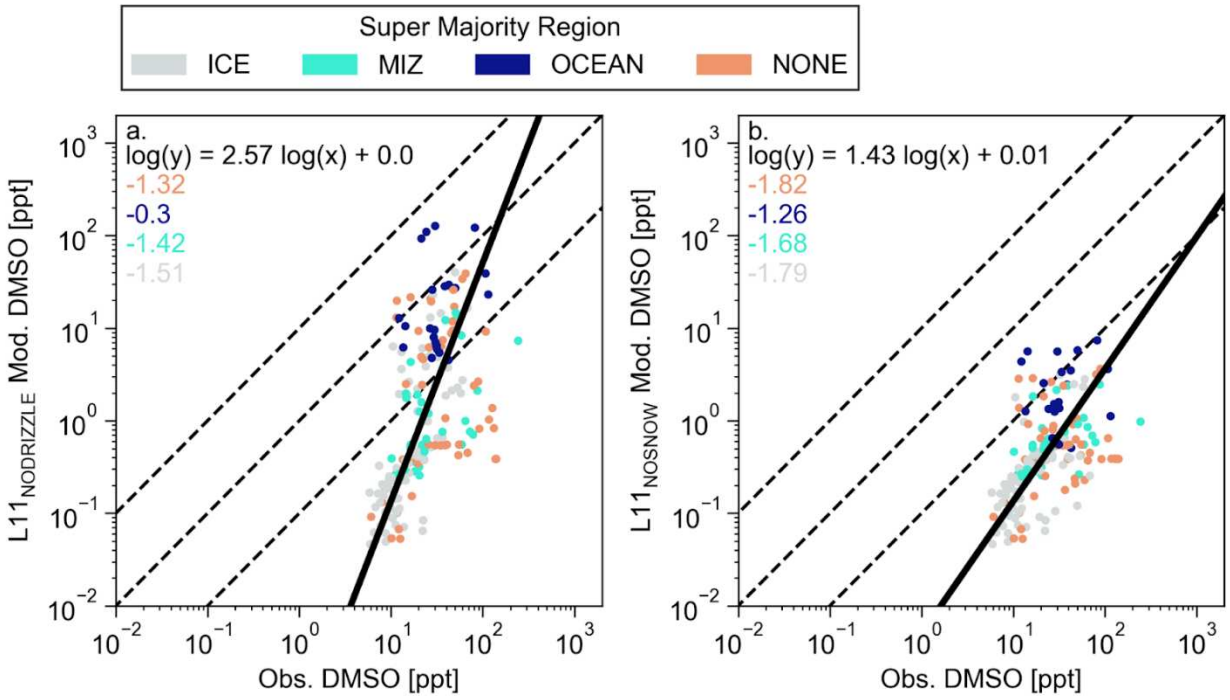

Figure C.9: Scatter plot comparing the Observed and Modeled DMSO from (a.) $L11_{NODRIZZLE}$, and (b.) $L11_{NOSNOW}$. The numbers on the panel correspond to the LMB colored by source region. Simulations are defined in Table 4.2, while source regions are defined in Table 4.3.

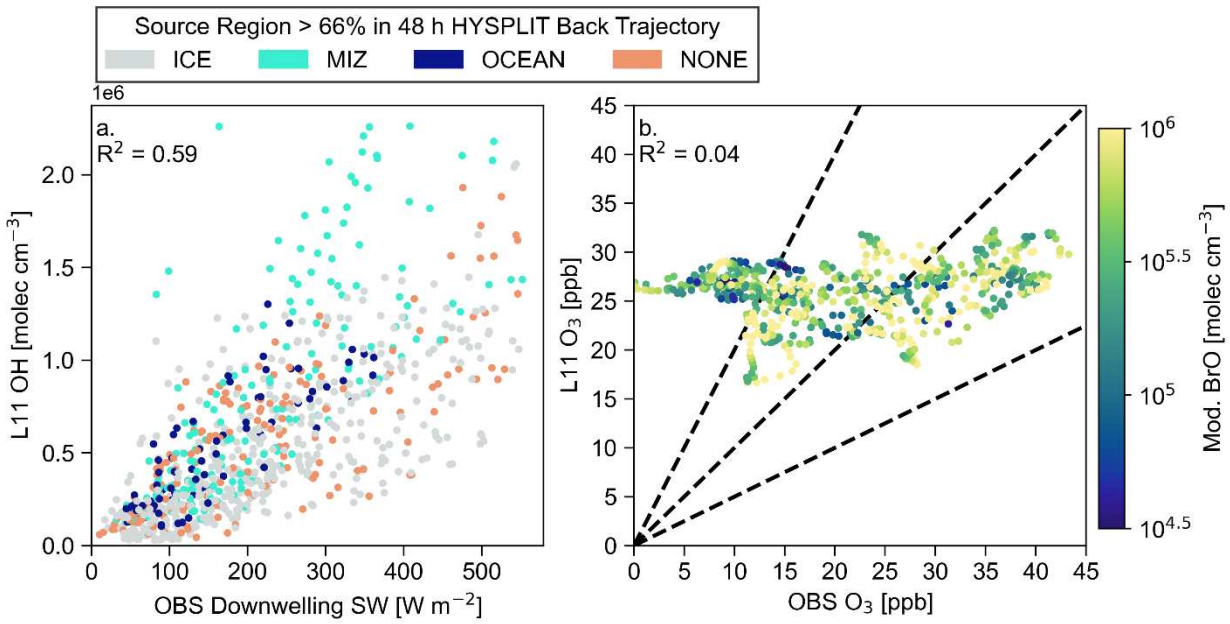

Figure C.10: (a.) L11 simulated OH as a function of observed downwelling shortwave (SW). (b.) One-to-one plot of L11 simulated and observed O_3.

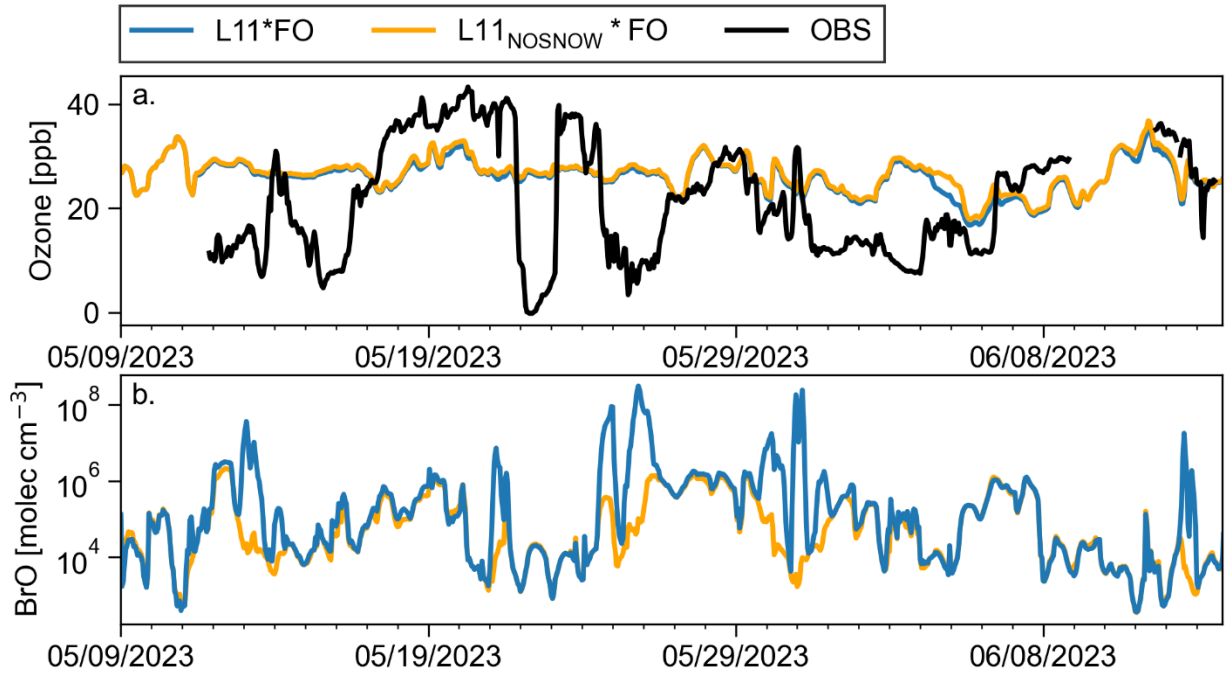

Figure C.11: (a.) Time series of O_3 during ARTofMELT for L11*FO, L11$_{NOSNOW}$*FO, and OBS. (b.) Time series of L11*FO and L11$_{NOSNOW}$*FO simulated BrO during ARTofMELT.

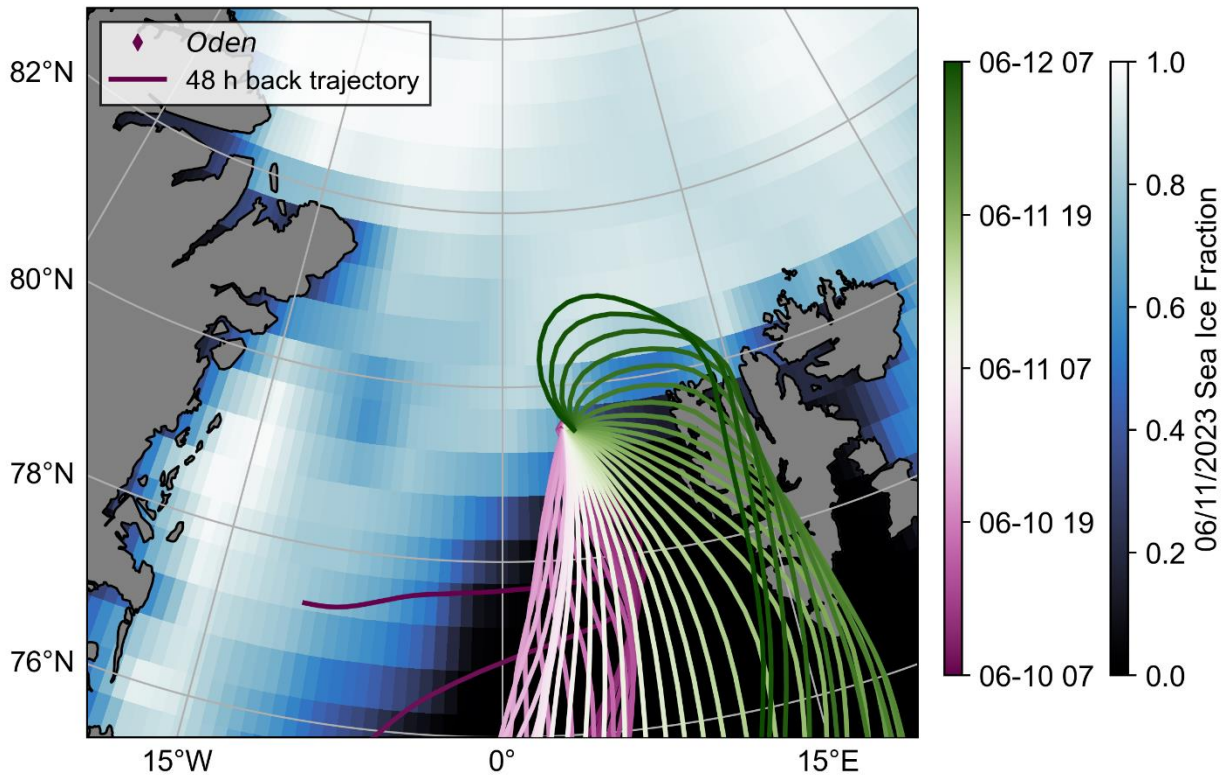

Figure C.12: 48 h back trajectories from 06/10/2023 07 UTC to 06/12/2023 07 UTC starting from *Oden*.

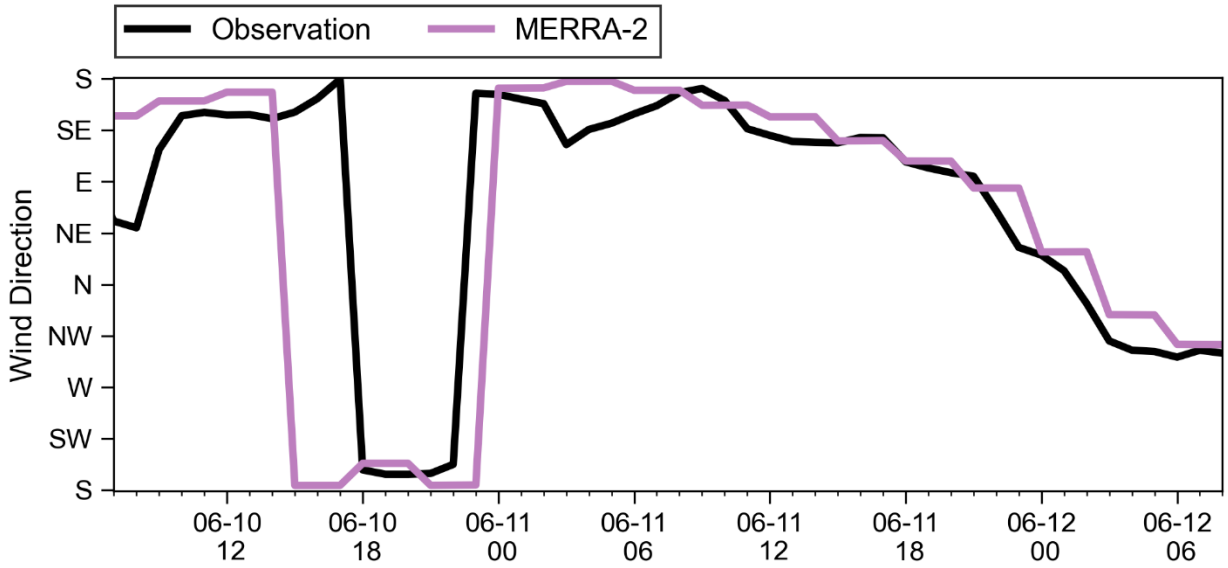

Figure C.13: Time series of the observed and MERRA-2 wind direction during the case study from June 10 to 12.

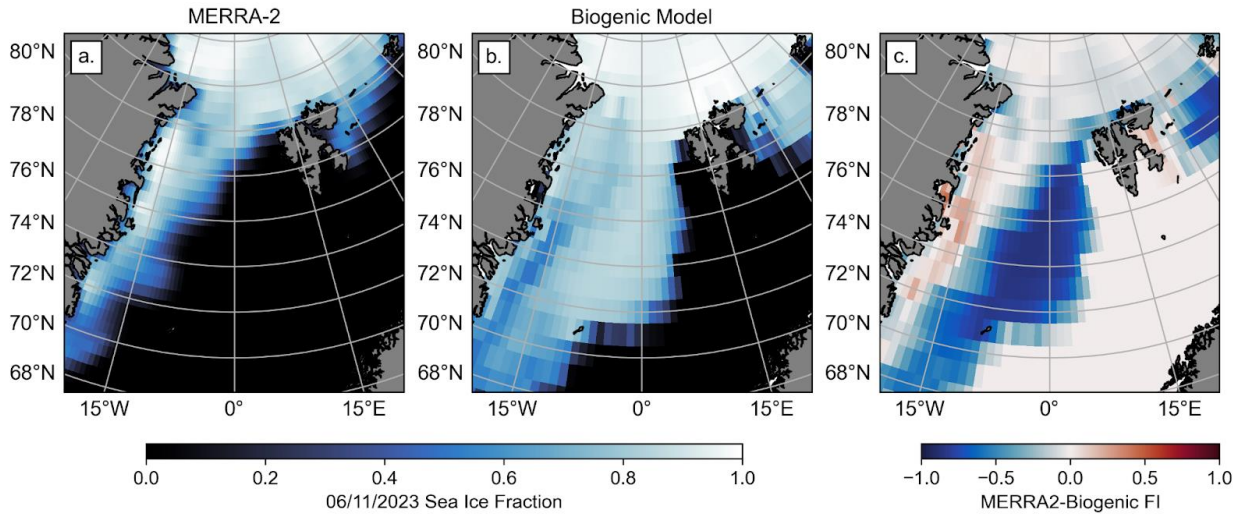

Figure C.14: (a.) MERRA-2 sea ice fraction for 06/11/2023. (b.) Sea ice fraction from the biogenic ocean model for 06/11/2023. (c.) Difference between MERRA-2 and the biogenic sea ice fractions for 06/11/2023.

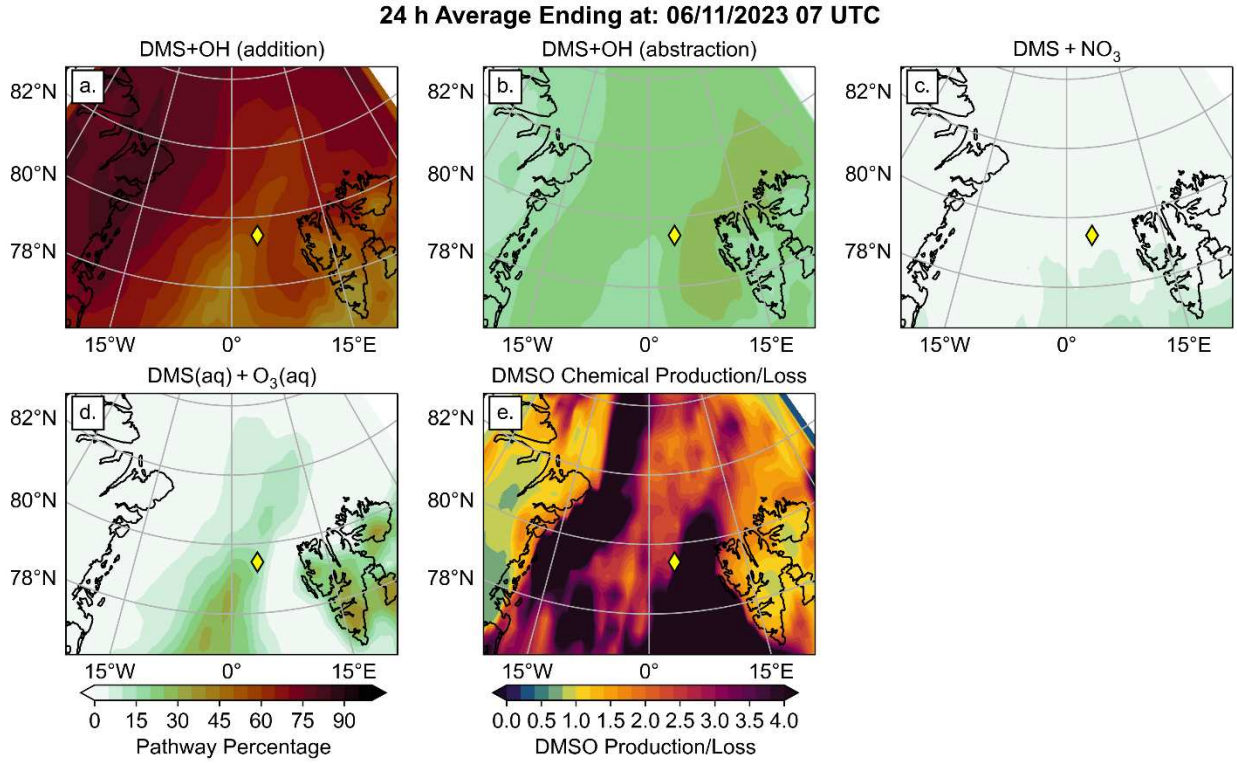

Figure C.15: Maps of the 24 h average ending at 06/11/2023 at 07 UTC for (a.)-(d.) primary DMS oxidation pathways (the other DMS oxidation pathways had less than 5% contribution for the entire study area), (e.) DMSO chemical production to DMSO chemical loss ratio. The yellow diamond shows the location of *Oden* at 06/11/2023 at 07 UTC. All of these maps are from the L11*FO simulation.

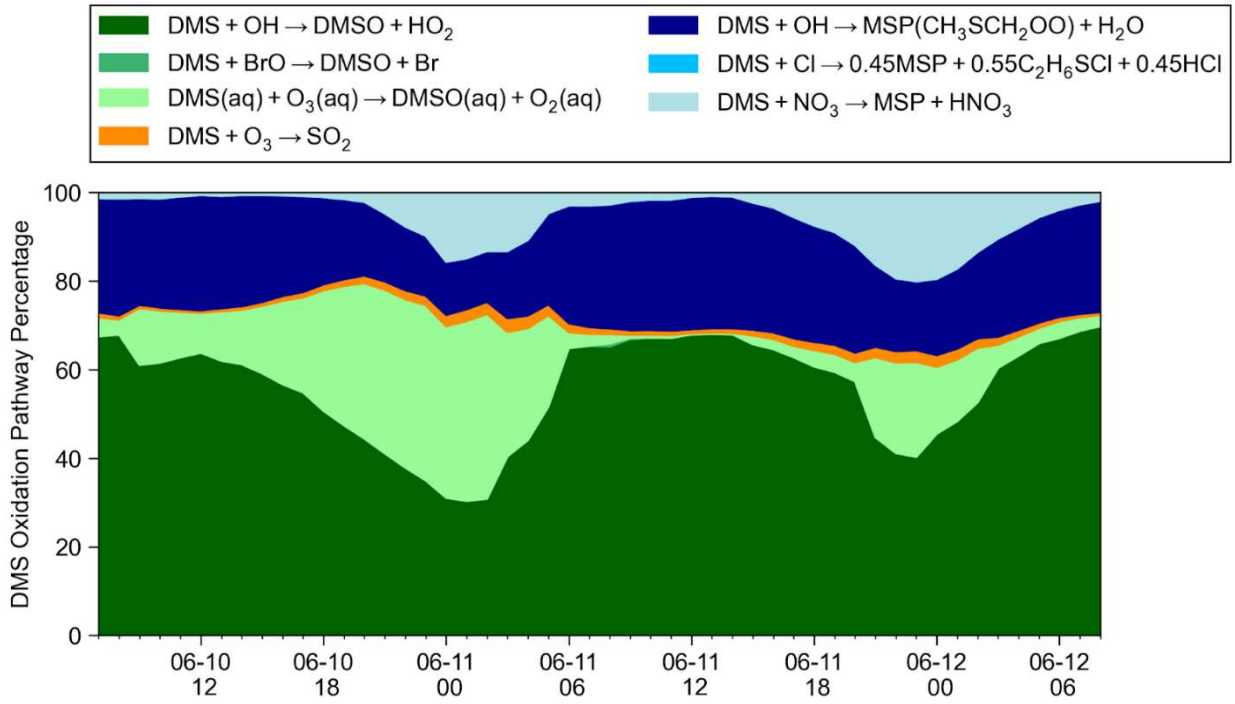

Figure C.16: The DMS oxidation pathway percentages for the L11*FO simulation during the case study from June 10 to June 12.

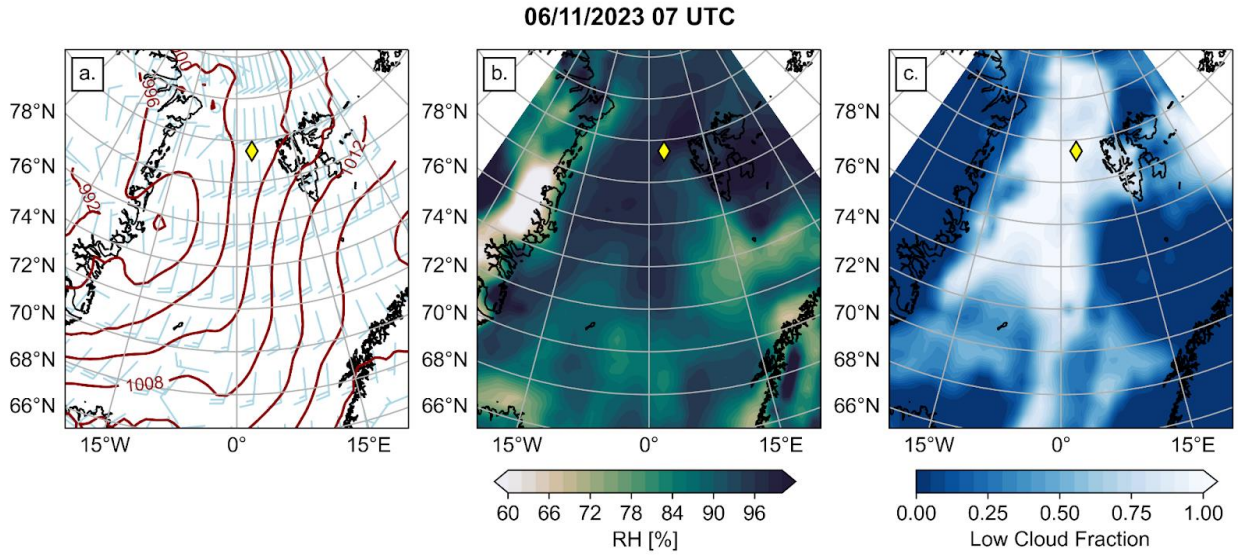

Figure C.17: Map of (a.) isobars (red lines) and wind barbs (light blue), (b.) the relative humidity, and (c.) the low cloud fraction from the MERRA-2 reanalysis for June 11, 2023 at 07 UTC. The yellow diamond shows the location of *Oden* at 06/11/2023 at 07 UTC.

Appendix D: Supplement to Processes Governing Atmospheric Aerosol in the North Atlantic Arctic Spring

Appendix D Figures

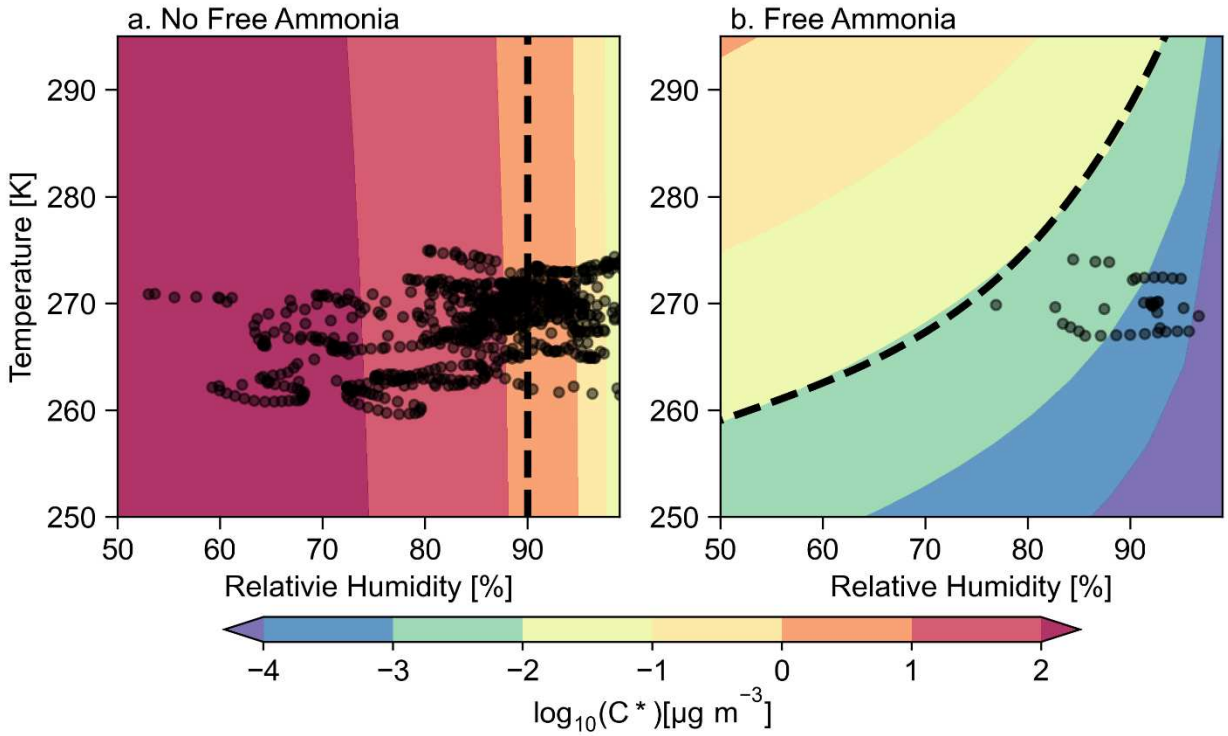

Figure D.1: The filled contours show the E-AIM predicted MSA equilibrium vapor pressure under conditions with (a.) no free ammonia and (b.) with free ammonia (re-made from Figure 1 of Hodshire et al. (2019)). The black dashed line at RH = 90% on (a.) represents the cut-off for representing MSA as VOC-like (left of line) and SVOC-like (right of line). The dashed line on (b.) is calculated using Eq. 1 of Hodshire et al. (2019): above the line MSA is treated as SVOC-like and below the line MSA is treated as ELVOC-like. The black points show where the GC-TOMAS points along the path of ARTofMELT in the model fall in this space. Following the methodology of Hodshire et al. (2019) a gas-phase mixing ratio of 10 ppt for ammonia is used as a cutoff between no free ammonia and free ammonia.

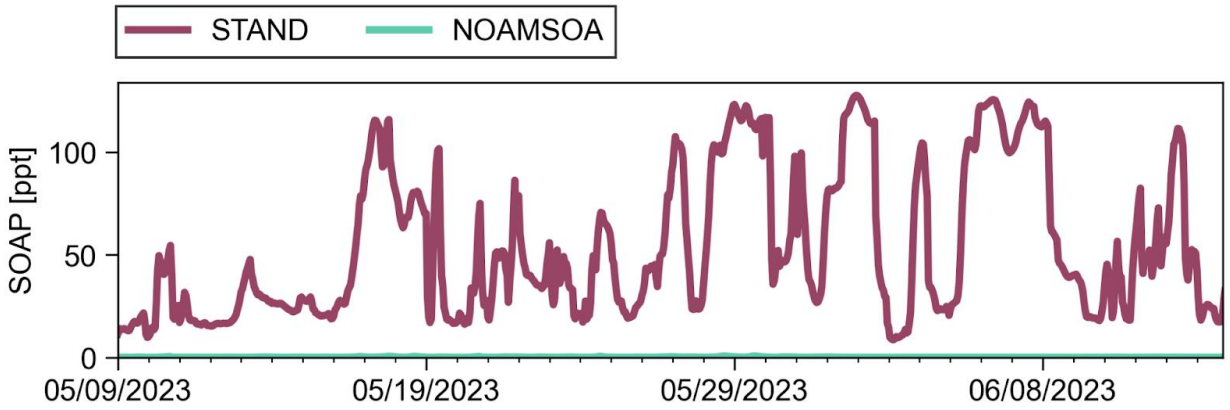

Figure D.2: Time series during ARTofMELT for the GC-TOMAS lumped SOA precursor for the STAND simulation and NOAMSOA simulation.

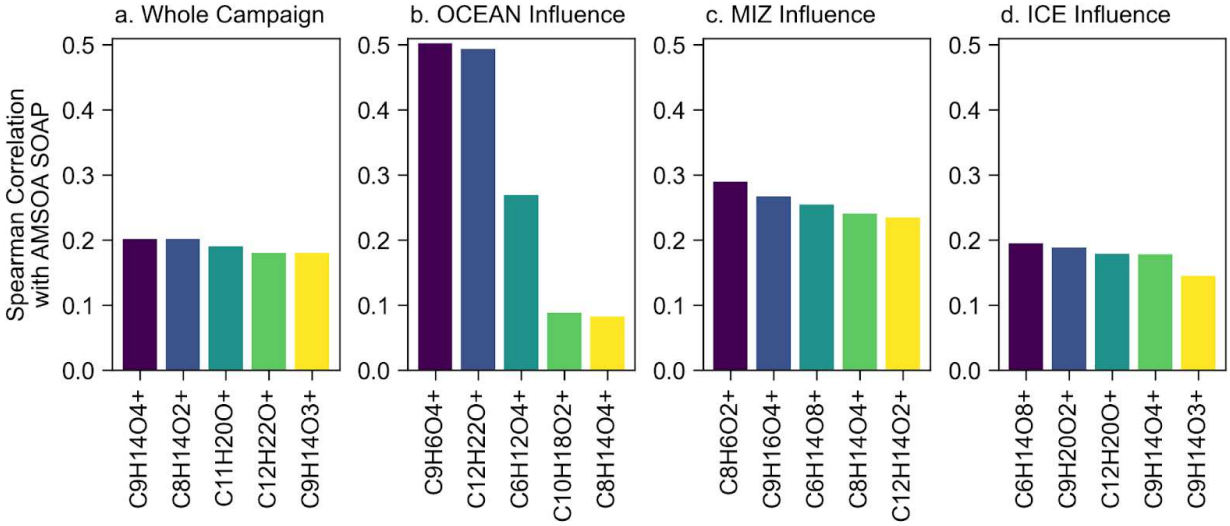

Figure D.3: Spearman correlation between GC-TOMAS AMSOA SOA precursors and observed reactive organic carbon along the ARTofMELT ship track for (a.) the whole campaign, (b.) when there is OCEAN influence, (c.) when there is MIZ influence, and (d.) ICE influence. Note that while more reactive organic carbon species were measured, we only show the top 5 highest correlations for the different source regions. The AMSOA SOA precursor is determined as the difference between the SOA precursor concentrations in the STAND and NOAMSOA simulations. Source regions are defined in Table 4.3.

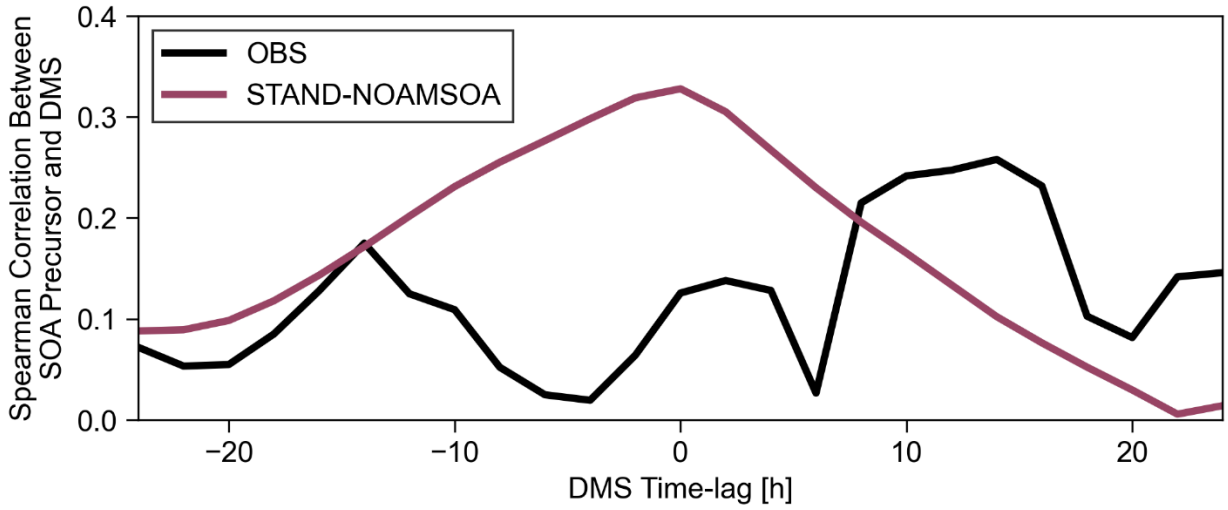

Figure D.4: In black, the spearman correlation between observed reactive organic carbon (potential SOA precursors) and observed DMS as a function of DMS time-lag. In magenta, the spearman correlation between the AMSOA SOA precursor (the difference between the STAND and NOAMSOA simulations) and the STAND simulated DMS.

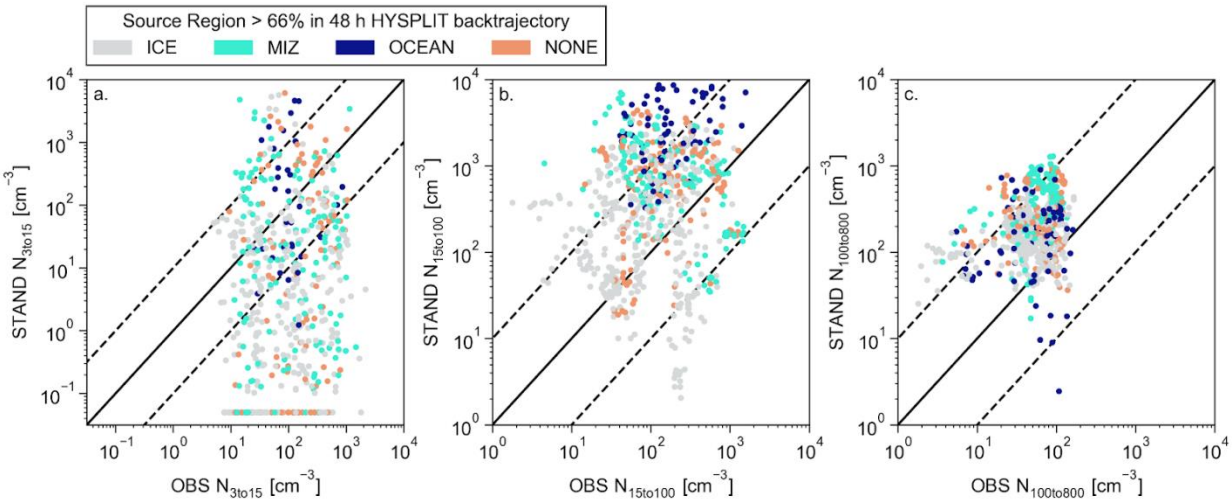

Figure D.5: Scatter plot of observed versus STAND simulated N_{3to15} (a.), $N_{15to100}$ (b.), and $N_{100to800}$ (c.) colored by source region as defined in Table 4.3.

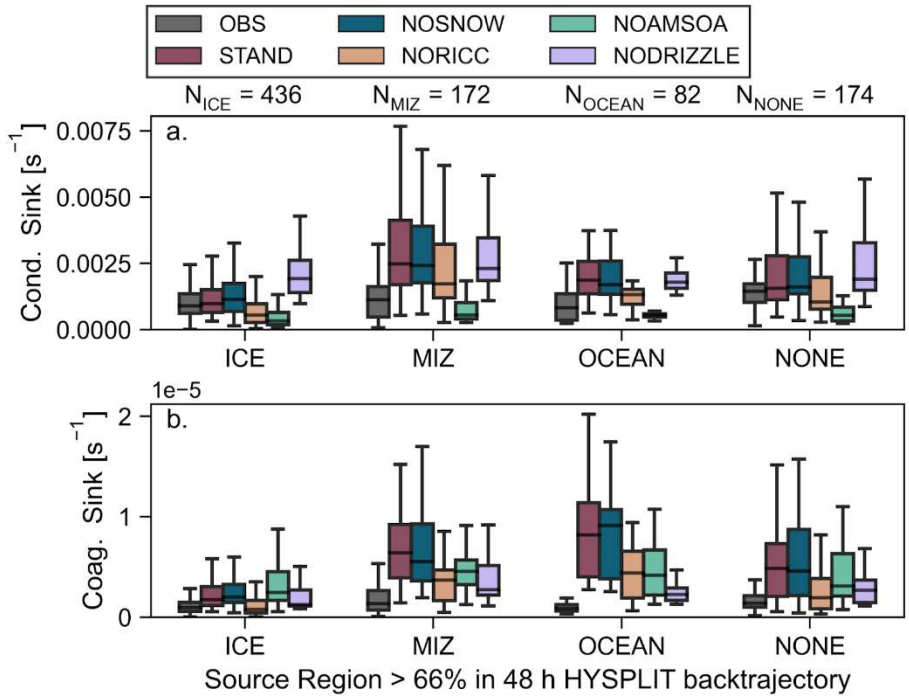

Figure D.6: (a.) Condensation Sink and (b.) Coagulation Sink during ARTofMELT for grouped by source region as defined in Table 4.3.

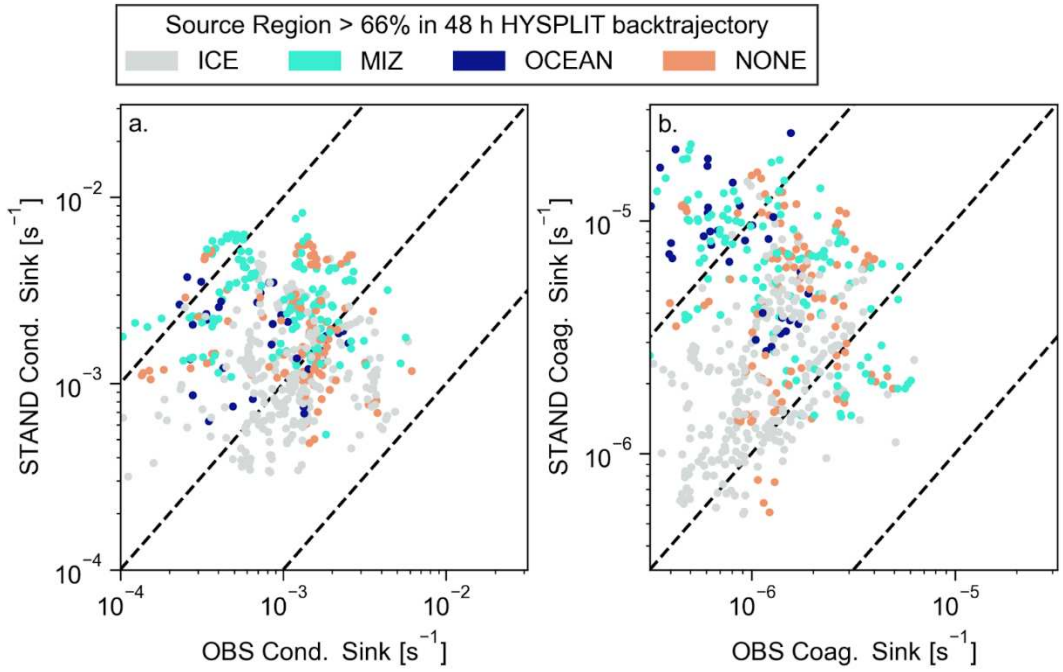

Figure D.7: Scatter-plot of the observed and STAND simulation (a.) condensation sink and (b.) coagulation sink colored by source region as defined in Table 4.3.

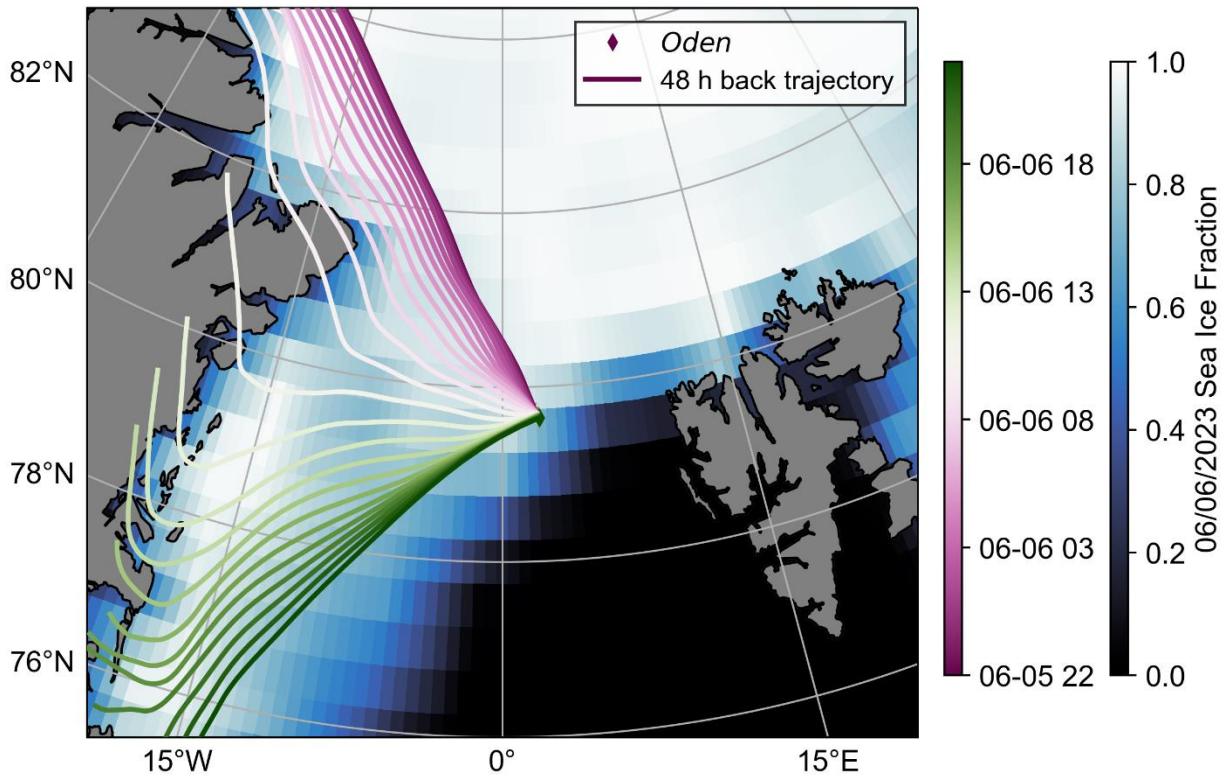

Figure D.8: Map of the HYSPLIT back trajectories using MERRA-2 reanalysis for the case study looking at June 6, 2023. All back trajectories are run for 48 h starting from *Oden*.

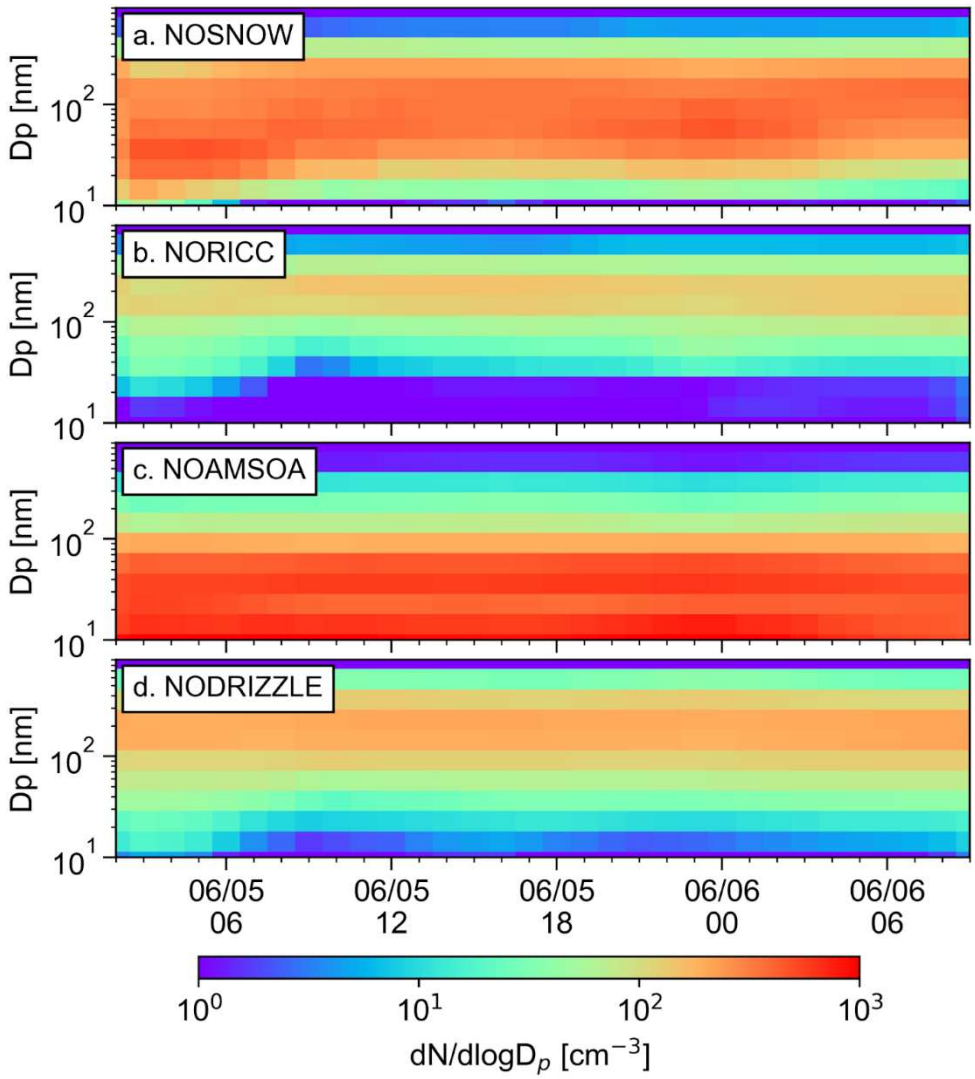

Figure D.9: (a.) to (d.) The aerosol size distribution from each of the sensitivity simulations along the back trajectory from Villum to *Oden*. The time series goes from 06/05/2023 02 UTC (one hour after the Villum overpass) to 06/06/2023 09 UTC (one hour before reaching *Oden*).

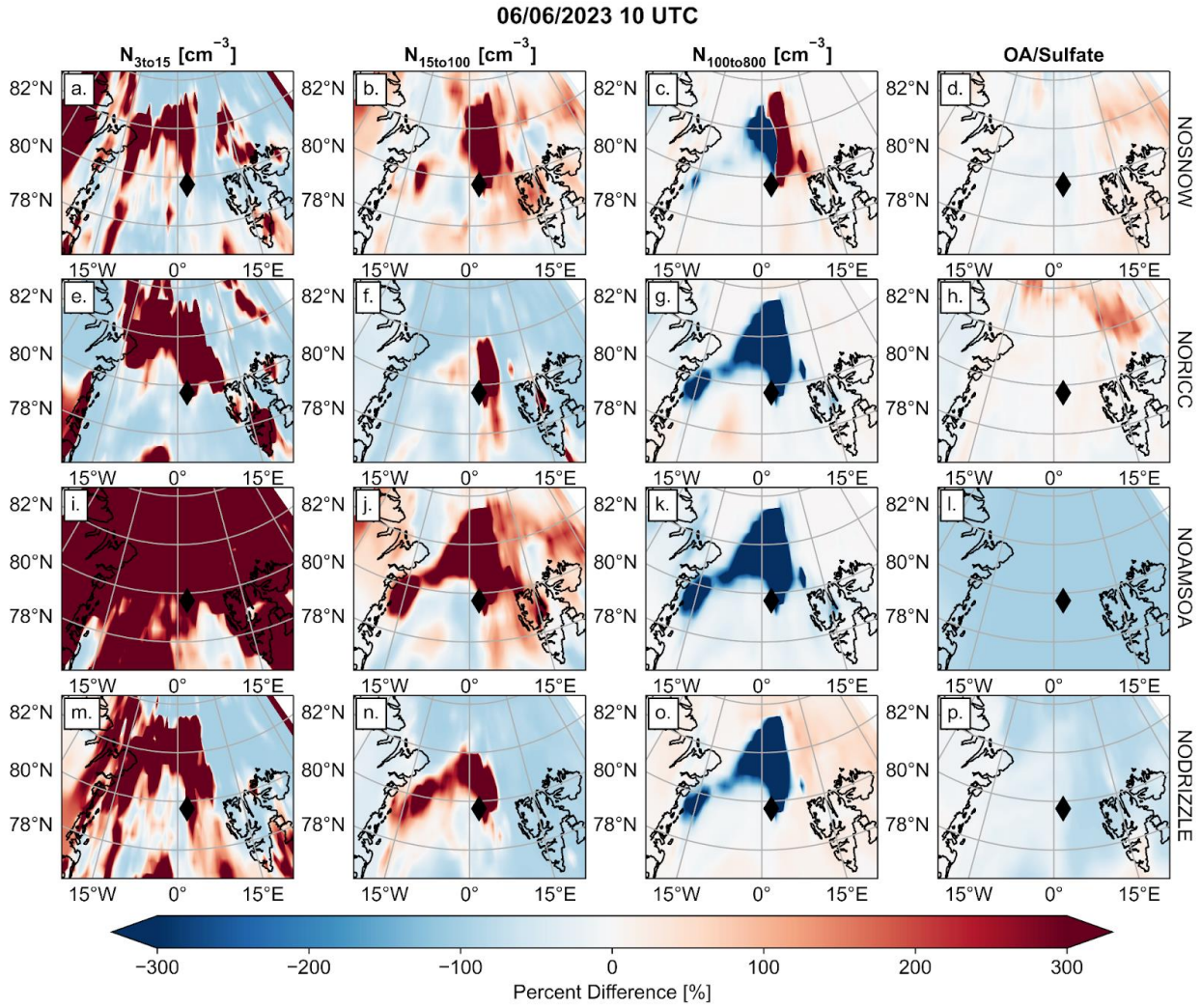

Figure D.10: Percent difference between a sensitivity simulation and the STAND simulation with the sign defined such that a larger value in the STAND simulation is negative for 06/06/2023 at 10 UTC (the STAND simulation is subtracted from the sensitivity simulation). The diamond shows the location of *Oden* at this time.

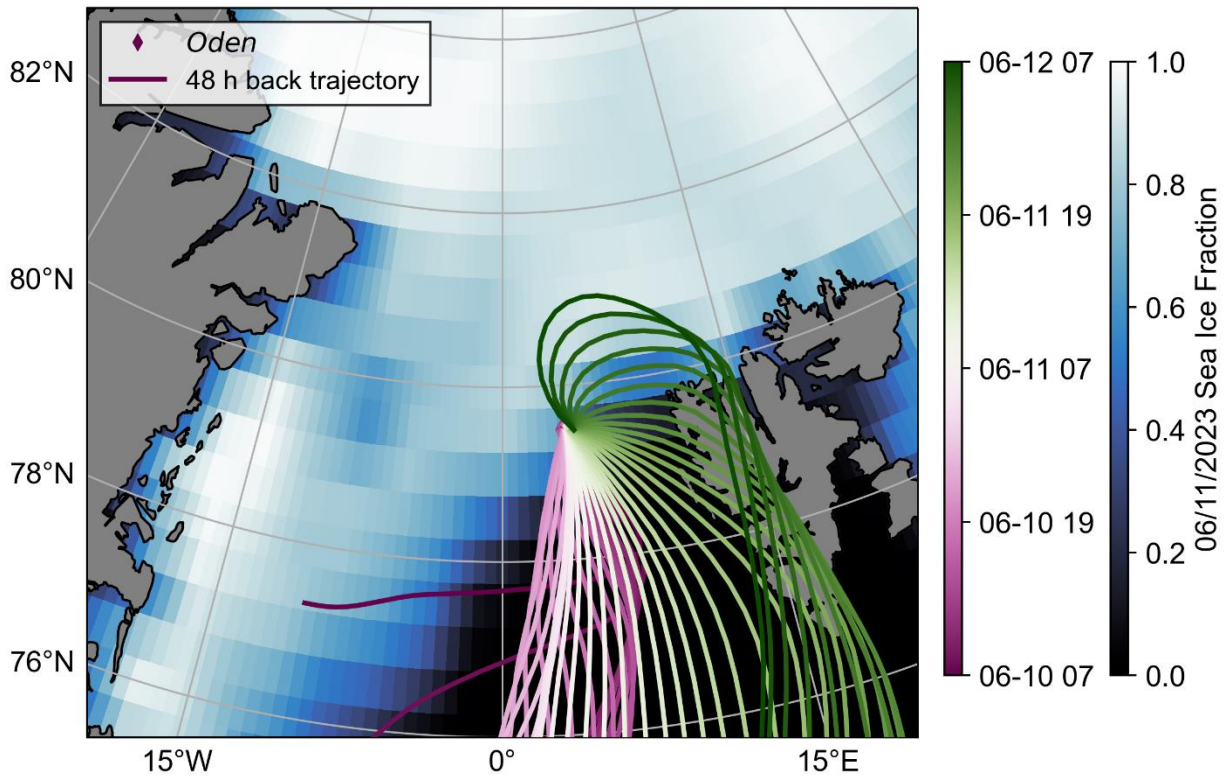

Figure D.11: Map of the HYSPLIT back trajectories using MERRA-2 reanalysis for the case study looking at June 11, 2023. All back trajectories are run for 48 h starting from *Oden*.

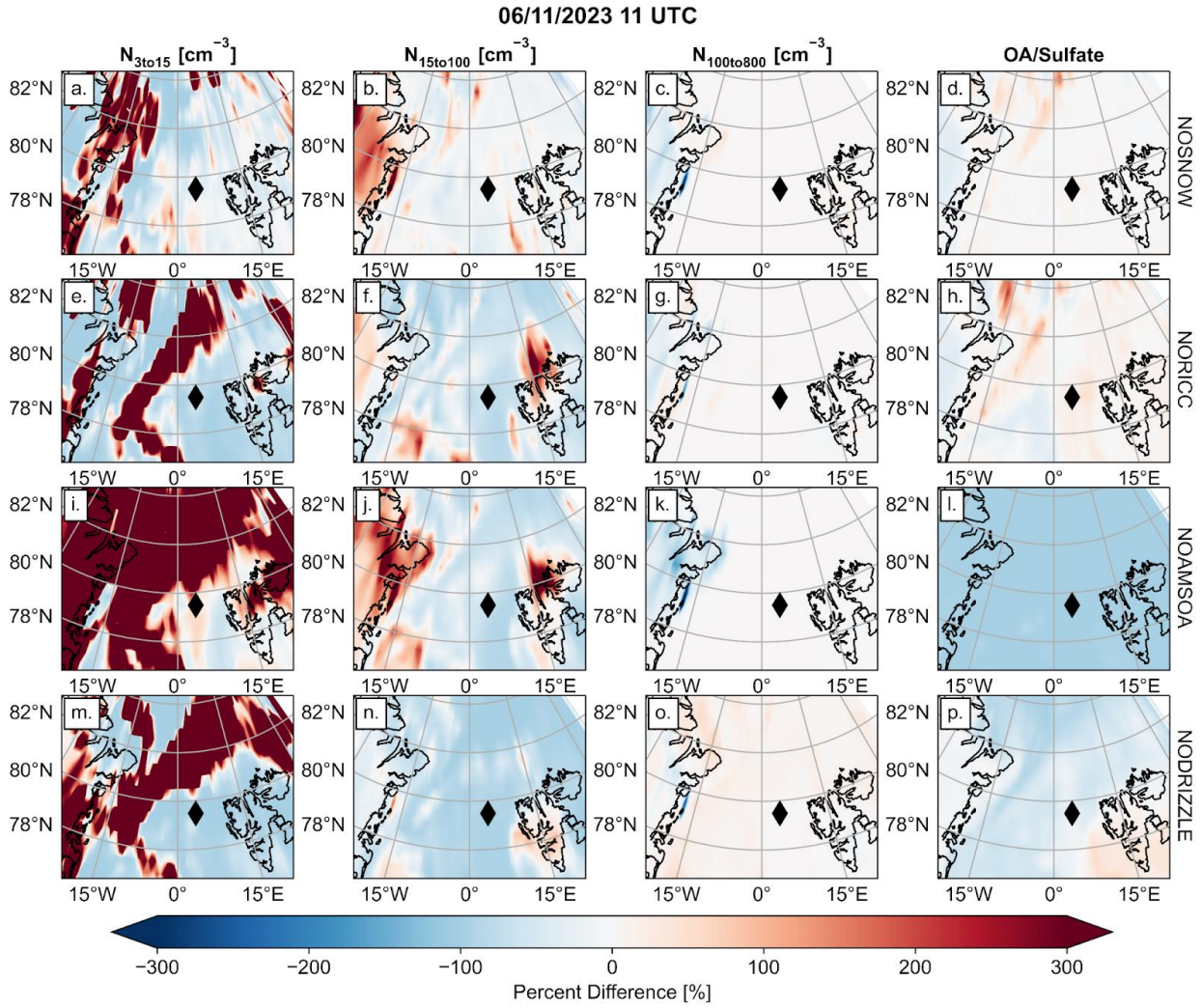

Figure D.12: Percent difference between a sensitivity simulation and the STAND simulation with the sign defined such that a larger value in the STAND simulation is negative for 06/11/2023 at 11 UTC (the STAND simulation is subtracted from the sensitivity simulation). The diamond shows the location of *Oden* at this time.